SAPIENZA
UNIVERSITÀ DI ROMA

INRS
Institut national de la recherche scientifique

Radiation resistance properties of electronic devices interacting with different radiation sources

Sapienza University of Rome
PhD in Accelerator Physics (XXXVI cycle)

Beatrice D'Orsi
ID number 1634446

Advisors
Prof. Patrizio Antici
Prof. Mauro Migliorati

Co-Advisor
Dr. Alessia Cemmi

Academic Year 2023/2024

Thesis defended on September 30, 2024
in front of a Board of Examiners composed by:

Prof. Maria Cristina Morone (chairman)
Prof. Giandomenico Amendola
Dr. Elias Metral

Radiation resistance properties of electronic devices interacting with different radiation sources
PhD thesis. Sapienza University of Rome

This thesis has been typeset by LaTeX and the Sapthesis class.

Author’s email: beatrice.dorsi@uniroma1.it, beatrice.dorsi@inrs.ca

All'amore della mia vita,
mia figlia Stella,
e ai miei genitori
che hanno sempre creduto in me.

Abstract

In high-radiation environments, such as those found in high-energy physics, space, and ignition facilities, it is paramount to employ components and devices capable of withstanding the stressful conditions imposed by these harsh settings. To understand the radiation-induced effects and ensure the proper functioning of systems used in these hostile conditions, preliminary tests of the devices against radiation are necessary.

In this joint doctoral thesis, comprising work performed at La Sapienza University of Rome, the Institut National de la Recherche Scientifique (INRS) in Canada, and the ENEA Research Centers of Casaccia and Frascati in Italy, a study of radiation-induced damage on electronic devices was carried out. Various radiation sources and characterization methods were employed for this purpose.

At the Advanced Laser Light Source (ALLS) laboratory of INRS, laser-accelerated protons with a broad energy spectrum were used to test electronics with a new and innovative stress test source. More conventional sources for irradiation tests, such as ^{60}Co gamma radiation available at the Calliope facility of the ENEA Casaccia R.C., and protons and neutrons from the TOP-IMPLART facility and the Frascati Neutron Generator, respectively, located at the ENEA Frascati R.C., were also used.

To further enrich the characterization of the electronic devices, electron irradiations are planned at the REX facility of the ENEA Frascati R.C. To determine the most suitable irradiation conditions at REX, a dosimetric intercalibration between the Calliope facility and the REX facility was performed within the framework of the ASI Supported Irradiation Facilities (ASIF) program. The results of this intercalibration are presented.

In the final part of the work, the radiation resistance properties of two types of electronic devices were examined by performing parametric tests on the components before and after irradiation with various radiation sources. Additionally, the Total Ionizing Dose (TID) effect and the displacement damage caused by the Non-Ionizing Energy Loss (NIEL) contribution were analyzed for all the stress tests performed. Specifically, for each radiation source used, the dose deposited by ionizing processes and the dose deposited by non-ionizing processes were calculated. This procedure made it possible to determine the dose required by different types of radiation to cause the same level of damage, allowing a comparison of the irradiation efficiency of laser-driven protons with conventional radiation sources.

Résumé

Dans les environnements à forte radiation, tels que ceux rencontrés en physique des hautes énergies, dans l'espace et dans les installations d'ignition, il est primordial d'utiliser des composants et des dispositifs capables de résister aux conditions stressantes imposées par ces milieux difficiles. Pour comprendre les effets induits par les radiations et assurer le bon fonctionnement des systèmes utilisés dans ces conditions hostiles, des tests préliminaires des dispositifs contre les radiations sont nécessaires.

Dans cette thèse de doctorat conjointe, comprenant des travaux effectués à l'Université La Sapienza de Rome, à l'Institut National de la Recherche Scientifique (INRS) au Canada, et aux centres de recherche ENEA de Casaccia et Frascati en Italie, une étude des dommages induits par les radiations sur des dispositifs électroniques a été réalisée. Diverses sources de radiation et méthodes de caractérisation ont été utilisées à cet effet.

Au laboratoire Advanced Laser Light Source (ALLS) de l'INRS, des protons accélérés par laser avec un large spectre d'énergie ont été utilisés pour tester des dispositifs électroniques avec une nouvelle source de test de stress innovante. Des sources plus conventionnelles pour les tests d'irradiation, telles que les radiations gamma ^{60}Co disponibles à l'installation Calliope du centre ENEA de Casaccia, et les neutrons et protons du générateur de neutrons de Frascati et de l'installation TOP-IMPLART, respectivement situés au centre ENEA de Frascati, ont également été utilisées.

Pour enrichir davantage la caractérisation des dispositifs électroniques, des irradiations électroniques sont prévues à l'installation REX du centre ENEA de Frascati. Pour déterminer les conditions d'irradiation les plus appropriées à REX, une intercalibration dosimétrique entre l'installation Calliope et l'installation REX a été réalisée dans le cadre du programme ASI Supported Irradiation Facilities (ASIF). Les résultats de cette intercalibration sont présentés.

Dans la dernière partie du travail, les propriétés de résistance aux radiations de deux types de dispositifs électroniques ont été examinées en effectuant des tests paramétriques sur les composants avant et après irradiation avec diverses sources de radiation. En outre, l'effet de la dose ionisante totale (TID) et les dommages de déplacement causés par la contribution de la perte d'énergie non ionisante (NIEL) ont été analysés pour tous les tests de stress effectués. Plus précisément, pour chaque source de rayonnement utilisée, la dose déposée par les processus ionisants et la dose déposée par les processus non ionisants ont été calculées. Cette procédure a permis de déterminer la dose nécessaire pour que différents types de rayonnement provoquent le même niveau de dommages, permettant ainsi de comparer l'efficacité d'irradiation des protons accélérés par laser avec celle des sources de rayonnement conventionnelles.

Contents

Introduction **vii**

1 Radiation environments **1**
1.1 High-luminosity accelerators 1
  1.1.1 The Large Hadron Collider 2
1.2 Space environment 5
1.3 Fusion reactors 9
  1.3.1 Divertor Tokamak Test facility 11

2 Radiation effects on electronic and optoelectronic devices **15**
2.1 Electronic devices 16
  2.1.1 Intrinsic and extrinsic semiconductors 17
  2.1.2 PN junctions 18
  2.1.3 Bipolar junction transistors 21
  2.1.4 Optoisolators 25
2.2 Radiation effects in semiconductors 26
  2.2.1 Non ionizing energy loss 27
  2.2.2 Ionization damage 33
  2.2.3 Deposited dose 35
  2.2.4 Radiation effects on bipolar junction transistors 36
  2.2.5 Radiation effects on optoisolators 39

3 Experimental setup and facilities **41**
3.1 Advanced Laser Light Source laboratory 41
  3.1.1 TNSA mechanism 45
  3.1.2 Laser-driven ions characteristics 48
3.2 Calliope gamma irradiation facility 51
  3.2.1 Calliope facility dosimetric systems 52
3.3 TOP-IMPLART proton linac 58
3.4 Frascati Neutron Generator 61
3.5 Removable Electron to X-ray source accelerator 64

4 Calliope gamma irradiation facility and REX electron beam dosimetric intercalibration **66**
4.1 Alanine calibration curves determination at Calliope facility 67
4.2 Dose mapping of REX irradiation chamber with alanine-EPR dosimeters 72

5 Electronics irradiation: experimental results 83
- 5.1 Experimental measurements . . . 85
- 5.2 Bipolar junction transistors characterization . . . 86
  - 5.2.1 Before irradiation characterization . . . 88
  - 5.2.2 Gamma irradiation . . . 89
  - 5.2.3 Laser-driven proton irradiation . . . 104
  - 5.2.4 Proton irradiation . . . 109
  - 5.2.5 Neutron irradiation . . . 115
- 5.3 Dose deposition study . . . 123
  - 5.3.1 Gamma radiation deposited dose . . . 123
  - 5.3.2 Laser-driven protons deposited dose . . . 126
  - 5.3.3 Conventional protons deposited dose . . . 129
  - 5.3.4 Neutrons deposited dose . . . 130
- 5.4 Results comparison . . . 130
- 5.5 Optoisolators characterization . . . 136
  - 5.5.1 Gamma irradiation . . . 138

Conclusion and perspectives 145

Bibliography 158

Introduction

Electronic devices are used for the production of electronic circuits employed in many fields. The operational features of these devices can be damaged by the adverse radiation environments present in several applications. For example, particle physics high-luminosity accelerators, space environments and ignition facilities may affect the functioning of electronics due to the high radiation levels. The damage caused to the devices differs for each energy deposition process and consequently for the different radiation sources (synchrotron radiation, cosmic rays, particles of different origin). Both the high-luminosity machines and space environments are composed of mixed particles. Therefore, it is of fundamental importance to characterize the electronic devices and radiation detectors used in high radiation environments to ensure their correct functioning during operation. This study is focused on the effects of ionizing radiations. It is important to note that, although we refer to the radiation as "ionizing", it is not the only way in which radiation deposits energy into matter, as will be shown.
The main effects caused by the interaction of incoming particles and electronics are atomic displacements and energy loss by ionization (or by collision). Atomic displacements result from Non-Ionizing Energy Loss (NIEL) processes, where the energy of the incoming particle causes the displacement of an atom or the dissipation of energy in lattice vibrations. Ionization, on the other hand, involves the excitation or emission of atomic electrons. The proportion of energy deposited by NIEL processes compared to ionization processes varies depending on the particle type. Radiation-induced defects can be categorized into two types: bulk damage, also known as Displacement Damage (DD), caused by NIEL processes and quantified as the Displacement Damage Dose (DDD) or NIEL dose, and surface damage, which results from the trapping of free charges generated by ionizing radiation. The accumulation of these trapped charges is quantified as the Total Ionizing Dose (TID), which builds up as ionizing radiation produces electron-hole pairs, leading to charge trapping in insulating layers, such as oxide layers in semiconductors. These defects affect the electrical behavior of semiconductor devices and must be investigated after irradiation.

To simulate the adverse radiation environments that an electronic device may encounter during operation, irradiation can be performed in laboratories using different particle sources. TID effects are typically achieved through exposure to ionizing radiation, such as gamma rays or electrons. In contrast, DD is induced by particles such as protons and neutrons. Protons are effective at displacing atoms in the material crystal lattice due to their mass and charge. Neutrons, while uncharged

and not directly causing ionizing effects, are especially effective at displacing atoms due to their interactions with atomic nuclei.
In the last two decades, laser-driven particle acceleration, obtained by irradiating a solid target with an ultra-intense ($I > 10^{18}$ W/cm^2) short-pulse (<1 ps), has been extensively investigated due to its various potential applications in many fields. One of the possible applications is related to the stress testing of materials. In particular, laser-accelerated protons can be used in place of or together with protons from more conventional sources because of their ability to produce damage on a very short time scale.

In this thesis project, the investigation of the radiation hardness of two kinds of electronic components is reported, with particular attention given to the demonstration of the effectiveness of dose delivery by laser-generated protons. Specifically, two kinds of Bipolar Junction Transistors (BJTs), NPN and PNP, and optoisolators were irradiated. The BJTs were subjected to gamma radiation, laser-driven protons, protons and neutrons from conventional accelerator and the optoisolators to gamma radiation.

The first part of this work provides an overview of radiation environments characteristic of many research fields and their effects on electronics. Chapter 1 describes the radiation levels that electronics must withstand in well-known experiments and missions. Chapter 2 summarizes the main features of BJTs and optoisolators, detailing radiation effects in semiconductors and the specific impacts on BJTs and optoisolator parameters, with a focus on TID and NIEL dose deposition.

Chapter 3 reports on the facilities where irradiation tests were conducted. Specifically, laser-driven proton irradiation was carried out at the Advanced Laser Light Source (ALLS) laboratory of the Institut National de la Recherche Scientifique (INRS) in Varennes, Montreal, Canada. In the section describing the ALLS facility, the most routinely employed mechanism to accelerate ions using laser-plasma interaction is detailed, along with the main features of the accelerated ions. Gamma irradiation tests were performed at the Calliope gamma irradiation facility of the ENEA Casaccia Research Centre in Rome, Italy. Along with the description of the Calliope facility, an overview of the main dosimetric systems employed in this facility is presented. Subsequently, the TOP-IMPLART facility of the ENEA Frascati Research Centre in Frascati, Italy, where protons from a linear accelerator were used for the tests, is presented. Following this, the Frascati Neutron Generator (FNG) at the ENEA Frascati Research Centre, the facility where neutron irradiation was conducted, is reported. Finally, the REX facility of the ENEA Frascati Research Centre, which comprises a linear electron accelerator, is described.

The second part of this thesis focuses on a campaign of dosimetric measurements performed within the framework of the ASI Supported Irradiation Facilities (ASIF) program. One of the most effective dosimetric techniques used was alanine-EPR dosimetry, which detects stable free radicals induced by ionizing radiation (e.g., gamma rays or electrons) in the crystalline L-α-alanine amino acid using Electron Spin Resonance (EPR) spectroscopy. This method, due to its wide dose range and dose rate and energy independence for energies around a few MeV, is well suited for REX electron beam dosimetric intercalibration. Dosimetric measurements for dose rate distribution inside the REX chamber were performed using alanine-EPR dosimeters calibrated with the absolute Fricke solution at the Calliope facility. Specifically, alanine dosimeters were irradiated at various points within the REX chamber with different irradiation times and at varying distances from the electron source. The obtained results are presented in Chapter 4.

The last part of the project presents the experimental results obtained after irradiation. Chapter 5 initially provides a description of the experimental setup used for electrical measurements of the devices. Afterward, the characterization of BJTs before irradiation is shown. Subsequently, the results obtained after irradiation with ^{60}Co gamma radiation, laser-driven protons, and protons and neutrons from conventional accelerators of BJTs are presented. Various device parameters were characterized before and after irradiation to assess the radiation resistance properties of the components. As described in Chapter 3, the irradiation facilities provided irradiation conditions based on different parameters (e.g. number of shots, total absorbed dose, particle fluence). To compare the different radiation sources and to evaluate the dose delivery efficiency of the employed radiation source, with particular attention to the laser-driven protons source, a value of deposited dose after irradiation was obtained for each facility. Chapter 5 details the procedure followed to determine the deposited dose value. Finally, the results of optoisolators tests conducted before and after irradiation with ^{60}Co gamma photons are presented.

Chapter 1

Radiation environments

Over the last century, significant efforts have been made across various research fields to expand our understanding of the world around us. For instance, High Energy Physics (HEP) experiments, such as those conducted at the Large Hadron Collider (LHC), have contributed to a more precise comprehension of the subatomic realm, while advancements in technology have enabled humanity to explore life beyond Earth through space missions. However, both HEP experiments and space missions, along with ignition facilities and nuclear reactors, operate in hostile environments where different radiation sources are present. Consequently, specialized equipment and devices are required to withstand these conditions, as high levels of radiation can degrade their performance. The operational conditions are particularly demanding for electronic devices and radiation detectors, as failures in these systems can critically compromise the performance of machinery in particle physics and nuclear experiments, or compromise the success of space missions.

The radiation effects on electronics vary depending on the device characteristics, the type of radiation, and the radiation environment in which they operate. Adverse environments are characterized by distinct types of radiation and energy distributions. Below, a descriptions of high-luminosity machines, space radiation environments and fusion reactors are provided.

1.1 High-luminosity accelerators

In a collider, various components of the detection equipment are exposed to radiation from numerous sources, with intensity levels varying across different operational areas. Dedicated activities are essential for developing and qualifying electronic systems tailored to the experiment needs. The selection of electronics is guided by evaluating radiation levels in different machine locations. This process involves combining measurements from past experimental runs, simulations and considerations to define the necessary specifications. For example, the radiation sources present in accelerators like the Large Hadron Collider (LHC) are detailed in the following [1].

1.1.1 The Large Hadron Collider

The LHC is the most powerful particle accelerator in the world and it is the last element of the chain of CERN accelerators complex. It is a 27 km long ring that has been designed to provide proton-proton collision with a center of mass energy of 13 TeV, accelerating two proton beams, in contra-rotating directions, up to an energy of 6.5 TeV each. The two beams collides in four points of the accelerator ring corresponding to four of the main LHC experiments: A Toroidal LHC ApparatuS (ATLAS), the Compact Muon Solenoid (CMS), A Large Ion Collider Experiment (ALICE) and the LHC beauty (LHCb).

The fundamental figure to quantify collider performances is the luminosity $\mathcal{L}$. It is defined as the ratio of the interaction rate R to the total cross section σ_T for a particular interaction:

$$\mathcal{L} = \frac{R}{\sigma_T}. \tag{1.1}$$

So the instantaneous luminosity represents the potential number of collisions per unit time and it depends on the kinematic and geometrical features of the beam. For a collider such as LHC, it can be expressed as:

$$\mathcal{L} = \frac{N^2 n_b f}{4\sqrt{\epsilon_x \epsilon_y \beta_x^* \beta_y^*}} \mathcal{F}(\alpha) \tag{1.2}$$

where N is the number of particles per bunch, n_b is the number of bunches, f is the revolution frequency and $\mathcal{F}(\alpha)$ is a correction factor due to the angle at which beams collide. The denominator represents the effective bunch section, where ϵ denotes the transverse emittance and β^* is the amplitude function at the collision point.

The instantaneous luminosity decreases during a data-taking according to the exponential law:

$$\mathcal{L}(t) = \mathcal{L}_{max} e^{-\frac{t}{\tau}} \tag{1.3}$$

where τ is given by the contribution of many effects that deteriorate the luminosity, such as the growth of the emittance or the drop of beam intensity.

The integral over time of the instantaneous luminosity represents the integrated luminosity:

$$L_{int} = \int_0^t \mathcal{L}(t')dt'. \tag{1.4}$$

The number of proton-proton collisions in a time interval is proportional to the integrated luminosity. It is usually multiplied by the cross section of a specific physics process to obtain the expected number of events for that process. It is usually expressed in inverse femtobarns fb^{-1}.

The LHC is made up of eight octants (as shown in Figure 1.1) and the central part of each octant is called Insertion Region (IR) and is connected to the next one by a curved section known as arc. Each LHC arc has one Dispersion Suppressor (DS) on each end that acts as a connection between the arc and the IR and consists of four individually powered quadrupole magnets each separated by two dipole magnets [2]. Each IR within the LHC has a specific function. Four of these regions (IR1, IR2, IR5, and IR8) correspond to the beams Interaction Points (IPs) and house the detectors

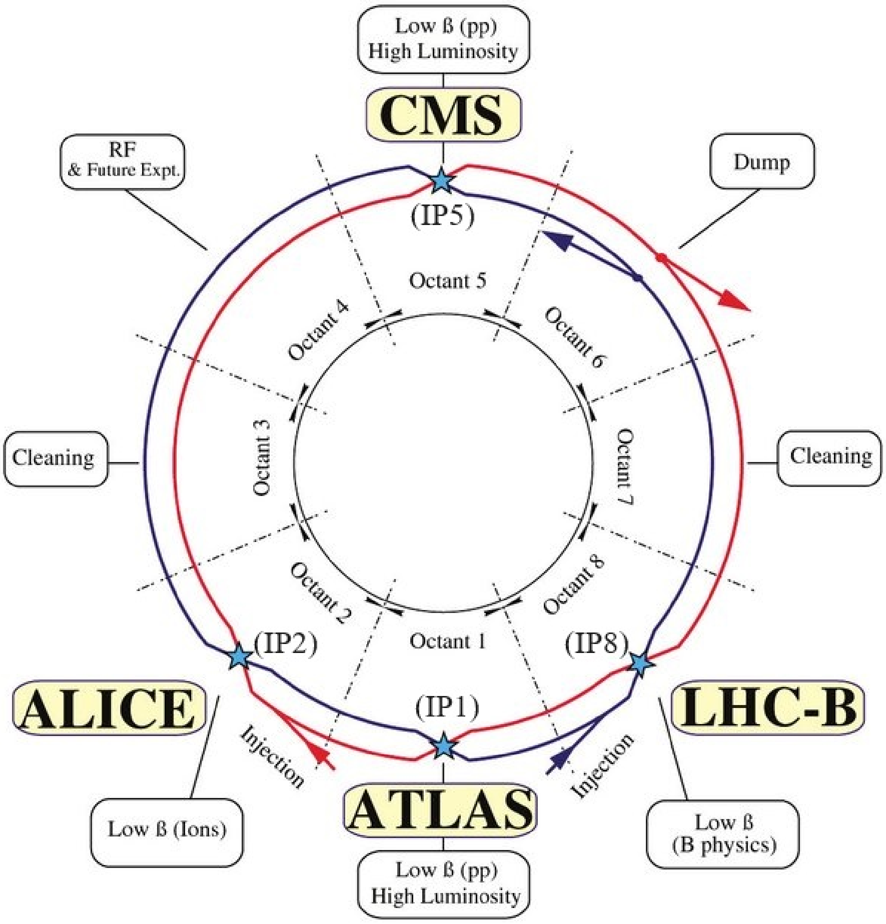

Figure 1.1. Scheme of the LHC ring [2].

of the main four LHC experiments (ATLAS, ALICE, CMS and LHCb respectively). IR3 and IR7 host the beam collimation systems, while IR4 is dedicated to radio frequency cavities and IR6 is utilized for beam extraction and dump systems [1]. Some experimental facilities and equipment of the LHC are situated in shielded areas outside the main tunnel. Consequently, the radiation field in the LHC is characterized by a wide variety of particle types and energies, greatly depending on the machine location.

The radiation environments near IP1 and IP5 (Fig. 1.1) are particularly significant concerning the performance requirements of electronics due to the high luminosity and associated collision debris [2, 3, 4].

The upgrade of the LHC, known as the High-Luminosity LHC (HL-LHC) [5], will introduce increased radiation levels that must be considered when selecting electronic systems. The HL-LHC aims to achieve a 14 TeV center-of-mass energy and an integrated luminosity of 3000 fb^{-1}, one order of magnitude higher than the nominal LHC design value. Consequently, new equipment needs to be installed along the LHC to accommodate the increased luminosity, which results in a higher number of collisions and particles arriving on the accelerator components. The HL-LHC is expected to produce between five and ten times more collisions than the LHC during its previous runs, posing new challenges for machine equipment features.

The main radiation sources can be categorized into three types. The first is associated with the production of collision debris (mainly photons and pions) from proton-proton inelastic interactions, generating approximately 120 secondary particles per single proton-proton collision [2], particularly relevant in the proximity of the experimental regions. The second source arises from beam-machine interactions, such as interactions with collimators and the beam pipe, generating a cascade of secondary particles and serving as the primary radiation source in many areas of the collider. The third source results from interactions between the beam and residual gas molecules inside the vacuum pipe. Additionally, particles entering the so-called debris collimators and the materials surrounding the detectors initiate hadronic and electromagnetic showers that continue until most of the charged particles have been absorbed, contributing to the radiation affecting the accelerator equipment.

To describe the radiation environment of the HL-LHC [1] concerning its impact on electronic equipment, the following quantities are useful:

- **Total Ionizing Dose (TID)**: this is the energy deposited through ionization processes per unit mass of the target, expressed in Gray (Gy), with 1 Gy = 1 J/kg;

- **Silicon 1 MeV neutron equivalent (n_{eq}) fluence (1 MeV n_{eq})**: this dedicated variable quantifies Displacement Damage (DD) in silicon. It is defined as the fluence of 1 MeV neutrons needed to produce an equivalent amount of DD as that caused by the physical particles under study. The fluence is expressed in units of neutrons per cm^{-2};

- **High Energy Hadron equivalent (HEH_{eq}) fluence**: this represents fluence of all hadrons with energies greater than 20 MeV, measured in hadrons per cm^{-2}. It also includes a contribution from intermediate energy neutrons

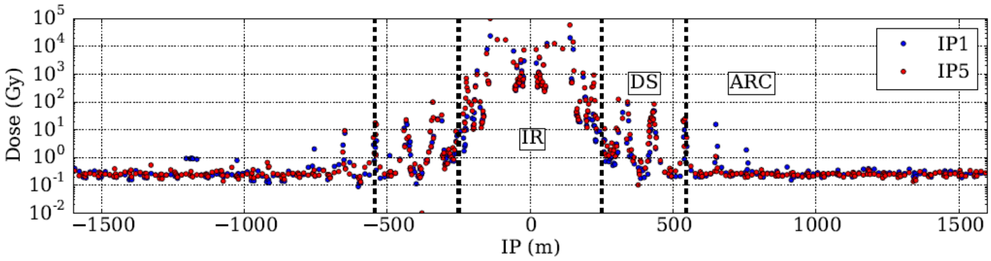

Figure 1.2. TID values during LHC 2016 proton-proton runs in IP1 and IP5 [2].

ranging from 0.2 MeV to 20 MeV;

- **Thermal neutron equivalent fluence**: this quantifies the fluence of neutrons at thermal energies (approximately 25 meV) with an additional contribution from other energy ranges, typically to account for their overall impact on materials.

TID and 1 MeV n_{eq} refer to cumulative radiation effects, as described in detail in Chapter 2, while the others are able to cause Single Event Effects (SEEs) generated through indirect ionization and nuclear reactions for HEH and thermal neutron fluence, respectively.

TID and 1 MeV n_{eq} are typically expressed as expected integral values throughout the full experiment lifetime. The typical range of interest for TID and 1 MeV n_{eq} levels over the full HL-LHC operation period is 1 Gy - 10 kGy and 10^{10}-10^{14} n_{eq} cm^{-2} [1]. It has to be noted that the analysis of locations in the accelerator with TID levels up to 10 MGy is very important for possible degradation of materials such as polymers.

Measurements of the integrated TID levels during the LHC 2016 proton-proton runs have been performed (the correspondent integrated luminosity is 40 fb^{-1}) [2] and, as reported in Fig. 1.2, different radiation levels characterize the locations around the interaction point and the TID value ranges from 10 kGy/year in the IR to ∼1 Gy/year in the arc.

1.2 Space environment

Nowadays, the requirements of space missions and the constant evolution of electronic technologies utilized for payloads and spacecraft, coupled with the imperative to adhere to space environment constraints, especially radiation, present significant challenges for component engineers and designers.

The space radiation environment within the solar system is characterized by three primary sources: Galactic Cosmic Rays (GCRs), primarily high-energy protons, solar radiation, which includes a continuous solar wind of particles emitted by the sun and sporadic solar flares and radiation belts composed of particles trapped around planets [6].

The main radiation effects on electronics caused by the harsh space environment result from the accumulation of TID and Displacement Damage Dose (DDD), with the latter being specifically attributed to NIEL processes [6, 7], as well as Single-Event Effects (SEEs). These effects depend on several factors, such as spacecraft orbits (see Figure 1.3), which vary in inclination, shape, altitude, and mission duration.

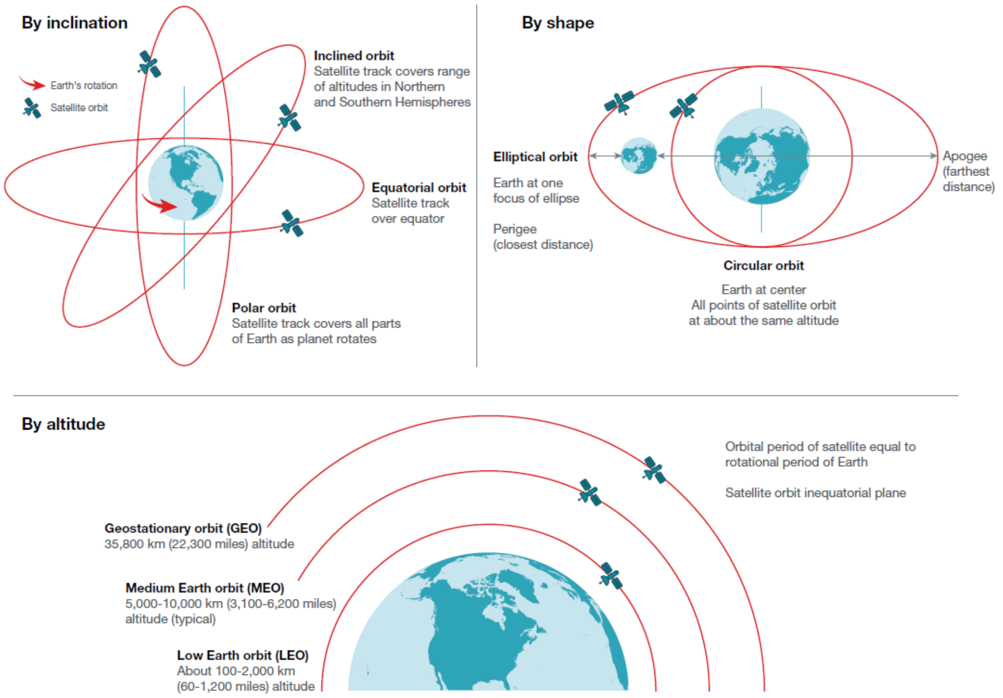

Figure 1.3. Possible orbit kinds and relative properties [6].

The space between the stars, known as the interstellar medium, primarily consists of hydrogen with a small fraction of helium and heavier elements. This interstellar gas has an extremely low density ranging from 10^{-4} to 10^{6} atoms/cm^3 and moves in response to various processes such as magnetic, thermodynamic, gravitational and radiation forces. At the boundary where the interstellar medium ends, the interplanetary medium of the solar system begins. This transition occurs at the outer extent of the Sun magnetic field and solar wind, known as the heliopause, which encloses the heliosphere. The heliosphere is a spherical region encompassing the Sun and the planets, acting as an electromagnetic shield against some of the incident GCR flux. Approximately 75% of cosmic-ray particles are intercepted by the heliosphere, primarily because they possess kinetic energies of less than $\sim$50 MeV and are unable to penetrate the heliosphere barrier due to the energy of the solar wind within it. GCRs are thought to be primarily accelerated by shock waves resulting from supernova explosions propagating through the interstellar medium. The composition of GCRs mainly comprises 89% ionized hydrogen (protons) and 9% ionized helium (alpha particles), with the remaining 2% consisting of heavier ions and electrons. Most GCRs possess kinetic energies around 1 GeV, with the flux decreasing as energy increases beyond this point. Below approximately 100 MeV, the flux is deflected by the heliosphere.Additionally, the interplanetary magnetic field plays a role in influencing GCRs within the heliosphere, making it challenging for them to penetrate deeply into the inner solar system.

The most intense source of radiation in the solar system is the sun, with its photosphere and corona being significant contributors to solar radiation. The photosphere, the visible layer of the sun, emits photons and is surrounded by a super-heated plasma region known as corona [6]. Solar activity can be categorized into solar wind, solar flares, and Coronal Mass Ejections (CMEs). The sun corona, with a temperature of about 10^6 K, allows energetic particles that comprise the solar wind to escape. These particles, including highly energetic photons, electrons, protons, helium ions and a small number of heavier ions, continuously stream out of the corona in all directions. Solar wind is generally less harmful to spacecraft electronics and crews compared to sporadic solar storm phenomena, as the majority of the flux consists of lower-energy particles ranging from a few eV to hundreds of eV, with a significant portion of the lower-energy flux deflected and trapped by planetary magnetic fields. However, solar flares and CMEs can pose significant risks to microelectronic reliability, as particles are accelerated to much higher energies ranging from 10 keV to 1 GeV. Flares occur as sudden, rapid, and intense variations in brightness, resulting from the sudden release of built-up magnetic energy. During a solar flare event, radiation is released across the full electromagnetic spectrum, from radio waves to gamma rays. Additionally, solar radiation includes contributions from Solar Energetic Particles (SEPs), comprising electrons, protons, and heavier ions with energies ranging from 1 MeV to 1 GeV, which are accelerated during solar flares or CME-induced shock waves.

Lower-energy GCRs and particles from the solar wind can be trapped by a planet magnetic field of sufficient strength, forming radiation belts. The Earth magnetic field traps protons and electrons, creating toroidal regions of trapped charged particles. These belts are thicker at the equator, where the magnetic field is stronger, and they thin out towards higher and lower latitudes, eventually dissipating at the poles. The inner belt contains electrons with kinetic energies in the range of approximately 1-5 MeV and protons with energies around 10 MeV, while the outer belt consists mainly of electrons with energies ranging from 10 to 100 MeV. Particle fluxes within the inner and outer belts reach values of approximately 10^4 to 10^6 particles per cm^2 per second, while the flux of particles between the Earth surface and the inner belt is around 10-100 particles per cm^2 per second. In the region between the two belts, the flux is approximately 10^3 to 10^4 particles per cm^2 per second. The Earth magnetic field is tilted about 11° relative to the rotation axis, causing the radiation belts to be misaligned with the Earth surface. Consequently, over South America, off the coast of Brazil, the inner radiation belt, typically extending from altitudes of 1000 to 12000 km, drops to heights between 200 and 800 km, forming what is known as the South Atlantic Anomaly (SAA) [6, 8]. Particle fluxes in the SAA are significantly higher than anywhere else in Earth orbit at that altitude. For example, most of the radiation dose exposure that the International Space Station (ISS) receives occurs while it flies through the SAA. Although electrons and protons trapped in the belts have lower energies than most GCRs or Solar Energetic Particles (SEPs), they are characterized by much higher fluxes and can be hazardous to crew and electronics during extended missions. Therefore, mission paths are specifically designed to minimize spacecraft exposure to radiation belts. In some cases, electronics are powered down during passages through radiation belts to mitigate TID effects, which

are worsened by the presence of electric fields.
Radiation doses during the lifespan of space missions can be estimated once the type, energy, and flux of the particles in the radiation environment are known. For instance, the International Space Station (ISS) operates in Low Earth Orbit (LEO) and is used for research and technological development projects. The radiation environment in LEO consists of a mixture of the previously described radiation sources. Additionally, atmospheric radiation, made up of naturally occurring radioactive isotopes, and spacecraft-generated radiation, which includes secondary electrons and electromagnetic interference generated by spacecraft systems and their components, must be considered for LEO missions [9]. Data obtained from dosimeters used in experiments aboard the ISS during missions in LEO show that the expected absorbed dose values inside the station range from approximately 10^{-2} Gy/year to less than 3 Gy/year in the worst-case scenario [9]. Radiation environments in interplanetary missions are more challenging for spacecraft and instrumentation. For example, the expected TID for the JUICE mission [10] is about 10^4 Gy for a typical aluminum shielding thickness of 1.5 mm, considering approximately 12 years of mission duration, as reported in Figure 1.4. In the case of the Solar Orbiter [11], the estimated TID for the total mission duration (7 years) is around 1 kGy [9].

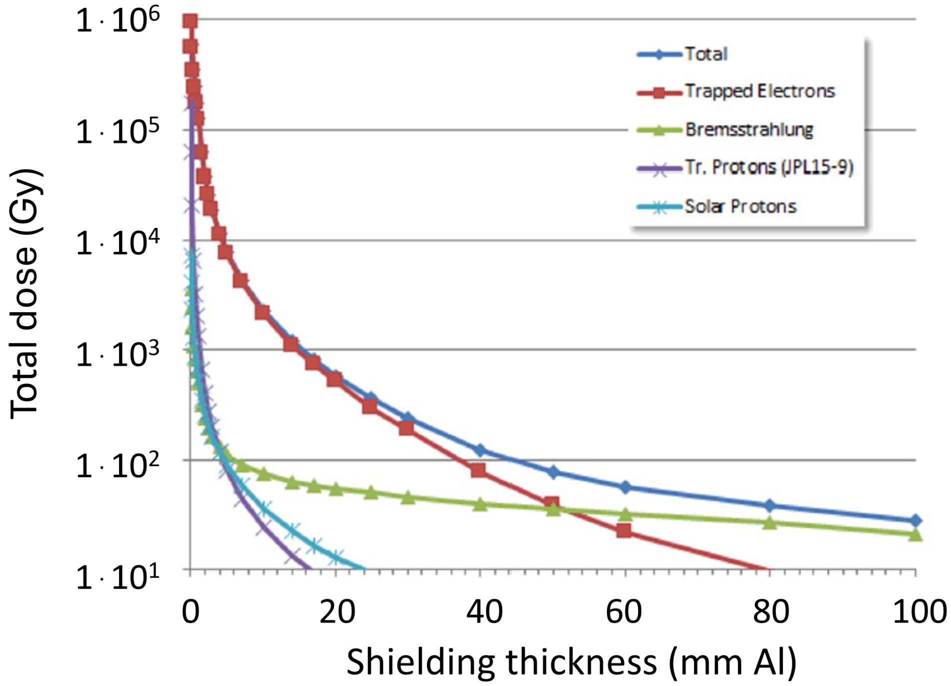

Figure 1.4. Expected total dose values in silicon after 12 years of JUICE mission as a function of aluminum shielding [9].

1.3 Fusion reactors

Fusion reactors aim to use fusion reactions to produce nearly unlimited, CO_2-free energy. Fusion occurs naturally in the Sun, where hydrogen atoms fuse at approximately 15 million degrees Celsius due to the Sun strong gravitational forces. To replicate fusion on Earth, deuterium and tritium atoms must be heated to temperatures around 100 million degrees Celsius to achieve the necessary collisions and subsequent fusion reactions. When these hydrogen atoms collide, they form a plasma. In the deuterium-tritium fusion reaction, a deuterium nucleus fuses with a tritium nucleus, producing one helium nucleus, one free neutron, and 17.6 MeV of energy. Two approaches are used to achieve controlled nuclear fusion: Magnetic Confinement Fusion (MCF) and Inertial Confinement Fusion (ICF). MCF relies on magnetic fields to contain the hot plasma and sustain the fusion process, while ICF uses rapid compression, typically through lasers, to heat and compress fuel pellets to fusion conditions.

Examples of fusion reactors using MCF include Tokamaks (derived from the Russian "toroidal magnetic chamber"). They are donut-shaped machines used for controlled thermonuclear fusion to contain the hot plasma.
At the core of a tokamak fusion reactor lies a complex interplay of magnetic fields essential for confining the superheated plasma where fusion reactions occur. These magnetic fields come in three forms:

- **Toroidal fields**: generated by toroidal coils to guide the plasma along the machine axis of symmetry;
- **Vertical fields**: Produced by external coils to control plasma positioning;
- **Poloidal fields**: induced by electric currents within the plasma itself to maintain equilibrium.

A schematic of the functioning principle of a tokamak is shown in Figure 1.5. To maintain plasma stability and prevent contact with the reactor walls is fundamental, as any contact would result in a sudden temperature drop and plasma disruption.
Once the plasma is established through electric current heating, additional methods such as microwave irradiation or injecting energetic neutral particles using specialized accelerators can be employed for heating. Sustaining the plasma temperature requires continuous energy input. However, once fusion reactions start at the requisite temperature, they generate the majority of the energy necessary to maintain the plasma heat. Consequently, in a functioning reactor, only a fraction (around 10%-30%) of the energy input is needed to sustain the plasma temperature [13, 14].
Inertial Confinement Fusion facilities utilize high-energy lasers or particles to rapidly compress and heat a tiny target, initiating fusion reactions in a controlled manner [15, 16, 17]. Examples of ICF facilities include the National Ignition Facility (NIF) located at Lawrence Livermore National Laboratory in Livermore, California, USA [18], and the Laser Mégajoule (LMJ) near Bordeaux, France [19].
In ICF, a small spherical target containing the fuel, a mixture of deuterium and tritium (D-T), is prepared. Two approaches can be followed for ICF: laser direct drive

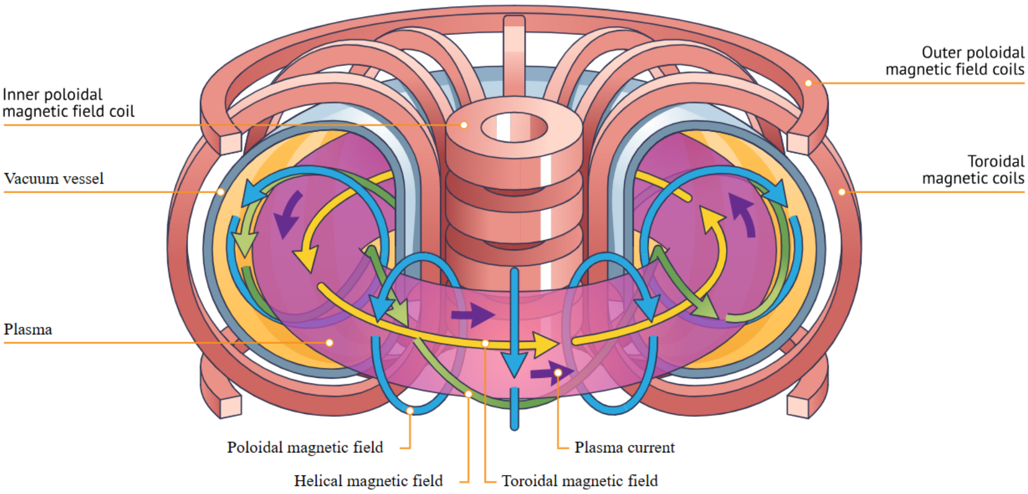

Figure 1.5. Functioning principle of a tokamak [12].

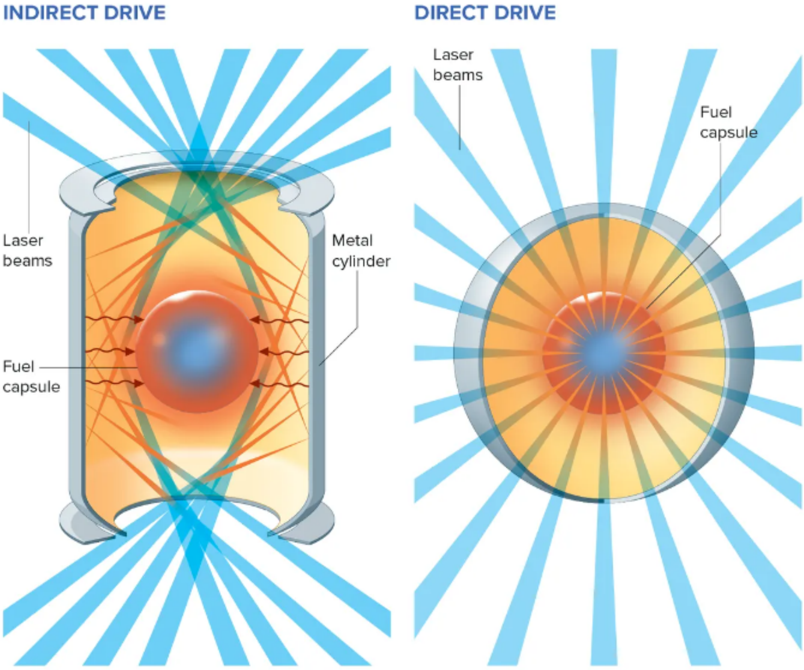

Figure 1.6. ICF approaches to fusion: laser indirect drive and laser direct drive [20].

and laser indirect drive, schematized in Figure 1.6. In the indirect-drive method, lasers hit the inner surface of a hollow cylinder surrounding the fuel capsule, creating X-rays that transfer energy to the fuel capsule. In the direct-drive method, powerful lasers strike directly on the target. In both cases, the laser system, consisting of multiple precisely controlled beams, is aimed to compress and heat the target to the extreme conditions required for nuclear fusion. The outer layers of the target rapidly heat and expand, generating a shockwave that travels inward. As the shockwave converges at the center, it compresses the D-T mixture to very high densities and temperatures, causing the deuterium and tritium nuclei to collide and fuse, releasing energy as high-energy neutrons and alpha particles. The goal is to achieve ignition, where the energy released from fusion exceeds the energy input, sustaining the fusion reactions.
In December 2022, the NIF reached a significant milestone in nuclear fusion research [21]. Using 192 high-powered lasers, a small fuel pellet containing the D-T mixture was compressed, producing a fusion reaction that generated more energy than was used to initiate the reaction. Specifically, the experiment produced 3.15 megajoules (MJ) of output energy from an input of 2.05 MJ, achieving a net energy gain of approximately 54%. This accomplishment demonstrates the feasibility of creating a controlled fusion reaction that can produce more energy than it consumes, a crucial requirement for a viable fusion power plant.

One significant advantage of fusion energy is that, unlike conventional power plants, fusion reactors produce helium as a harmless byproduct without emitting CO_2 or toxic fumes. Deuterium-tritium fuel was chosen for fusion because it reaches fusion conditions at a lower temperature compared to other elements, simplifying reactor design. This choice, coupled with the abundance of deuterium and the prospect of tritium generation from lithium, underscores the immense promise of fusion energy as a clean, virtually limitless power source. Despite current engineering challenges, ongoing research in fusion energy holds great potential for future sustainable energy solutions.
In such an adverse environment, electronic devices are exposed to high-intensity transient electromagnetic components in the radiofrequency and microwave regime, known as Electromagnetic Pulses (EMPs), as well as irradiation from various sources such as neutrons, electrons, X-rays, gamma rays, and UV radiation, all of which can lead to system malfunctions. Moreover, electronics maintenance during an experiment is often not feasible. Therefore, it is paramount to thoroughly test electronic systems used in fusion reactors prior to putting them into operation [22]. Currently, experimental facilities are being developed to demonstrate the potential of fusion reactors. Both MCP and ICF approaches are part of ongoing efforts to harness fusion energy as a clean and abundant source of power for the future. As an example, the expected radiation environment in the Divertor Tokamak Test (DTT) facility will be briefly described.

1.3.1 Divertor Tokamak Test facility

The Divertor Tokamak Test (DTT) facility [23, 24] is a significant fusion experiment currently under construction at the ENEA Frascati Research Center in Italy.

The DTT plays a crucial role in advancing fusion research, with a primary focus on investigating and developing innovative solutions for managing and extracting the heat generated by the fusion process. A 28-year experimental program is foreseen, with 6 months of operation alternating with 6 months of shutdown per year.

DTT will operate in high-performance (H-mode) conditions, expecting a 2.5 MeV neutron yield rate of $1.5 \cdot 10^{17}$ n/s from Deuterium-Deuterium reactions. Additionally, high-energy neutrons at 14 MeV will be generated from Deuterium-Tritium reactions, with a projected maximum neutron yield rate of $1.5 \cdot 10^{15}$ n/s. The design of the tokamak components is significantly influenced by the intense neutron and gamma irradiation and high neutron-induced activation [25].

The magnet system consists of 18 Toroidal Field (TF) Nb_3Sn coils, operating at a peak field of 11.8 T and a conductor current of 44.0 kA, six independently fed Central Solenoid (CS) modules operating at 13.2 T and 29.9 kA, and six Poloidal Field (PF) coils, with two operating at 8.5 T and 35.0 kA and the other four at lower fields and currents. The PF system also includes six copper in-vessel coils. The Vacuum Vessel (VV) is constructed with a double-wall structure featuring 15 mm thick ribs separated by a neutron shield [26]. It will be situated inside the main magnet system, providing a vacuum environment for the plasma. Its main components include the main vessel, port structures, and the supporting system. The main vessel has a toroidal shape with a D-shaped cross-section. The primary out-vessel components are the port collars, thermal shield, and cryostat. The Cryostat Vessel (CV) is a vacuum-tight container surrounding the entire tokamak, providing the vacuum necessary for the superconducting magnets [27]. A three-dimensional cross-section of the DTT is shown in Figure 1.7.

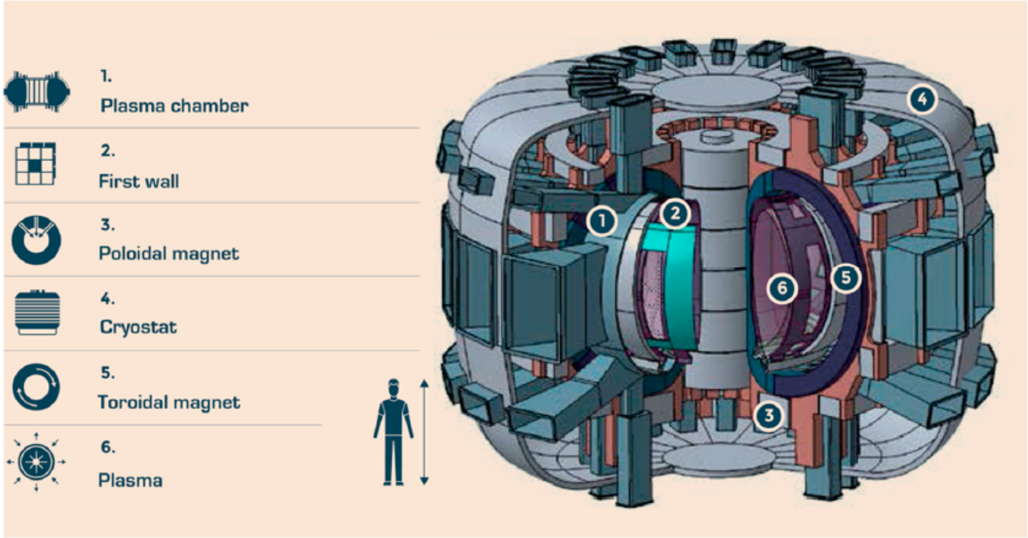

Figure 1.7. 3D cross-section of DTT [28].

The three dimensional spatial distributions of neutrons and secondary gamma rays inside the building during H-mode operation are reported in Figure 1.8 [26].

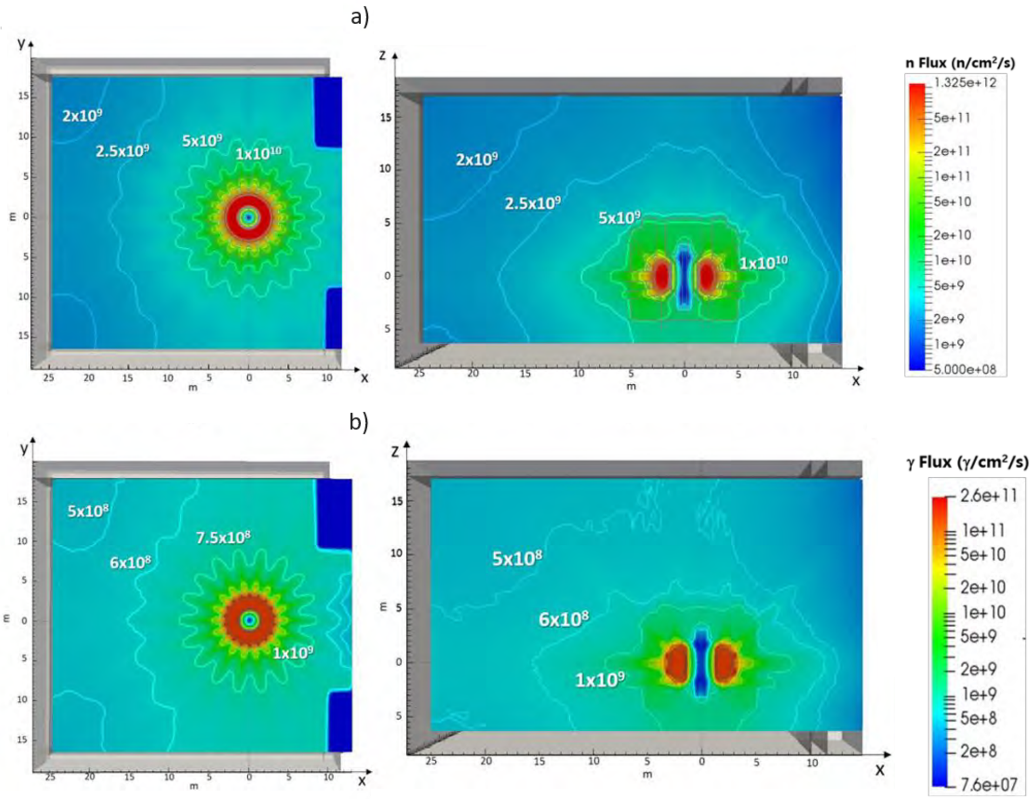

Figure 1.8. Expected fluxes of neutrons (a) and gamma (b) inside the building during high-performance phase [26].

At the cryostat level, the neutron flux is approximately 10^{10} n cm^{-2} s^{-1} and the gamma flux is about 10^9 γ cm^{-2} s^{-1}. At a distance of about 10 meters from the center of the machine, the neutron flux decreases to below $5 \cdot 10^9$ n cm^{-2} s^{-1} and the gamma flux to below $7.5 \cdot 10^8$ γ cm^{-2} s^{-1}. The maximum absorbed dose due to neutrons and gamma radiation in the in-vessel coils and TF coil insulator at the end of life are approximately 1.2 MGy and 90 kGy, respectively. In the building outside the cryostat, the dose rate in silicon due to neutrons and gamma radiation ranges from $2 \cdot 10^{-3}$ Gy/s to $1 \cdot 10^{-2}$ Gy/s depending on the position, which corresponds to a cumulative absorbed dose of 0.5–2.5 kGy that the electronics must withstand by the end of the experiment, considering $2.49 \cdot 10^5$ s of continuous operation at full power [25]. As described in this chapter, radiation levels in High Energy Physics are typically reported in the literature in terms of TID and 1 MeV neutron equivalent (1 MeV n$_{eq}$) fluence levels [1]. For space missions and fusion reactor environments like the Divertor Tokamak Test facility, total ionizing dose and total absorbed dose values can be found in the literature [9, 25, 29, 30], accounting for the contributions of different particle types. In summary, the radiation levels characterizing these harsh environments, which electronics must withstand over their lifetime, are detailed in Table 1.1. This table provides an overview of radiation levels encountered by electronics in demanding environments, presented as examples. The importance of robust design and materials capable of withstanding high levels of TID and neutron fluence becomes evident. This capability is crucial for ensuring the reliability and longevity of electronic systems in such challenging conditions.

Table 1.1. Radiation levels characterizing high radiation environments. The value of 1 MeV neutron equivalent fluence for HL-LHC is extimated over the full experiment lifetime.

	Radiation levels
HEP: **HL-LHC**	TID: 1 Gy/year - 10 kGy/year 1 MeV neutron equivalent fluence: 10^{10}-10^{14} n$_{eq}$/cm^2
Space: aboard ISS in **LEO**	TID: 0.01 - 3 Gy/year
Space: **JUICE** interplanetary mission	TID: $\simeq$ 1 kGy/year
Fusion reactors: **DTT** facility	Total dose: $2 \cdot 10^{-3}$ - $1 \cdot 10^{-2}$ Gy/s

Chapter 2

Radiation effects on electronic and optoelectronic devices

Electrical, Electronic and Electromechanical (EEE) components are the foundational pillars of any electronic system and, therefore, are employed even in harsh environments. It is crucial to understand how these components behave in environments where they may be exposed to various types of damage from ionizing radiation and electromagnetic waves.

When an electromagnetic wave interacts with semiconductor devices, it creates what are known as Electromagnetic Pulse (EMP) effects. EMP phenomena span a wide range within the electromagnetic spectrum, from very low frequencies below one hertz to ultrahigh frequencies (up to 3 GHz). This interaction can induce harmful current and voltage surges in electrical and electronic systems, potentially causing electrical or thermal breakdowns [31, 32]. These effects can be temporary, with systems often returning to normal operation once the radiation pulse has ended [33], or they can lead to permanent damage, potentially destroying the electronics.

The ionizing radiation effects in electronic devices are broadly divided into two main categories: Single Event Effects (SEEs) and gradual cumulative effects [6, 34, 35, 36]. Cumulative damage results from the dose accumulated over the entire lifetime of the electronics exposed to a radiation environment. These effects are significant when devices are exposed to radiation for extended periods. Cumulative effects are categorized into Total Ionizing Dose (TID) and Displacement Damage Dose (DDD), as previously described. When a device sensitive to TID or DDD reaches its maximum tolerance of accumulated TID or DDD, it will exhibit damage. Therefore, it is crucial to characterize a given component before deploying it in a radiation environment to ensure its quality and durability throughout the experiment or to predict when failure will occur. Conversely, SEEs are critical in real-time applications. They are failures resulting from the passage of a single particle that deposits energy in the electronic device. Hence, they can occur at any moment from the beginning of the operational period in a radiation environment [37]. SEEs can be destructive or non-destructive and include various phenomena such as memory upsets, latchup, or burnout.

Based on the radiation resistance properties guaranteed during manufacturing, EEE components can be categorized into different classes, as described in the next section.

In this work, Bipolar Junction Transistors (BJTs) and optoisolators were characterized before and after irradiation with several radiation sources to evaluate their radiation resistance properties, as well as the dose delivery and efficiency of laser-accelerated particles, an innovative radiation source, compared to conventional and well-established stress test sources such as gamma rays, neutrons, and protons from linear accelerators. BJTs and optoisolators, when exposed to radiation, can be subjected to the aforementioned types of damage. Specifically, the damage due to TID and DD dose effects will be investigated in this thesis project.

Semiconductors, typically silicon, form the basis of electronic devices such as diodes, transistors, integrated circuits and optoelectronic devices. The first part of this chapter qualitatively discusses the electronic properties of intrinsic and extrinsic semiconductors and introduces the basic principles of PN junctions, which are crucial for understanding the fundamental of semiconductor devices, particularly their role in transistor operation. Following this, the main parameters and operating principles of BJTs and optoisolators are presented.
The second part of this chapter focuses on the radiation-induced effects in semiconductors, specifically on BJTs and optoisolators.

2.1 Electronic devices

Electronic devices can be classified into three main categories based on their guaranteed radiation performance: *Commercial Off-The-Shelf* (COTS), *radiation tolerant*, and *radiation hardened* (*rad-hard*) components. All these types of components are used in space applications, high luminosity machines and fusion reactors.
COTS electronics include any electronic device that is not certified to be radiation tolerant or rad-hard. According to NASA, COTS are defined as “parts where the manufacturer solely establishes and controls the specifications for performance, configuration, and reliability" [38]. They are much cheaper than the other types, readily available, and exhibit good electrical performance. Radiation tolerant electronics can handle higher radiation levels than COTS devices but can tolerate less radiation exposure than rad-hard components. Radiation hardened devices can be employed in very harsh environments with a low probability of malfunctioning during their use. Since they are designed to withstand high levels of radiation, they require additional time and manufacturing processes to be realized, making them more expensive and harder to procure than COTS and radiation tolerant components [39, 40].

Nowadays, COTS components are widely used due to their advantages, such as low cost, high performance and ease of availability, even in the LHC equipment [2, 41, 42] and in space environments [38, 43, 44]. Therefore, they need to be carefully qualified and characterized against radiation effects to properly evaluate the risks associated with their use.

In this work, both COTS and radiation tolerant components radiation resistance properties have been investigated. Specifically, the studied BJTs are commercial off-the-shelf devices while the optoisolators are qualified as radiation tolerant.

2.1.1 Intrinsic and extrinsic semiconductors

Intrinsic semiconductors, such as silicon (Si) or germanium (Ge) in their crystalline form, exhibit specific properties due to their atomic structure. Each silicon atom in the crystal lattice forms covalent bonds with four nearest neighbors, creating a stable lattice structure (Figure 2.1).

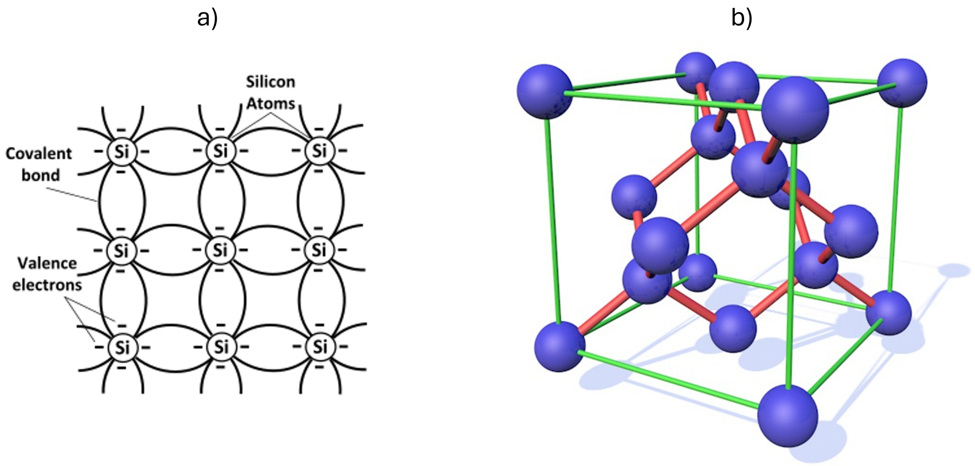

Figure 2.1. Two-dimensional (a) and three-dimensional (b) covalent bonds in silicon lattice [45].

At room temperature, the behavior of charge carriers in intrinsic semiconductors is primarily influenced by thermal energy. These materials possess a band gap between the valence band (where electrons are bound to atoms) and the conduction band (where electrons can move freely as charge carriers). At absolute zero temperature (0 K), all electrons occupy the valence band, and the conduction band remains empty due to the band gap energy.
As thermal energy is introduced (room temperature being approximately 300 K), some electrons gain enough energy to transition across the band gap from the valence band to the conduction band, breaking covalent bonds in the process. This creates electron-hole (e^-- h^+) pairs, where an electron moves to the conduction band, leaving behind a hole in the valence band (Figure 2.2).
These thermally generated electron-hole pairs act as charge carriers, significantly contributing to the electrical conductivity of intrinsic semiconductors [46].

Semiconductors are essential in electronics because their electrical properties can be precisely adjusted by introducing impurities. Extrinsic semiconductors are semiconductor materials intentionally doped with specific impurities to alter their electrical characteristics. This intentional doping disrupts the natural balance between electrons and holes, which is characteristic of intrinsic semiconductors.
In intrinsic semiconductors, the number of electrons and holes is equal due to thermal

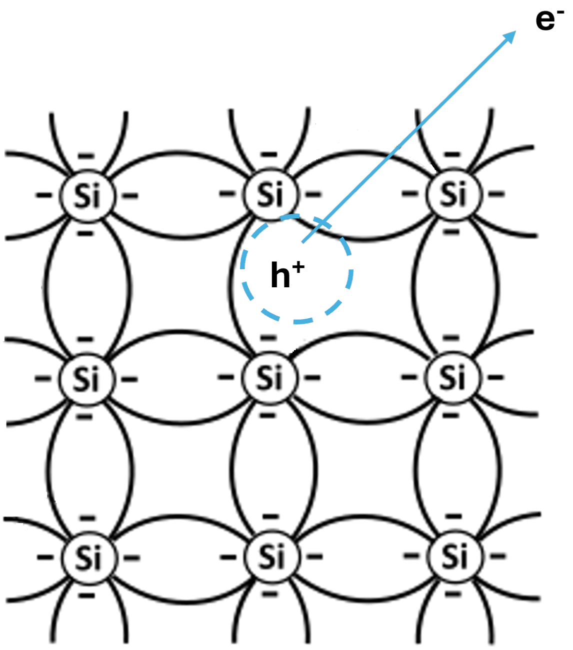

Figure 2.2. Two-dimensional broken covalent bonds in silicon lattice. An electron-hole (e^-- h^+) pair is created due to thermal energy.

generation processes. However, doping with impurities in extrinsic semiconductors introduces additional charge carriers.

For example, doping semiconductor materials like silicon or germanium (Group IV elements) with elements such as phosphorus (P) or arsenic (As) from Group V of the periodic table introduces additional electrons. These Group V elements have one more electron compared to Group IV elements, leading to an excess of negative charge carriers and converting the material into an N-type semiconductor. This doping effect can be visualized in Figure 2.3. In Figure 2.3, the pentavalent impurity (Group V element) replaces one of the Group IV atoms in the semiconductor lattice. Four of the five valence electrons of the impurity form covalent bonds with neighboring atoms, while the fifth electron remains weakly bound to the impurity atom. This weakly bound electron acts as a free electron, contributing to the increased conductivity of the n-type semiconductor.

Conversely, doping with elements like boron (B) or gallium (Ga) from Group III introduces holes, resulting in a surplus of positive charge carriers, converting the material into a p-type semiconductor.

This deliberate modification of semiconductor properties through doping is crucial for tailoring conductivity, mobility, and other electrical characteristics, making semiconductors versatile for various electronic applications.

2.1.2 PN junctions

A PN junction is one of the simplest and fundamental semiconductor structures, playing a crucial role in various electronic devices. PN junctions are created by

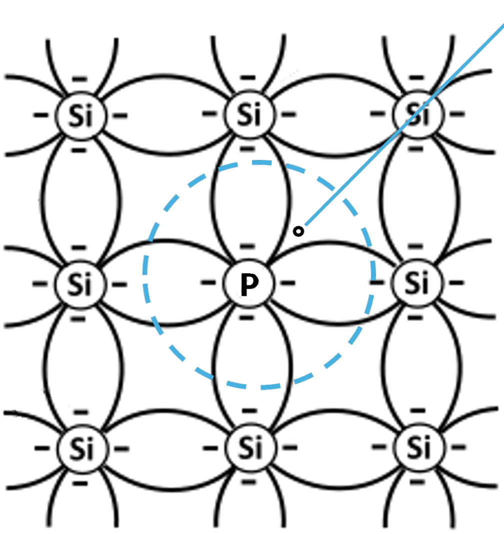

Figure 2.3. Two-dimensional representation of a silicon lattice with one atom substituted by a phosphorus (P) impurity (Group V element). The excess electron (e^-) acts as a free electron.

joining p-type and n-type semiconductor materials, which have different doping characteristics.

When a p-type semiconductor is joined with an n-type semiconductor, charge carriers undergo diffusion: electrons move from the n-type region to the p-type region, and holes move from the p-type region to the n-type region. As electrons and holes diffuse across the junction, they recombine, leaving behind positive charged ions in the n-type region and negatively charged ions in the p-type region. This process creates a depletion region around the junction, depleted of free charge carriers (electrons and holes).

Across the depletion region, an electric field is established due to the difference in charge between the ionized atoms, creating a potential barrier (built-in potential barrier) that prevents further free carrier diffusion. Figure 2.4 illustrates a schematic of a PN junction, depicting the depletion region and the resulting potential barrier.

A PN junction can be forward biased if a positive voltage is applied to the p-type region and a negative voltage to the n-type region. This configuration reduces the width of the depletion region, allowing current to flow as electrons and holes are pushed towards the junction.

Conversely, if a positive voltage is applied to the n-type side and a negative voltage to the p-type side, the PN junction is reverse biased. This increases the width of the depletion region, preventing current flow as the potential barrier is heightened.

Band diagram representation

In both the p-type and n-type materials, the valence band is filled with electrons

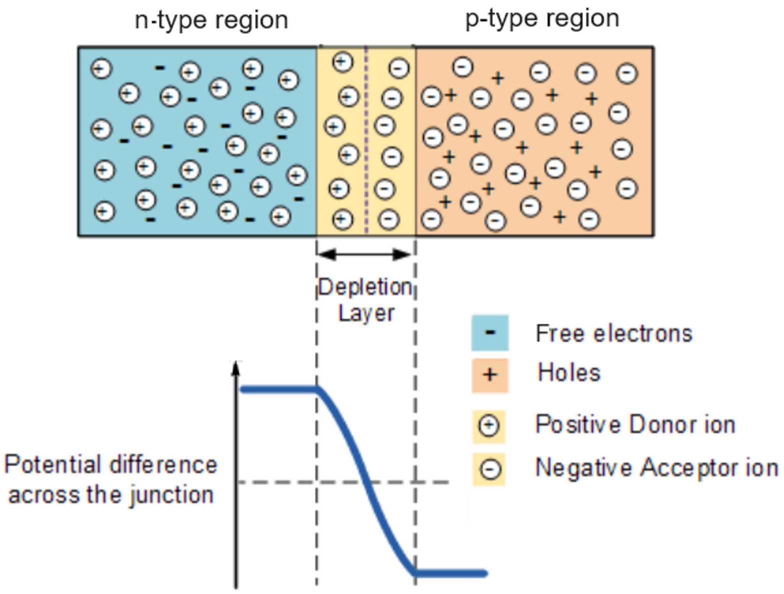

Figure 2.4. PN junction and potential barrier due to the charge difference. Adapted from [47].

at lower energy levels, while the conduction band is empty or partially filled with electrons at higher energy levels. The band diagram of a PN junction shows that the energy bands of p-type and n-type regions align differently across the junction: in the p-type side, the Fermi level (which represents the highest energy level occupied by electrons at absolute zero) is closer to the valence band due to the excess holes. In the n-type side, the Fermi level is closer to the conduction band due to the excess electrons. When the p-type and n-type materials are joined, the energy bands bend at the junction, aligning the Fermi levels. A scheme of the band diagram at equilibrium (no bias applied to the p-type and n-type regions) is presented in Figure 2.5. The potential barrier is visible in the energy band diagram, showing the energy

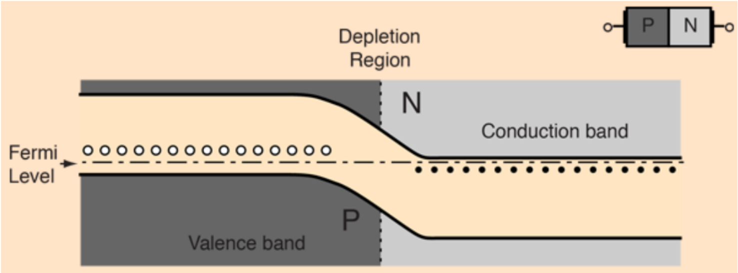

Figure 2.5. Band diagram of a PN junction at equilibrium. The upward direction in the diagram represents increasing electron energy [48].

difference that charge carriers must overcome to move across the junction.

When the PN junction is forward biased, the energy bands flatten out as the external voltage reduces the built-in potential barrier. Electrons in the n-type region gain enough energy to cross into the p-type region, and holes in the p-type region move into the n-type region. A scheme of a band diagram of a forward biased PN junction is shown in Figure 2.6.

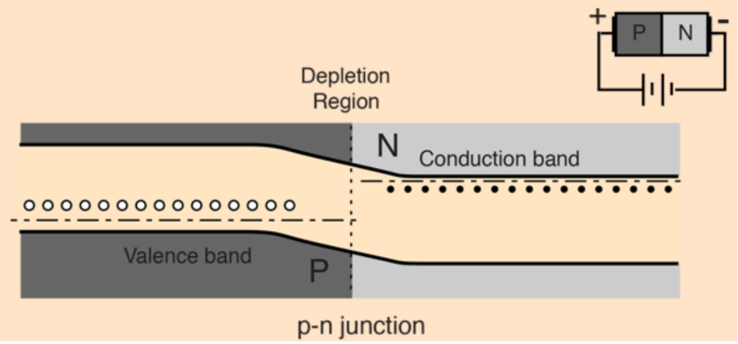

Figure 2.6. Band diagram of a forward biased PN junction. The upward direction in the diagram represents increasing electron energy [48].

When the PN junction is reverse biased the energy bands bend further, increasing the potential barrier. Charge carriers are repelled from the junction, preventing current flow. The bands diagram of a reverse biased PN junction is depicted in Figure 2.7.

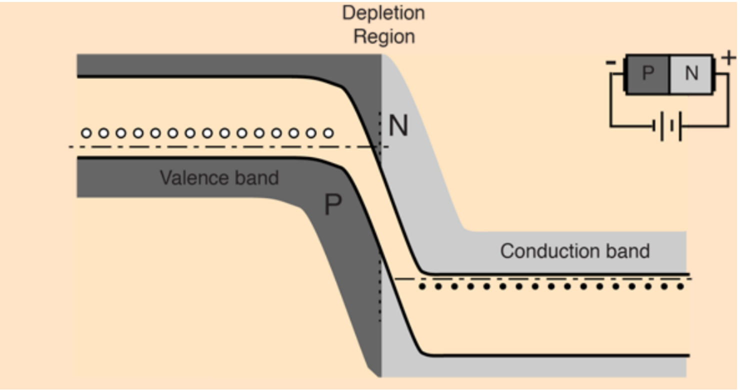

Figure 2.7. Band diagram of a reverse biased PN junction. The upward direction in the diagram represents increasing electron energy [48].

This ability to control current flow through biasing makes the PN junction crucial for the operation of semiconductor devices such as diodes, transistors, and optoelectronic components. Understanding and managing these biasing conditions are fundamental in designing and utilizing these devices effectively in electronic circuits.

2.1.3 Bipolar junction transistors

Bipolar Junction Transistors (BJTs) are among the most important semiconductor devices, widely used in electronic systems due to their high performance. They are employed in various applications, including high and low power systems, switching,

amplification, and general purposes. BJTs are particularly valuable in Bipolar Complementary Metal-Oxide-Semiconductor (BiCMOS) circuits and analog Integrated Circuits (ICs) due to their characteristics [49]. These characteristics enable their use across a wide range of temperatures [50] and in diverse applications [51, 52].
A BJT is defined as bipolar because both electrons and holes are involved in the conduction process. It has three terminals and consists of three doped semiconductor regions separated by two PN junctions. The three terminals are connected to semiconductor regions, namely the Collector (C), the Base (B) and the Emitter (E). BJTs can be of two types: NPN and PNP, according to the doping of the three regions.
In an NPN BJT, the thin p-type semiconductor (base) is sandwiched between the two n-type regions (emitter and collector), while in a PNP BJT, the thin n-type base is enclosed between the p-type emitter and collector. In both cases, the emitter region is heavily doped compared to the other regions.
A schematic of an NPN BJT is provided in Figure 2.8 as an example. In a simplified scheme, when no voltage is applied to the BJT, there is no flow of current between the two junctions. When both junctions are polarized, current flows through the BJT. In particular, a properly biased transistor that conducts correctly, has the base-emitter junction forward biased (the voltage between the base and the emitter V_{BE} is positive) and the collector-base junction reverse biased (the voltage between the collector and the emitter V_{CE} is positive). The junctions of a BJT can be biased in three different ways: common emitter, common base and common collector. The most common BJT connection is the common emitter configuration (Fig. 2.9). In an NPN BJT, negative current carriers (electrons) are injected from the emitter to the base region and holes go from the base to the collector: this constitutes transistor action. Since the base-collector junction is reverse biased, the current that flows in the junction is low. The electrons going from E to B are minority carriers in the B and, if the base layer is sufficiently thin, they can diffuse toward the base collector junction without recombining with the majority carriers (holes) in the B. Therefore, the electrons flow in the collector will be similar to that in the emitter.

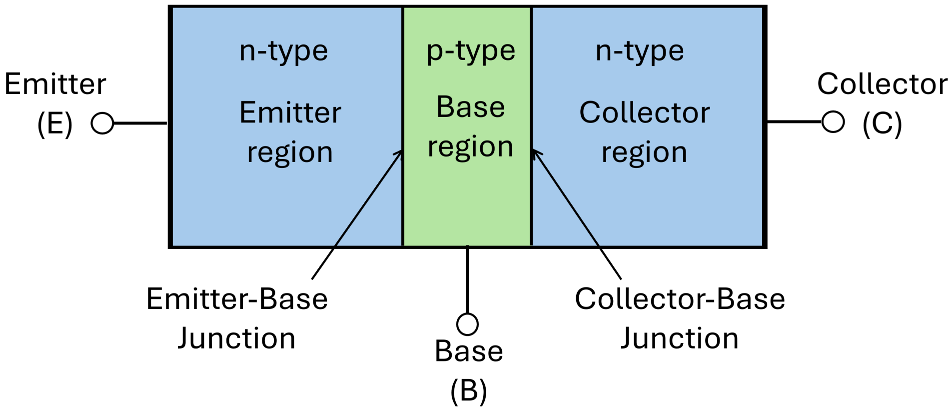

Figure 2.8. Scheme of an NPN BJTs.

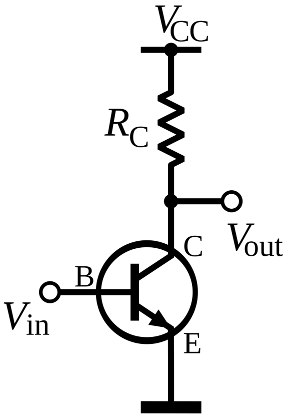

Figure 2.9. NPN BJT common emitter configuration [53].

The standard equation for currents flowing in a transistor is given by: $I_E = I_B + I_C$, where I$_E$, I$_B$ and I$_C$ are the emitter, base and collector currents, respectively. The conventional current flow in a BJT is represented by arrows, as shown in Figure 2.10 for both PNP and NPN BJTs. In the following, some parameters of NPN BJTs are described.

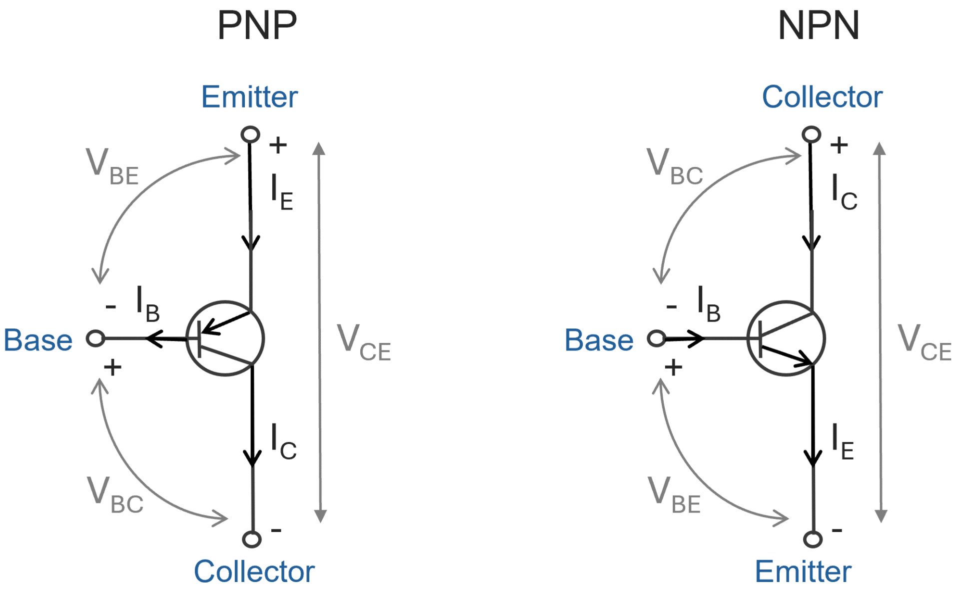

Figure 2.10. Scheme of voltage drops and of currents flowing in PNP and NPN BJTs [54].

The base current I$_B$ is made up of three components: $I_B = I_{E_p} + I_{C_p} + I_{BB}$, where I$_{E_p}$ represents holes that flow from B to E, I$_{C_p}$ is the current corresponding to the holes going from C to B and I$_{BB}$ is the recombination current due to the holes that enter the base through the B terminal to replace the holes that recombined with the electrons coming from the emitter region. I$_{BB}$ can be expressed as: $I_{BB} = I_{E_n} + I_{C_n}$.

To characterize BJTs, some important parameters can be defined:

- **Common-base current gain** α_0: it is given by the ratio between the electron current at the collector and the emitter current: $\alpha_0 = \frac{I_{Cn}}{I_e}$ and it is $\alpha_0 \approx$1 for a well-made transistor;
- **Emitter efficiency** γ: it is the ratio between the electrons current injected in the base and the emitter current: $\gamma = \frac{I_{en}}{I_E} = \frac{I_{En}}{I_{En}+I_{Ep}}$ and it holds $\gamma \approx$1;
- **Transport coefficient of the emitter current** α_T: it is the ratio between the current due to the electrons that reach the collector and the current given by the electrons injected into the emitter: $\alpha_T = \frac{I_{Cn}}{I_{En}}$. For a good transistor with a thin base layer, $\alpha_T \approx$1.

The above described parameters are linked by the relation:

$$\alpha_0 = \frac{I_{C_n}}{I_E} = \frac{I_{C_n}}{I_{E_n} + I_{E_p}} = \frac{I_{C_n}}{I_{E_n}} \cdot \frac{I_{E_n}}{I_{E_n} + I_{E_p}} = \alpha_T \gamma \tag{2.1}$$

By considering that the reverse current of holes from C to B (I$_{C_p}$) is negligible compared to forward current of holes from B to E (I$_{E_p}$) and using the definition of α_T, it is possible to rewrite the base current as follows:

$$\begin{aligned} I_B &= I_{E_p} + (I_{E_n} - I_{C_n}) - I_{C_p} \\ &\sim I_{E_p} + (I_{E_n} - I_{C_n}) \\ &= I_{E_p} + (1 + \alpha_T) I_{E_n} \end{aligned} \tag{2.2}$$

The two terms in the last row have similar intensities since I$_{E_n}$ > I$_{E_p}$, due to the heavier doping of the emitter compared to the base. However, I$_{E_n}$ is multiplied by $(1 + \alpha_T)$, where $\alpha_T \approx$1.

BJTs can be used as an amplifier or as a switch. When used as an amplifier, the collector current can be controlled by adjusting a low base current. In this configuration, the most important feature to characterize the BJT functioning is the transistor current gain β, defined as:

$$\beta = \frac{I_C}{I_B} \tag{2.3}$$

By considering Equation 2.2 and the relation I$_C$~I$_{C_n}$ (since I$_{C_n}$ > I$_{C_p}$), the current gain can be expressed as:

$$\beta = \frac{I_C}{I_B} \sim \frac{I_{C_n}}{I_B} = \frac{I_{C_n}}{I_{E_p} + (1 - \alpha_T) I_{E_n}} \tag{2.4}$$

By using the definitions of α_T and γ, it holds:

$$\beta = \frac{\alpha_T I_{E_n}}{(I_{E_p} + I_{E_n}) - \alpha_T I_{E_n}} = \frac{\alpha_T \gamma}{1 - \alpha_T \gamma} \tag{2.5}$$

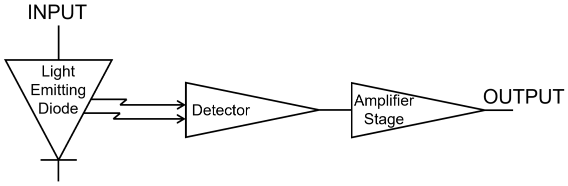

Figure 2.11. Block diagram of a typical optocoupler [55].

Therefore, for a good transistor for which holds $\alpha_T\gamma \approx 1$, the gain is high ($\beta \approx 100$-250) [46] and varies according to the BJT type and manufacturer (as will be shown in Chapter 5).

BJTs can also be used in digital mode as a switch. In particular, it is considered to be "on" when it is in saturation state (BE and BC junctions are forward biased allowing the maximum current flow from collector to emitter), where an additional increase in the base current does not cause any further increase in the collector current. In saturation, the current gain β_{sat} is significantly reduced compared to the active region. It is typically around 10-20% of the active region β. Conversely, the BJT is "off" when it is in cutoff mode (BE and BC junctions both reverse-biased) and no current is flowing. In cutoff mode, both the collector current I_C and the base current I_B are effectively zero and the concept of current gain ($\beta = \frac{I_C}{I_B}$) does not apply in a meaningful way.

2.1.4 Optoisolators

Optoisolators (or optocouplers) are used in several electronic systems because they are able to provide efficient electrical isolation of microelectronic signals and are useful for circuit that need to be isolated from each other for safety. An optoisolator is made of a photodetector and an amplifier, usually a phototransistor, optically coupled with a Light-Emitting Diode (LED). In Figure 2.11, a typical optocoupler block diagram is shown. A current is first applied to the LED, which emits light (visible or infrared) proportional to the current flowing through the device. When the light hits the photodetector, it starts to conduct. The optocoupler provides a very high degree of isolation between the electrical signal that drives the LED and the output of the amplifier because there is no direct electrical connection between them, only the optical signal [55]. It can be realized in two different configurations: sandwich structure and lateral structure. In the former, the LED is directly placed on the photodetector silicon die with just a thin layer of optical coupling medium between them (Fig. 2.12a). The latter consists of a side-emitting LED and a photodetector that are coupled by means of a coupling material, and its functioning relies on total internal reflection from the coupling compound (Fig. 2.12b).
The main parameters [56] of an optoisolator are:

- **Forward current I$_F$**: it is the maximum current that can flow through the LED when it is forward-biased;
- **Reverse voltage V$_R$**: it specifies the maximum reverse voltage that can be

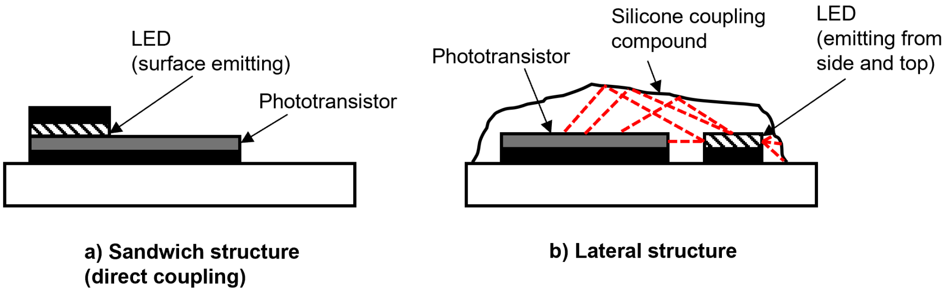

a) Sandwich structure (direct coupling)

b) Lateral structure

Figure 2.12. Diagram of two optoisolator configurations [55].

applied to the LED terminals without causing damage;

- **Collector current I$_C$**: it refers to the output current from the phototransistor when it is activated by the LED. It depends on the amount of light emitted by the LED;
- **Collector to emitter voltage V$_{CE}$**: when a forward current I$_F$ is applied to the LED, it emits light, which in turn activates the phototransistor. V$_{CE}$ is the voltage drop between the collector (C) and emitter (E) terminals of the phototransistor when it is conducting;
- **Current Transfer Ratio CTR**: it is defined as the ratio between the output collector current (I$_C$) and the input LED current (I$_F$). It is the equivalent of the BJT gain and indicates how efficiently the optoisolator transfers current from the input to the output.

Optocouplers rely on components with specific features and well-defined microscopic structures, making them highly sensitive to even slight changes in their characteristics.

2.2 Radiation effects in semiconductors

Semiconductor materials, typically silicon, serve as the fundamental elements of electronic devices and are commonly employed as radiation detectors for position and energy measurements. Radiation-induced defects refer to lattice imperfections caused by high-energy radiation, which can significantly impact the electrical and optical properties of semiconductor crystals. Various forms of damage, including surface or lattice defects, occur when incoming particles deposit their energy into silicon.

The interaction between incoming particles and matter primarily involves two mechanisms: energy loss due to ionization (or collisions) and NIEL processes. In ionization, incoming particles interact with atomic electrons, causing their excitation or ejection. In contrast, NIEL processes involve interactions where the energy transferred by the incoming particle leads to atomic displacement or collisions that displace atoms from their lattice positions, resulting in energy dissipation through lattice vibrations.

Damage to silicon devices from ionization typically affects surface layers, whereas bulk damage mainly arises from NIEL processes (displacement damage). Generally, energy deposition through non-ionizing processes is lower compared to ionization [57].

One of the simplest radiation-induced bulk defects in a crystal is a vacancy or an atom displaced to a relatively stable position within the interstice. These defects, consisting of a vacancy and interstitial atom pair, are known as Frenkel Pairs (FP) or Frenkel defects and are classified as point-like defects [58, 59, 57]. The creation of a Frenkel defect is associated with a threshold energy, denoted as E_d, which represents the energy required to displace an atom into an interstice. Clusters of defects form when incident particles, such as fast neutrons, impart sufficient energy to recoil atoms, resulting in extensive cascades of displacements.

The importance of damage caused by a particular process depends on its relative cross-section compared to other potential processes.

Bulk damage effects caused by energetic particles have been shown to be proportional to the displacement damage cross-section, equivalent to the NIEL. This proportionality, known as the NIEL scaling hypothesis, depends on the NIEL-value, which varies with particle type and energy. However, deviations from the NIEL scaling hypothesis have been observed in oxygenated silicon and for low-proton energies ($\leq$ 10 MeV) in standard silicon [60].

Regions damaged by radiation in the silicon bulk act as electrically active defects with deep levels within the band gap of silicon. The generation of these additional traps causes a decrease in carrier lifetime and an increase in reverse current [59].

2.2.1 Non ionizing energy loss

Displacements occur when the primary interaction causes a recoil atom to be displaced from its lattice position. These displaced atoms, known as Primary Knock-on Atoms (PKAs), primarily generate Frenkel defects, which consist of a pair of point defects (highly localized imperfections emerging within a crystal) where a vacancy (V) exists alongside an atom positioned in an interstitial site (I), as illustrated in Figure 2.13. In collisions with sufficient transferred energy, PKAs can collide with other lattice atoms, generating additional V-I ions. At thermal equilibrium, recoil atoms typically reside in interstitial positions, unless some recombine with vacancies. While some point defects remain isolated, when recoil energies significantly exceed the displacement threshold energy (E_d), cascading displacements occur, leading to the formation of closely grouped defects termed clusters [61]. Thermal energy facilitates the migration of some defects throughout the crystal, eventually allowing for their annihilation through the recombination of V-I pairs or the creation of stable defects in conjunction with pre-existing impurities or induced defects. The presence of defects and clusters thereof induces alterations in the semiconductor properties. In radiation-induced defects, the value of the displacement threshold energy E_d in silicon typically ranges from about 13 to 33 eV and an isotropic value of 25 eV is often assumed [59].

The displacement damage cross section D(E), which accounts for both particle-semiconductor (e.g. silicon) interactions and the energy released in creating atomic displacements, is used to express the damage effects caused by energetic particles in

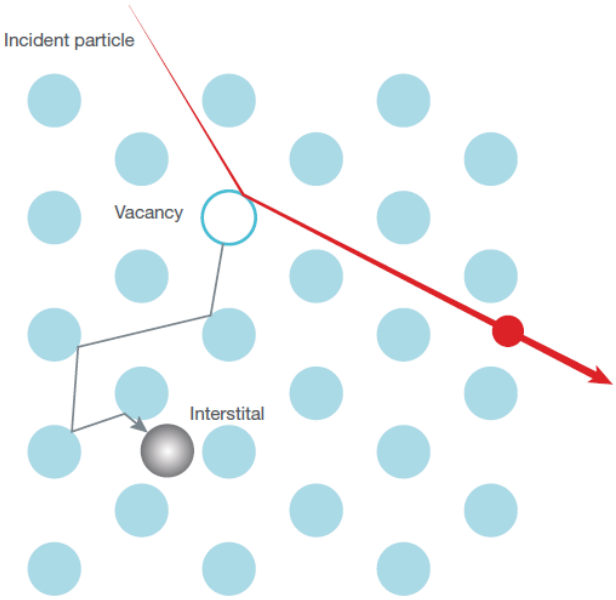

Figure 2.13. Illustration of a Frenkel defect in a crystal lattice consisting of a vacancy (white) and an interstitial ion (gray) pair [6].

the bulk of any material [62]. It is defined as:

$$D(E) = \sum_k \sigma_k(E) \int f_k(E, E_R) P_k(E_R) dE_R \tag{2.6}$$

Here, E represents the energy of the incoming particle, $\sigma_k(E)$ is the cross section for the k-th nuclear interaction, $f_k(E, E_R)dE_R$ denotes the probability that the recoil atom generated during the k-th reaction has kinetic energy between E_R and $E_R + dE_R$, and $P_k(E_R)$ is the partition energy for the k-th recoil nucleus, representing the fraction of the recoil energy deposited through displacement [59].
The displacement function is proportional to the NIEL function according to the relation:

$$NIEL(E) = \frac{N_A}{A} \cdot D(E) \tag{2.7}$$

where N_A is the Avogadro constant and A the atomic weight of the considered medium.
The function D(E) is tipically expressed in units of $MeV \cdot mb$ whereas the NIEL-value is given in $\frac{MeV cm^2}{g}$. Their values depend on the particle type and energy. For silicon with $A = 28.086\ \frac{g}{mol}$, the relation between D(E) and the NIEL value is: 100 $MeV mb = 2.144 \cdot 10^{-3}\ \frac{MeV cm^2}{g}$. The value of D(E) for 1 MeV neutron is the ASTM standard $D_{neutron}(1MeV) = 95$ MeV mb.
Moreover, based on the NIEL scaling hypothesis, which assumes a proportionality between NIEL value and damage effects, the damage efficiency of any particle with a given kinetic energy E can be described by the *hardness factor k*. The hardness

factor $k_{particle}$ for a specific particle type is defined as [57, 62]:

$$k_{particle}(E) = \frac{D_{particle}}{D_{neutron}(1MeV)} \tag{2.8}$$

Therefore, instead of D(E), the normalized values $\frac{D(E)}{95MeVmb}$ are often used. The behavior of $\frac{D(E)}{95MeVmb}$ as a function of the particle energy is shown in Figure 2.14 for neutrons, protons, electrons and pions [62]. The hardness factor k can also be derived by normalizing the particle fluence $\Phi_{particle}$ to the equivalent fluence of 1 MeV neutrons $\Phi_{1MeVn_{eq}}$, as expressed by [59]:

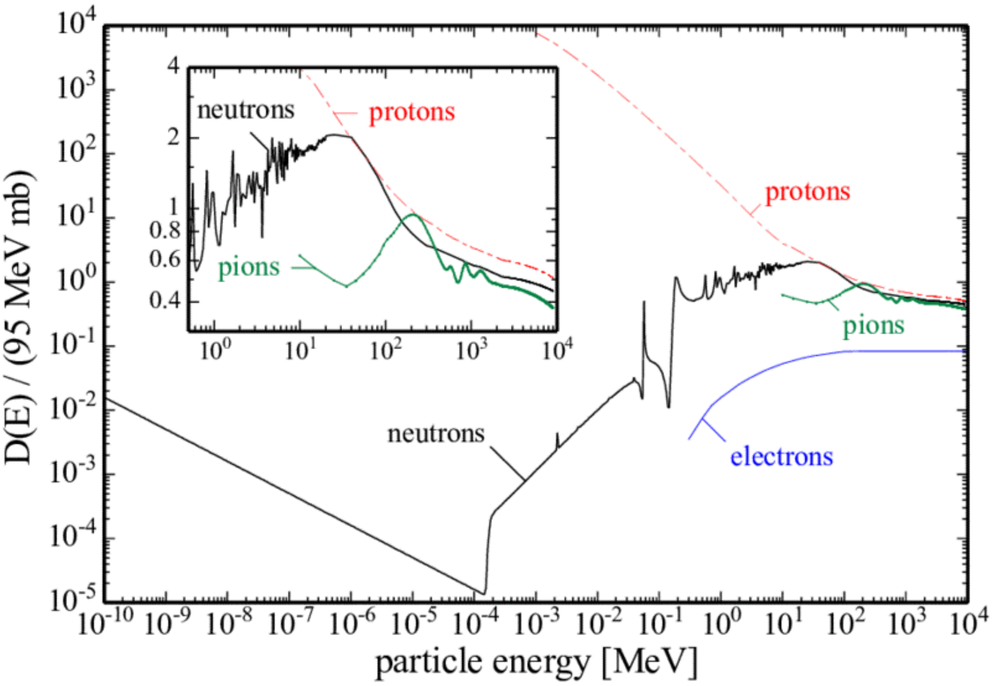

Figure 2.14. Trend of the normalized displacement damage function $\frac{D(E)}{95MeVmb}$ for silicon as a function of the particle energy for neutrons, protons, electrons and pions [62, 63].

$$\Phi_{1MeVn_{eq}} = k_{particle}\Phi_{particle} \tag{2.9}$$

The energy deposited through atomic displacement per unit volume, denoted as E$_{dis}$, can be calculated using Equation 2.6. For silicon, this quantity is expressed as:

$$E_{dis} = n_{Si}\int_{E_{min}} D(E)\phi(E)dE \tag{2.10}$$

where E$_{dis}$ is expressed in $\frac{MeV}{cm^3}$, E_{min} is the minimum impinging particle energy required to displace a silicon atom, $n_{Si} = \frac{N_A}{A_{Si}}\rho_{Si}$ is the atomic density expressed in number of atoms per cm^3 in the silicon bulk, A$_{Si}$ and ρ_{Si} are the atomic weight and the density of silicon, respectively, and $\phi(E)$ is the spectral fluence in $\frac{particle}{MeVcm^2}$ [59, 62].

Moreover, the displacement threshold energy E$_d$ can be used to estimate the concentration of Frenkel pairs generated per cm^3 when an incoming particle transfers energy E$_{dis}$ to the lattice. This estimation is commonly performed using Equation 2.10 and the *modified Kinchin-Pease formula* [64, 65] which provides a model for calculating the number of FP produced in a displacement cascade in crystalline materials as a result of atomic displacements [66]. The relation is expressed as follows:

$$FP \sim \frac{E_{dis}}{2.5E_d} \tag{2.11}$$

The initial damage, i.e., the number of atoms directly displaced and their energy spectrum, induced by incident radiation on a semiconductor, depends on the type of interaction and the nature and energy of the incoming particles. The primary displaced atoms can subsequently trigger a cascade of displacements upon complete dissipation of the primary recoil energy (secondary interactions). Within this cascade, energy dissipation involves a combination of elastic interactions (known as nuclear or elastic energy loss), primarily resulting in displacements and inelastic processes (referred to as electronic or inelastic energy loss), wherein moving displaced atoms excite or ionize atomic electrons during their passage.

The primary recoil energy is deposited by the ionization energy E$_{loss}$ (including that deposited by recoiling atoms in the cascade, when it occurs) and the damage energy (also known as partition or defect-producing energy) E$_{de}$, accounting for displacements and sub-threshold collisions, which transfer energies lower than the displacement threshold energy E$_d$. In these latter interactions, the knock-on atom cannot escape from its lattice position, and the energy is dissipated in lattice vibrations. For a recoil silicon nucleus with kinetic energy E$_{Si}$ and atomic number Z$_{Si}$ = 14, the corresponding energy E$_{de}$ is determined using the following relationship:

$$E_{de} = \frac{E_{Si}}{1 + k_d g(\epsilon_d)} \tag{2.12}$$

where $\epsilon_d = 2.147 \cdot 10^{-5} E_{Si}$, $g(\epsilon_d) = \epsilon_d + 0.40244\epsilon_d^{3/4} + 3.4008\epsilon_d^{1/6}$ and $k_d = 0.14620$ are all dimensionless factors. From Equation 2.12, it is possible to derive the expression for the fraction of energy deposited by ionizing (f_{ion}) and non-ionizing (f_{niel}) processes:

$$f_{niel} = \frac{E_{de}}{E_{Si}} = \frac{1}{1 + k_d g(\epsilon_d)} \tag{2.13}$$

$$f_{ion} = \frac{E_{loss}}{E_{Si}} = 1 - \frac{E_{de}}{E_{Si}} = \frac{k_d g(\epsilon_d)}{1 + k_d g(\epsilon_d)} \tag{2.14}$$

The trends of f_{niel} and f_{ion} for neutrons are represented in Figure 2.15.
Radiation causes the formation of several structures of primary defects in silicon, with configurations that differ depending on the charge state of the defect. At room temperature, these defects exhibit mobility with low activation energies for their movement. For instance, activation energies for vacancy migration vary for n- and p-type materials, influenced by resistivity, typically ranging from 18 to 45 meV [59]. Consequently, not all primary defects lead to stable secondary defects or defect

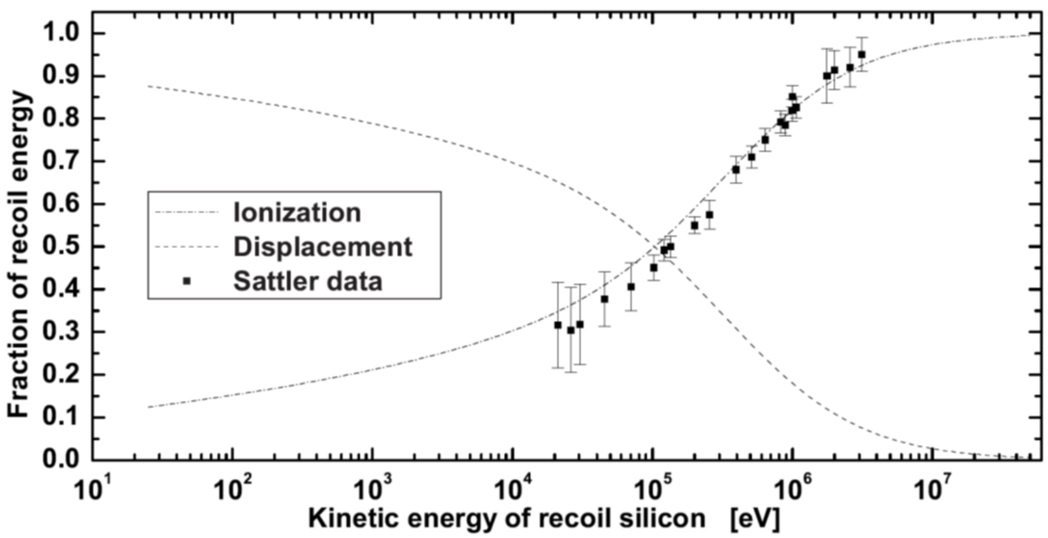

Figure 2.15. NIEL and ionization energy loss processes fractions of recoil silicon [59] (experimental data are from [67]).

complexes, as a significant fraction may anneal, such as through interstitial filling of a vacancy. Nevertheless, these defects can also combine with other point defects and impurities (interstitial and substitutional) to form more stable defects. Examples include the divacancy (midband trapping center [68]), known as the G7-centre (V–V or V2), where two adjacent lattice sites are vacant; vacancy–oxygen complexes termed A-centre or B1-centre; vacancy–dopant impurity complexes (e.g., V–P or V–As in n-type silicon) known as E-centre or G8-centre and others. In Figure 2.16, an A-centre and an E-centre in silicon are shown. The complex defects are mainly E-centres localized 0.4 eV below the conduction band, while the divacancies generate entrapment and trap levels 0.35 eV below the valence band and create many trap levels in the center of the forbidden band. In Table 2.1, the main induced defects in silicon and their energy positions are reported [69].

Electrically active radiation-induced defects have been thoroughly investigated using various experimental techniques, such as Electron Paramagnetic Resonance (EPR) spectroscopy, Thermally Stimulated Current (TSC), photoluminescence and Deep Level Transient Spectroscopy (DLTS) [58, 59].

The radiation-induced bulk defects can be partially or totally recovered after annealing treatments [69, 70].

Radiation damage in materials is often quantified using a measure known as Displacements Per Atom (DPA), which indicates how frequently atoms are displaced from their original lattice sites due to incoming particles. This metric is crucial in facilities such as inertial and magnetic confinement fusion facilities, where materials are subjected to intense radiation environments. DPA is calculated using the formula:

$$DPA = \phi\sigma \tag{2.15}$$

where ϕ is the beam fluence (number of incident particles per unit area in cm^{-2}) and σ is the cross-section of the displacement process (probability of interaction

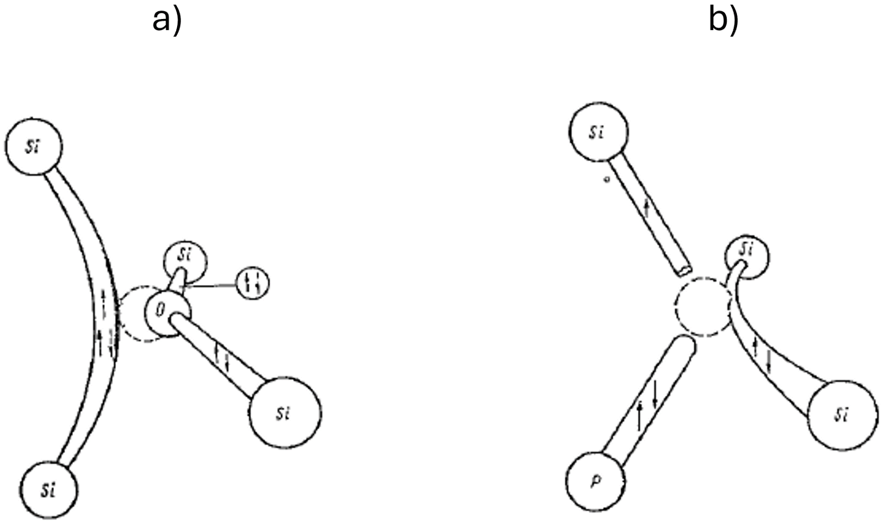

Figure 2.16. A-centre (association of a vacancy with an oxygen atom) in silicon (a) and E-centre (association of a vacancy with a donor impurity atom) in silicon (b). Adapted from [58].

Table 2.1. Energy levels in silicon forbidden band and radiation able to induce them [69].

Position of energy levels (eV)	Kind of radiation
E_c-0.17 E_c-0.15	Neutrons (back-scattered, fast) Electrons (0.5 MeV, 1.5 MeV) ^{60}Co γ rays
E_c-0.4	Neutrons (back-scattered, fast) Electrons (0.5 MeV, 1.5 MeV)
E_c-0.54	Electrons (0.5 MeV, 1.5 MeV) ^{60}Co γ rays
E_v+0.45 E_v+0.43 E_v+0.4	Electrons (0.5 MeV, 1.5 MeV)
E_v+0.35 E_v+0.3	Neutrons (back-scattered) Electrons (0.5 MeV, 1.5 MeV)

between incident particles and material atoms). DPA values directly correlate with the creation of Frenkel Pairs. To determine the actual number of displaced atoms from a given DPA value, one would multiply the DPA value by the total number of atoms in the material sample or detector [71, 72].

While both DPA and NIEL quantify radiation damage, they serve distinct purposes in assessing and mitigating the effects of radiation in various technological contexts. In summary, DPA quantifies physical displacement in structural materials, while NIEL measures energy deposition in semiconductors. Both metrics are essential for understanding and managing radiation effects in different technological applications.
As reported in [72], a simulation was carried out to evaluate DPA and NIEL results in a silicon detector 400 μm thick. The ratio of DPA/NIEL as a function of the energy of the impinging particle is shown in Figure 2.17 for protons, neutrons and pions. From Figure 2.17, it is evident that high energy pions show the same ratio as protons, while neutrons lead to more damage in terms of DPA [72].

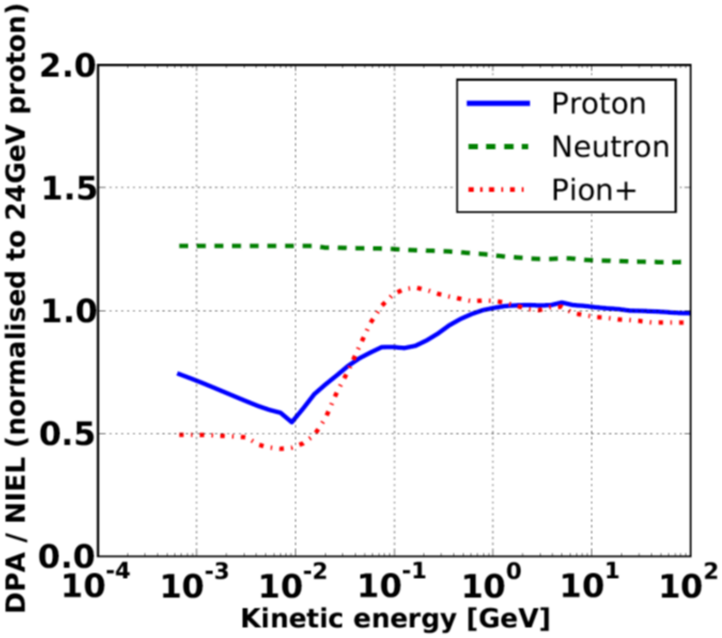

Figure 2.17. Simulated results of the ratio DPA/NIEL for a 400 μm thick silicon detector as a function of the kinetic energy of the impinging particle. The curves are normalized to the value for 24 GeV protons [72].

2.2.2 Ionization damage

Charged particles, such as electrons, positrons, protons and α particles, lose their energy primarily due to the interaction between the electric fields of the charged particles and the electrons of the atoms in the medium. Since the radiation damage induced in electronic devices by charged particles and high-energy photons is mainly related to energy deposition processes via collision-energy losses, specifically, by the excitation and ionization of atoms near the particle path, which creates free electron-hole pairs [69, 59, 58], these energy losses are referred to as ionization losses. The electrons generated after ionization can further ionize atoms through electron-atom collisions or cause displacement damage. Notably, collision energy loss is the dominant process at energies below the so-called *critical energy*, while above this energy, the primary interaction is due to radiation energy loss (emission of photons).

The main effects associated with ionization processes are increased conductivity of the semiconductor material and charge trapping. In silicon, the energy required for the creation of an electron-hole pair is 3.6 eV, which is three times greater than the silicon energy gap (1.1 eV). The mean energy required for the creation of an electron-hole pair in several semiconductors and insulators as a function of the bandgap energy is shown in Figure 2.18 [69, 73]. Regarding the number of electron-hole pairs created per incident radiation absorbed in the material, it is approximately $4.05 \cdot 10^{13}$ per cm^2·rad(Si) in silicon [74], where rad(Si) refers to the dose deposited in silicon, measured in units of rad, as explained below. Displaced silicon atoms can dissipate their energy within the medium through both electronic and nuclear energy losses. Consequently, neutrons can also lead to ionization and

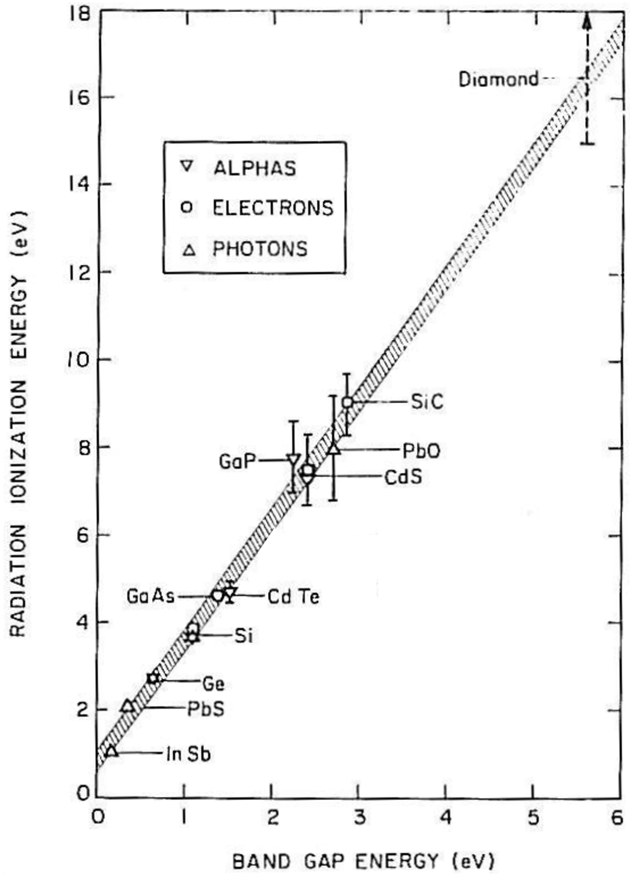

Figure 2.18. Mean energy needed for the creation of electron-hole pair as a function of the bandgap energy for several crystals [74].

excitation processes since they deposit energy by causing recoil silicon atoms to interact with the medium atoms.

Ionizing radiation can also cause an effect known as "surface damage." This occurs due to the presence of charge carrier trapping sites at the interface between the silicon and the silicon oxide (SiO_2) gate insulator layer. When ionizing radiation deposits energy in the oxide, electron-hole pairs are generated and move in the electric fields. Electrons are quickly collected at the positive electrode, while holes migrate toward the Si-SiO_2 interface. Along their path, holes encounter a region with a high trap density, particularly near the interface, leading to the entrapment of several holes. This entrapment generates a positive charge storage, modifying the operating features of the device [59, 69].

2.2.3 Deposited dose

The physical quantity that provides a quantitative correlation between radiation and its effects is the absorbed dose D. It is defined as the ratio of the energy dE released from radiation in a certain volume of matter to the mass dm contained in that volume [75]:

$$D = \frac{dE}{dm} \tag{2.16}$$

In the International System of Units (SI), the absorbed dose is measured in Grays (Gy):

$$1Gy = 1\frac{J}{kg} \tag{2.17}$$

The absorbed dose per unit of time represents the dose rate.

The dose deposited in electronics is often expressed in rad. The relationship is as follows:

$$1rad = 0.01Gy \tag{2.18}$$

In the absence of nuclear transformations, the absorbed dose in silicon devices is attributed to the energy deposited by the ionizing energy-loss processes of primary particles, recoil atoms (i.e. the PKAs generated within the semiconductor medium), and NIEL processes.

For neutrons in nuclear reactors, the contribution of NIEL processes to the absorbed dose (D^{NIEL}) can be calculated by means of Equation 2.10. For a silicon medium, it holds:

$$D^{NIEL} = \frac{E_{dis}}{1.45 \cdot 10^{10}}[Gy] \tag{2.19}$$

with E_{dis} in MeV/cm^3. For instance, in the Triga [76] reactor, where fast neutrons (with kinetic energies above 10 keV and a fluence of $2.33 \cdot 10^{13}$ n cm^{-2}) are present, the deposition of energy through ionization and non-ionization processes differs by 10-11% [59, 77].

In the case of incoming ions, such as those encountered in the space radiation environment, the energy deposited by ionization significantly exceeds that deposited by NIEL processes. Specifically, ionization doses are nearly 4 orders of magnitude larger compared to those from NIEL processes.

As outlined in [59], for particle energies typical of space and high-energy physics environments, the energy deposited by ionization is about 3–4 orders of magnitude greater than that deposited by damage energy for charged particles and isotopes. However, for fast neutrons, the difference is marginal.

2.2.4 Radiation effects on bipolar junction transistors

Radiation-induced defects significantly impact the bulk properties of silicon, which can be investigated through the electrical behavior of semiconductor devices post-irradiation. After irradiation, centers with energy levels near the mid-gap (proximate to the intrinsic Fermi level) play a crucial role in carrier generation, thereby elevating leakage current within the depleted region of silicon devices. These centers function as generation-recombination centers, thereby influencing the semiconductor material overall behavior. Specifically, when these defect centers capture free carriers, they facilitate electron–hole recombination, occurring in two stages: first, a free carrier of one type (electron or hole) is captured by the defect center, followed by the capture of a carrier of the opposite type. This two-step process is pivotal in reducing the minority-carrier lifetime in the material.

This reduced lifetime significantly contributes to the performance degradation of semiconductor devices, particularly bipolar junction transistors. In BJTs, the gain β is greatly influenced by the minority-carrier lifetime. With irradiation introducing more recombination centers, the minority-carrier lifetime decreases, resulting in a decline in the common emitter current gain β of the transistor and an elevation of the saturation voltage $V_{CE(sat)}$. The degradation of β is a primary concern regarding the reliability and performance of such devices. The minority carrier (recombination) lifetime (τ) in semiconductors is a critical parameter that quantifies how long a minority carrier (electron or hole, depending on the type of semiconductor) persists before recombining. The recombination process can occur through various mechanisms, such as radiative recombination, Shockley-Read-Hall (SRH) recombination, or Auger recombination [78].

In the context of irradiation effects on semiconductors, the degradation of electrical properties is often described using a damage coefficient, which represents the rate at which these properties deteriorate due to exposure to radiation. For the minority carrier lifetime, this relationship can be expressed as follows:

$$\frac{1}{\tau_{irr}} - \frac{1}{\tau_0} = \Delta(\frac{1}{\tau}) = K \cdot \Phi \tag{2.20}$$

where τ_{irr} is the minority carrier lifetime after irradiation, τ_0 is the initial minority carrier lifetime before irradiation, K is the lifetime damage coefficient, typically measured in cm^2/s, and Φ is the irradiation fluence, representing the number of incident particles per unit area. In this equation:

- $\frac{1}{\tau_0}$ represents the intrinsic recombination rate before irradiation;
- $K \cdot \Phi$ accounts for the increase in recombination centers due to irradiation, which enhances the recombination rate and thus decreases the carrier lifetime.

The damage coefficient K depends on the type of radiation (e.g., protons, neutrons, gamma rays), the energy of the radiation, and the specific semiconductor material.

Charged particles induce both surface and bulk damage in transistors, resulting in current gain degradation. The reciprocal of current gain can be modeled as [68, 79]:

$$\frac{1}{\beta} = \frac{1}{\beta_0} + \frac{1}{\beta_S} + \frac{1}{\beta_B} = \frac{sW_BA_s}{D_BA_e} + \frac{\sigma_bW_B}{\sigma_eL_e} + \frac{W_B^2}{2D_B\tau_B} \tag{2.21}$$

where s is the surface recombination rate, A_s is the area for surface recombination, W_B is the base width, D_B is the minority carrier diffusion constant in the base, A_e is the cross-sectional area of the conduction path (roughly the same as the emitter junction area), σ_b and σ_e are the base and the emitter conductivities, respectively, L_e is the minority carrier diffusion length in the emitter and τ_B is the minority carrier lifetime in the base [49, 68].

The first term on the right side of Equation 2.21 represents the contribution from surface recombination, the second term relates to emitter efficiency, which typically determines the initial current gain, and the third term corresponds to volume recombination. The first two terms are only slightly affected by displacement damage, while the third term primarily governs the degradation under high displacement damage dose conditions. As evident from Equation 2.21, the term $\frac{1}{\beta_B}$ is the only one that depends on lifetime. For a homogeneous doping profile of the base, it can be shown that the transit time (τ_{tr}) of the minority carrier injected from the emitter to the collector through the base is given by [59]:

$$\tau_{tr} = \frac{W_B^2}{2D_B} \tag{2.22}$$

Therefore, the dependence of $\frac{1}{\beta_B}$ on the carrier lifetime can be expressed as follows:

$$\frac{1}{\beta_B} = \frac{\tau_{tr}}{\tau_B} \tag{2.23}$$

After irradiation, assuming that the transistor maintains a significant common emitter gain $\beta_{B,irr}$ and that the diffusion constant (D_B) of the minority carriers in the base remains nearly unchanged, τ_{tr} stays almost constant. Therefore, $\beta_{B,irr}$ can be expressed as as:

$$\frac{1}{\beta_{B,irr}} = \frac{\tau_{tr}}{\tau_{B,irr}} \tag{2.24}$$

where $\tau_{B,irr}$ is the lifetime of the minority carriers after irradiation.

Therefore, by combining Equation 2.20, Equation 2.23 and Equation 2.24, the change in the reciprocal of the current gain caused by displacement damage, given by the *Messenger-Spratt equation*, can be obtained [80]:

$$\Delta(\frac{1}{\beta})_B = \frac{1}{\beta_{B,irr}} - \frac{1}{\beta_B} \simeq \tau_{tr}(\frac{1}{\tau_{B,irr}} - \frac{1}{\tau_B}) = K\frac{\Phi}{\omega_T} \tag{2.25}$$

where $\beta_{B,irr}$ is the current gain after irradiation due to bulk recombination, β_B is the current gain before irradiation and $\omega_T = \frac{1}{\tau_{tr}} = \frac{2D_B}{W_B^2}$ is the cutoff angular frequency and corresponds to the frequency at which the common-emitter current gain drops to unity. Thus, the Messenger-Spratt equation, which provides a model

for understanding the degradation of current gain in BJTs after irradiation, is often employed for characterizing radiation-induced damage in BJTs.
When saturation effects are absent, the concentration of recombination centers in silicon can be assumed to be proportional to the energy released during atomic-displacement processes, particularly through NIEL processes. This correlation suggests a direct relationship between the number of recombination centers and the concentration of Frenkel pairs generated by these displacement processes. Consequently, Equation 2.20 can be formulated as [59, 57, 77]:

$$\Delta(\frac{1}{\beta})_B = \frac{\lambda}{\omega_T} FP \tag{2.26}$$

where λ is almost independent of the incoming particle but depends on the kind and on the doping profile of the base region. Equation 2.26 is the so-called *generalized Messenger-Spratt equation* and it is used to describe the degradation of the common-emitter current gain β in bipolar transistors due to displacement damage from high-energy particles. It predicts a linear dependence of the inverse of the gain variation on the concentration of Frenkel Pairs generated by these particles, reflecting an approximate NIEL scaling. A key point is that the degradation in current gain β is inversely proportional to the energy deposited by NIEL processes, providing a valuable tool for predicting the performance of bipolar transistors in radiation-rich environments [81].

Ionization damage in NPN transistors leads to the formation of interface traps and net positive charges in the oxide layer overlying the emitter-base junction. This damage has significant effects on the device characteristics, primarily increasing the base surface current. This increase in base current is attributed to two main factors: increased surface recombination rate and spreading of the emitter-base depletion region. The surface recombination rate increases due to the formation of recombination centers at the Si/SiO$_2$ interface covering the emitter-base junction. These recombination centers serve as sites where electron-hole pairs recombine, which increases the surface recombination velocity. The increased surface recombination velocity directly affects the minority carrier lifetime and the overall recombination dynamics within the device. The ionization-induced spreading of the depletion region reduces the effective base width, which can impact the injection efficiency of carriers from the emitter to the base. As the depletion region extends further into the base, more of the base region becomes depleted of carriers, effectively increasing the base current required to maintain a given collector current [49, 79, 82]. An illustration of the base-emitter junction of an NPN BJT is reported in Figure 2.19.
In general, for a mixed radiation damage, the total variation in reciprocal of the current gain is given by the variation due to surface and bulk contribution, that can be regarded as independent of each other, as follows [79]:

$$\Delta(\frac{1}{\beta}) = \Delta(\frac{1}{\beta})_B + \Delta(\frac{1}{\beta})_S \tag{2.27}$$

where $\Delta(\frac{1}{\beta})_S = \frac{1}{\beta_S} - \frac{1}{\beta_0}$ is the change in the reciprocal of gain caused by surface damage.

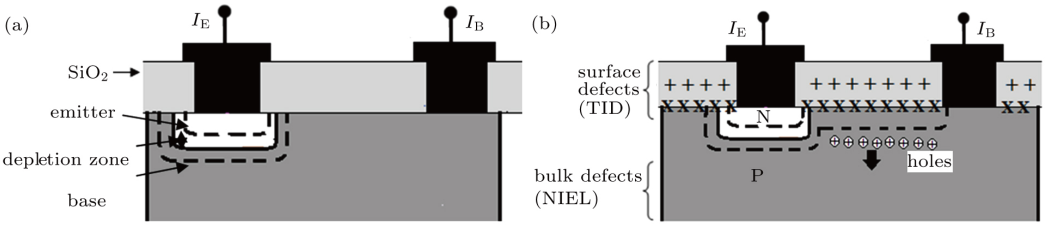

Figure 2.19. Scheme of an NPN BJT emitter base junction before (a) and after (b) irradiation [79].

2.2.5 Radiation effects on optoisolators

Optocouplers, also known as optoisolators, are composed of highly precise and meticulously grown microscopic structures that exhibit very low tolerance for even slight changes in their characteristics. When these components are exposed to radiation, the radiation transfers energy to the materials of the components, thereby altering the localized material properties. These changes can significantly affect the functionality and parametric performance of the components, with the extent of the impact depending on the type of radiation and the location within the optocoupler where the energy is deposited.

Optoisolators are sensitive to SEEs, TID and DD dose. The former can occur in the photodetectors and amplification circuitry of the optocoupler. Single Event Transients (SETs) are transient disruptions caused by a single ionizing particle striking the device, leading to temporary malfunctions or signal distortions. In photodetectors, SETs can cause spurious signals, while in amplification circuitry, they can induce noise or glitches. TID effects result from the cumulative exposure to ionizing radiation, which can cause gradual degradation of the optocoupler performance. This includes shifts in threshold voltages, increased leakage currents, and degradation of CTR. TID effects typically impact the long-term reliability and functionality of the device. DD dose effects are caused by non-ionizing energy loss, where the radiation displaces atoms in the crystal lattice, creating defects. This leads to changes in the electronic properties of the materials, such as reduced carrier lifetimes and mobility. In optocouplers, DD can degrade the efficiency of light emission and detection, as well as affect the amplification properties.

The performance degradation mechanisms that are most important for each component of the optocoupler are summarized in Table 2.2. Radiation can reduce

Table 2.2. Performance degradation mechanism for each component of an optoisolator [55].

Component	Degradation mechanism
LED	DD dose
Photodetector	TID, SET
Amplification circuit	TID, SET
Coupling medium	TID

the efficiency of LEDs by creating defects that act as non-radiative recombination centers, thereby reducing the light output [83]. The effects induced on the photodetector are: increased dark current and noise that in turn reduce the signal-to-noise ratio and overall sensitivity. Radiation-induced shifts in transistor parameters (e.g., threshold voltage, gain) can lead to reduced amplification performance and increased noise. Ionizing radiation induces the entrapment of charge by defects within the optical medium, resulting in the formation of color centers. Subsequently, these color centers absorb signal photons, leading to a degradation in light transmission efficiency [84]. Nevertheless, this degradation is not necessarily permanent, color centers can heal through annealing. The formation and annealing of color centers take place simultaneously, and the degree of optical medium degradation depends on the relative rates of these processes.

In conclusion, radiation can significantly affect optocouplers by modifying material properties and compromising component performance [55].

Chapter 3

Experimental setup and facilities

This thesis project investigates the radiation resistance properties of two types of electronic components: bipolar junction transistors and optoisolators, with a particular focus on demonstrating the effectiveness of dose delivery using laser-generated protons. The BJTs were subjected to innovative radiation sources such as laser-driven protons, as well as conventional sources including gamma radiation, protons, and neutrons from standard accelerators. Optoisolators, currently, have only been tested with gamma radiation. The following sections provide detailed descriptions of the facilities where these irradiation tests were performed. Firstly, this chapter presents an overview of the Advanced Laser Light Source (ALLS) facility at the Institut National de la Recherche Scientifique (INRS) in Varennes, Canada, where laser-accelerated proton irradiation took place. Subsequently, the mechanisms involved in ion acceleration under specific laser-plasma interaction conditions are described, along with the main characteristics of the accelerated particles.
Irradiations using conventional sources were conducted at various laboratories within the ENEA agency. Gamma irradiation was performed at the Calliope Gamma Irradiation Facility, located at the ENEA Casaccia Research Center in Italy. A comprehensive overview of this facility, along with the dosimetry systems used and an introduction to Electron Paramagnetic Resonance (EPR) theory, is provided. Proton and neutron irradiations were conducted at the TOP-IMPLART facility and the Frascati Neutron Generator (FNG), respectively, at the ENEA Frascati Research Center in Italy. Detailed descriptions of these facilities are also included.
Future steps of this thesis project include electron irradiation of electronic devices at the REX facility of the ENEA Frascati Research Center. An overview of this facility is provided at the conclusion of this chapter.

3.1 Advanced Laser Light Source laboratory

The Advanced Laser Light Source Laboratory (ALLS) is located at the Institut National de la Recherche Scientifique (INRS) in Varennes, Québec, Canada [85]. It hosts a 150 TW Ti:Sapphire laser system that operates at a maximum repetition rate of 2.5 Hz with a central wavelength of $\lambda_0 = 800$ nm. This system features a double-Chirped Pulse Amplification (CPA) [86] configuration capable of delivering up to 3.3 J in a pulse duration of 22 fs [87]. The laser beamline employs a cross-wave polarizer as part of a beam-cleaning technique before injection into the second CPA. This results in an Amplified Spontaneous Emission (ASE) pre-pulse contrast of less than 10^{-10} at 100 ps before the main pulse and a steep power rise with a contrast of less than 10^{-6} at -3 ps. The main features of the laser system are detailed in Table 3.1. The beam can be focused on solid or gaseous targets and laser–matter interactions under such conditions lead to the generation of secondary sources with unique properties. Ions can be accelerated by irradiating a solid target with an ultra-intense laser using the Target Normal Sheath Acceleration (TNSA) mechanism, which will be explained in the next section. In particular, protons (H^+) with a broad energy spectrum can be generated. A picture of the bunker with the ion acceleration beamline used for the irradiation tests performed in this work is shown in Figure 3.1. The laser-driven acceleration occurs in vacuum inside the red chamber (Fig. 3.1). This chamber hosts the solid target onto which the laser impinges. A 400-holes target holder (Fig. 3.2) can be employed, allowing for 400 shots per each pumping cycle, with approximately 4 pumping cycles per day. The target holder is mounted on a system that allows shots to be performed automatically at a maximum repetition rate of approximately 0.625 Hz, which corresponds to one shot every four laser pulses. The laser beam, 100 mm wide, is focused down to a spot size of $w_{FWMH} = 5$ μm, resulting in a peak intensity of $I_0 \sim 1.3 \cdot 10^{20}$ W/cm^2. The p-polarized laser pulses strike the target at an angle of 20° with respect to the target normal. At the end of the ion acceleration beamline, there is a Thomson Parabola (TP) spectrometer placed at 0° with respect to the target normal axis, with a Microchannel Plate (MCP) serving as the main ion detector [88], enabling high repetition-rate shots. A schematic of the setup inside the irradiation chamber and of the Thomson spectrometer is shown in Figure 3.3.

Table 3.1. Main ALLS laser beam parameters.

Laser beam peak power	150 TW
Central wavelength	800 nm
Pulse repetition rate	2.5 Hz
Energy per pulse	Up to 3.3 J
Pulse duration	22 fs
Beam diameter	170 mm
Picosecond contrast	$\sim 1 \cdot 10^{-10}$

As depicted in Figure 3.3, the ions enter the TP through a 500 μm pinhole positioned 1.8 m away from the solid target. They then pass between two 6 cm long copper electrodes, separated by 2 cm and operating at ±7.5 kV, and traverse a 0.46 T magnetic field generated by 10 cm long permanent magnets. Subsequently, the ions drift for 7.5 cm before being collected by the MCP detection system.

The spectra of the ions accelerated through laser-plasma interaction can be retrieved from the parabolic traces obtained from the TP spectrometer image. A typical TP image, showing the mentioned parabolic traces, is presented in Figure 3.4, along

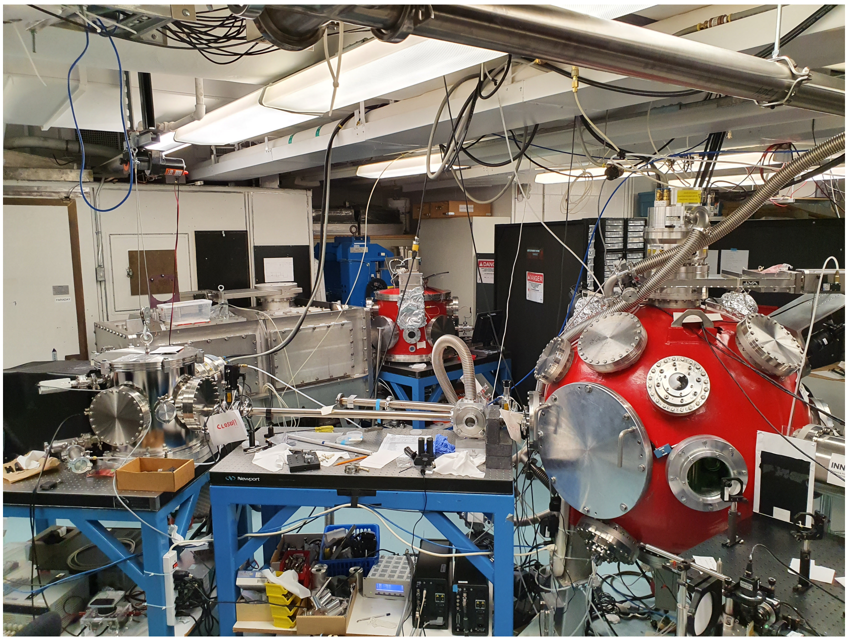

Figure 3.1. Picture of the ion acceleration beamline (from right to left): chamber where the laser-solid target interaction takes place (red chamber), proton beam axis and Thomson Parabola.

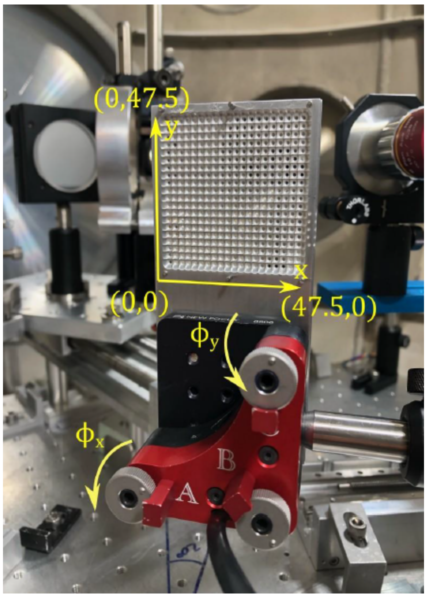

Figure 3.2. Picture of the target holder. The grid is a 47.5 mm x 47.5 mm square. The picomotors A (Φ_x) and B (Φ_y) allow to move the target holder in the x and y directions.

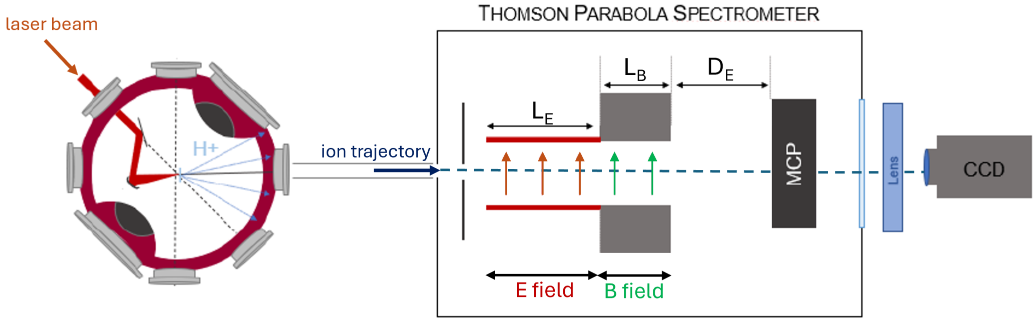

Figure 3.3. Schematic of the irradiation chamber and Thomson parabola. The assembly of the TP spectrometer consists of L_E = 6 cm long copper electrodes and L_B = 10 cm long permanent magnets. The drift D_E between the end of the magnets and the MCP measures 7.5 cm.

with the assignment of the most intense traces to the ion species. [88].

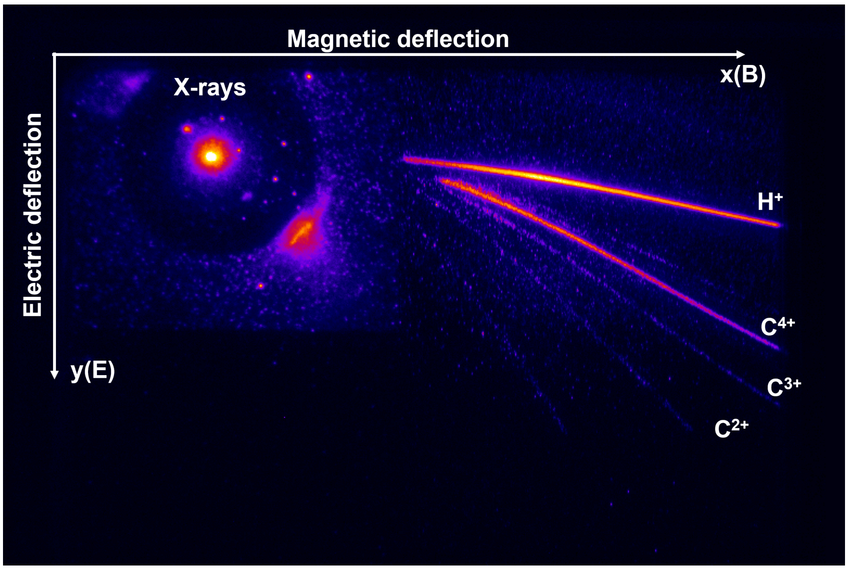

Figure 3.4. A typically obtained TP image. The unlabeled parabola were not considered due to their too low intensity.

On the proton axis, there is also a mini-chamber that allows for carrying out experiments that require irradiation of samples in a dedicated chamber. The chamber is for example used for laser-Particle Induced X-rays Emission (laser-PIXE) experiments [89, 90]. Laser-PIXE is a specific application of conventional PIXE techniques, which are used for elemental analysis of materials. In conventional PIXE, high-energy particles such as protons or alpha particles are directed onto a sample. In laser-PIXE, the high-energy particles are generated using a laser instead of a conventional particle accelerator.

3.1.1 TNSA mechanism

The most routinely employed acceleration mechanisms, according to which ions are accelerated during the interaction of an ultra-intense (I $>$ 10^{18} W/cm^2), ultra-short ($\leq$ 1 ps) laser pulse irradiating a thin solid target of micrometric thickness, is the target normal sheath acceleration [91, 92].
Lasers with intensities exceeding 10^{18} W/cm^2 are characterized by electric fields of an order of magnitude higher than those binding electrons to atoms. Thus, when this kind of laser impinges onto a gaseous or solid target, it can induce rapid photoionization. Laser-induced ionization is possible with a laser intensity larger than the atomic intensity $I_a = 3.5 \cdot 10^{16}$ W/cm^2. However, complex phenomena such as tunnel ionization and multi-photon ionization allow solid target ionization even by lasers with intensities that are orders of magnitude lower than I_a [93, 94].
For this thesis project, laser-accelerated protons obtained from irradiating a solid thin foil target were utilized. Therefore, the subsequent discussion will focus on the case of a solid thin foil target.

The process begins with a thin target being irradiated by a high-intensity (I $>$ 10^{18} W/cm^2) laser. When the laser radiation hits the front side of the target, it ionizes and heats the material, causing it to become a plasma. This plasma forms due to the intense energy deposition from the laser. A plasma is a system of N charges coupled to one another via their self-consistent electric and magnetic fields [95], in which the forces acting between nearby charges are much lower than the long-range Coulomb force [96]. Furthermore, thanks to the charge compensation mechanism, a plasma presents a globally neutral behavior on large volumes and timescales that fail at distances larger or of the order of the Debye length λ_D, defined as:

$$\lambda_D = \sqrt{\frac{\epsilon_0 k_B T_e}{n_e q_e^2}} = \frac{v_{th}}{\omega_p} \tag{3.1}$$

where ϵ_0 is the vacuum permittivity, k$_B$ is the Boltzmann constant, T$_e$ is the electronic temperature, n$_e$ is the electronic plasma density, q$_e$ is the electronic charge, and v$_{th}$ is the electron thermal velocity. Typically, the Debye screening length in laboratory plasmas can range from hundreds of angstroms up to hundreds of micrometers. The quantity ω_p is related to the so-called plasma frequency f$_p$ by the relation f$_p = \omega_p/2\pi$. It represents the natural frequency at which electrons in the plasma oscillate collectively.
In the approximation of a non-collisional plasma (or collisionless plasma), where the mean free path of particles due to collisions is much larger than its characteristic length scales, electromagnetic forces dominate the plasma dynamics. According to [96], an electromagnetic wave, such as a laser pulse, can propagate in a plasma with uniform density only if its frequency ω is higher than the plasma frequency ω_p. This condition arises because the plasma responds to electromagnetic waves differently depending on their frequency relative to ω_p:

- if $\omega < \omega_p$, the plasma is opaque to the electromagnetic wave, meaning the wave is quickly absorbed or reflected by the plasma;

- if $\omega > \omega_p$, the electromagnetic wave can propagate through the plasma with reduced absorption.

This can be expressed in terms of the critical density n$_{cr}$. The critical density is the electron density (n$_e$) at which the plasma frequency ω_p equals the frequency ω_L of the electromagnetic wave (e.g. laser pulse). It is given by:

$$n_{cr} = \frac{m_e \epsilon_0 \omega_L^2}{q_e^2} \simeq \frac{1.1 \cdot 10^{21}}{(\lambda_L[\mu m])^2} cm^{-3} \tag{3.2}$$

where λ_L is the wavelength of the laser in micrometers, m$_e$ is the electron mass, ϵ_0 is the vacuum permittivity and q$_e$ is the electron charge. When n$_e$ > n$_{cr}$, the plasma is called *overdense*, and the incident electromagnetic wave cannot propagate and becomes evanescent. Conversely, when n$_e$ < n$_{cr}$, the plasma is called *underdense*, and the incident electromagnetic wave can propagate [97, 98].
It is worth mentioning that when the laser pulse hits the plasma surface perpendicularly, the conditions described apply directly. However, when the laser impinges on the plasma at an angle θ, the effective critical density must be adjusted by the angle of incidence, specifically by a factor of $cos^2\theta$. This means the critical density for oblique incidence is effectively increased by $cos^2\theta$ [96].

After formation, the plasma expands into the surrounding vacuum. The plasma density profile is characterized by a steep gradient at the front, caused by the rapid motion of ablated material, inducing a shockwave. Behind this front, the density gradually decreases as the plasma plume expands, spreading its material over a larger volume [99]. Therefore, laser-plasma interactions differ depending on whether the laser features short (picoseconds-femtoseconds) or long enough pulses (hundreds of nanoseconds). Indeed, the primary interaction of a high-intensity short laser pulse with a solid target strongly depends on the contrast of the laser pulse, defined as the ratio of unwanted preceding laser light to the main pulse [91]. This preceding light is capable of generating a plasma and can be due to:

- **Amplified spontaneous emission** that is characterized by a contrast in the range 10^{-6}-10^{-10} and lasts few nanoseconds;
- **Laser pedestal** that provides 10^{-4}-10^{-7} times the intensity of the main laser pulse and can last picoseconds or nanoseconds.

Hence, the main laser pulse will interact with an expanding plasma featuring a smoother density profile. To ensure the plasma generated by the laser-matter interaction remains relatively unexpanded upon the main pulse arrival, a high prepulse contrast ratio of at least 10^{-6} compared to the maximum intensity must be upheld up to nanoseconds before the interaction. Additionally, to avoid perturbing the rear face of the target before the arrival of the main pulse, it is crucial that the prepulse energy remains sufficiently low.

Laser ion acceleration begins with the creation and penetration of hot electrons, whose energy spectrum is dependent on the laser intensity, within the thin solid target. The focused laser pulse propels these electrons from the front surface of the target in the forward direction through relativistic ponderomotive force. With sufficient energy, these electrons can escape the target and, due to multiple small-angle scatterings with the target material, reach the vacuum at the rear side with a maximum half-opening angle of 20-25° (the full-cone angle of the electron distribution depends on the target thickness [91]), resulting in the formation of a dense charge-separation sheath. Subsequently, a quasi-static longitudinal electric field, extending over a distance on the order of the Debye length λ_D, is established following the formation of the hot electron sheath due to the retention of electrons near the back surface of the target.

The electric field generated is comparable to the laser electric field (approximately in the range of TV/m) and is sufficiently robust to deflect electrons back into the target, inducing their recirculation, and to ionize atoms at the rear surface of the target. As atoms become ionized, they are accelerated by this electric field. Since electrons are re-accelerated back into the target within a few femtoseconds, they are always present outside the rear surface of the target, resulting in a quasi-static electric field, considering the ion acceleration time. This electric field, perpendicular to the target rear side, facilitates the acceleration of ions normally with respect to the target. The processes leading to ion acceleration are schematically depicted in Figure 3.5 [91].

The accelerated particles are mainly protons and heavier ions, contained in contaminants located on the back surface of the target (e.g. organic compounds created by the vacuum pumping process).

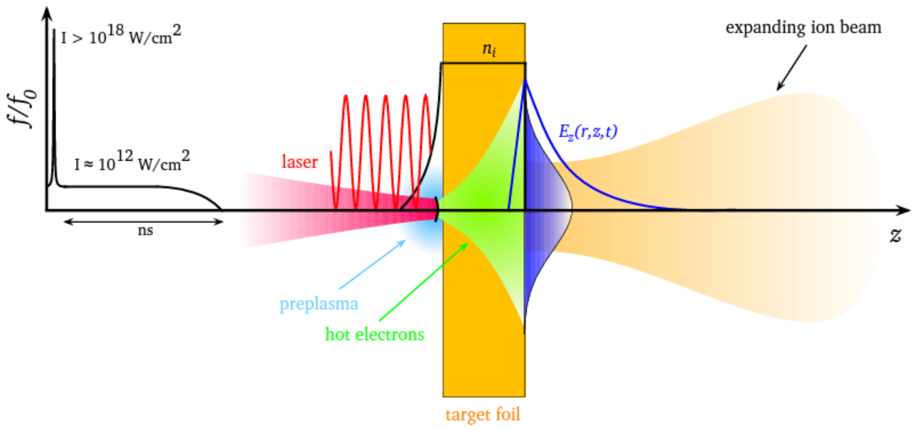

Figure 3.5. Target normal sheath acceleration scheme. When a thin target is irradiated by an intense laser pulse, a preplasma is created at the front side of the target by the laser prepulse. Thus, the main high-intensity laser pulse interacts with the plasma and accelerates hot electrons, mainly in the forward direction. The electrons propagate through the target with a full-angle diverge that depends on the target thickness. When the electrons leave the target, generate a dense sheath at its rear side and, as a results of the charge separation, an electric field is created. This field is high enough to ionize the rear surface atoms and to accelerate the ions in the target normal direction [91].

The features of the laser-accelerated ions are described in the following subsection.

3.1.2 Laser-driven ions characteristics

The target normal sheath acceleration mechanism primarily accelerates light ions, such as protons, located on the back side of the thin foil target, as previously described. Each laser shot results in the emission of ion bunches, ranging from 10^8 to 10^{12} protons per shot, exhibiting a broad energy spectrum and a well-defined cut-off energy spanning from a few MeV to several tens of MeV. Laser-accelerated ions features distinctive characteristics, including cut-off energy, energy spectrum, ion source size and opening angle, which have been extensively investigated and enable laser-driven ions to be applied across various ion beam analysis techniques, such as Particle Induced X-ray Emission (PIXE) [100, 92, 101, 102, 89].

In recent years, numerous experiments have been conducted to characterize the primary features of laser-driven ion beams and explore laser parameters, target composition, and geometry to achieve higher maximum energy and optimize the acceleration regime [103]. Indeed, factors such as the polarization state of the laser [100], the duration of the laser pulse and the selection of the target material and thickness are of paramount importance in obtaining the desired ion characteristics tailored to specific applications [86, 104, 105, 106, 107].

Energy spectrum

The typical ion energy spectrum resulting from the TNSA mechanism is characterized by an exponential broad energy distribution that decreases in intensity as the energy increases. It features a cut-off energy dependent on the driving electron temperature. Regardless of the target composition, protons are accelerated first due to their higher charge-to-mass ratio. These protons originate from water vapor and hydrocarbon contamination present on the target surface due to constraints in achieving optimal vacuum conditions [91].

In the field of laser-driven ion acceleration, the primary focus has often been on achieving the highest possible maximum energy and charge for ion bunches. Several experimental efforts have been made to optimize various aspects of the target used in these laser interactions. Key parameters that have been explored include:

- **target composition**: different materials can affect the efficiency of energy transfer from the laser to the protons [106];
- **target thickness**: this can influence the dynamics of the ion acceleration process. There is a slight increase in the maximum energy of the accelerated protons for thinner targets [106]. However, to expose ultrathin (hundreds of nanometers) targets to relativistic intensities in laser-driven ion acceleration experiments, the level of amplified spontaneous emission and pre-pulses intrinsic to chirped pulse amplification laser systems must be lowered to prevent early heating and deformation of the target;
- **target shape**: various geometrical configurations can help in focusing or dispersing the laser energy more effectively;
- **surface texture**: surface modifications, such as nanostructuring, can enhance

the absorption of the laser pulse, leading to more efficient ion acceleration. Recently, the use of flat foils perforated with nanometric holes as TNSA target has also been investigated [108].

The maximum proton energy achieved from laser-irradiated targets in experiments using different laser systems (characterized by various parameters [109, 110]) is shown in Figure 3.6 as a function of the laser intensity.

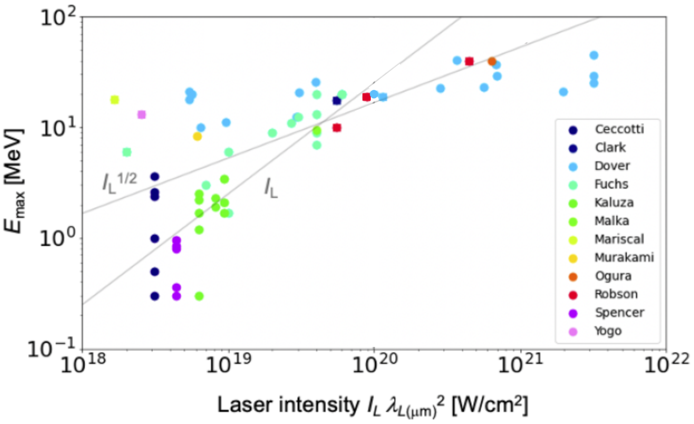

Figure 3.6. Maximum proton energies observed experimentally as a function of laser intensity. Adapted from [110].

In relation to the TNSA mechanism, theoretical studies predict that the energies of accelerated ions could reach several hundred megaelectronvolts. However, experimental validation of these predictions has not yet been achieved, as the highest proton energy attained is approximately 100 MeV [111, 112].

Another crucial characteristic of accelerated ion beams is the particle number, which is linked to the laser-to-proton conversion efficiency. Currently, experiments have detected up to $6 \cdot 10^{13}$ particles for proton energies exceeding 4 MeV [91].

Beam size and opening angle

The spatial and spectral distribution of the ions can be measured using Radiochromic Films (RCFs) [101, 113, 114] which increase their optical density when exposed to ionizing radiation [115].
The ion beam source size emerging from the rear surface of the target is typically wider than the laser spot size impinging on the front surface of the target. For example, in Figure 3.7, data obtained from three different experiment (Trident, LULI-100 TW and Z-Petawatt) are shown for the energy distribution as a function of the source radius. The source radius was observed to be a few micrometers for higher proton energies and hundreds of micrometers for lower energies. The energy-source-size distributions depicted in Figure 3.7 are well-fitted by a Gaussian function, enabling the characterization of the energy dependence on the source size

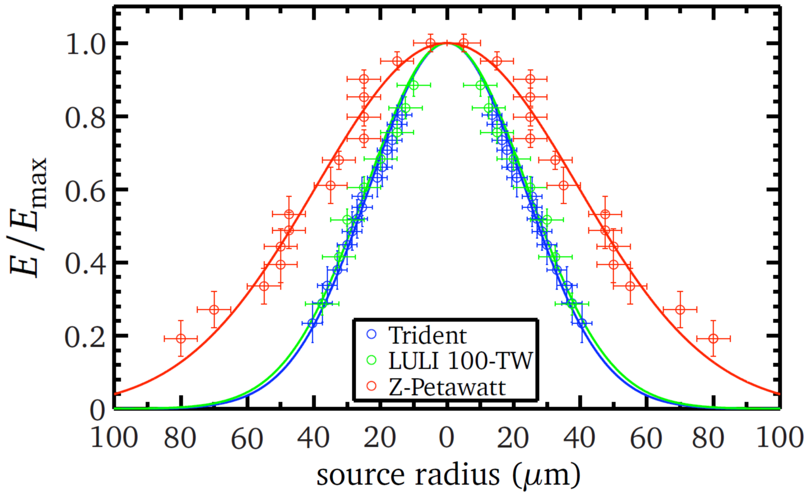

Figure 3.7. Energy-source-size distribution data from Trident (blue circles), LULI-100 TW (green circles) and Z-Petawatt (red circles). The y-axis is normalized to the maximum energy of the corresponding proton beam: 19 MeV for Trident, 16.3 MeV for LULI-100 TW and 20.3 MeV for Z-Petawatt. [91].

d:

$$E = e^{\frac{-(4ln(2)d)^2}{\sigma^2}} \tag{3.3}$$

where 2σ is the Full Width Half Maximum (FWHM).
Furthermore, the beam divergence angle was observed to be energy-dependent [91, 114, 116], notably decreasing with increasing proton kinetic energy. Figure 3.8 displays the results obtained for the half opening angle distribution as a function of the normalized proton energy for the laser systems depicted in Figure 3.7. Higher-energy protons exhibit the smallest opening angles. The laser systems described are characterized by a parabolic dependency (LULI-100 TW and Z-Petawatt) and a linear dependency (Trident) regarding the opening angle as a function of energy. This dependency arises from the initial shape of the hot electron sheath at the target surface [91, 117].

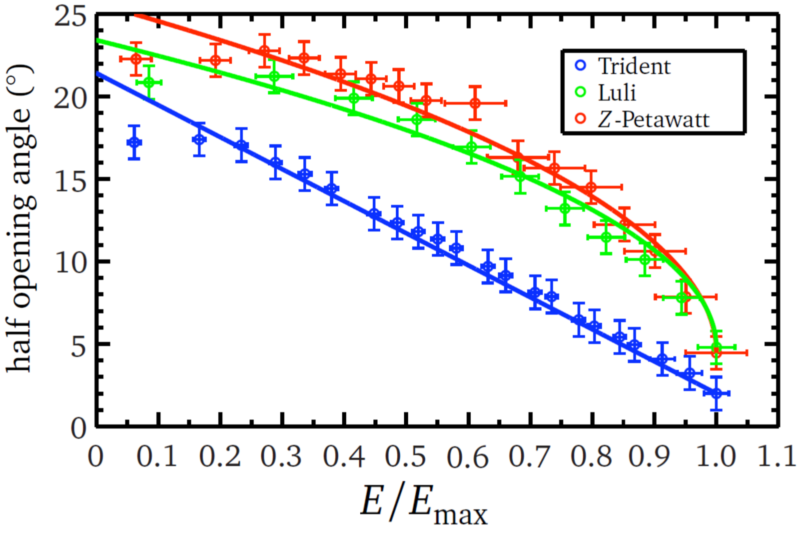

Figure 3.8. Half-opening angle distribution as a function of proton energy for data from Trident (blue circles), LULI-100 TW (green circles) and Z-Petawatt (red circles). The x-axis is normalized to the maximum energy of each proton beam: 19 MeV for Trident, 16.3 MeV for LULI-100 TW and 20.3 MeV for Z-Petawatt [91].

3.2 Calliope gamma irradiation facility

The Calliope gamma irradiation facility of the ENEA Casaccia R.C. is a pool-type facility equipped with a ^{60}Co radio-isotopic source array in a large volume (7.0 × 6.0 × 3.9 m) shielded cell [118]. The source rack is composed of 25 ^{60}Co source rods (with an active area of 41 × 90 cm^2) placed in a planar geometry (Fig. 3.9).

Figure 3.9. a) Calliope source rack in the pool and b) source rack within the irradiation cell (picture acquired by remote camera).

In a simplified decay scheme of ^{60}Co, two photons of 1.17 MeV and 1.33 MeV are emitted in coincidence (Fig. 3.10).
The ^{60}Co radioactive isotope of cobalt is characterized by a half-life $T_{1/2}$ of 5.27 years. For a radioactive isotope such as ^{60}Co, given its half-life, it is possible to

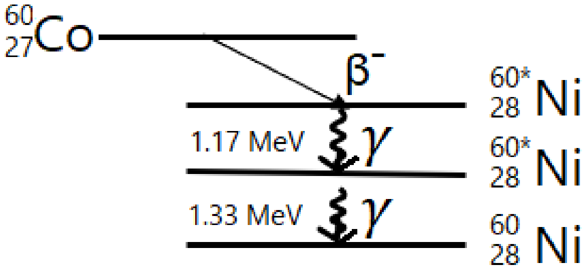

Figure 3.10. Simplified ^{60}Co decay scheme.

define the activity, which is the number of decays per unit time:

$$A = -\frac{dN}{dA} = \frac{ln(2)}{T_{1/2}}N \tag{3.4}$$

where N is the number of atoms in the source. The current activity for the Calliope plant is $1.97 \cdot 10^{15}$ Bq.
By positioning a sample at various distances from the source rack within the irradiation cell, it is feasible to irradiate it at different dose rate values. Specifically, the maximum available dose rate is 6.2 kGy/h (as of June 2024) near the source rack. A steel platform, depicted in Figure 3.9b, is installed to perform irradiation at high dose rate values. The storage pool dimensions are 2.0 x 4.5 x 8.0 m^3 with two separate emergency-storage wells at the bottom.

Additionally, the Calliope facility houses a characterization laboratory and a dosimetric laboratory. Various dosimetric systems are used, depending on the absorbed dose range of interest. All dosimeters undergo periodic calibration using the Fricke absolute dosimeter and are employed when the latter is not applicable, as detailed in the following subsection.

3.2.1 Calliope facility dosimetric systems

At the Calliope facility, various dosimetric systems are employed, each suited to different absorbed dose ranges: Fricke solution (20–200 Gy), Red Perspex (5–50 kGy), radiochromic (1 kGy–3 MGy), alanine-Electron Paramagnetic Resonance (alanine-EPR) (1 Gy–500 kGy), Thermo Luminescent Dosimetry (TLD) (0.1 mGy–100 Gy), and electronic RADFET (0.01–1000 Gy) dosimeters. The Fricke solution serves as an absolute dosimeter, while the relative solid-state and electronic dosimeters (alanine-EPR, Red Perspex, TLD, and RADFET) are periodically calibrated with it. These relative dosimetric systems are used to determine the dose rate when the Fricke solution is not applicable. In the following, the Fricke and alanine-EPR dosimetry systems are described, along with the procedure and methodology used to calibrate alanine dosimeters using the absolute Fricke solution.

Fricke dosimetry system

The Fricke dosimeter consists of an acidic solution of $FeSO_4$, operating on the principle of radiation-induced oxidation of ferrous ions (Fe^{2+}) to ferric ions (Fe^{3+}) in low pH conditions and in the presence of oxygen. The Fricke dosimeter exhibits a linear response in the 20–200 Gy dose range. Its response remains unaffected by radiation energy in the range of 0.1–16 MeV and by dose rates ranging from 0.2 to 1×10^7 Gy/s. During irradiation, temperature variations between 1 °C and 60 °C have negligible effects on the dosimeter's response. The limited absorbed dose range (20–200 Gy) is due to inaccurate measurements below 20 Gy and oxygen consumption at higher absorbed doses.

The Fricke dosimeter is considered an absolute dosimeter because it directly provides the absorbed dose by measuring the change in absorbance, also known as Optical Density (OD), of the solution due to irradiation. The absorbance measurement is often used to determine the concentration of a substance in a solution based on the Beer-Lambert Law that describes the relationship between the absorption of light by a substance and the properties of that substance [119]. The absorbance is defined as:

$$A = Log_{10}(\frac{I_0}{I}) \tag{3.5}$$

where I_0 is the incident light intensity and I is the intensity of light transmitted after traversing the sample.

To quantitatively analyze the concentration of Fe^{3+} produced by irradiation in the Fricke dosimeter, the absorbance of the solution at 304 nm is measured using a UV-Vis spectrophotometer. Figure 3.11 illustrates an example setup of this measurement.

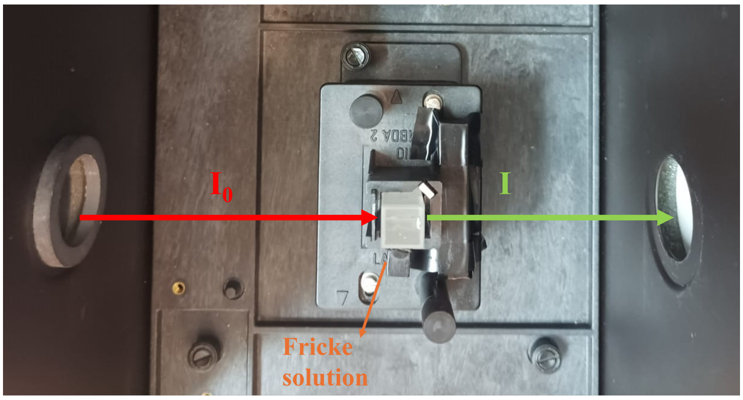

Figure 3.11. Example setup of Fricke dosimeter measurement using a UV-Vis spectrophotometer. I_0 represents incident light intensity (red arrow) and I is transmitted light intensity (green arrow) after passing through the cuvette containing Fricke solution.

The relationship between the absorbed dose (in Gy) and the optical density (OD) for the Fricke dosimeter is given by:

$$D = \Delta(OD) \cdot \epsilon \cdot G(Fe^{3+}) \cdot \rho \cdot l \tag{3.6}$$

where $\Delta(OD)$ is the change in the solution's optical density due to irradiation, ϵ is the molar extinction coefficient of ferric ions at 304 nm ($\epsilon(\mathrm{Fe}^{3+}) \simeq 220$ m^2/mol), G(Fe^{3+}) is the number of ferric ions produced per unit of absorbed energy (G(Fe^{3+}) = (1.61 ± 0.03) × 10^6 mol/J for a ^{60}Co source), ρ is the density of the irradiated solution ($\rho = 1024$ kg/m^3), and l is the optical path length ($l = 1$ cm).

Alanine-EPR dosimetry system

The alanine-EPR dosimetry system is suitable for gamma rays, electrons, and X-rays, offering several advantages: it features high signal stability, a wide absorbed dose range (20 Gy – 200 kGy), and is nearly independent of dose rate and energy. It is also relatively insensitive to environmental factors such as light, humidity, and temperature. The alanine-EPR dosimetry system is considered one of the most effective dosimetric techniques and is based on detecting stable free radicals induced by ionizing radiation in the crystalline L-α-alanine amino acid through Electron Paramagnetic Resonance (EPR) spectroscopy [120]. When alanine amino acid (CH_3-$CHNH_2$-COOH) is irradiated, it forms a stable CH_3-$\dot{C}$H-COOH free radical at room temperature.

At the Calliope facility, alanine-EPR dosimeters are calibrated using absolute Fricke dosimetry. The calibration process involves several steps:

- **Measurements of absorbed dose rate**: the absorbed dose rate at specific positions in the irradiation cells is measured using the Fricke method;
- **Alanine irradiation**: alanine pellets are then irradiated in the same positions within the irradiation cell where the dose rate was measured using Fricke dosimetry;
- **Calculation of absorbed dose**: the absorbed dose is determined by considering the dose rate measured by the Fricke method (corrected for the decay of the ^{60}Co source which accounts for the decrease in radioactivity of the ^{60}Co source over time) and the irradiation time of the alanine pellets;
- **Calibration curve determination**: after irradiation, each alanine pellet is analyzed to investigate the quantity of free radicals induced by ionizing radiation. These measurements are used to establish a calibration curve correlating the quantity of free radicals with the absorbed dose.

In the following, an introduction to EPR spectroscopy, employed for alanine analysis, is provided.

Electron Paramagnetic Resonance (EPR) spectroscopy

Electron Paramagnetic Resonance spectroscopy, also known as Electron Spin Resonance spectroscopy, provides insights into both the type and quantity of free radicals present in samples, making it a valuable tool for studying the characteristics and behavior of these radical species [121]. This spectroscopy is used to investigate the structure and behavior of radicals in materials that contain unpaired electrons. Electrons, being charged particles with mass and spin $s = \frac{1}{2}$, possess intrinsic magnetic properties characterized by their spin quantum number m_s which can be $m_s = +\frac{1}{2}$ (spin-up) or $m_s = -\frac{1}{2}$ (spin-down). The rotation of the electron (its spin) generates a magnetic moment. In the presence of an external magnetic field B_0, the energy levels associated with the two spin states of the electron, which are normally degenerate (having the same energy), become separated due to the interaction between the external magnetic field and the magnetic moment of the electron. This phenomenon is illustrated in Figure 3.12.

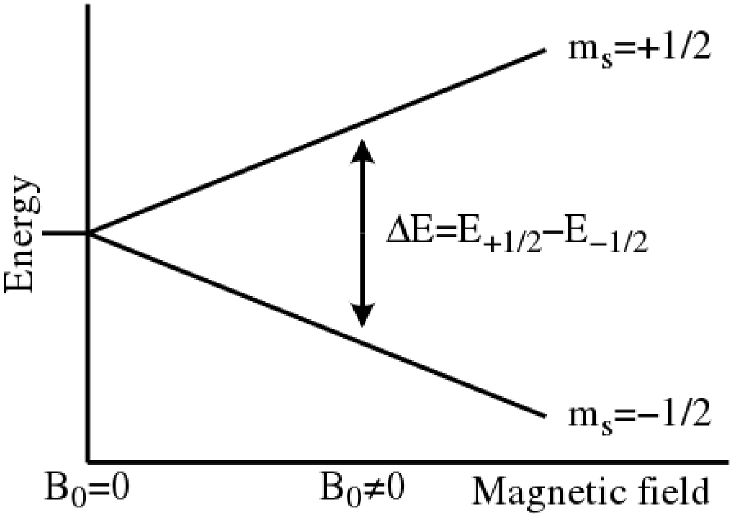

Figure 3.12. Splitting of the electron spin energy levels due to the interaction of the external magnetic field B_0 with the electron magnetic moment, as a function of the applied magnetic field B_0.

The energy difference associated to the two spin levels is defined as:

$$\Delta E = g_E \mu_B B_0 \tag{3.7}$$

where B_0 is the applied magnetic field, μ_B is a constant named Bohr magneton ($\mu_B = 9.27 \cdot 10^{-21}$ erg/gauss) and g_E is a dimensionless factor, called g-factor. The g-factor characterizes the ratio between the magnetic moment and the angular momentum of a particle and for a free electron it is equal to $g_E = 2.0023$. Since both g_E and μ_B are constant, the energy splitting is proportional to the magnetic field strength. When the electron is exposed to an electromagnetic field characterized by a frequency ν that meets the resonance condition:

$$h\nu = g_E \mu_B B_0 = E_{+1/2} - E_{-1/2} \tag{3.8}$$

the transition between the two energy levels is allowed, enabling the unpaired electron to absorb a photon with energy $h\nu$ and move between these states [122]. Equation 3.8 represents the core equation in EPR spectroscopy. In this technique, the frequency ν is determined by the dimensions of the resonant cavity of the spectrometer, while the applied magnetic field B_0 is varied. This is crucial for tuning the resonance of the magnetic states of the electrons within the cavity, allowing observation of their response to the magnetic field. The g-factor depends on the nature of the half-filled orbital, meaning the type of atomic or molecular orbitals containing unpaired electrons. In some cases, the g-factor may also depend on the orientation of the orbital relative to the applied magnetic field. For example, the orientation of p or d orbitals in a crystal field can affect the value of the g-factor.

An EPR spectrometer comprises a cavity situated within an electromagnet, enabling continuous variation of the applied magnetic field. It includes a microwave source that emits microwave radiation into the cavity, a sample cell placed inside the cavity to interact with both the microwaves and the varying magnetic field and a detector capable of measuring the intensity of the radiation absorption. Solid-state diodes are often used as detector as they are sensitive to microwave energy, detecting absorption lines when the energy level separation matches the microwave frequency. Most external components, such as the source and detector, are housed within a microwave bridge control [123]. Figure 3.13 illustrates a schematic diagram of an EPR spectrometer.

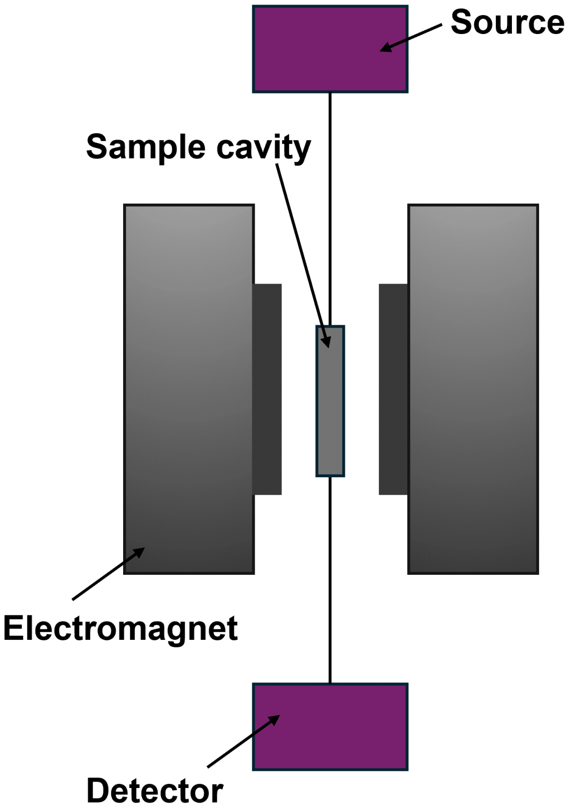

Figure 3.13. Scheme of a typical EPR spectrometer. Adapted from [123].

Concerning alanine-EPR dosimeter measurements, the alanine samples are placed into a vertical quartz tube and then inserted into the EPR microwave cavity where the magnetic field can be adjusted (quartz tubes are preferred in EPR spectroscopy because they are highly resistant to the formation of free radicals compared to other types of glass or insulating materials). When the external magnetic field of the spectrometer matches the energy difference between the split levels, absorption occurs, and a signal is detected. EPR spectra are recorded as the first derivative of this absorption signal. This method enhances the intensity of the detectable signal, making it easier to observe and analyze EPR spectra even under low absorption conditions.

An example of an alanine-EPR spectrum after irradiation is shown in Figure 3.14, highlighting the maximum peak-to-peak height (h_{pp}), a commonly used parameter in EPR spectroscopy. From Figure 3.14, it is evident that the alanine spectrum after irradiation features five main peaks. The area of the EPR signal (the double integral of the spectrum since the spectrum is the derivative of the absorption signal) and the maximum peak-to-peak height (h_{pp}) are directly proportional to the number of radiation-induced radicals, which correlates with the absorbed dose.

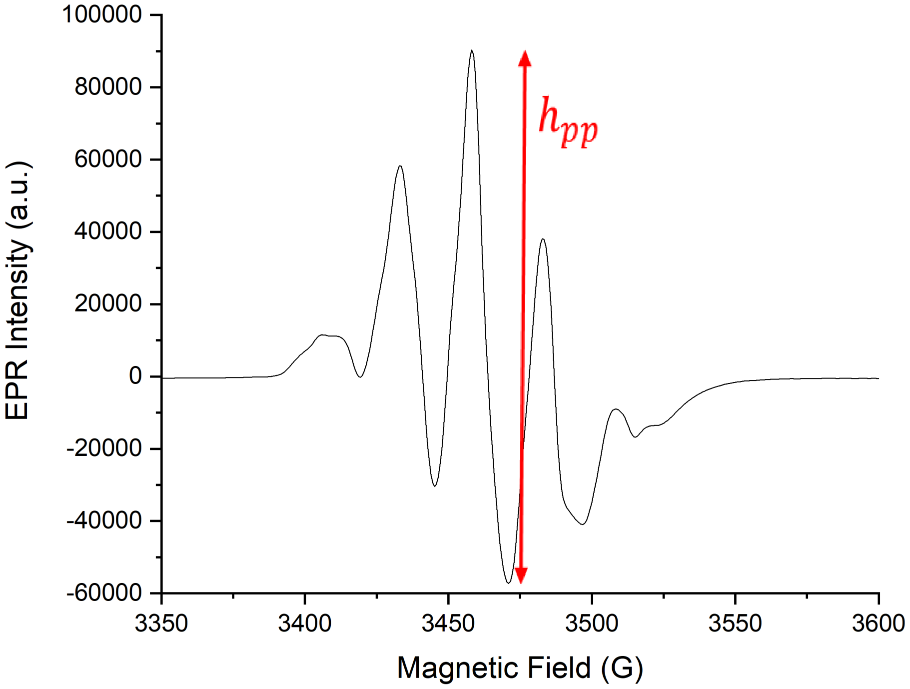

Figure 3.14. EPR spectrum of an alanine pellet after irradiation. The maximum peak-to-peak height (h_{pp}) is shown.

At this point, it is worth specifying that alanine dosimeters are water-equivalent, so the dose values obtained with both Fricke and alanine-EPR dosimetry systems refer to water. To determine the energy deposition and penetration of photons in different materials, it is necessary to introduce the mass attenuation coefficient ($\frac{\mu}{\rho}$)

and the mass energy absorption coefficient ($\frac{\mu_{en}}{\rho}$) [124, 125].
The mass attenuation coefficient is defined as:

$$\frac{\mu}{\rho} = \frac{1}{x} ln(\frac{I_0}{I}) \tag{3.9}$$

where μ is the attenuation coefficient, ρ and x are the density and thickness of the material traversed by the radiation and I_0 and I are the incident and emerging intensities of the mono-energetic photon flux. The mass energy absorption coefficient accounts for the energy absorbed by the material from secondary processes produced by radiation. It is defined as:

$$\frac{\mu_{en}}{\rho} = (1-g)\frac{\mu_{tr}}{\rho} \tag{3.10}$$

where g represents the average fraction of the kinetic energy of secondary charged particles that is lost in radiative processes, and $\frac{\mu_{tr}}{\rho}$ is the mass energy transfer coefficient. The mass energy transfer coefficient is the product of the mass attenuation coefficient and the fraction of energy transferred to charged particles as kinetic energy by interacting incident photons [124]. The mass energy transfer coefficient represents the portion of the mass attenuation coefficient responsible for generating kinetic energy in charged particles. If all the transferred energy is fully absorbed locally, then $\frac{\mu_{tr}}{\rho}$ equals $\frac{\mu_{en}}{\rho}$.
By knowing the dose absorbed in one material, the dose absorbed in another material can be calculated using the mass energy absorption coefficients of both materials. For example, using Fricke and alanine dosimeters, if the absorbed dose in water D_{water} is known, the dose in silicon $D_{silicon}$ can be calculated as follows:

$$D_{silicon} = D_{water} \frac{(\frac{\mu_{en}}{\rho})_{silicon}}{(\frac{\mu_{en}}{\rho})_{water}}. \tag{3.11}$$

The mass attenuation coefficient and mass energy absorption coefficient for silicon are shown in Figure 3.15.

3.3 TOP-IMPLART proton linac

The TOP-IMPLART (Oncological Therapy with Protons - Intensity Modulated Proton Linear Accelerator for Therapy) facility at the ENEA Frascati Research Center is equipped with a multipurpose Radio Frequency (RF) proton linear accelerator, developed by ENEA in collaboration with the Italian National Institute of Health (ISS) and the Regina Elena National Cancer Institute (IFO) of Rome [127, 128]. It was designed for proton therapy applications, it boasts features that enable precise control of the intensity and energy released from pulse to pulse.
Situated within a bunker measuring 27 meters in length and 3 meters in width, the TOP-IMPLART facility is depicted in Figure 3.16.
The TOP-IMPLART linac consists of a 7 MeV commercial injector (Duoplasmatron Source, Radio Frequency Quadrupole (RFQ), and Drift Tube Linac (DTL)) produced by ACCSYS-Hitachi (PL7 model) operating at 425 MHz, and a high-frequency linear

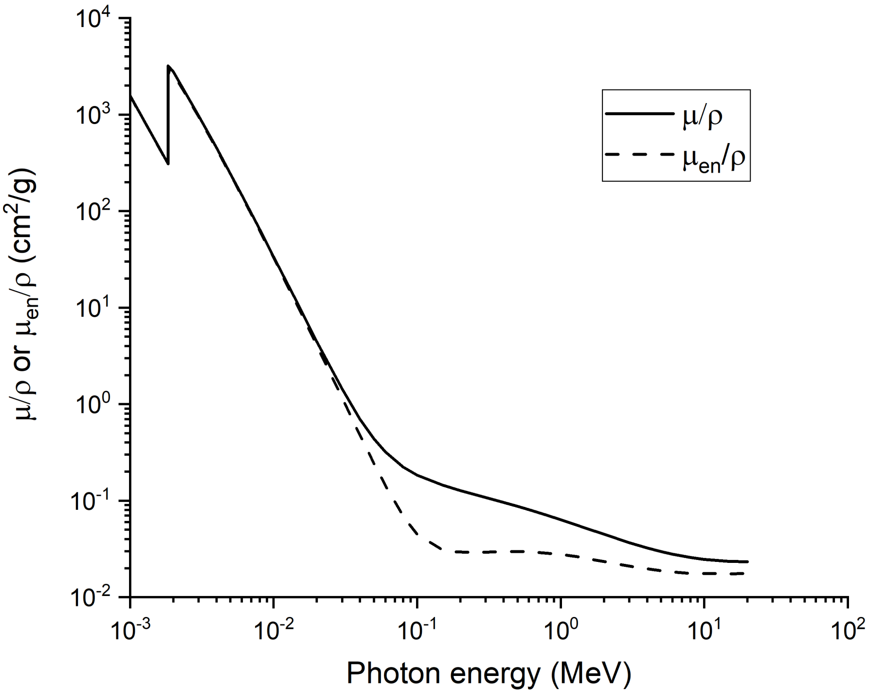

Figure 3.15. Silicon mass attenuation coefficient and mass energy-absorption coefficient as a function of the photon energy [126].

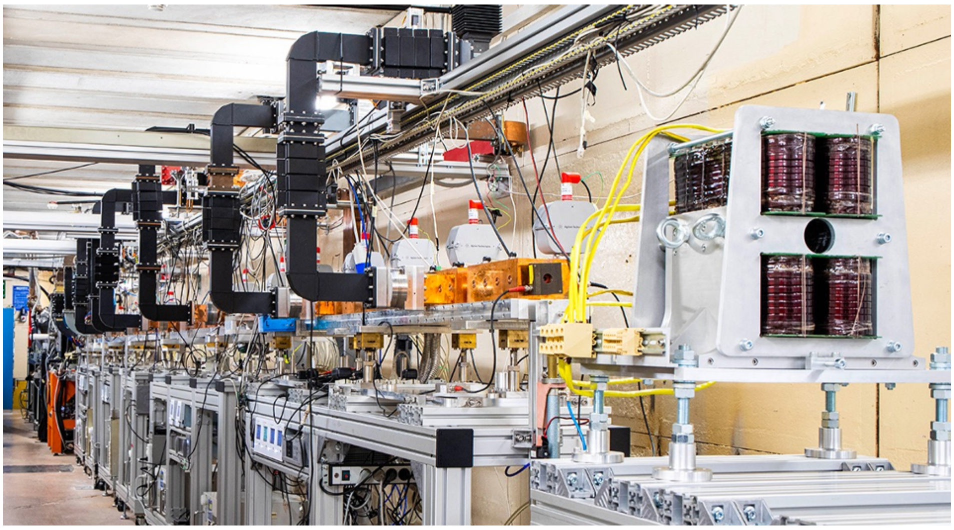

Figure 3.16. TOP-IMPLART facility.

accelerator operating at 2997.92 MHz, completely designed by ENEA. This latter segment is composed of Side Coupled Drift Tube Linac (SCDTL) structures up to 71 MeV.
Exiting the injector, there is a low-energy vertical extraction line with an energy range of 1 to 6 MeV. The minimum energy is obtained by powering only the RFQ and transporting the beam through the DTL. Intermediate energies (1 to 6 MeV) are achieved by varying the relative phase and/or the input RF power level of the DTL. These energies are selected using a 90° dipole magnet that acts as a spectrometer. The effective energy on a target placed outside the 50 μm Kapton window is in the 1 to 6 MeV range. The beam spot size is 16 mm in diameter with a homogeneity of $\pm 5\%$.

Within the energy range of 7 to 71 MeV, the linac is divided into eight SCDTL modules grouped into two sections, each powered by a 10 MW peak power klystron. The SCDTL accelerating structure was developed by ENEA [129] to satisfy the requirement of a high shunt impedance in the low-beta part of the TOP-IMPLART linac. Specifically, the SCDTL is a sequence of short DTL tanks, RF-coupled together by side coupling cavities, which explains the name SCDTL. In the DTL tanks, the accelerating function takes place, while in the intratank space, created by the coupling cavities, the focusing action is achieved with high gradient Permanent Magnet Quadrupoles (PMQs). The cells inside a tank of each SCDTL module have the same length $\beta\lambda$, where β represents the ratio of the average particle velocity to the speed of light in that tank, and λ denotes the wavelength of the RF field used to accelerate the particles. A schematic of the TOP-IMPLART accelerator is depicted in Figure 3.17.

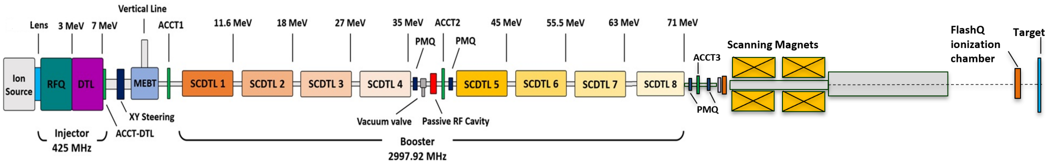

Figure 3.17. Scheme of the TOP-IMPLART linear accelerator.

The resultant beam, characterized by an energy spread (FWHM of the Gaussian energy distribution) of 600 keV, is bunched into pulses lasting 2.5 μs, each containing approximately $3 \cdot 10^8$ protons, operating at a repetition frequency of 25 Hz. The number of pulses can be selected based on the desired proton fluence. The beam spot diameter is less than 3 mm at the exit of the last SCDTL structure, but it increases to 17 mm FWHM at the end of the beam high energy transport line. Utilizing a pair of X-Y scanning magnets, it becomes feasible to irradiate samples over an area of up to 10 x 10 cm^2 at a nominal target distance of 2.60 m from the linac exit. The homogeneity on the target is a function of the spot mesh resolution: the higher the number of spots, the higher the homogeneity. The main parameters of the horizontal and vertical extraction lines of the TOP-IMPLART accelerator are summarized in Table 3.2 and Table 3.3, respectively.
At TOP-IMPLART facility, several systems are used for beam diagnostic such as Faraday cups, ionization chambers, radiochromic films, commercial micro-diamond

Table 3.2. TOP-IMPLART horizontal line main parameters.

Beam energy	71 MeV
Energy spread	0.6 MeV (FWHM)
Pulse duration	2.5 μs
Repetition rate	25 Hz
Beam size at SCDTL exit	<3 mm
Pencil beam size at target position	17 mm (FWHM)

Table 3.3. TOP-IMPLART vertical line main parameters.

Beam energy	1-6 MeV
Energy spread	0.2 MeV (FWHM)
Pulse duration	15-60 μs
Repetition rate	25 Hz
Typical beam spot	16 mm

dosimeter and Lithium Fluoride crystal detectors.

3.4 Frascati Neutron Generator

The Frascati Neutron Generator (FNG) is a compact neutron accelerator situated at the ENEA Frascati Research Center [130, 131]. It operates on T(d,n)^{4}He and D(d,n)^{3}He fusion reactions, producing nearly isotropic and almost monochromatic sources of 14 MeV and 2.5 MeV neutrons, respectively. The accelerator is housed within a large shielded hall measuring 11.5 × 12 m^2 with a height of 9 m. The target where the fusion reaction occurs is positioned 4 m away from the bunker wall to minimize contaminations from scattered particles in the neutron spectrum. In Figure 3.18 a photograph of the FNG is shown, while in Figure 3.19 a schematic of the generator is illustrated.
Deuterium ions of various species (D^+, D_2^+, D_3^+) are generated by a duoplasmatron source, with D^+ ions selected by passing through a 90° deflecting magnet. Subsequently, deuterium ions are accelerated up to 270 kV and 1 mA current using an electrostatic accelerator. For the production of 14 MeV neutrons, D^+ ions are accelerated by a magnetic quadrupole triplet onto a tritiated titanium target, while a deuterated target is employed for the production of 2.5 MeV neutrons. The maximum neutron yields are 10^9 n/s and 10^{11} n/s for 14 MeV and 2.5 MeV neutrons, respectively.

By placing the samples in different positions relative to the FNG target, where the DT fusion reaction occurs, different neutron fluxes are available. The distribution of 14 MeV neutron fluence per source particle, obtained using a Monte Carlo N-Particle

Figure 3.18. A picture of the Frascati neutron generator.

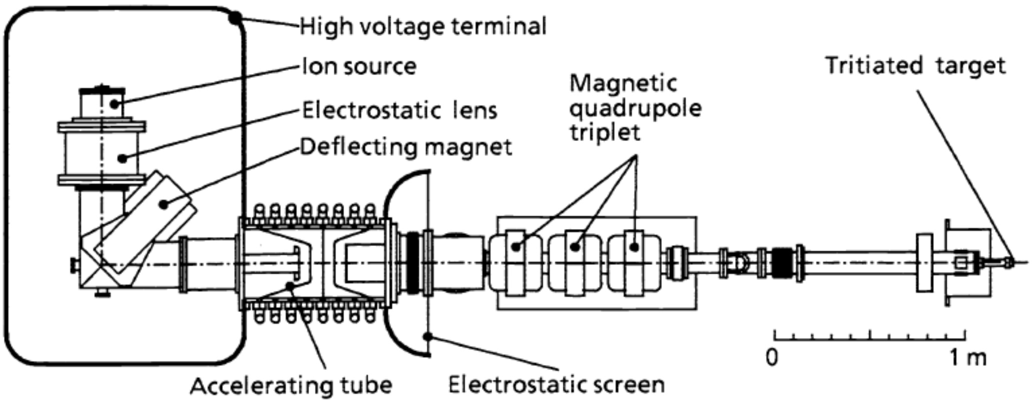

Figure 3.19. Scheme of the FNG assembly [130].

®(MCNP®) code, is presented in Figure 3.20 for both the horizontal and vertical planes at a distance of 5 cm from the DT target. As shown in Figure 3.20b, at a distance of 5 cm from the target, the flux is homogeneous over an area of approximately 1 cm^2.

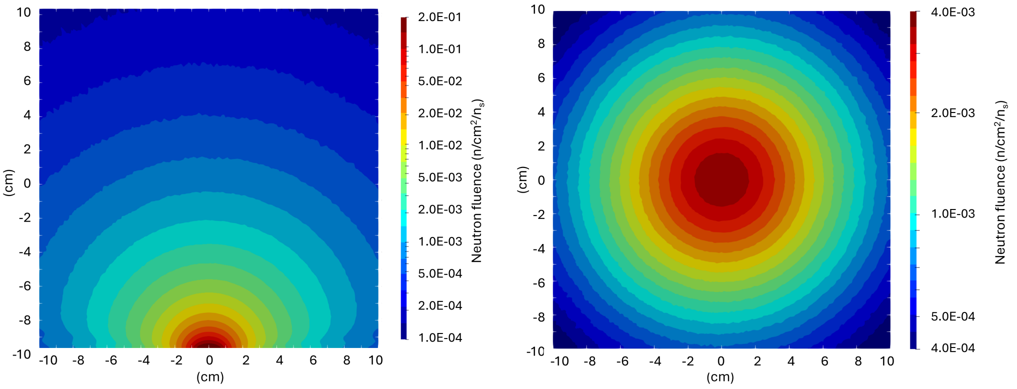

Figure 3.20. 14 MeV neutron fluence distribution maps on the (a) horizontal plane and on the (b) vertical plane at 5 cm from the DT target. The fluence is expressed in $n/cm^2/n_s$ where n_s represents the source neutrons generated per second by FNG. To obtain the flux, the fluence per source neutron must be multiplied by the number of neutrons produced per second. MCNP®data, provided by Dr. Andrea Colangeli (ENEA Nuclear Department, Division of Fusion Energy Development, Frascati R. C.).

The neutron emission rate is determined using the associated α particle technique [131]. In this method, a silicon detector placed inside the drift vacuum tube, 2 m away from the target, counts the alpha particles produced, providing the absolute number of 14 MeV neutrons. Additionally, neutron yield and flux can be determined via MCNP®simulation with an uncertainty of 3%.

For the determination of 2.5 MeV neutron emission, the foil activation technique is employed. A ^{115}In foil is irradiated, and the resulting gamma emission, following the reaction ^{115}In(n,n')^{115}In^m, is measured using a germanium detector, with an associated uncertainty of ±7%. The main parameters of the FNG neutron beams are summarized in Table 3.4.

Table 3.4. FNG main parameters.

	D-T mode	**D-D mode**
Neutron energy	14.1 MeV	2.5 MeV
Maximum neutron yield	$1 \cdot 10^{11}$ n/s	$1 \cdot 10^{9}$ n/s
Maximum neutron flux	$5 \cdot 10^{9}$ $n/cm^2/s$	$5 \cdot 10^{7}$ $n/cm^2/s$
Maximum irradiation time	50 hours (1 target)	Continuous

The FNG is a multipurpose neutron source, contributing to activities spanning space, fusion, biology and medical applications [131].

3.5 Removable Electron to X-ray source accelerator

The Removable Electron to X-ray source (REX) of the ENEA Frascati Research Center is a facility based on an S-band on-axis coupled electron linear accelerator and on its radiofrequency system [132]. A picture of the REX electron bunker is shown in Figure 3.21.

Figure 3.21. Picture of the REX irradiation bunker.

The REX linac produces a 5 MeV electron beam with a maximum Pulse Repetition Frequency (PRF) of 20 Hz. Additionally, by positioning a high atomic number material (such as tungsten, gold, or platinum) conversion unit at the linac extraction point, X-rays can be obtained through the bremsstrahlung process.

The RF pulsed standing wave linac is housed in an external vacuum chamber and is driven by a 2 MW peak power magnetron, capable of generating a 3.4 μs FWHM pulsed electron beam with a maximum beam current of 120 mA. Irradiation takes place in a $40 \times 40 \times 80$ cm^3 lead-shielded irradiation chamber, allowing for a maximum irradiation time of approximately 30 consecutive minutes. A schematic of the REX plant is depicted in Figure 3.22.

The main parameters of the REX electron beam are reported in Table 3.5.

At REX accelerator, radiochromic films, alanine dosimeters and Markus ionization chamber are used for beam diagnostic and dosimetry.

As detailed in Chapter 4, dosimetric measurements to assess the dose rate distribution inside the REX chamber were conducted using alanine-EPR dosimeters. These dosimeters were calibrated with the absolute Fricke solution at the Calliope facility. Specifically, the REX electron beam characteristics were determined by irradiating alanine dosimeters at various points within the REX chamber, at different distances from the electron source.

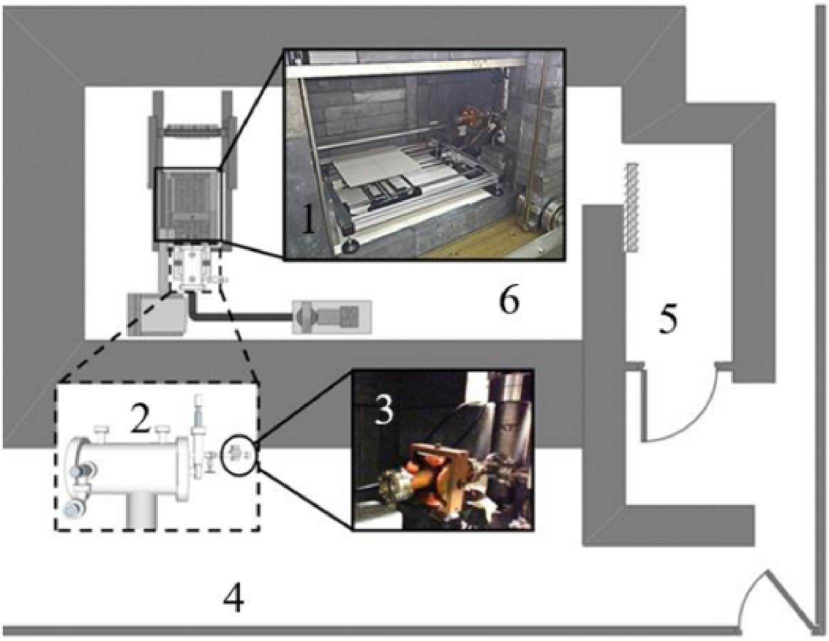

Figure 3.22. Scheme of the REX facility. (1) Irradiation chamber, (2) vacuum vessel containing the linac, (3) linac extraction point, (4) control room and (5) bunker access are highlighted [133].

Table 3.5. REX main parameters.

Pulse length	3.4 μs
Maximum pulse current	120 mA
Maximum electrons per pulse	$2.5 \cdot 10^{12}$ e/pulse
Maximum PRF	20 Hz
Maximum average current	8.2 μA
Maximum electrons per second	$5.1 \cdot 10^{13}$ e/s

Chapter 4

Calliope gamma irradiation facility and REX electron beam dosimetric intercalibration

Dosimetry has historically been associated with radiology due to the necessity of controlling the radiation levels emitted by X-ray machines. This necessity arises from a combination of ensuring patient and worker safety, complying with regulatory standards, optimizing diagnostic quality, and advancing public health protections. In 1925, the First International Congress of Radiology established the organization known as the International Commission on Radiological Units (ICRU) to address the concepts of radiation measurement and standardization in radiology. Essentially, dosimetry involves measuring the dose of ionizing radiation using dosimeters [125]. Ionizing radiation refers to radiation that can ionize matter either directly or indirectly through secondary radiation. Although termed ionizing, this is not the only mechanism by which energy is transferred to a material. For dosimetry, ionizing radiation includes energetic charged particles, X-rays, γ-rays, and neutrons of all kinetic energies [125].
Radiation dosimetry is applied to measure quantities such as absorbed dose, energy released by indirectly ionizing radiation (e.g., photons and neutrons), and the number of particles incident at a specific point. A radiation dosimeter is considered absolute if it can measure radiation without requiring calibration in a known radiation field. Examples of absolute dosimeters include ionization chambers and Fricke chemical dosimeters.

An ionization detector, often referred to as an ionization chamber, operates based on the principle of ionization produced within a gas-filled chamber when radiation interacts with the gas molecules. The detector consists of a sealed chamber filled with a suitable gas, such as air, argon, or a mixture of gases, where an electric field is established by applying a polarizing voltage across two electrodes.
When ionizing radiation enters the chamber, it interacts with the gas molecules, causing ionization. This process generates positively charged ions and free electrons, which migrate towards the oppositely charged electrodes. The collection of these ions and electrons at the electrodes forms a small electric current known as the

ionization current.

The energy from the incoming radiation is converted into this measurable electric current, which is directly proportional to the intensity of the radiation. For instance, in the case of air, to determine the absorbed dose, the number of collected ions is multiplied by the average energy required to produce an ion pair in dry air, which is approximately $W_{air} = 33.97$ eV/ion pair = $33.97\ J \cdot C^{-1}$ [134].

Regarding the Fricke chemical dosimeter, as shown in Chapter 3, it is a solution used to evaluate the deposited dose by measuring the chemical change induced by irradiation in the solution. Specifically, the change in absorbance after exposure is measured [125], as detailed in Section 3.2.1.

Absolute dosimeters are essential for accurately measuring the radiation dose absorbed by a sample at a specific location within an irradiation cell.

To expand on the radiation resistance study described in Chapter 5, electronic devices will undergo electron irradiation at the REX facility. Given the absence of a dedicated absolute dosimetric system at REX, crucial dosimetric measurements were performed to establish the irradiation conditions for these devices. This effort included an intercalibration between the Calliope gamma source and the REX electron beam. This work was performed in the framework of the Italian Space Agency Supported Irradiation Facilities program (ASIF program). ASIF is a collaborative initiative involving the Italian Space Agency (ASI), the National Institute for Nuclear Physics (INFN), and the ENEA agency, aiming to coordinate a network of irradiation facilities across Italy to support both national and international space missions [135].

In this chapter, the cross calibration of the Calliope facility and the REX electron beam is presented. Firstly, up-to-date calibration curves of the alanine-EPR dosimetry system were obtained using the Fricke dosimetry system at the Calliope facility. Subsequently, alanine dosimeters were irradiated at the REX facility to assess the radiation dose distribution within its irradiation chamber, utilizing the prior calibration established at Calliope. This process enabled the determination of suitable irradiation conditions for electronic devices. The chapter details the experimental measurements conducted for the initial calibration of the alanine dosimetry system at Calliope and for evaluating the dose distribution at REX.

The establishment of these dosimetric procedures is fundamental for ensuring accurate and reliable irradiation conditions, essential for the comprehensive study of electronic device radiation resistance.

4.1 Alanine calibration curves determination at Calliope facility

To intercalibrate the Calliope gamma source and the REX electron beam, the alanine-EPR dosimetry system was utilized due to its suitability for both gamma and electron dosimetry [120]. Initially, alanine dosimeters were calibrated at the Calliope facility using Fricke solution, as described in Section 3.2.1.

For the intercalibration of Calliope and REX facilities, alanine dosimeters from Aerial [136] were employed. These dosimeters consist of pressed alanine powder pellets with wax as a binding material (approximately 5%). The pellets, shown in Figure 4.1, are approximately 2.3 mm thick and have a diameter of about 4.0 mm. Alanine-EPR analysis was conducted using a Bruker *e*-scan EPR spectrometer (Figure 4.2), operating at 9.4 GHz in the X-band with a microwave power of 0.14 mW and a magnetic field range of 3350–3650 G.

Figure 4.1. Picture of alanine pellets from Aerial.

Figure 4.2. Bruker *e*-scan EPR spectrometer.

To optimize the measurement procedure, multiple measurements of an irradiated alanine pellet positioned at various heights (z) within the spectrometer cavity were performed. Figure 4.3 illustrates the dependency of the maximum peak-to-peak amplitude (h_{pp}) of EPR signals normalized to pellet mass as a function of height z [137]. This optimization determined the optimal placement of pellets approximately 12.3 cm from the top of the spectrometer case to maximize signal intensity.

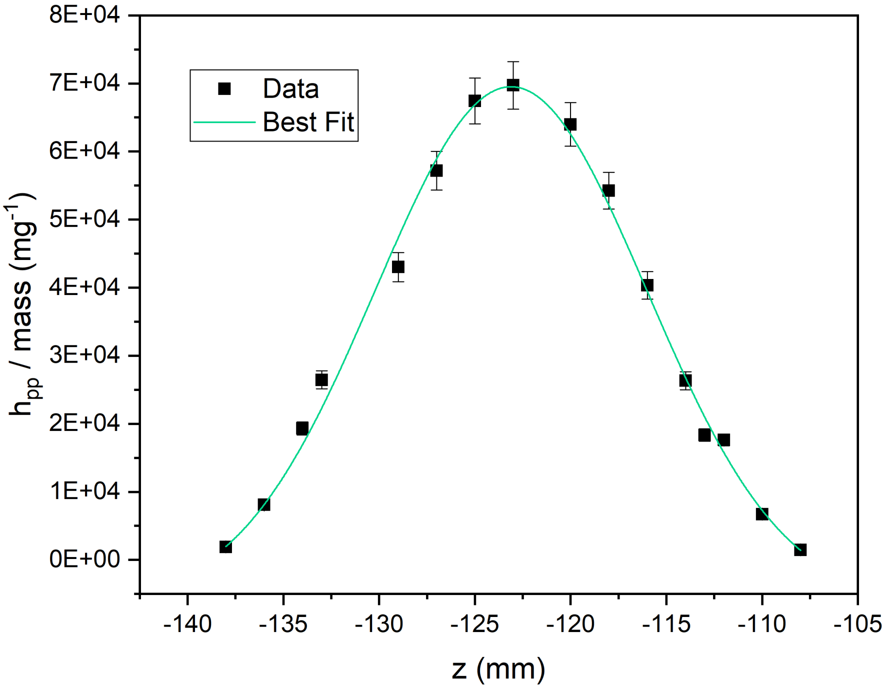

Figure 4.3. Maximum peak-to-peak amplitude normalized to pellet mass as a function of height z in the EPR spectrometer cavity.

Following optimization, alanine pellets were irradiated at specific positions within the Calliope irradiation cell, with dose rates determined using Fricke dosimetry. Absorbed doses were calculated based on irradiation times and subsequently correlated with free radical formation in alanine dosimeters, measured by EPR, to establish calibration curves. Specifically, two distinct calibration curves were developed for low-dose and high-dose ranges (Figures 4.4 and 4.5), reflecting different EPR parameters.

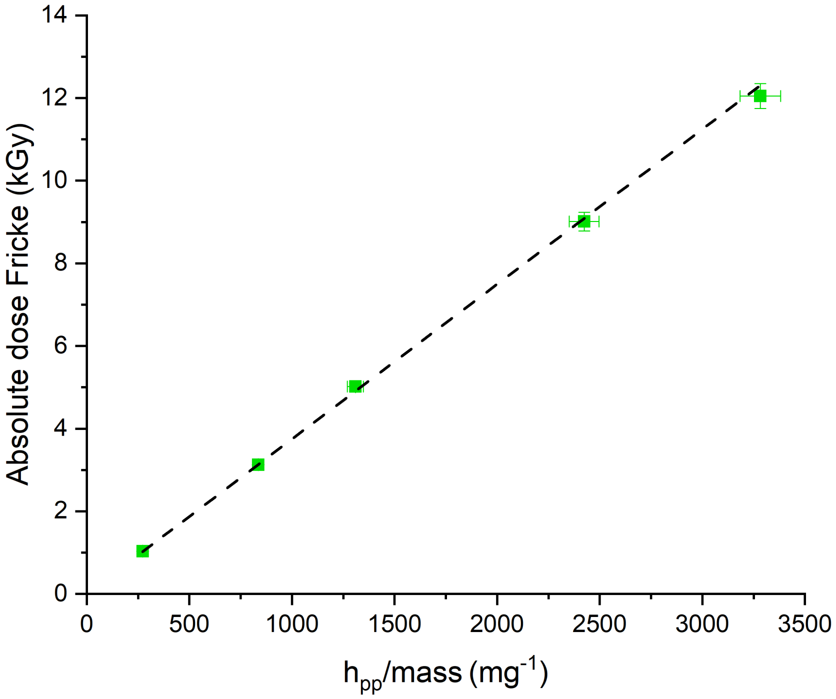

Figure 4.4. Alanine-EPR low dose range calibration curve.

The calibration curve for alanine-EPR dosimetry indicates the total absorbed dose (D^{total}) dependence on the amplitude of the maximum peak-to-peak height of the EPR spectrum normalized to the alanine pellet mass ($\frac{h_{pp}}{mass}$). The low-dose range calibration curve corresponds to absorbed dose values below 12 kGy. The interpolation of experimental data presented in the calibration curve obtained for the low-dose range gives:

$$D^{total} = 0.00375\frac{h_{pp}}{mass} \tag{4.1}$$

For the high-dose range calibration curve (above 12 kGy), the experimental data yield:

$$D^{total} = -12.4 + 0.0093\frac{h_{pp}}{mass} - 6.73E - 7(\frac{h_{pp}}{mass})^2 + 3.43E - 11(\frac{h_{pp}}{mass})^3 \tag{4.2}$$

These calibration curves allow for accurate determination of absorbed doses within alanine pellets following irradiation, based on EPR measurements of h_{pp}/mass

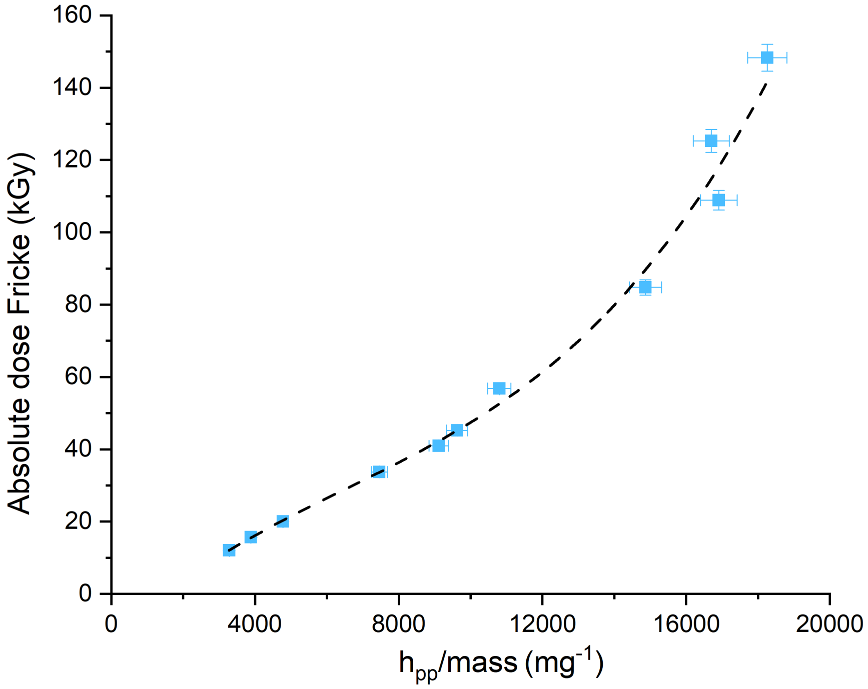

Figure 4.5. Alanine-EPR high dose range calibration curve.

values. This methodology was instrumental for calibrating alanine dosimeters at the Calliope facility and subsequently assessing radiation dose distribution within the REX irradiation chamber, as detailed in the following sections. This evaluation is crucial in determining optimal irradiation conditions for electron tests on electronic devices.

4.2 Dose mapping of REX irradiation chamber with alanine-EPR dosimeters

To identify suitable electron irradiation conditions for electronics, experimental dosimetric measurements were performed at the REX facility using a 5 MeV electron beam. As described in Chapter 3, the REX facility employs several dosimetric systems. The output radiation is routinely characterized using radiochromic films (EBT3, HD-V2), a Markus type ionization chamber [138], and a Faraday collector. These detectors provide information on transverse homogeneity, radiation flux, and machine reproducibility. However, for an accurate dose estimate, comparison with an absolute dosimeter is necessary, particularly for electron modalities characterized by very high dose rates. Specifically, HD-V2 radiochromic films are used for electron beam diagnostics and dosimetry, while the PPC05 Markus type ionization chamber from IBA [138] is primarily used for X-rays due to its limited suitability for the high dose rates typical of electron beams in the REX irradiation chamber. HD-V2 radiochromic films can handle dose rates of hundreds of Gray per second for short periods, whereas the PPC05 Markus type ionization chamber can manage approximately 0.2 Gy/s for a total dose rate of 1 kGy. Radiochromic films are not considered absolute dosimeters since they require calibration. Typically, calibration of individual batches of radiochromic films is performed using an RGB approach, where each color channel (red, green, and blue) provides a dose value based on the measured optical density. This method, which utilizes flatbed scanners with varying characteristics, has been extensively used in external beam radiotherapy to improve film dosimetry precision [139]. At the REX facility, however, a different method is used, with a universal calibration curve providing dose estimates from the radiochromic films. This approach, which relies on gray-scale readings, ensures consistent calibration across different film types [36]. To enhance accuracy and validate the calibration curve consistency and reliability, a cross-calibration with alanine dosimeters is performed. In the absence of a dedicated absolute dosimetric system for the REX electron beam, the alanine dosimetry system, calibrated at the Calliope facility with ^{60}Co photons, serves as an absolute dosimeter. Alanine dosimeters response is not significantly affected by the type of radiation, whether photons or electrons. The response in electron beams is only 1-2% lower than that in ^{60}Co [120]. Consequently, alanine pellets were irradiated with the REX 5 MeV electrons, and dose values were obtained using alanine-EPR calibration curves from the Calliope facility. To investigate the dose distribution within the REX irradiation chamber, the dosimeters were positioned at different points on a 20 × 20 cm^2 sample holder, as shown as example in Figure 4.6 for three pellets placed on the central row (9th row). The distance between adjacent holes of the holder is 1 cm. The alanine pellets were identified according to their position on the sample holder (i.e. the

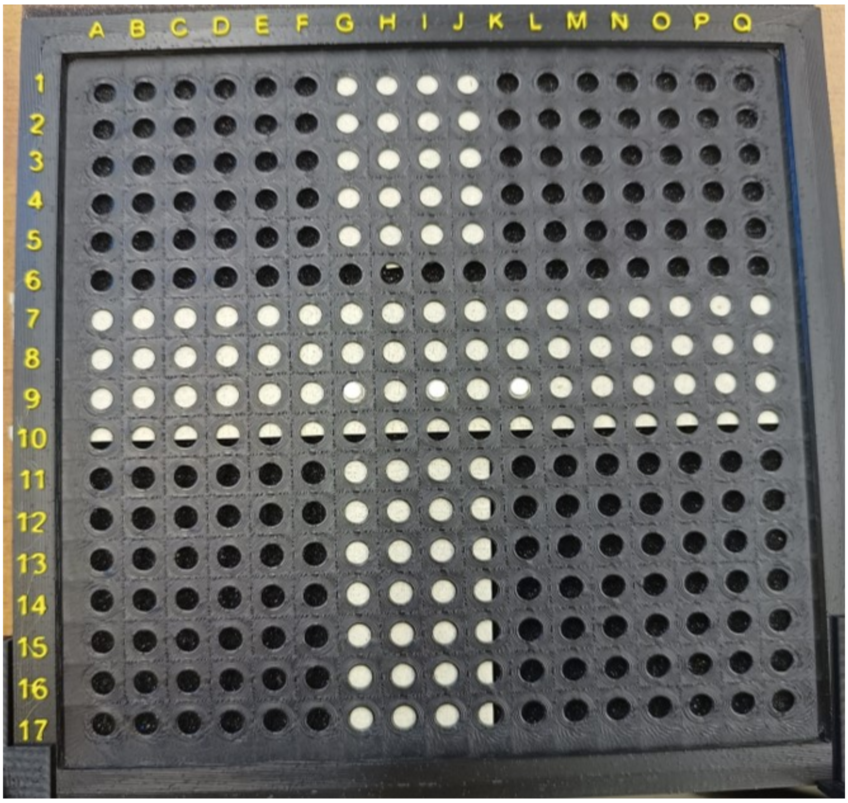

Figure 4.6. Picture of three alanine pellets positioned on the central row of the 20 × 20 cm^2 sample holder.

letter of the column and the number of the row from Figure 4.6). Three irradiation tests were performed with the sample holder positioned at 20 cm, 30 cm, and 40 cm from the exit point of the electron linac, transversely with respect to the beam, as shown in Figure 4.7. The hole I9 of the sample holder was centered with respect to the exit of the linac.

Figure 4.7. Electron irradiation setup of alanine pellets at the REX facility.

For all irradiation tests, the Pulse Repetition Frequency (PRF) was set at 15 Hz. The irradiation conditions (distance of the sample holder from the linac exit, irradiation time and PRF) are summarized in Table 4.1.

Table 4.1. Summary of alanine irradiation conditions at REX facility with a 5 MeV electron beam.

Irradiation test	**Distance (cm)**	**Time (s)**	**PRF (Hz)**
1	20	15.2	15
2	30	60.2	15
3	40	90.1	15

Each irradiated alanine pellet was measured three times with the EPR Bruker *e*-scan described in the previous section. Between repeated measurements, the dosimeter was rotated around its longitudinal axis. The reading reproducibility of the dosimeter for a given irradiation condition was about 1-2%. The mean value of the three measurements of the maximum peak-to-peak amplitude of the EPR spectrum

normalized to the sample mass was considered.
The mean value of h_{pp}/mass obtained for each irradiated alanine pellet was reported in the alanine calibration curve made at the Calliope facility to obtain an absorbed dose value. Specifically, for each dosimeter, a dose value was obtained with the low dose range calibration curve (Figure 4.4), substituting h_{pp}/mass in Equation 4.1. The results obtained are presented in Tables 4.2, 4.3 and 4.4 for all the irradiation conditions.

Table 4.2. Summary of the results obtained after irradiation with a 5 MeV electron beam of alanine pellets positioned at different points on the sample holder (identified by the letter of the column and the number of the row from Figure 4.6) at a distance of 20 cm from the linac exit. The uncertainty of the mean h_{pp}/mass value is ±1% and the error on the absorbed dose and dose rate due to calibration uncertainties is 5%.

Alanine position	Mean h_{pp}/mass (mg^{-1})	Absorbed dose (Gy)	Dose rate (Gy/s)
F9	147.7	554	36.5
G9	405.0	1519	100.2
H9	938.0	3517	232.0
I6	357.7	1341	88.5
I7	815.9	3060	201.8
I8	1367.1	5127	338.2
I9	1630.2	6113	403.2
I10	1248.7	4683	308.9
I11	692.8	2598	171.4
I12	281.7	1057	69.7
J9	1911.8	7169	472.9
K9	1511.0	5666	373.8
L9	755.7	2834	186.9
M9	306.0	1147	75.7
N9	82.7	310	20.5

The maximum dose rate was found 20 cm from the linac exit, specifically in hole J9, which is 1 cm from the center position I9, aligned with respect to the exit point. In Figure 4.8, the dose rate variation with the distance from the linac exit in the position I9 is plotted. From Figure 4.8 it is evident that the dose rate decreased significantly with the distance from the linac exit.

Considering the absorbed dose values corresponding to alanine pellets irradiated on the 9th row of the sample holder, the transverse distributions of the dose at fixed distances from the linac exit were obtained. Specifically, the transverse dose rate

Table 4.3. Summary of the results obtained after irradiation with a 5 MeV electron beam of alanine pellets positioned at different points on the sample holder (identified by the letter of the column and the number of the row from Figure 4.6) at a distance of 30 cm from the linac exit. The uncertainty of the mean h_{pp}/mass value is ±1% and the error on the absorbed dose and dose rate due to calibration uncertainties is 5%.

Alanine position	**Mean h_{pp}/mass (mg^{-1})**	**Absorbed dose (Gy)**	**Dose rate (Gy/s)**
E9	504.6	1892	31.4
G9	1382.8	5185	86.1
I5	734.3	2753	45.7
I7	1728.9	6483	107.7
I9	2395.5	8983	149.2
I11	1717.3	6440	107.0
I13	730.2	2738	45.5
K9	2177.6	8166	135.6
M9	1092.1	4095	68.0
O9	353.0	1324	22.0

Table 4.4. Summary of the results obtained after irradiation with a 5 MeV electron beam of alanine pellets positioned at different points on the sample holder (identified by the letter of the column and the number of the row from Figure 4.6) at a distance of 40 cm from the linac exit. The uncertainty of the mean h_{pp}/mass value is ±1% and the error on the absorbed dose and dose rate due to calibration uncertainties is 5%.

Alanine position	**Mean h_{pp}/mass (mg^{-1})**	**Absorbed dose (Gy)**	**Dose rate (Gy/s)**
E9	869.7	3261	36.2
G9	1661.2	6229	69.1
I5	1114.9	4181	46.4
I7	1903.4	7138	79.2
I9	2402.5	9009	100.0
I11	2005.1	7519	83.4
I13	1207.3	4527	50.2
K9	2325.5	8721	96.8
M9	1561.2	5855	65.0
P9	516.6	1937	21.5

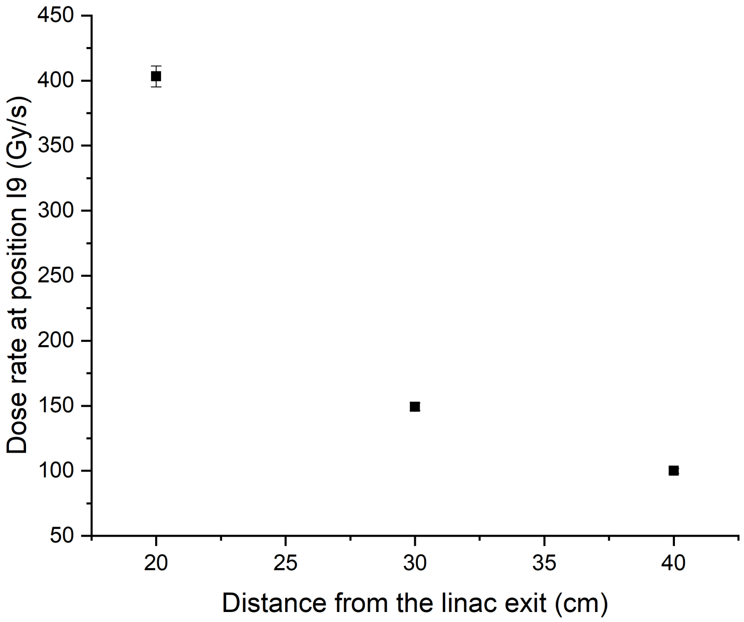

Figure 4.8. Dose rate variation with distance from the linac exit in the central position of the sample holder.

beam profiles obtained for the irradiation performed at 20 cm, 30 cm and 40 cm are shown in Figure 4.9. For all the studied distances from the linac exit, the transverse profiles exhibit a similar symmetric decrease in dose rate away from the central position. These profiles are crucial for understanding the spatial distribution of the dose rate within the irradiation chamber, which is essential for dosimetric studies and ensuring uniform irradiation of samples.

Radiochromic films were irradiated under the same electron irradiation conditions as the alanine dosimeters for comparative analysis. Specifically, 20 × 20 cm^2 HD-V2 Gafchromic films by Ashland [140] were positioned perpendicularly to the electron beam propagation between two slabs of water-equivalent solid phantom by Scanditronix (density of 1.035 g/cm^3), as depicted in Figure 4.10, at distances of 30 cm and 40 cm from the linac exit. It is noteworthy that unlike alanine, that is sensitive to radiation in a wide dose range, HD-V2 Gafchromic films are suitable for doses ranging from 10 to 1000 Gy [36]. Therefore, they were irradiated for 5 seconds. After irradiation, the radiochromic films were scanned using an Epson flatbed Expression 11000XL scanner. An example of the HD-V2 image after irradiation at 30 cm from the linac exit is shown in Figure 4.11. The acquired images were processed using Matlab® code, which converted the pixel values of the radiochromic films into absorbed dose values based on the calibration curve reported in [36]. The transverse distribution profiles of the absorbed dose, normalized to the maximum value, obtained with alanine and Gafchromic systems are shown in Figure 4.12a-b

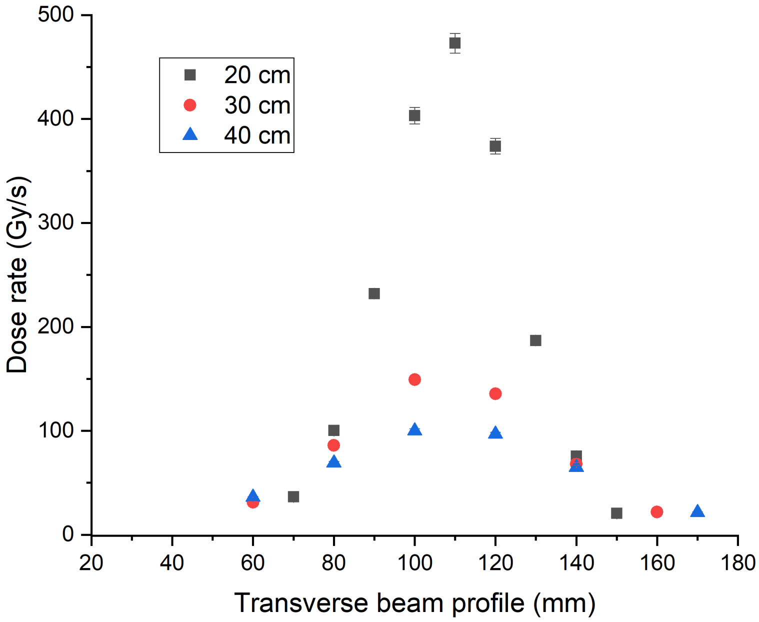

Figure 4.9. Transverse beam profiles obtained with alanine dosimetry system after irradiation at 20 cm, 30 cm and 40 cm from the linac exit.

Figure 4.10. Setup for Gafchromic film electron irradiation at the REX facility, 40 cm from the linac exit.

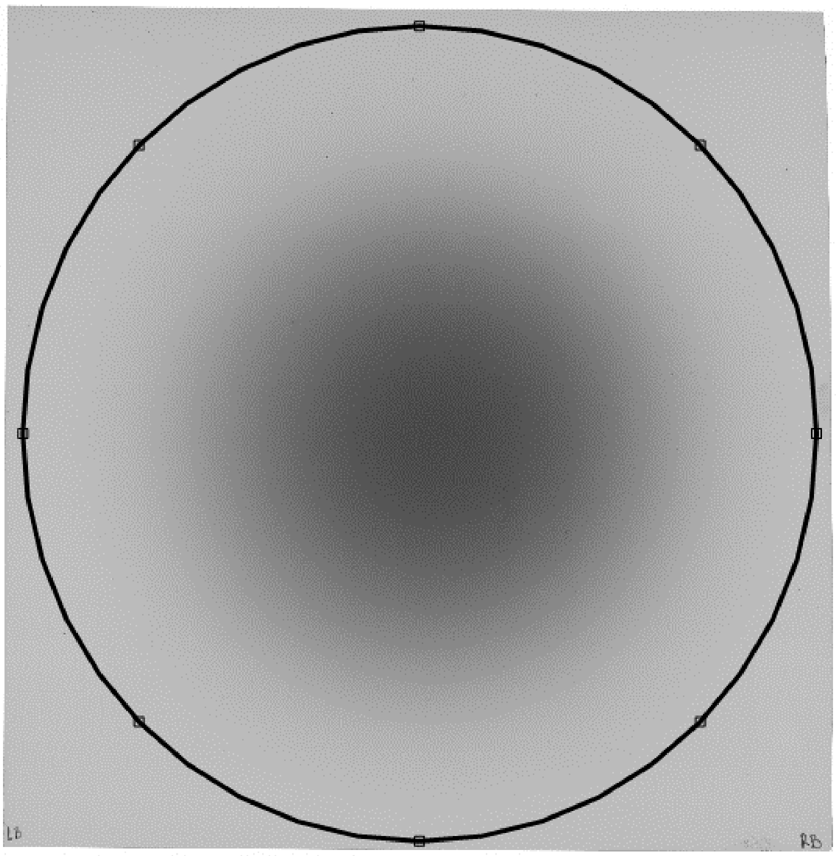

Figure 4.11. HD-V2 Gafchromic film after irradiation at 30 cm from the linac exit. The image was acquired using an Epson flatbed Expression 11000XL scanner.

for irradiations performed at 30 cm and 40 cm from the linac exit, respectively. Figure 4.12 shows that the results from radiochromic films are consistent with those

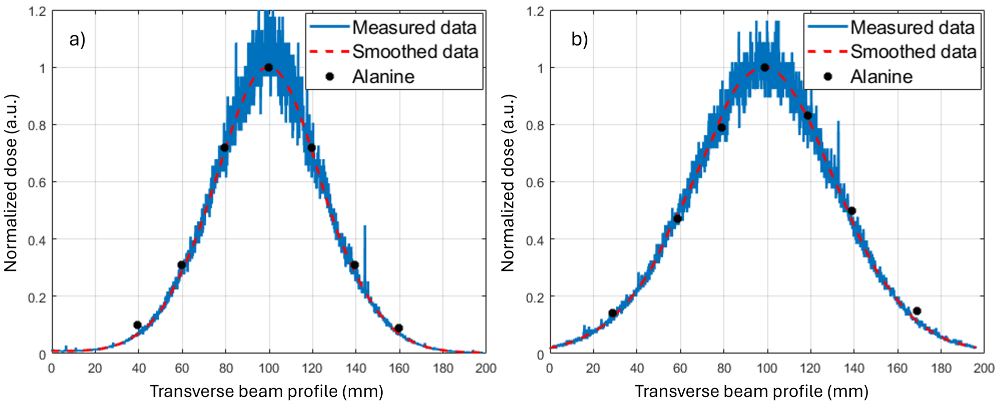

Figure 4.12. Transverse beam profiles normalized to the maximum dose value, obtained with HD-V2 Gafchromic films (Measured data and Smoothed data) and with the alanine dosimetry system for irradiations performed at (a) 30 cm and (b) 40 cm from the linac exit.

from the alanine dosimetry system. Specifically, alanine dosimeters calibrated at the Calliope facility align with measurements from HD-V2 Gafchromic films calibrated using the universal calibration curve from [36]. This agreement further validates the reliability of the calibration method employed for dose estimation at REX.

Radiochromic films were also employed to assess beam homogeneity, specifically using the Full Width at 80% of Maximum (FW80%M) parameter as an indicator. This parameter represents the width at 80% of the maximum dose, corresponding to the diameter of a circular spot with ±10% homogeneity. The values of the Full Width at Half Maximum (FWHM) and the FW80%M along with those of the maximum dose and dose rate at the spot center and the mean doses and dose rates calculated over the circular spot corresponding to FW80%M, are reported in Table 4.5 for irradiations performed at distances of 30 cm and 40 cm from the linac exit, respectively. Using the pulse repetition frequency (PRF = 15 Hz) employed for the irradiation, the dose per pulse values were calculated for tests conducted at distances of 30 cm and 40 cm from the linac exit for both HD-V2 Gafchromic films and the alanine dosimetry system. Specifically, the dose rate at the central position of the alanine holder I9 (Figure 4.6) was used for alanine dosimeters, while the mean dose over FW80%M was used for radiochromic films. The results are summarized in Table 4.6.

Based on the obtained results and the previous discussion, it is evident that the REX beam exhibits divergence, with higher dose values observed at shorter distances from the linac exit. Moreover, the beam intensity peaks at the center and shows a transverse profile characterized by approximately ±10% homogeneity within a circle of about 32 mm and 43 mm diameter at 30 cm and 40 cm from the linac exit, respectively.

The reported results indicate that the dosimetric intercalibration of the Calliope

Table 4.5. Parameters corresponding to the transverse beam profile for irradiations performed at distances of 30 cm and 40 cm from the REX linac exit.

	d = 30 cm	**d = 40 cm**
FWHM (mm)	57.1	77.3
FW80%M (mm)	31.9	42.5
Maximum dose (Gy)	964	491
Maximum rose rate (Gy/s)	192.8	98.2
Mean dose (Gy)	896.9	456.7
Mean dose rate (Gy/s)	179.4	91.3

Table 4.6. Dose per pulse obtained with alanine dosimeters (central position of alanine holder I9) and HD-V2 Gafchromic films (mean dose over FW80%M). The uncertainty in the dose per pulse for alanine dosimeters due to calibration uncertainties is 5%. For HD-V2 Gafchromic films, the uncertainty in the dose per pulse estimation is 10%.

	d = 30 cm	**d = 40 cm**
Alanine Dose per pulse (Gy/pulse)	10.5	6.6
HD-V2 Dose per pulse (Gy/pulse)	12	6.1

and REX facilities using alanine-EPR dosimeters provided crucial insights into the beam distribution within the REX irradiation chamber and allowed for the determination of suitable irradiation conditions (dose and dose rate) for electronic components exposed to 5 MeV electrons. Specifically, as a future step, it would be interesting to irradiate the studied electronic components at a distance of 20 cm from the linac exit. The dose rate at position I10 of the alanine holder, at the specified distance, is approximately 1.1 kGy/h in water. By considering the stopping power of electrons in both water and silicon, an approximate dose rate in silicon can be determined. Specifically, this setup allows for irradiation at a dose rate of approximately 1 kGy(Si)/h, enabling components to be irradiated under conditions that closely replicate those used during high dose rate gamma irradiation tests (described in Chapter 5).

Chapter 5

Electronics irradiation: experimental results

In this chapter, the results obtained from the irradiation tests are reported. Commercial off-the-shelf bipolar junction transistors and radiation tolerant optoisolators were investigated both before and after radiation exposure. A summary of the tests performed is provided in Table 5.1. As shown in Table 5.1, electron irradiation has not yet been performed but will be carried out in a future phase to complete the research described in this thesis.

Table 5.1. Summary of the irradiation tests performed.

	NPN BJT	**PNP BJT**	**Optoisolator**
Laser-driven protons	✓	×	×
Gamma	✓	✓	✓
Protons	✓	✓	×
Neutrons	✓	✓	×
Electrons	×	×	×

The components were characterized before and after each irradiation test to investigate the effects of different radiation sources and the radiation resistance properties of the components, as detailed in the following sections.
Since, as reported in the literature [69], radiation-induced defects can be partially or completely recovered through thermal treatments, two thermal annealing tests were conducted after irradiation to evaluate the recovery of these defects. Specifically, according to ESCC Basic Specification No. 22900 [141], which regulates the irradiation test method, in the first test, the samples were kept at room temperature for 24 hours post-irradiation. In the second test, the samples were placed in a furnace at 100 °C for 168 hours. After each annealing test, the samples were characterized again.

Silicon NPN and PNP BJTs from the same batches were studied. Specifically, the BJTs used for this project are small signal transistors in TO-18 metal cases, namely 2N2222A (NPN BJTs) and 2N2907A (PNP BJTs) [142, 143]. A picture of a 2N2907A is shown in Figure 5.1 as an example. Both 2N2222A and 2N2907A

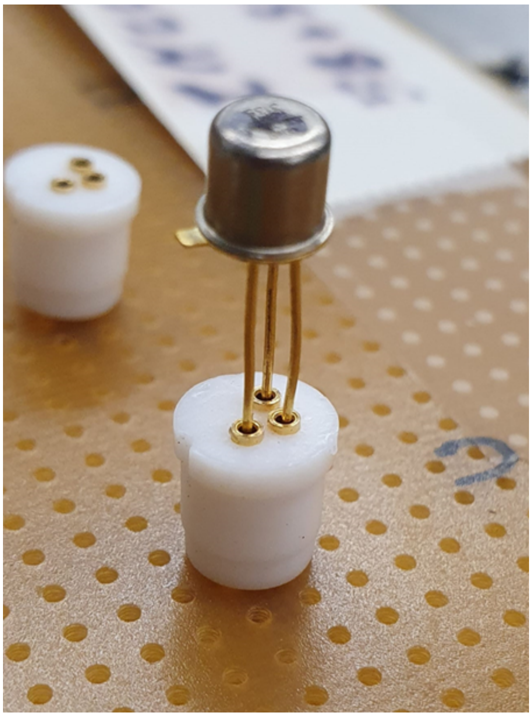

Figure 5.1. Picture of a 2N2222A BJT in a TO-18 metal case placed on an irradiation board.

are commercial off-the-shelf transistors. These BJTs are very common and were chosen because they are widely used for general-purpose switching applications at collector currents up to 600 mA. They feature useful current gain over a wide range of collector currents, low leakage currents, and low saturation voltage. Furthermore, they are much less expensive than radiation-hardened ones.

In the first part of this chapter, the results obtained for the BJTs are presented, while in the last section, the gamma radiation-induced effects on optoisolators are shown. In Section 5.2.2, the results obtained after gamma irradiation are shown. In particular, two irradiation tests were conducted at two different dose rate values, up to an absorbed dose of 1 kGy. In Section 5.2.3, the results obtained after irradiation with laser-driven protons are presented. The effects induced in BJTs after irradiation with protons from conventional accelerator and neutrons are presented in Section 5.2.4 and Section 5.2.5, respectively.

The results from gamma, laser-driven proton, conventional proton, and neutron irradiations will be expressed in terms of ^{60}Co absorbed dose, number of shots, proton fluence, and neutron fluence, respectively. Given that the employed stress test sources are heterogeneous radiation sources, the irradiation conditions are provided using different parameters. To compare the obtained results, Section 5.3 outlines the procedure followed to determine the dose delivered by all the employed radiation sources. Specifically, both the NIEL and TID contributions to the deposited dose were considered.

The investigated radiation tolerant components are OLS249 optoisolators [144]. A picture of the OLS249 along with its block diagram is shown in Figure 5.2. It consists of an LED optically coupled to an NPN phototransistor, mounted and coupled in a custom hermetic surface-mount technology leadless chip carrier package. Its features make it suitable, for example, as an interface for Complementary Metal Oxide Semiconductor (CMOS) technology with Low Power Schottky Transistor-Transistor Logic (LSTTL) or Transistor-Transistor Logic (TTL). The results obtained after gamma irradiation of the optoisolators are shown in Section 5.5.

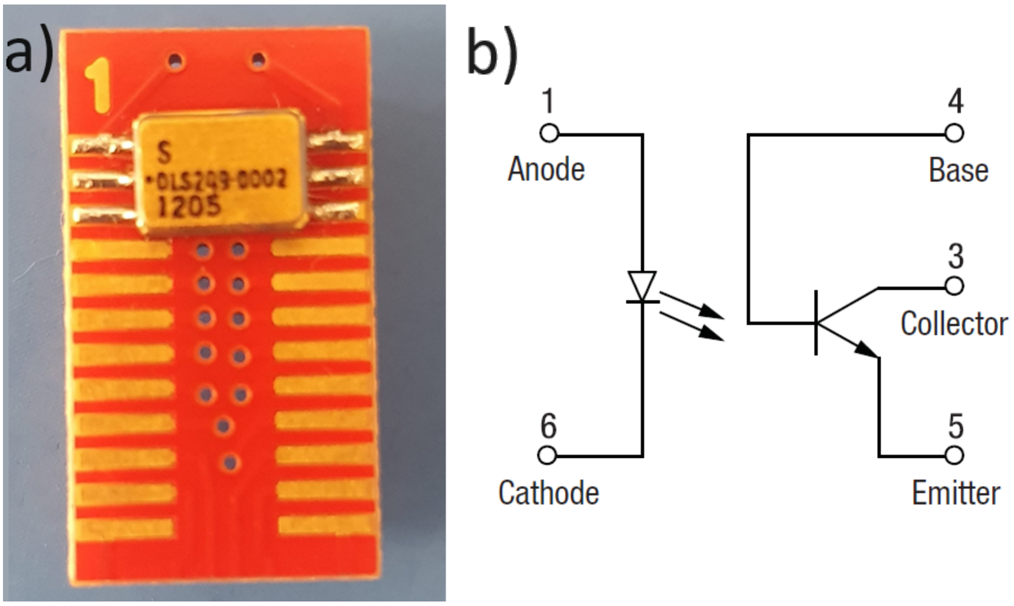

Figure 5.2. Picture of OLS249 (a) and the corresponding block diagram (b).

The results of the annealing tests after each irradiation test for both BJTs and optoisolators are presented at the end of the corresponding section.

5.1 Experimental measurements

All samples were characterized before and after irradiation by evaluating several parameters. Parametric tests of the components were performed in collaboration with the Italian engineering company *IMT s.r.l.* [145]. A LabVIEW test program was used to automate the evaluation of the sample parameters. A screenshot of the LabVIEW test program for NPN BJTs characterization measurements is shown in Figure 5.3 as an example.

The Keysight B2902A Precision Source/Measure Unit (SMU) [146] was employed to source and measure both the current and voltage of the Device Under Test (DUT). The Keysight E3649A 100W was used as the power supply [147]. During the parametric measurements, the DUT was plugged into an M232H module [148], which was connected to the computer running the LabVIEW software.

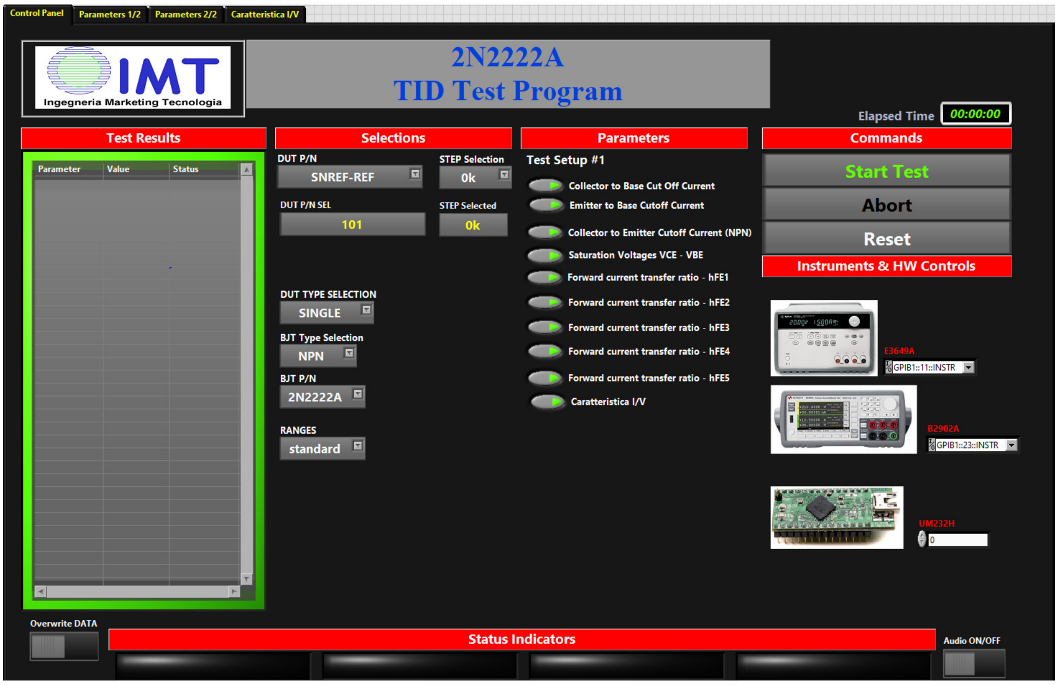

Elapsed Time 00:00:00

DUT P/N: SNREF-REF
STEP Selection: 0k
DUT P/N SEL: 101
STEP Selected: 0k
DUT TYPE SELECTION: SINGLE
BJT Type Selection: NPN
BJT P/N: 2N2222A
RANGES: standard

E3649A: GPIB1::11::INSTR
B2902A: GPIB1::23::INSTR
UM232H: 0

Figure 5.3. Screen of the LabVIEW test program used for the characterization of NPN BJTs.

5.2 Bipolar junction transistors characterization

The main parameter affected by irradiation in BJTs is the current gain β, as explained in Chapter 2. Therefore, the following post-irradiation analysis primarily focuses on investigating the β parameter.

The operation of BJTs relies on the flow of minority carriers, whose numbers decrease after irradiation due to increased recombination rates in the base region, thus reducing the minority carrier lifetime [49, 59, 79]. This decrease is the primary mechanism that describes the degradation of the current gain β. Consequently, for a given base current, the collector current I$_C$ decreases. Since BJT operation can be compromised if β falls out of specification, this parameter was characterized before and after irradiation to establish the threshold dose beyond which component functionality is significantly damaged.

Following the device test conditions reported in its technical datasheet, the gain was measured at a fixed value of V$_{CE}$ (V$_{CE}$ = 10 V) for five different collector current values. Specifically, the gain values were obtained by injecting various base currents I$_B$ until the desired collector current I$_C$ was achieved. The corresponding base current values and gains were recorded at each point. This procedure yielded five different gain values (β_1, β_2, β_3, β_4 and β_5) corresponding to different collector current values, as shown in Table 5.2. For the aforementioned measurements, a common emitter circuit built around the BJT was utilized.

To determine whether the devices characteristics are acceptable after irradiation, the allowed ranges specified in the technical datasheets [142, 143] for the measured

Table 5.2. Collector current test conditions for current gain measurements. The tests were conducted with a fixed $V_{CE} = 10$ V.

Test	Current gain $\boldsymbol{\beta}$	**Collector current I_C**
1	β_1	0.1 mA
2	β_2	1 mA
3	β_3	10 mA
4	β_4	150 mA
5	β_5	500 mA

current gains are considered. These ranges are presented in Table 5.3.

Table 5.3. Ranges of allowed values for β_1, β_2, β_3, β_4 and β_5.

	NPN		**PNP**	
	Min.	**Max.**	**Min.**	**Max.**
$\boldsymbol{\beta_1}$	50		75	
$\boldsymbol{\beta_2}$	75	325	100	450
$\boldsymbol{\beta_3}$	100		100	
$\boldsymbol{\beta_4}$	100	300	100	300
$\boldsymbol{\beta_5}$	30		50	

As detailed in Chapter 2, the degradation of current gain due to radiation exposure is often characterized by the change in the reciprocal of the current gain, $\Delta(1/\beta) = 1/\beta^{irr} - 1/\beta^0$ [59, 77]. Therefore, the behavior of $\Delta(1/\beta)$ as a function of absorbed dose is reported in the following sections.

Other parameters such as cutoff currents and saturation voltages were also evaluated to assess their trends after radiation exposure. Cutoff currents refer to small leakage currents that flow when the device is in the cutoff region. The cutoff currents I_{CBO}, I_{EBO} and I_{CEO} (collector to base, emitter to base, and collector to emitter, respectively) were measured.

Regarding saturation voltages, the collector-to-emitter saturation voltage $V_{CE(sat)}$ and the base-to-emitter saturation voltage $V_{BE(sat)}$ were measured. They represent the voltage drops across the collector and emitter terminals, and across the base and emitter terminals, respectively, when the transistor is in the saturation region. The test conditions for cutoff currents and saturation voltages are summarized in Table 5.4.

Eventually, the I_C-V_{CE} characteristics were measured both before and after each irradiation test. These curves depict the collector current (I_C) versus the collector-to-emitter voltage (V_{CE}) obtained at a fixed base current I_B of 50 μA. To generate the I_C-V_{CE} characteristic curves, the collector current values corresponding to fixed V_{CE} values were recorded. The specific V_{CE} values used for testing the NPN and

Table 5.4. Test conditions for cutoff currents and saturation voltages for NPN and PNP transistors.

Cutoff currents			**Saturation voltages**	
	Test conditions			**Test conditions**
	NPN	**PNP**		**NPN and PNP**
$\mathbf{I_{CBO1}}$	$V_{CB} = 75$ V	60 V	$\mathbf{V_{CE(sat)1}}$	$I_C = 150$ mA, $I_B = 15$ mA
$\mathbf{I_{CBO2}}$	$V_{CB} = 60$ V	50 V	$\mathbf{V_{CE(sat)2}}$	$I_C = 500$ mA, $I_B = 50$ mA
$\mathbf{I_{EBO1}}$	$V_{EB} = 6$ V	5 V	$\mathbf{V_{BE(sat)1}}$	$I_C = 150$ mA, $I_B = 15$ mA
$\mathbf{I_{EBO2}}$	$V_{EB} = 4$ V		$\mathbf{V_{BE(sat)2}}$	$I_C = 500$ mA, $I_B = 50$ mA
$\mathbf{I_{CEO}}$	$V_{CE} = 50$ V			

PNP BJTs I_C-V_{CE} characteristics are listed in Table 5.5.

Table 5.5. Values of V_{CE} used for testing the I_C-V_{CE} characteristic curves of NPN and PNP BJTs.

NPN V_{CE} test condition (V)												
0.01	0.025	0.04	0.06	0.08	0.1	0.3	0.6	1	5	10	15	20
PNP V_{CE} test condition (V)												
-0.01	-0.04	-0.06	-0.08	-0.1	-0.3	-0.6	-1	-5	-10	-15	-20	

5.2.1 Before irradiation characterization

Before irradiation, the current gains of both NPN and PNP transistors were characterized. The measured current gains varied among each other for both sets of transistors. Specifically, one set of 55 NPN BJTs and one set of 55 PNP BJTs were analyzed. The mean values before irradiation, denoted as $\beta_k^{0,mean}$ (where the subscript 0 represents before irradiation and $k = 1, 2, 3, 4, 5$ represents the test conditions reported in Table 5.2), obtained for the current gains of the NPN and PNP BJTs sets, along with their respective percentage standard deviations $\sigma_{\beta_k^0}$, are presented in Table 5.6.

The standard deviations $\sigma_{\beta_k^0}$ in Table 5.6, for both the NPN and PNP BJTs sets, were calculated over a sample set of N = 55 units using the formula:

$$\sigma_{\beta_k^0} = \sqrt{\frac{\sum_{i=1}^{N}(\beta_k^{0,i} - \beta_k^{0,mean})^2}{N}} \tag{5.1}$$

where $\beta_k^{0,i}$ represents the individual current gain values of the unirradiated BJTs in the set, and $\beta_k^{0,mean}$ denotes the mean current gain value.

Table 5.6. Test conditions, mean values and percentage standard deviations of the current gains before irradiation. The tests were conducted with a fixed $V_{CE} = 10$ V.

		NPN		**PNP**	
	I_C test condition	**Mean value**	**Standard deviation (%)**	**Mean value**	**Standard deviation (%)**
β_1	0.1 mA	136.0	3%	218.0	9%
β_2	1 mA	96.2	2%	240.7	16%
β_3	10 mA	181.7	3%	240.0	16%
β_4	150 mA	107.7	2%	216.2	13%
β_5	500 mA	117.5	3%	95.7	7%

5.2.2 Gamma irradiation

Two gamma irradiation tests were performed on BJTs using two sets of samples. The first set consisted of four NPN BJTs irradiated at a dose rate of 3.3 Gy(Si)/h (dose rate in silicon) up to an absorbed dose of 1.1 kGy(Si) (dose in silicon). The second set included 18 NPN and 18 PNP samples irradiated at nine different absorbed dose levels (two NPN and two PNP samples for each irradiation condition) up to 515 kGy(Si) with a dose rate of 1 kGy(Si)/h. In the following, all values of dose and dose rate are referred to silicon.
The irradiation conditions and the results obtained are detailed in the following subsections.

Low dose rate irradiation test

The first gamma irradiation test was conducted on the four NPN BJTs (referred to as sample 1, sample 2, sample 3, and sample 4) of the first set in six steps, up to a total absorbed dose of 1 kGy at a dose rate of 3.3 Gy(Si)/h. A summary of the absorbed dose after each step is provided in Table 5.7.

Table 5.7. Steps of irradiation for the first set of samples irradiated with gamma radiation at a dose rate of 3.3 Gy/h.

Irradiation step	Absorbed dose per step (Gy)	Total absorbed dose (Gy)
1	74.0	74.0
2	71.8	145.8
3	73.5	219.3
4	233.4	452.7
5	224.8	677.5
6	308.8	986.3

After each irradiation step, the parameters described in the previous section were evaluated. The irradiation tests, electrical characterization and annealing tests following irradiation were conducted in accordance with ESCC Basic Specification No. 22900 (Issue 5) [141]. According to this specification, the electrical characterization was performed within 1 hour after the end of the exposure, and the interval between two irradiation steps did not exceed 2 hours. Both the irradiation and the characterization were performed at room temperature.

Two samples (sample 1 and sample 2) were irradiated under bias (+30 V), and two samples (sample 3 and sample 4) were irradiated unbiased. A schematic of the irradiation circuit diagrams is shown in Figure 5.4 for both biased and unbiased configurations.

After the final irradiation step, following the test sequence reported in the ESCC Basic Specification No. 22900 (Issue 5) [141], the BJTs were kept at room temperature for 24 hours for the first annealing test. Subsequently, another parametric test was conducted. Following this, the devices underwent annealing in a furnace at 100 °C for 168 hours and characterized again. The annealing tests were conducted under the same bias conditions as the irradiation tests.

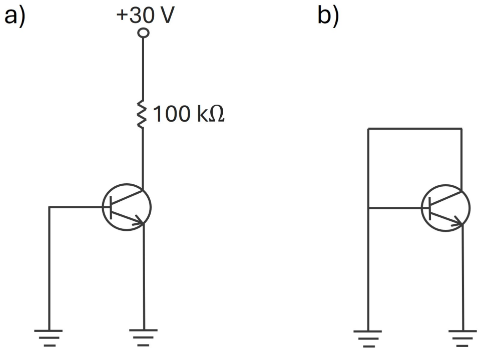

Figure 5.4. Circuit diagrams for irradiation in biased (a) and unbiased (b) configurations.

Cutoff currents and saturation voltages (as summarized in Table 5.4) were tested after irradiation. The results obtained for sample 1 are shown in Figure 5.5 as an example. The other BJTs exhibited similar behavior. These parameters were not modified after irradiation, except for the collector-to-emitter cutoff current I_{CEO}, which increased but remained well below the datasheet specifications ($I_{CEO} < 50$ nA).

Subsequently, current gains corresponding to different collector currents (as explained in Table 5.6) were checked after irradiation. The behavior of the current gains is shown in Figure 5.6 for samples 1 and 2 and in Figure 5.7 for samples 3 and 4.

It is evident that the current gains of the samples that were unbiased during irradiation (Fig. 5.7) were not modified by gamma radiation. In contrast, there is a slight decrease in current gains for the biased samples (Fig. 5.6) after exposure.

Specifically, for sample 1 (Fig. 5.6a), a decrease in the β parameter is noticeable at the lowest analyzed collector current value ($I_C = 0.1$ mA, corresponding to β_1). This

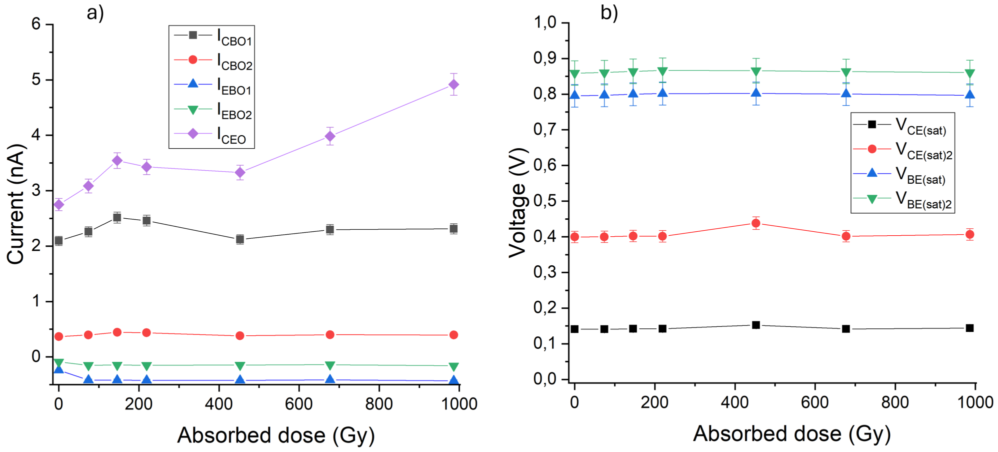

Figure 5.5. Trends of (a) cutoff currents (I_{CBO}, I_{EBO} and I_{CEO}) and (b) saturation voltages ($V_{CE(sat)}$ and $V_{BE(sat)}$) for sample 1 as a function of the dose deposited by gamma radiation. The error (±4%) is due to measurement uncertainty.

degradation is less pronounced up to about 200 Gy of absorbed dose, after which it stabilizes at a constant value up to 1 kGy. For this sample, β_2 slightly decreases after the first step of irradiation and then remains constant up to 1 kGy. β_3 and β_4 slightly decrease after the second step of irradiation, then reach a constant value, while β_5 remains unaffected by this radiation dose.

Regarding sample 2 (Fig. 5.6b), variations in current gain are evident for collector current values up to $I_C = 1$ mA. The decrease is more significant at the lowest collector current ($I_C = 0.1$ mA, corresponding to β_1), stabilizing after around 200 Gy up to 1 kGy absorbed dose. The effect is less pronounced at higher collector currents ($I_C = 1$ mA, $I_C = 10$ mA), where the current gain (β_2, β_3) reaches a constant value since the first step of irradiation. On the contrary, β_4 and β_5 remain unchanged up to 1 kGy absorbed dose.

For both sample 1 and sample 2, the damage observed is within acceptable limits, as defined by the range of allowed gain values reported in the sample datasheet, and they did not show recovery after the annealing tests.

In this radiation dose range (up to 1 kGy absorbed dose), appreciable bulk damage is not expected to occur. Instead, ionizing radiation primarily induces surface effects in BJTs.

High dose rate irradiation test

The second gamma irradiation test was conducted up to an absorbed dose of 515 kGy at a dose rate of 1.1 kGy/h to evaluate the effects of bulk damage. For this test, a set of 18 NPN and 18 PNP BJTs was used and irradiated under 9 different conditions (2 NPN and 2 PNP BJTs for each condition). A summary of the irradiation conditions is presented in Table 5.8. All the samples were biased (+30 V for NPN BJTs and -30 V for PNP BJTs) during irradiation. Figure 5.8 shows a picture of the samples placed on the irradiation boards positioned on the platform

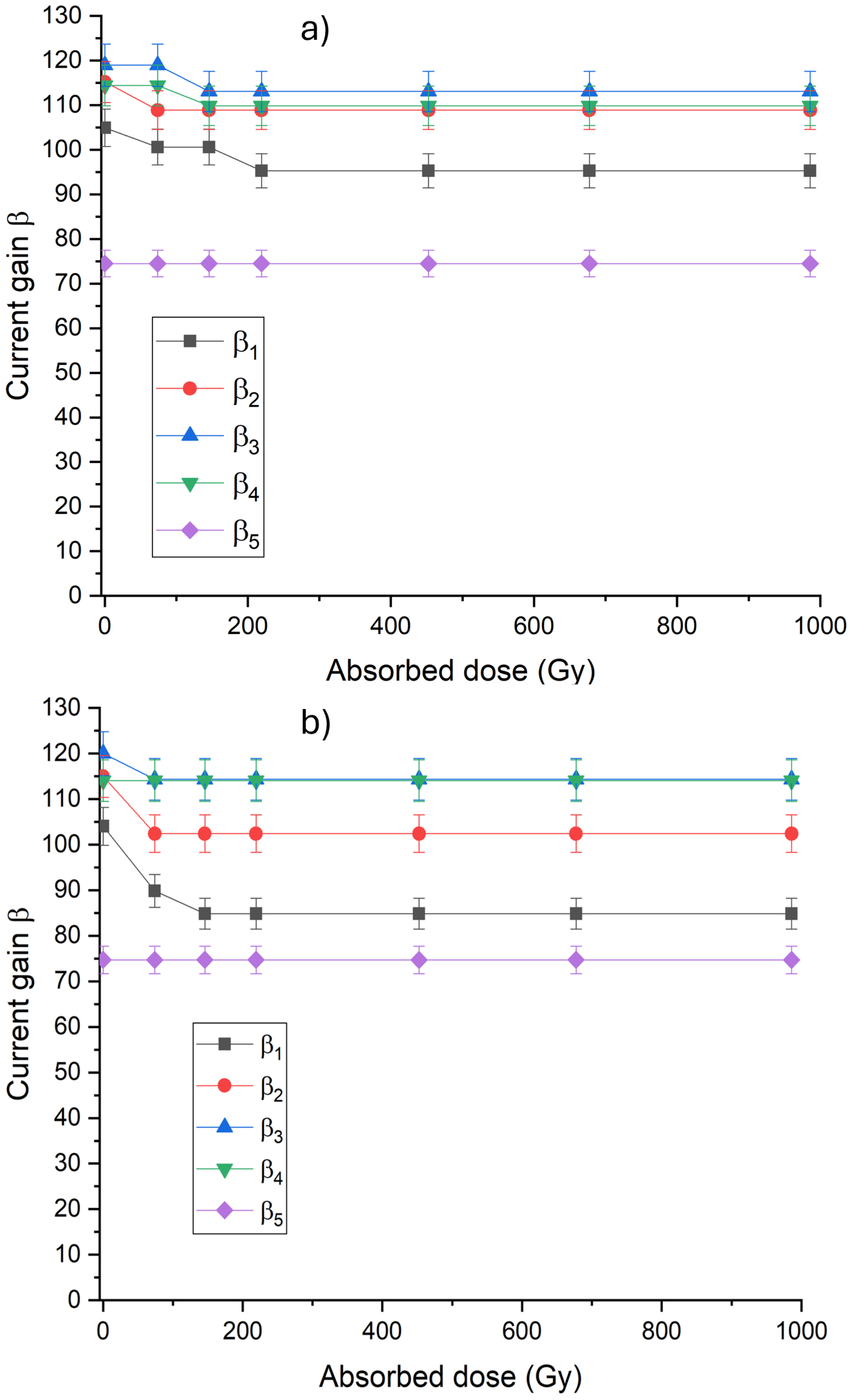

Figure 5.6. Trends of current gains β of sample 1 (a) and sample 2 (b) (biased samples) as a function of the dose deposited by gamma radiation for I_C = 0.1, 1, 10, 150, 500 mA. The error (±4%) is due to measurement uncertainty in the β parameter.

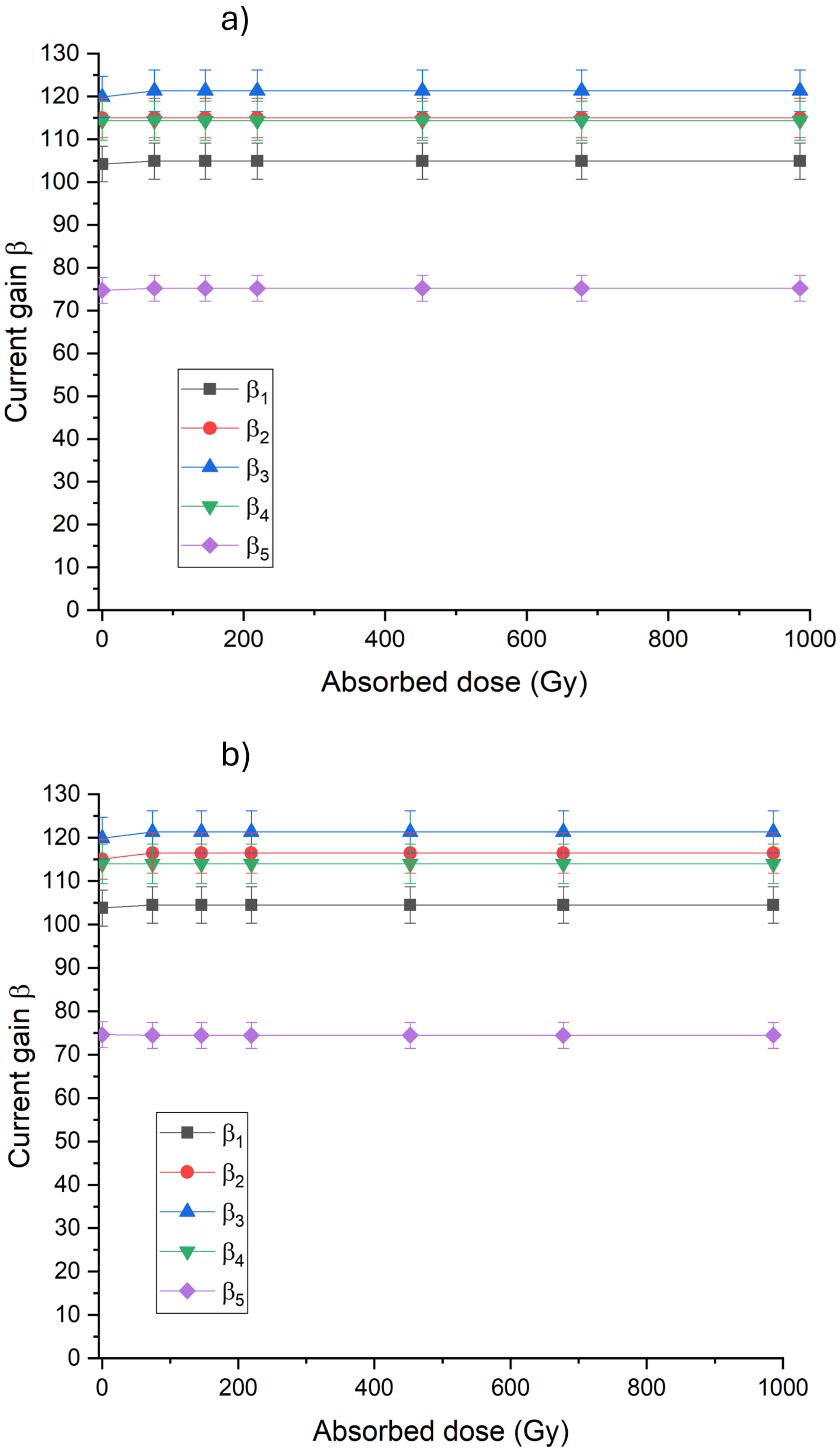

Figure 5.7. Trends of current gains β of sample 3 (a) and sample 4 (b) (unbiased samples) as a function of the dose deposited by gamma radiation for I_C = 0.1, 1, 10, 150, 500 mA. The error ($\pm 4\%$) is due to measurement uncertainty in the β parameter.

Table 5.8. Irradiation conditions for the second set of samples, irradiated with gamma radiation at a dose rate of 1.1 kGy/h. Four samples for each condition (2 NPN and 2 PNP BJTs) were involved.

Irradiation test	**Total absorbed dose (kGy)**
1	1.0
2	2.3
3	$2.6 \cdot 10^1$
4	$7.2 \cdot 10^1$
5	$1.2 \cdot 10^2$
6	$2.4 \cdot 10^2$
6	$3.2 \cdot 10^2$
6	$4.2 \cdot 10^2$
6	$5.2 \cdot 10^2$

of the Calliope gamma irradiation facility for the test.

Before and after irradiation, I_C-V_{CE} characteristics were acquired for both NPN and PNP BJTs at a fixed base current value of $I_B = 50\ \mu A$. The curves obtained are shown in Figure 5.9. For PNP transistors (Fig. 5.9b), the absolute values of I_C and V_{CE} were plotted.

It is evident for both NPN and PNP BJTs that the values of I_C decrease with increasing radiation dose. This decrease is more pronounced in PNP transistors in percentage terms. For example, at a collector-to-emitter voltage V_{CE} of 5 V, after irradiation at 240 kGy, the collector current I_C is reduced to 8% of its initial value for NPN transistors and to 4% of its initial value for PNP transistors.

Measurements of cutoff currents and saturation voltages were conducted before and after irradiation. The results, presented in Figure 5.10 for both NPN and PNP transistors, show that cutoff current measurements exhibit fluctuations, likely due to parasitic currents. Since cutoff currents are very small (in the nA range), the influence of parasitic currents can lead to inaccuracies, making precise measurements challenging. This is further evidenced by the fact that some measured cutoff current values occasionally fall below zero, which is physically nonsensical and highlights the impact of these parasitic effects. Despite these measurement challenges, the cutoff current values remained within the allowed ranges for both NPN and PNP transistors.

Regarding saturation voltage values, they were generally unaffected by irradiation up to 515 kGy, except for the collector-to-emitter saturation voltage $V_{CE(sat)2}$, measured at $I_C = 500$ mA and $I_B = 50$ mA. This parameter slightly increases from the first step of irradiation, rising almost linearly up to a 515 kGy absorbed dose for NPN BJTs (5.10c). In contrast, for PNP BJTs (5.10d), it increased after the second step of irradiation, reaching a value just over double the initial one at 515

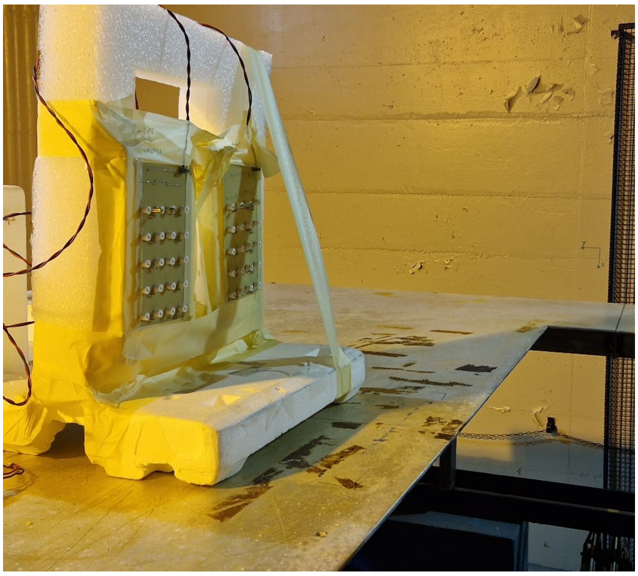

Figure 5.8. Picture of the setup for the second gamma irradiation test. NPN and PNP BJTs were placed on two separate boards biased with +30 V and -30 V, respectively. The gamma source is positioned on the right side of the picture. The samples were irradiated under room conditions.

kGy. Nevertheless, after irradiation at the maximum analyzed absorbed dose, the $V_{CE(sat)2}$ value remained within the technical datasheet's allowed range for both NPN ($V_{CE(sat)2} < 1$ V) and PNP ($V_{CE(sat)2} < 2.6$ V) transistors.

As discussed earlier, the current gain β is the most crucial parameter for characterizing the radiation effects on BJTs. The results for the current gains (measured as detailed in Table 5.6) are depicted in Figure 5.11 and in Figure 5.12 for NPN and PNP transistors, respectively. Regarding NPN BJTs (Fig. 5.11), the current gains β_1 (lowest collector current) and β_5 (highest collector current) decrease until reaching a constant value after 120 kGy of absorbed dose. For β_2 ($I_C = 1$ mA) the variation in current gain stabilizes after 72 kGy absorbed dose, while β_3 and β_4 decrease after each irradiation step. Conversely, for PNP BJTs (Fig. 5.12), all current gains exhibit a decreasing trend after each irradiation step. According to Table 5.3, for NPN transistors (Fig. 5.11b), β_1 and β_2 exited the allowed range after approximately 10 kGy absorbed dose, β_3 and β_4 after irradiation at approximately 1 kGy and 3 kGy, respectively, and β_5 remained within datasheet specification until around 100 kGy. For PNP transistors (Fig. 5.12b), β_1, β_2 and β_4 went out of specification in the range of approximately 15-20 kGy of dose deposited by gamma, while β_3 and β_5 remained within the allowed range until approximately 50 kGy and 70 kGy, respectively.
The resulting curves for the variation of the reciprocal of current gains $\Delta(1/\beta)$ are shown in Figure 5.13 and Figure 5.14 for NPN and PNP transistors, respectively.
Since low beta values characterize damaged samples, high values of $\Delta(1/\beta)$ occur for the damaged samples. The behavior of $\Delta(1/\beta)$ as a function of absorbed dose indicates the type of damage induced in the component after irradiation. In this case,

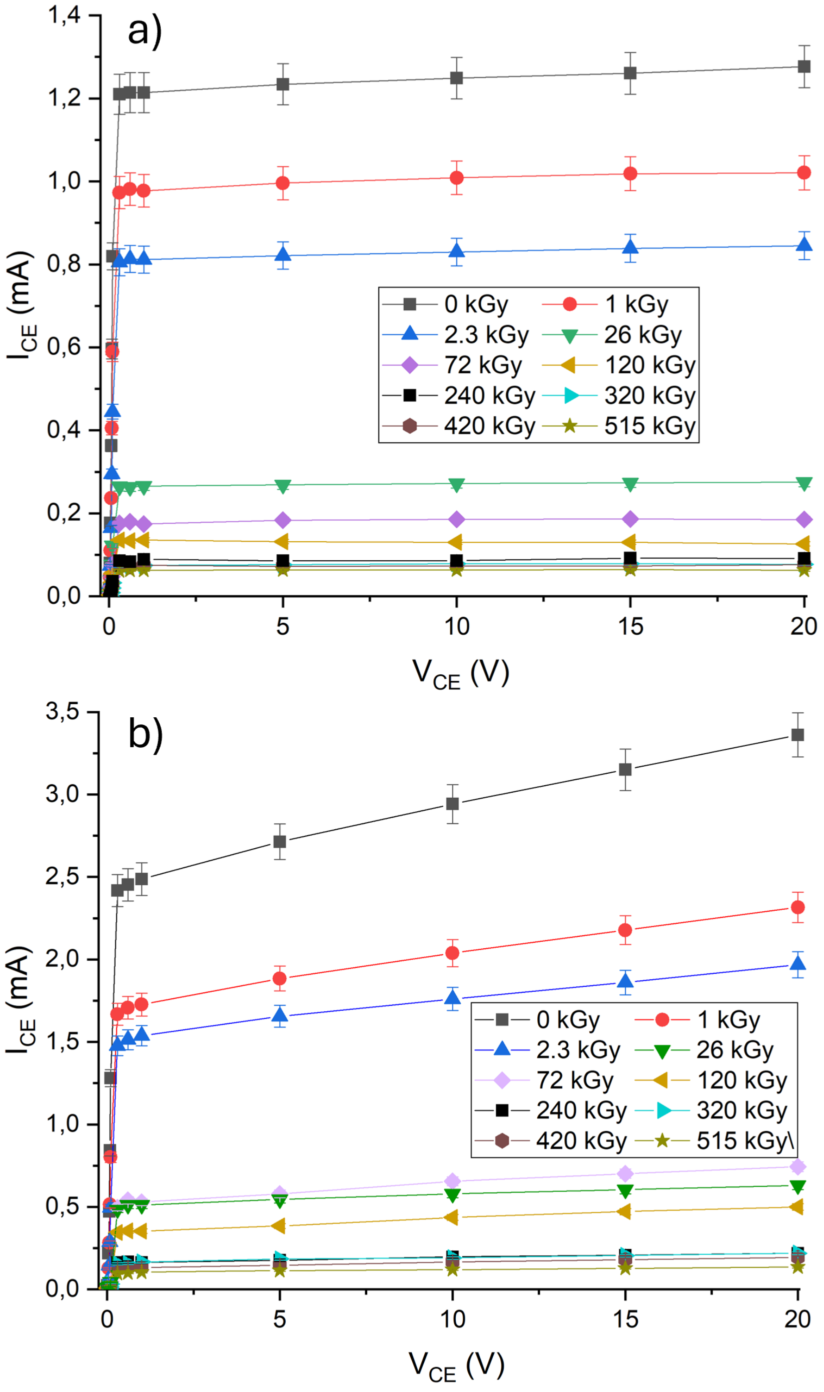

Figure 5.9. I_C-V_{CE} characteristic curves of NPN (a) and PNP (b) BJTs before and after irradiation at different absorbed dose values. For PNP transistors, the absolute values of I_C and V_{CE} are shown.

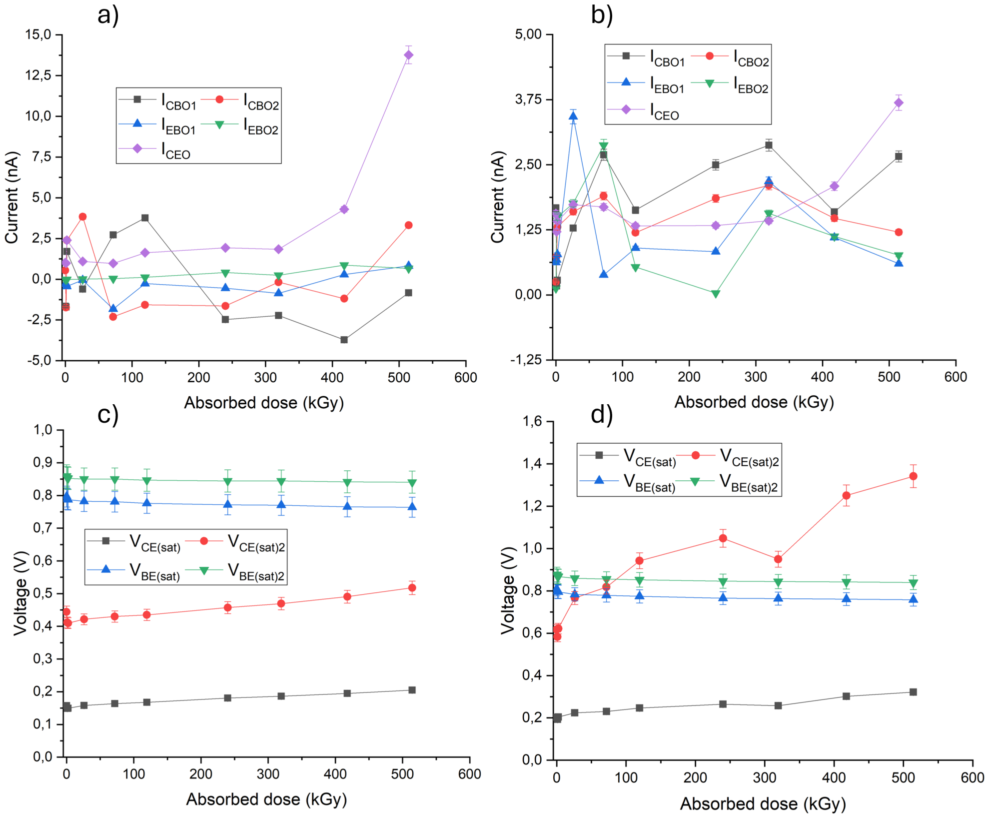

Figure 5.10. Trends of cutoff currents (I_{CBO}, I_{EBO} and I_{CEO}) for NPN (a) and PNP (b) transistors and saturation voltages ($V_{CE(sat)}$ and $V_{BE(sat)}$) for NPN (c) and PNP (d) transistors as a function of the dose deposited by gamma radiation. The error (±4%) is due to measurement uncertainty.

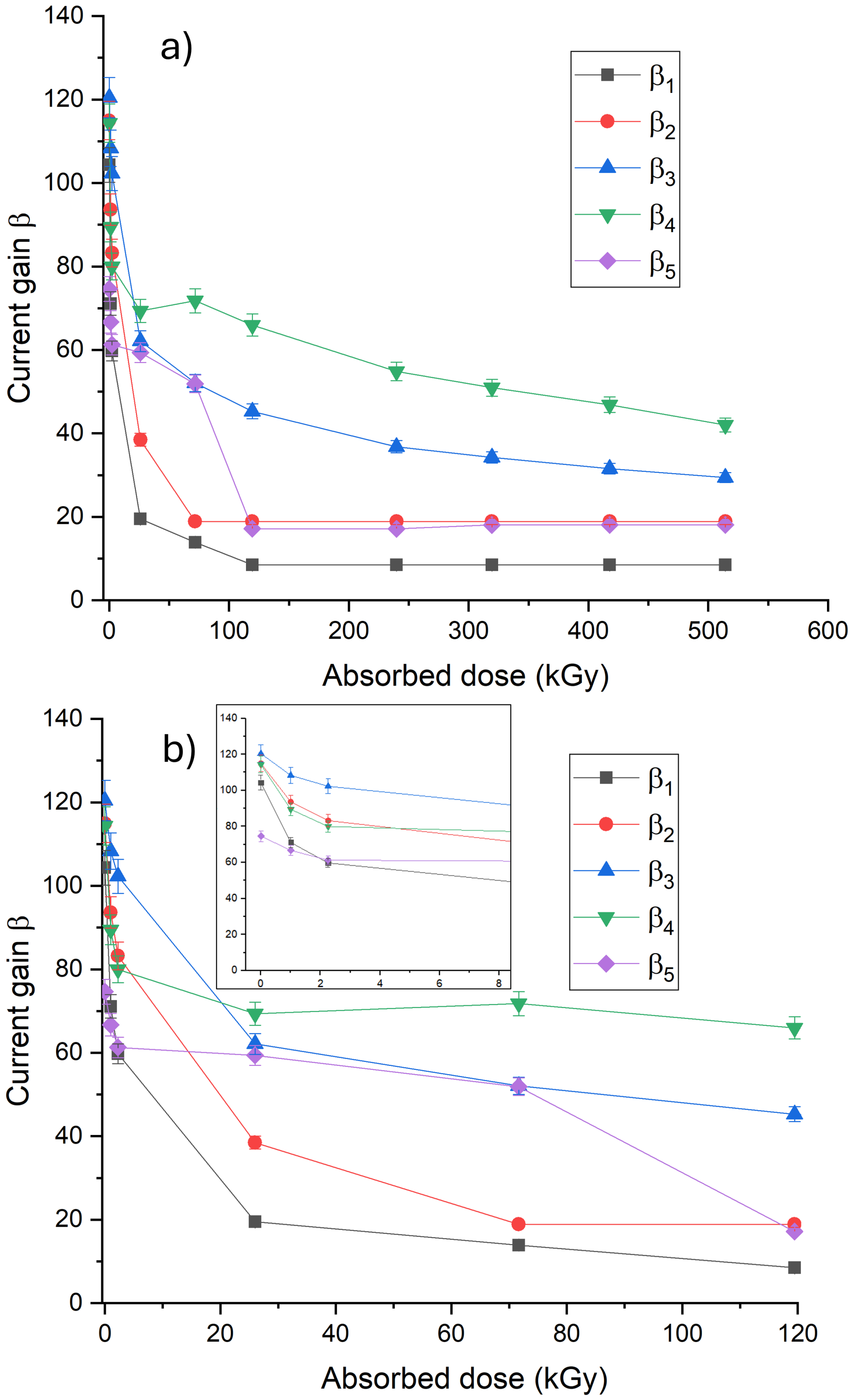

Figure 5.11. Trends of current gain β as a function of the dose deposited by gamma radiation for NPN BJTs across the entire range of absorbed doses (a) and specifically in the range 0-120 kGy (b). In the inset, the range 1-5 kGy absorbed dose is highlighted. The measurements were taken at collector currents I_C of 0.1, 1, 10, 150, and 500 mA. The error (±4%) is attributed to the measurement uncertainty of the β parameter.

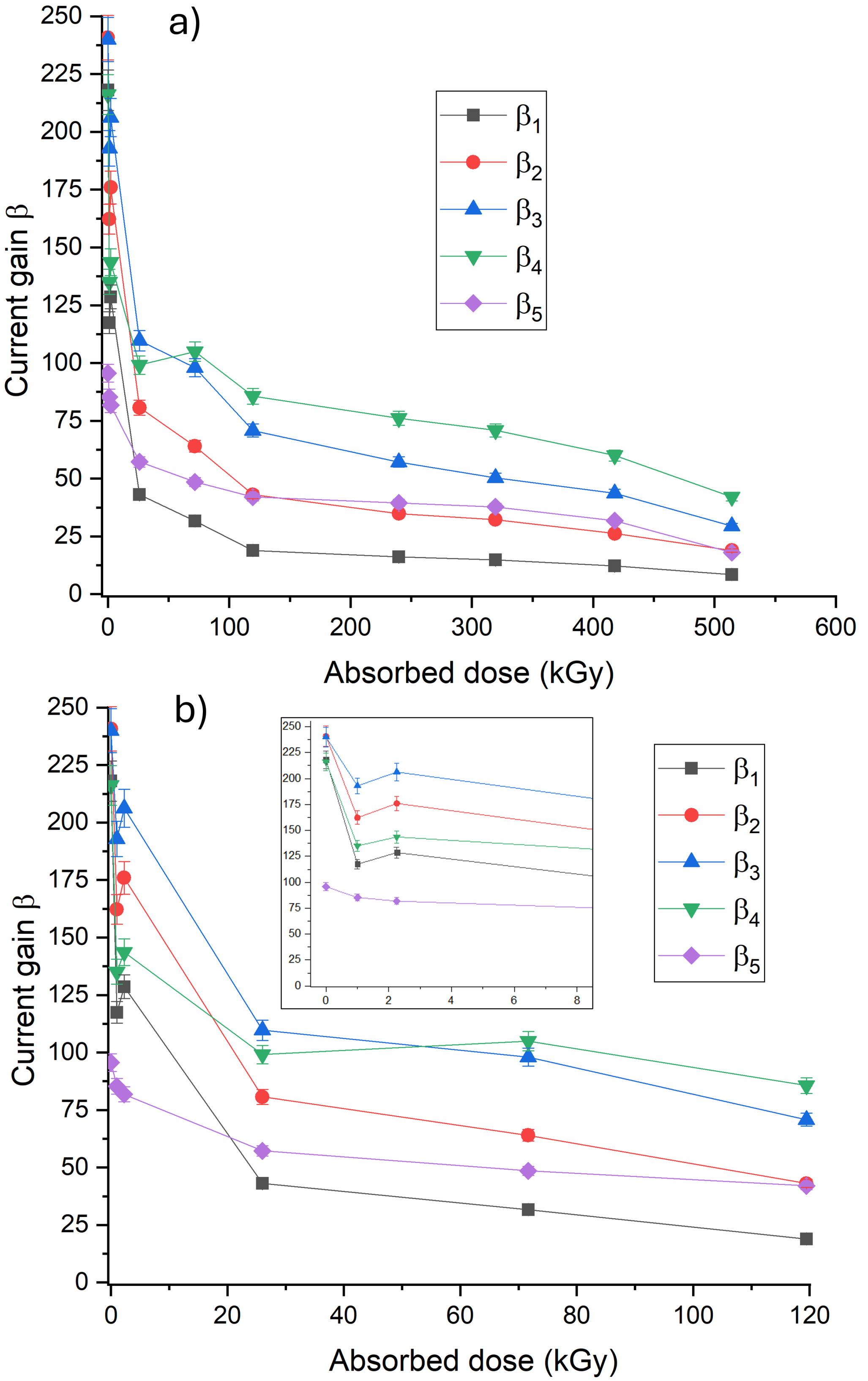

Figure 5.12. Trends of current gain β as a function of the dose deposited by gamma radiation for PNP BJTs across the entire range of absorbed doses (a) and specifically in the range 0-120 kGy (b). In the inset, the range 1-5 kGy absorbed dose is highlighted. The measurements were taken at collector currents I_C of 0.1, 1, 10, 150, and 500 mA. The error (±4%) is attributed to the measurement uncertainty of the β parameter.

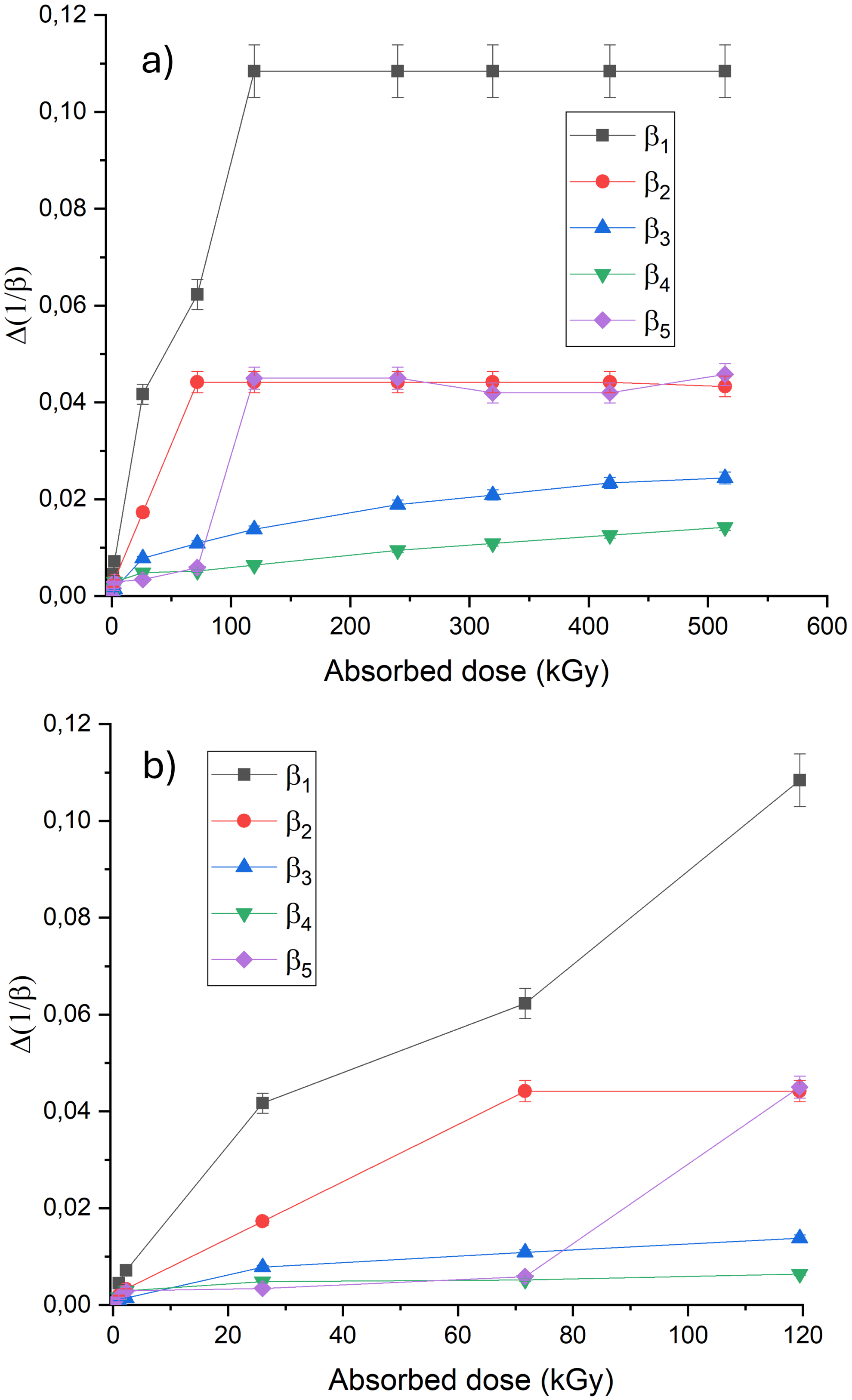

Figure 5.13. Trend of the reciprocal of current gain $\Delta(1/\beta)$ as a function of the dose deposited by gamma radiation, measured at I_C = 0.1, 1, 10, 150, 500 mA for NPN transistors across the entire range of absorbed doses (a) and specifically within the range 0-120 kGy (b). The reported error (±5 %) accounts for uncertainties in the measurement of the β parameter.

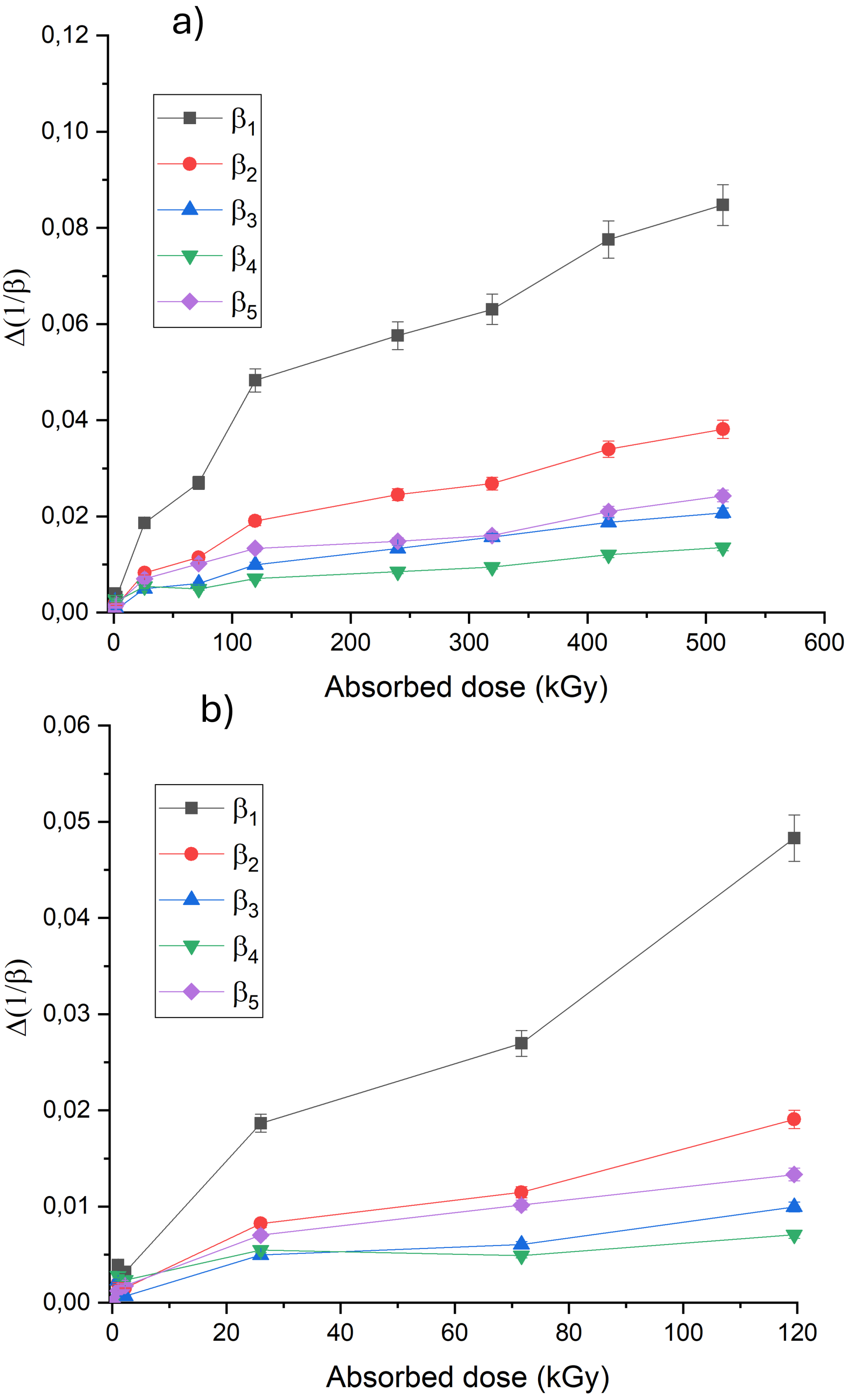

Figure 5.14. Trend of the reciprocal of current gain $\Delta(1/\beta)$ as a function of the dose deposited by gamma radiation, measured at $I_C = 0.1, 1, 10, 150, 500$ mA for PNP transistors across the entire range of absorbed doses (a) and specifically within the range 0-120 kGy (b). The reported error (±5 %) accounts for uncertainties in the measurement of the β parameter.

the curves in Figure 5.13 and Figure 5.14 exhibit a non-linear trend, particularly approaching saturation in NPN devices for collector current values corresponding to β_1, β_2 and β_5. This non-linear behavior is attributed to charge trapping in the oxide layer of the transistor and at the Si/SiO$_2$ interface. It suggests that damage from ionization effects dominates over damage from NIEL deposited dose, resulting in a non-linear trend [79, 149].
Moreover, it is evident that NPN transistors exhibit more damage after gamma irradiation compared to PNP transistors, as $\Delta(1/\beta)_{PNP}$ consistently exceeds $\Delta(1/\beta)_{NPN}$ across almost the entire range of absorbed doses. In Figure 5.15, the difference $\Delta(1/\beta)_{PNP} - \Delta(1/\beta)_{NPN}$ is plotted as a function of absorbed dose: it peaks in the range of 70-250 kGy and then decreases with increasing absorbed dose for β_1, β_2, and β_5, while remaining nearly constant for β_3 and β_4. This indicates that for collector current values of 0.1 mA, a mA and 500 mA, NPN transistors are more susceptible to gamma irradiation damage compared to PNP transistors. However, for collector currents of 10 mA and 150 mA, the response to gamma radiation is similar between NPN and PNP transistors across the entire dose range.

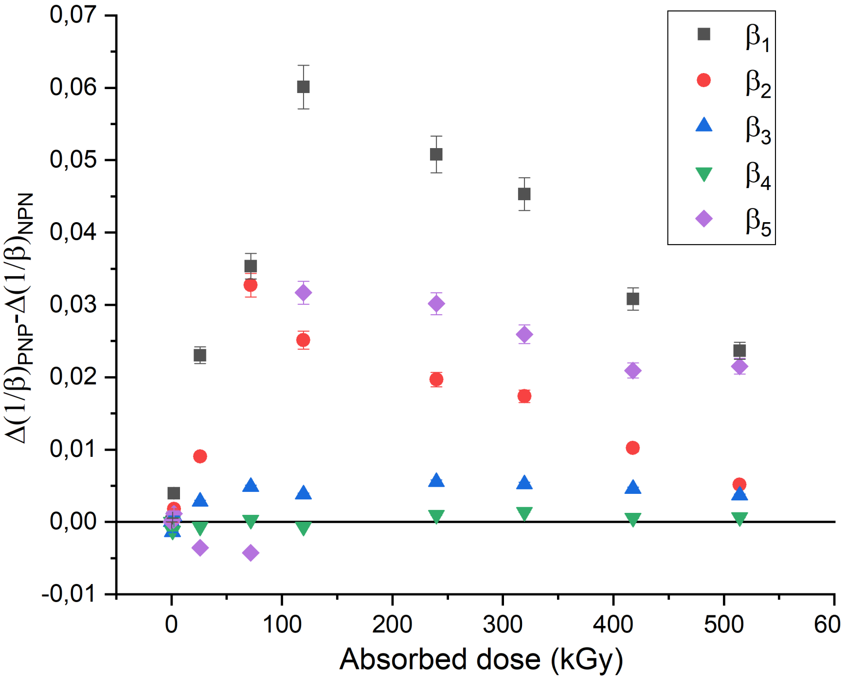

Figure 5.15. Difference $\Delta(1/\beta)_{NPN} - \Delta(1/\beta)_{PNP}$ as a function of the absorbed dose for β_1, β_2, β_3, β_4 and β_5, measured at collector currents of 0.1 mA, 1 mA, 10 mA, 150 mA and 500 mA, respectively. Error: (±5%).

After irradiation, the samples were kept for 24 hours at room temperature and 168 hours at 100 °C. The samples irradiated at absorbed dose values $\geq$26 kGy (heavily damaged BJTs) did not recover their current gain values after the annealing tests. In contrast, samples irradiated with absorbed doses up to 2.3 kGy showed a recovery in current gains after the annealing tests. The results of the annealing tests for NPN and PNP BJTs irradiated at 2.3 kGy absorbed dose are shown in Figure 5.16. For both NPN and PNP components, there was a noticeable recovery in current gains. However, while β_5 in NPN transistors reached a value higher than its initial one after the second step of annealing, the other current gains did not return to their pristine values.

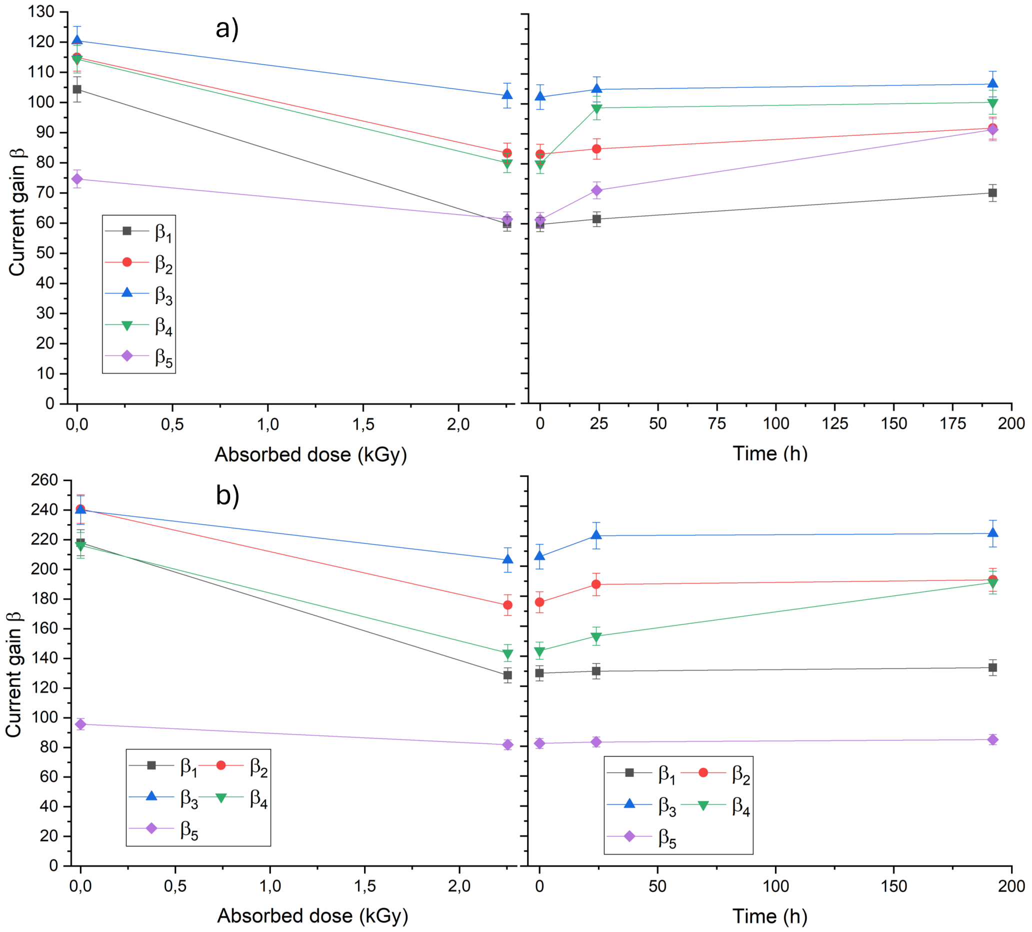

Figure 5.16. NPN (a) and PNP (b) current gain behaviors as a function of the hours of annealing tests (24 hours at room temperature followed by 168 hours at 100 °C) after irradiation at 2.3 kGy for $I_C = 0.1, 1, 10, 150, 500$ mA. Error: ($\pm 4\%$).

This shows that the effectiveness of the annealing tests depends on the absorbed dose of gamma irradiation and the resulting radiation-induced defects. Samples irradiated with absorbed doses up to 2.3 kGy showed a recovery in current gain values after the annealing tests, indicating that the annealing process was effective in partially restoring the electrical characteristics of both NPN and PNP BJTs.

Specifically, NPN and PNP transistors exhibited varying degrees of recovery in current gain values after annealing, depending on the collector current conditions used for the gain measurements. In contrast, samples irradiated at higher absorbed doses (≥26 kGy), classified as heavily damaged BJTs, did not recover their current gain values after the annealing tests. This suggests that the damage caused by gamma irradiation at these high doses was severe and could not be fully mitigated under the conditions of the applied annealing process.

5.2.3 Laser-driven proton irradiation

A set of six NPN transistors was irradiated with laser-driven protons under different conditions.
As explained in Section 3.1, using the Target Normal Sheath Acceleration (TNSA) mechanism, ions, predominantly protons, can be accelerated by focusing an ultra-intense ($I > 10^{18}$ W/cm^2), ultra-short (ps-fs) laser pulse onto a thin solid target. At the ALLS facility, protons with energies up to ∼5 MeV are generated from a single laser shot. The spectrum of protons available during the irradiation tests is depicted in Figure 5.17.

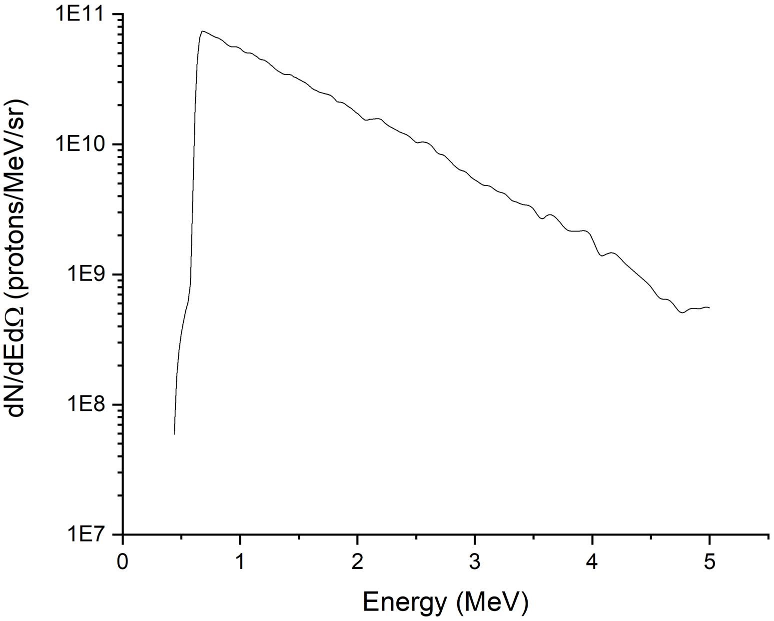

Figure 5.17. Laser-accelerated proton spectrum available at the ALLS facility. The y-axis is expressed in protons/MeV/sr.

Before the irradiation test with laser-accelerated protons, the samples were prepared by removing the lid from each BJT (Figure 5.18). This step was taken to prevent dose absorption by the lid and ensure that incoming particles reach the silicon region without energy losses, ensuring accurate irradiation of the silicon part. It is important to note that these conditions are more severe than those typically encountered in actual use and are usually applied in radiation resistance testing. This procedure, specified in the ESA-ESCC Basic Specification No. 22500 [150], is used for proton tests below 20 MeV. The lid of the sample consists of a 300 μm thick Nickel layer, capable of fully absorbing 5 MeV protons, which have a projected range of 73 μm in Nickel. It is important to note that this was not necessary with gamma radiation, as it is not attenuated by a 300 μm layer of Nickel [151].

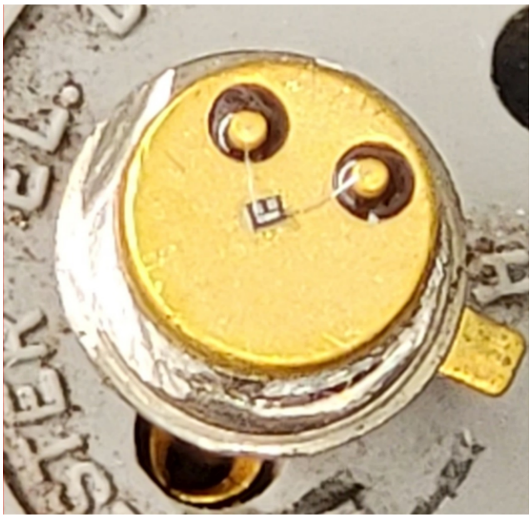

Figure 5.18. Picture of a decapped BJT.

For the irradiation, the devices were placed on a sample holder at a distance $d = 23.5$ cm from the proton source (i.e. the TNSA thin target where the laser-matter interaction takes place). All BJTs were unbiased during the exposure. The protons were generated by irradiating a 4.5 μm thick aluminum target with the laser described in Section 3.1.
The samples were irradiated with a variable number of shots at a repetition rate of 0.6 Hz. The irradiation parameters are summarized in Table 5.9.

Table 5.9. Laser-driven proton irradiation parameters.

Irradiation test	Number of shots
1	1
2	5
3	50
4	100
5	250
6	400

Before the irradiation test, all samples underwent characterization following the opening procedure. Some devices were damaged during this process: after opening, they were observed under an optical microscope, revealing that one of the bonding wires was broken (Figure 5.19), likely due to collisions with residuals from the opening process. Almost all of them were characterized by cutoff currents higher than the specification limits after decapping, but they were still considered functional since the current gain characteristics were not altered. An increase in cutoff currents is normal after decapping due to exposure of the die to the external environment; for example, moisture can create conductive paths, leading to increased leakage currents [152]. For this reason, the behavior of the cutoff currents after irradiation was not considered. On the contrary, the measured saturation voltages, were not affected by radiation and remained constant even after irradiation at the highest absorbed dose (data not shown).

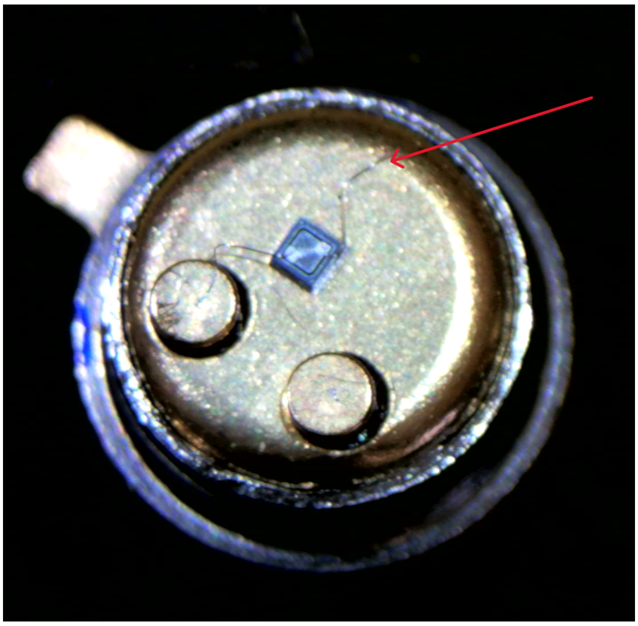

Figure 5.19. Microscope image of a NPN transistor after the decapping. The arrow indicates the broken bonding wire.

The results obtained for the current gains after the irradiation tests conducted with 50, 100, 250, and 400 shots are consistent, indicating that the gain values reach their minimum (worst operating point) after irradiation with 50 shots and cannot be further degraded. Therefore, for better visualization purposes, the following results are presented for samples irradiated with 1, 5, and 50 shots.
The I_C-V_{CE} characteristic curves before and after irradiation are shown in Figure 5.20. A decrease in collector current can be observed with increasing dose. Similar conclusions can be drawn from the behavior of current gains after irradiation. Figure 5.21 depicts the curves corresponding to the current gains β and their reciprocal variations $\Delta(1/\beta)$.

The β_3, β_4 and β_5 values are not available for the samples irradiated with a number of shots $\geq$50. In fact, these samples were irradiated during the first irradiation campaign of this thesis project, during which measurements of current gains for

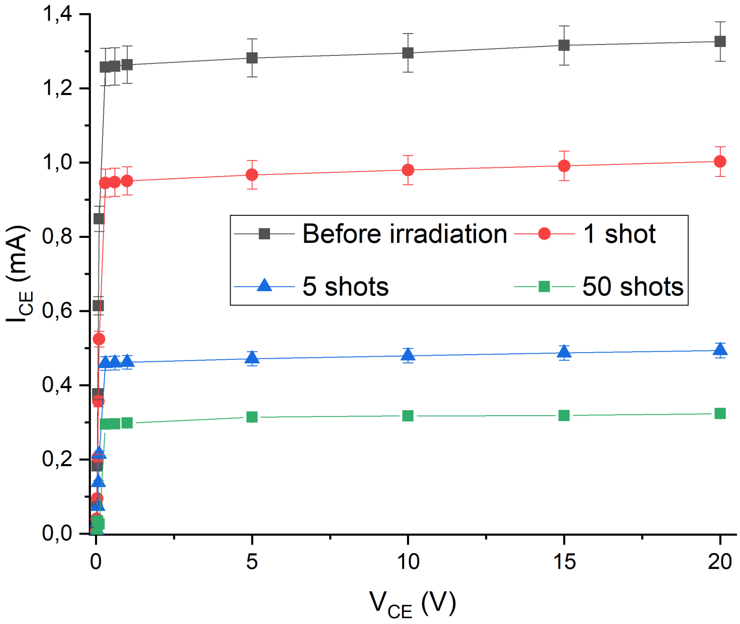

Figure 5.20. I_C-V_{CE} characteristic curves of NPN transistors before and after irradiation with varying numbers of shots.

collector current values of 10 mA, 150 mA and 500 mA (corresponding to β_3, β_4 and β_5) were not planned. Subsequently, to gather more information about the current gain trends after radiation exposure, all collector current values reported in Table 5.2 were evaluated.

From Figure 5.21, it is evident that after a few laser shots, the current gain values exit specification limits: specifically, β_3 and β_4 (with a minimum value of 100) exceed limits after approximately 2 shots, while β_1 and β_2 (with minimum values of 50 and 75, respectively) exit limits in the range of 3-4 shots. β_5 remains within the allowed range until 5 shots.

Before and after irradiation, the samples were examined with a Scanning Electron Microscope (SEM) to detect any morphological changes on the silicon die, but no appreciable modifications were observed (Figure 5.22).

The samples did not show any recovery after the two steps of annealing (data not shown), which suggests that the annealing process applied at this duration and temperature was insufficient to effectively repair the defects created by irradiation. This observation underscores the complexity and severity of the induced damage.

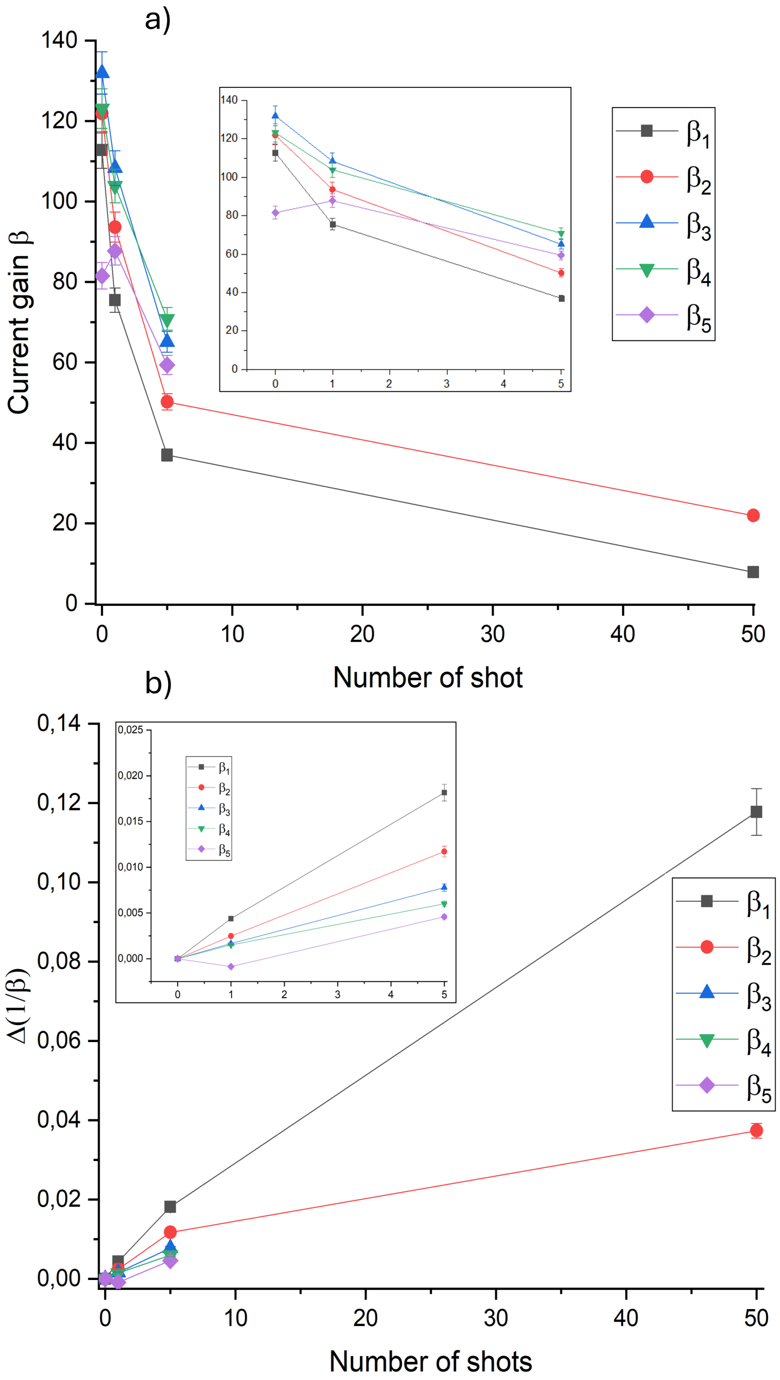

Figure 5.21. Behavior of (a) current gain β and (b) the reciprocal of current gain $\Delta(1/\beta)$ measured for I_C = 0.1, 1, 10, 150, 500 mA as a function of the number of shots. Insets show the trends of the current gain and the reciprocal of current gain are shown for I_C = 0.1, 1, 10, 150, 500 mA in the range of 0-5 shot.

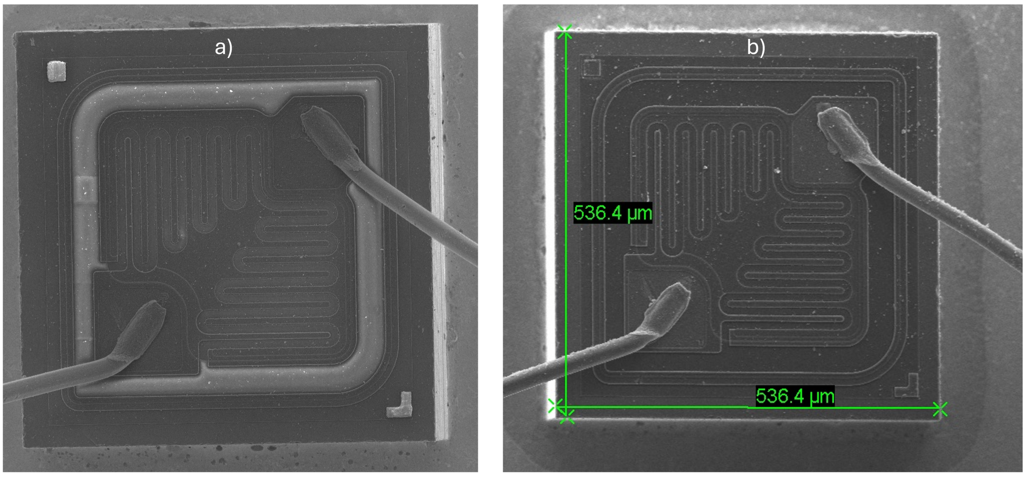

Figure 5.22. SEM image (magnification 400x) of a BJT die (a) before (acquired at INRS) and (b) after (acquired at ENEA Casaccia R.C.) laser-driven proton irradiation.

5.2.4 Proton irradiation

Protons with energy of 2.8 MeV (energy spread = 0.2 MeV), available at the TOP-IMPLART low-energy vertical line (Figure 5.23) were used to irradiate NPN and PNP transistors. This energy value was chosen to perform irradiation with protons from a conventional accelerator within the typical energy range (1-5 MeV) of laser-driven protons used at the ALLS facility. A picture of the samples positioned at the end of the vertical line of the TOP-IMPLART linac for the irradiation test is shown in Figure 5.24. Before the irradiation test, the homogeneity of the proton fluence at the samples position was checked using a radiochromic film. As depicted in Figure 5.24a, the samples were positioned within a circle with a radius of less than 8 mm to ensure uniformity of the proton fluence on them. The linac provided $1.28 \cdot 10^7$ protons per pulse at a rate of 25 pulses per second for irradiation. Different proton fluence conditions were achieved by varying the irradiation duration, as summarized in Table 5.10. For each irradiation condition, two NPN and two PNP samples were irradiated, totaling 12 samples. All devices were unbiased during irradiation. The values of the measured parameters presented below are the mean values obtained for NPN or PNP transistors irradiated under the same conditions.

Table 5.10. TOP-IMPLART proton irradiation conditions.

Irradiation test	Proton fluence (p/cm^2)
1	$3.38 \cdot 10^9$
2	$3.38 \cdot 10^{10}$
3	$2.5 \cdot 10^{11}$

Similar to laser-driven proton irradiation, all devices were decapped before exposure to prevent energy losses of incoming protons through the lid. After decapping, the

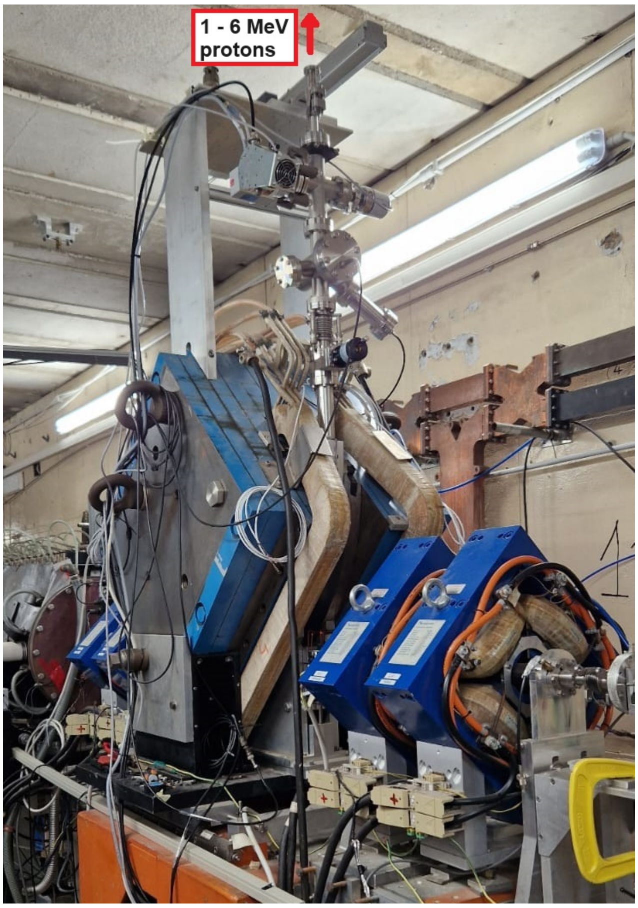

Figure 5.23. TOP-IMPLART vertical line for proton beams of 1-6 MeV.

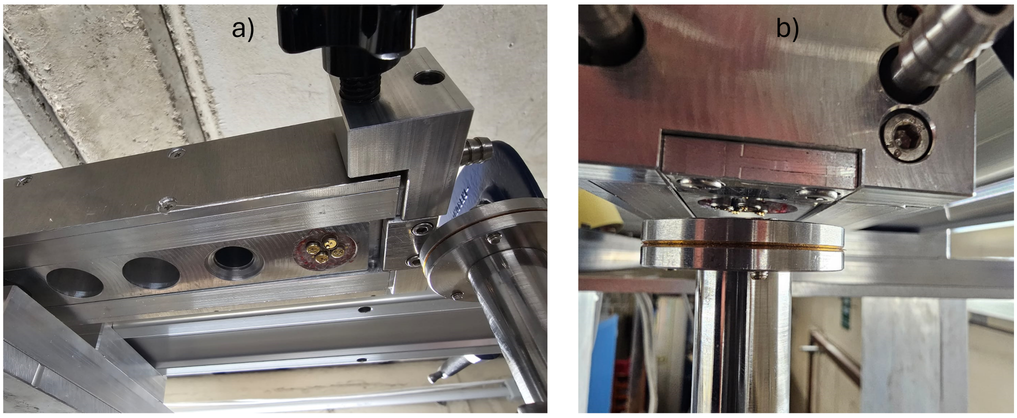

Figure 5.24. Picture of the samples positioned in the sample holder (a) and irradiation setup (b).

devices were characterized. For both NPN and PNP transistors, as discussed in the laser-accelerated proton irradiation section, while current gain values were not affected by the opening procedure, cutoff currents of the devices increased. Therefore, cutoff currents will not be considered in the results.

Saturation voltages measured before and after irradiation up to the proton fluences reported in Table 5.10 were not affected for both NPN and PNP transistors.

Measurement of I_C-V_{CE} characteristic curves was performed before and after irradiation at different proton fluence conditions for both NPN and PNP transistors. The curves obtained are shown in Figure 5.25. For PNP transistors, the absolute values of I_C and V_{CE} were plotted.

For both NPN and PNP BJTs, it is evident that I_C values remain unchanged after proton irradiation with a fluence of $3.38 \cdot 10^9$ p/cm^2, and then they start to decrease as the proton fluence increases.

The results for the current gains and the corresponding curves of the reciprocal of current gains are shown in Figure 5.26 and 5.27, respectively, for NPN (Figures 5.26a and 5.27a) and PNP (Figures 5.26b and 5.27b) transistors. The lowest value of proton fluence did not affect the current gain of NPN transistors for all conditions of collector currents. After irradiation at $3.38 \cdot 10^{10}$ p/cm^2, the β values corresponding to collector currents I_C of 0.1 mA, 1 mA, and 10 mA showed a decrease. However, up to this proton fluence, all the β values remained within the allowed range. After irradiation at $2.5 \cdot 10^{11}$ p/cm^2, the NPN devices were completely damaged as the current gain values went out of the ranges allowed by the sample datasheet.

Concerning PNP BJTs, the curves of current gains measured for collector currents IC of 0.1 mA and 1 mA ($\beta 1$ and β_2) decrease as the proton fluence increases. While the values of β_3, β_4, and β_5 decrease after irradiation at $3.38 \cdot 10^9$ p/cm^2, they remain constant up to $3.38 \cdot 10^{10}$ p/cm^2 and then decrease again after irradiation at $2.5 \cdot 10^{11}$ p/cm^2.

The annealing tests on these samples are still ongoing.

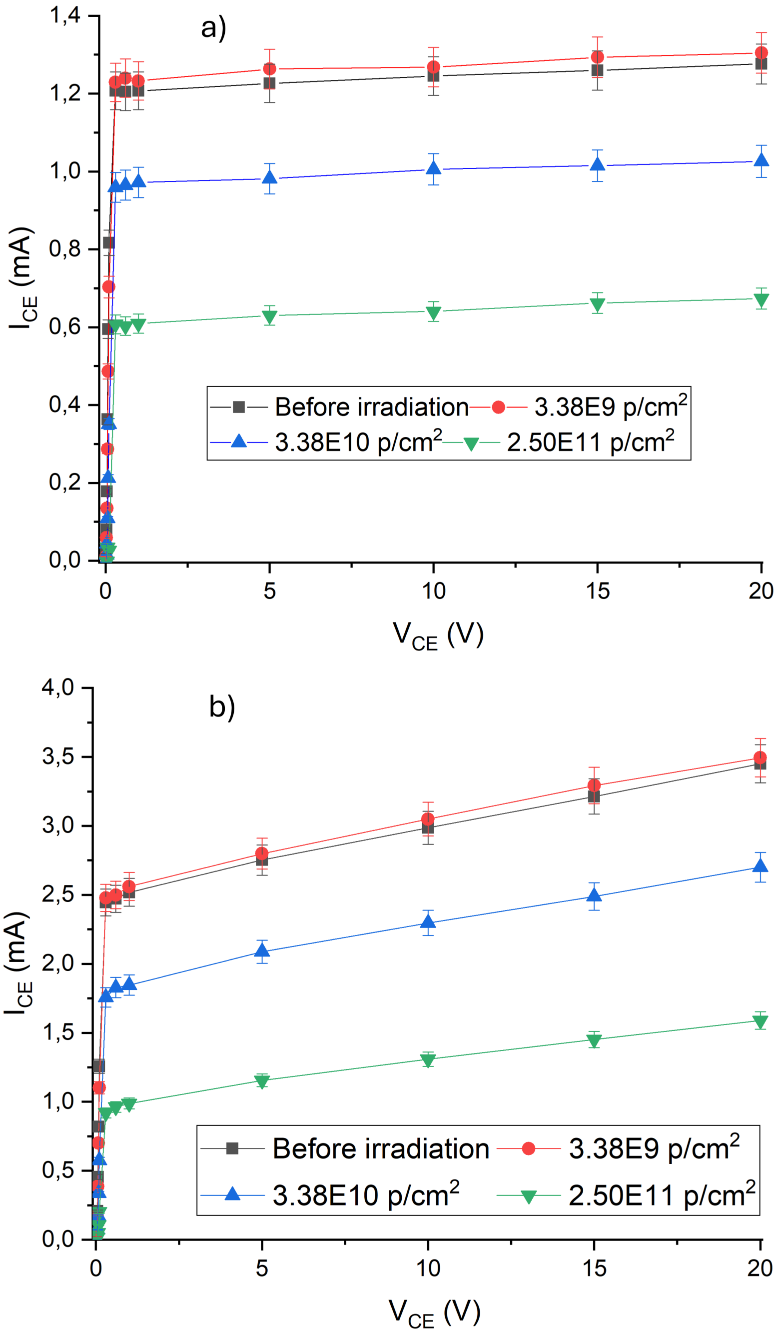

Figure 5.25. I_C-V_{CE} characteristic curves of NPN (a) and PNP (b) BJTs before and after irradiation at different proton fluence values. Insets show the magnified I_C-V_{CE} characteristics in the V_{CE} interval from 0 to 1 V. For PNP transistors, the absolute values of I_C and V_{CE} are shown.

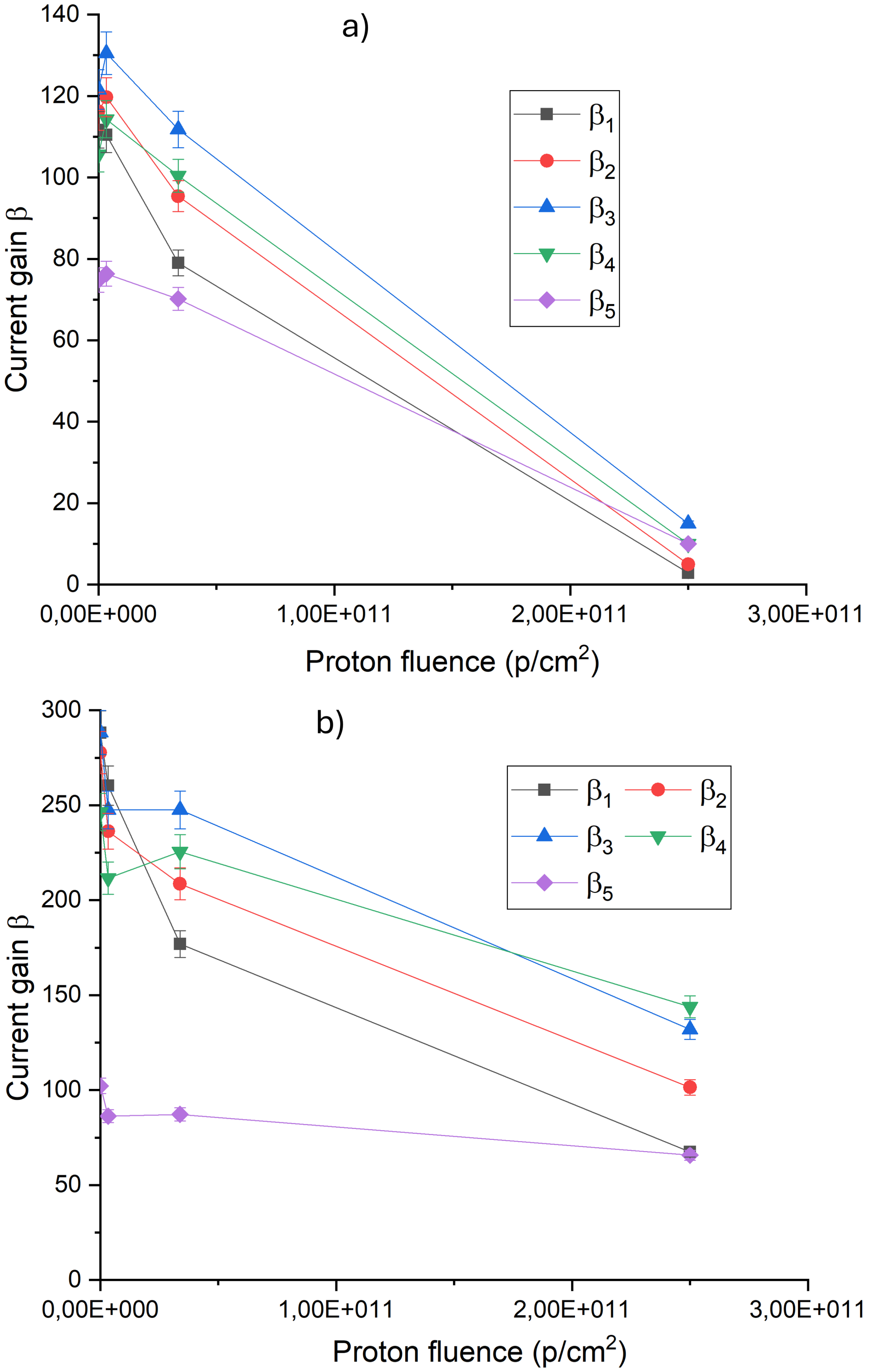

Figure 5.26. Current gains of (a) NPN and (b) PNP transistors as a function of proton fluence for $I_C = 0.1, 1, 10, 150, 500$ mA. Error: (±4%).

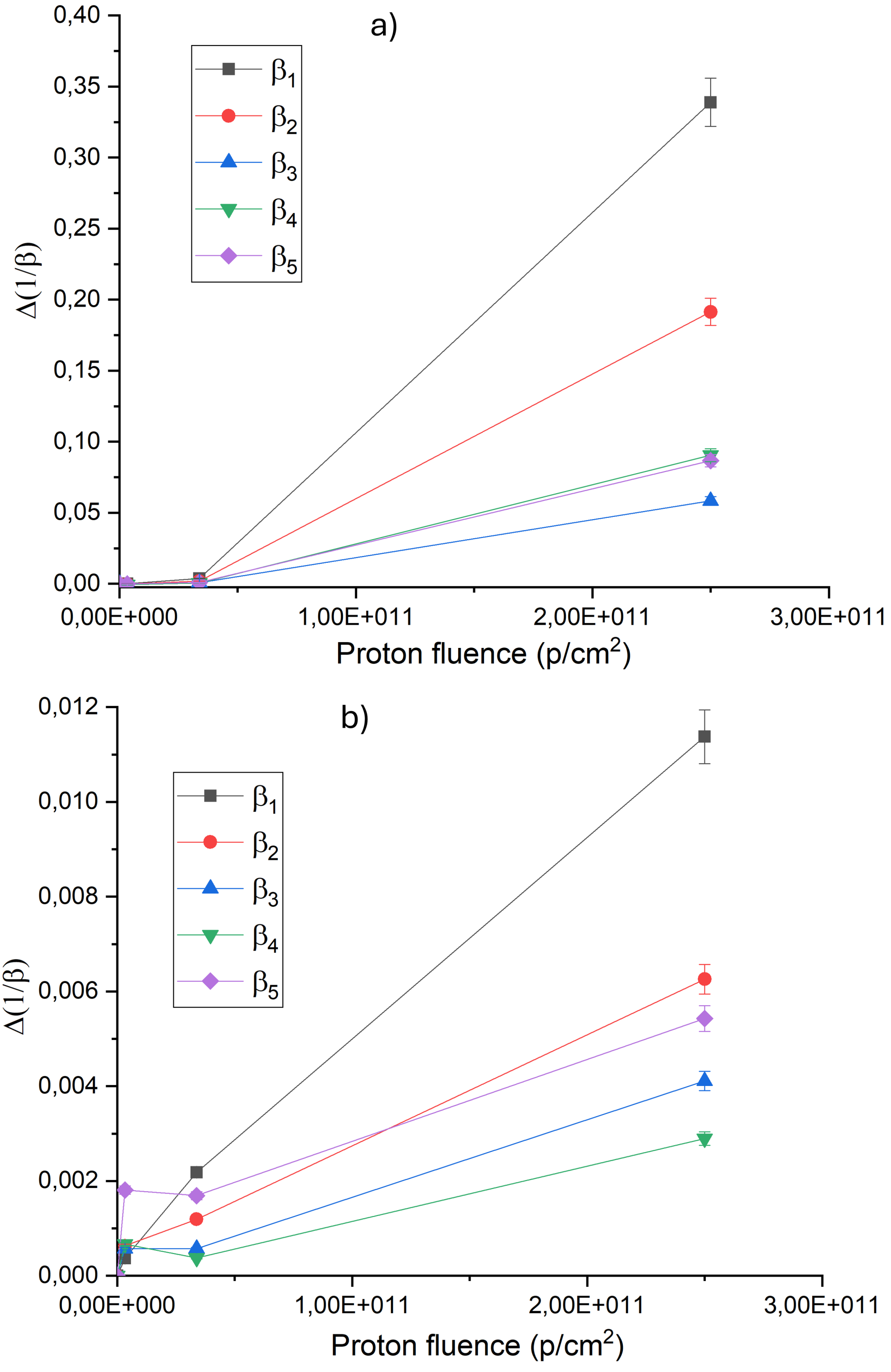

Figure 5.27. NPN (a) and PNP (b) behavior of $\Delta(1/\beta)$as a function of proton fluence for $I_C = 0.1, 1, 10, 150, 500$ mA. Error: ($\pm 5\%$).

5.2.5 Neutron irradiation

A set of 10 NPN transistors and 10 PNP transistors was irradiated at the Frascati Neutron Generator with 14 MeV neutrons. Figure 5.28 shows a picture of the setup, including samples, during the irradiation test, captured by a remote camera.

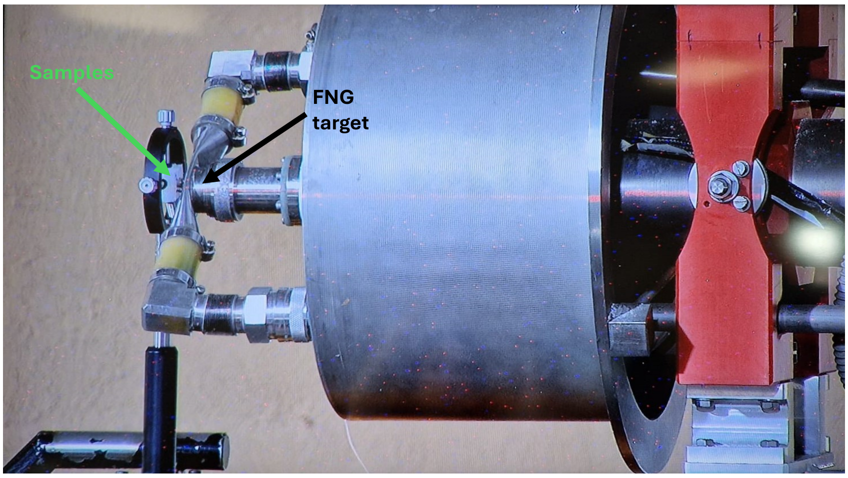

Figure 5.28. Picture of four samples in the sample holder positioned 0.5 cm from the FNG target during the irradiation test.

The samples were irradiated under five different neutron fluence conditions by varying their positions relative to the FNG DT target and the irradiation time, organized in groups of four (two NPN and two PNP BJTs). All devices were irradiated unbiased. The 14 MeV neutron irradiation conditions are detailed in Table 5.11.

Table 5.11. 14 MeV neutron irradiation conditions.

Irradiation test	**Neutron fluence (n/cm^2)**
1	$2 \cdot 10^9$
2	$2 \cdot 10^{11}$
3	$2 \cdot 10^{12}$
4	$1 \cdot 10^{13}$
5	$2 \cdot 10^{13}$

Measurements of the cutoff currents and saturation voltages were performed before and after irradiation and are presented in Figure 5.29 and Figure 5.30 as a function of neutron fluence for NPN and PNP transistors, respectively. For better visualization, a zoom in the neutron fluence range 0 - $2 \cdot 10^{11}$ n/cm^2 is shown for cutoff currents and saturation voltages in the insets of both Figure 5.29 and 5.30. Similar to samples irradiated at high doses with gamma radiation, the measured cutoff currents (Fig. 5.29a and Fig. 5.30a) exhibit fluctuations, likely due to parasitic currents. However, all values remained within specifications for both NPN and PNP transistors.

Regarding the saturation voltage values, there were no modifications observed after irradiation for NPN transistors (Fig. 5.29b). For PNP transistors (Fig. 5.30b), $V_{CE(sat)1}$ decreased after irradiation at $2 \cdot 10^9$ n/cm^2 and then remained constant, while $V_{CE(sat)2}$, $V_{BE(sat)1}$, and $V_{BE(sat)2}$ increased after irradiation at $2 \cdot 10^9$ n/cm^2 and remained constant up to a neutron fluence of $2 \cdot 10^{13}$ n/cm^2. Despite these changes, all measured saturation voltages remained within the allowed ranges.

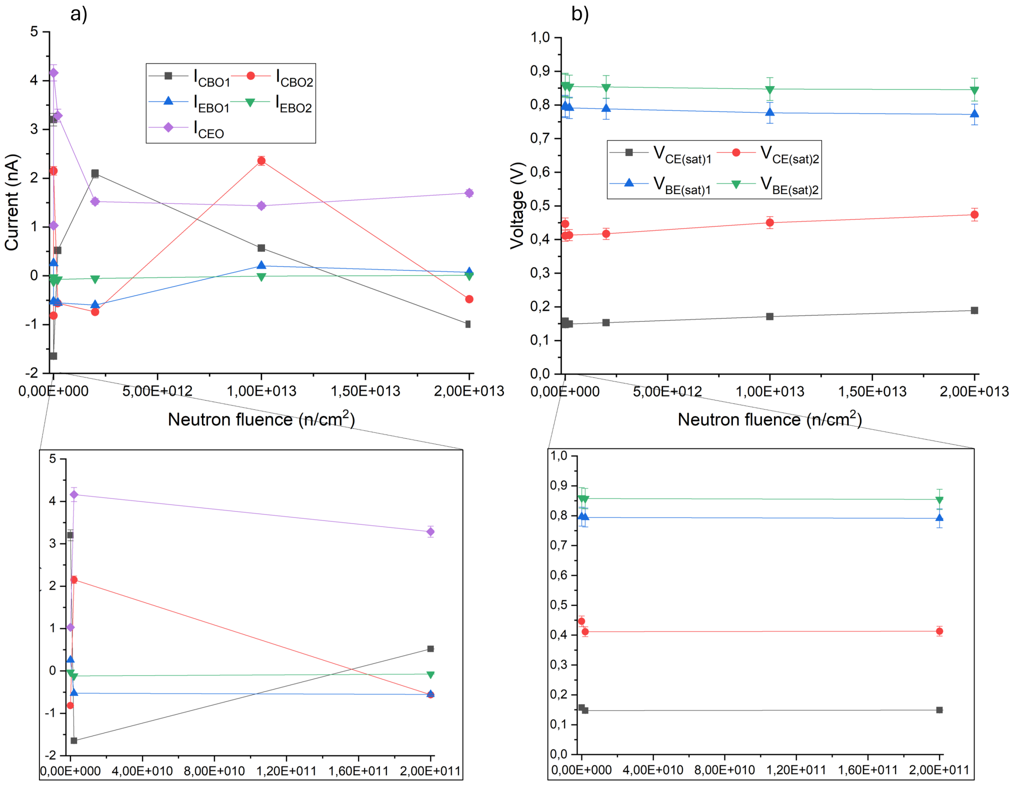

Figure 5.29. Trend of cutoff currents I_{CBO}, I_{EBO}, and I_{CEO} (a) and saturation voltages $V_{CE(sat)}$ and $V_{BE(sat)}$ (b) for NPN transistors as a function of neutron fluence. Insets show a zoom in the neutron fluence range 0 - $2 \cdot 10^{11}$ n/cm^2. Error bars (±4%) represent measurement uncertainties.

I_C-V_{CE} characteristic curves were measured before and after each condition of neutron irradiation for both NPN and PNP transistors. The curves obtained are depicted in Figure 5.31. Again, it is evident that PNP transistors are more damaged than NPN transistors after irradiation. Moreover, the I_C-V_{CE} curves are not modified until a neutron fluence of $2 \cdot 10^{11}$ n/cm^2 for NPN transistors, whereas slight modifications are observed up to the same neutron fluence for PNP devices.

The results obtained for the current gains and the correspondent curves of the reciprocal of current gains are shown in Figure 5.32 and 5.33, respectively, for NPN (Figures 5.26a and 5.27a) and PNP (Figures 5.32b and 5.33b) transistors. It can be seen that all the β values are unaffected up to a neutron fluence of $2 \cdot 10^{11}$ n/cm^2, after which they begin to decrease. Both β_5 for NPN devices and β_3 and β_5 for PNP devices remained within specifications even at the highest neutron fluence irradiation condition. However, for NPN BJTs, β_1 and β_2 deviated from the allowed

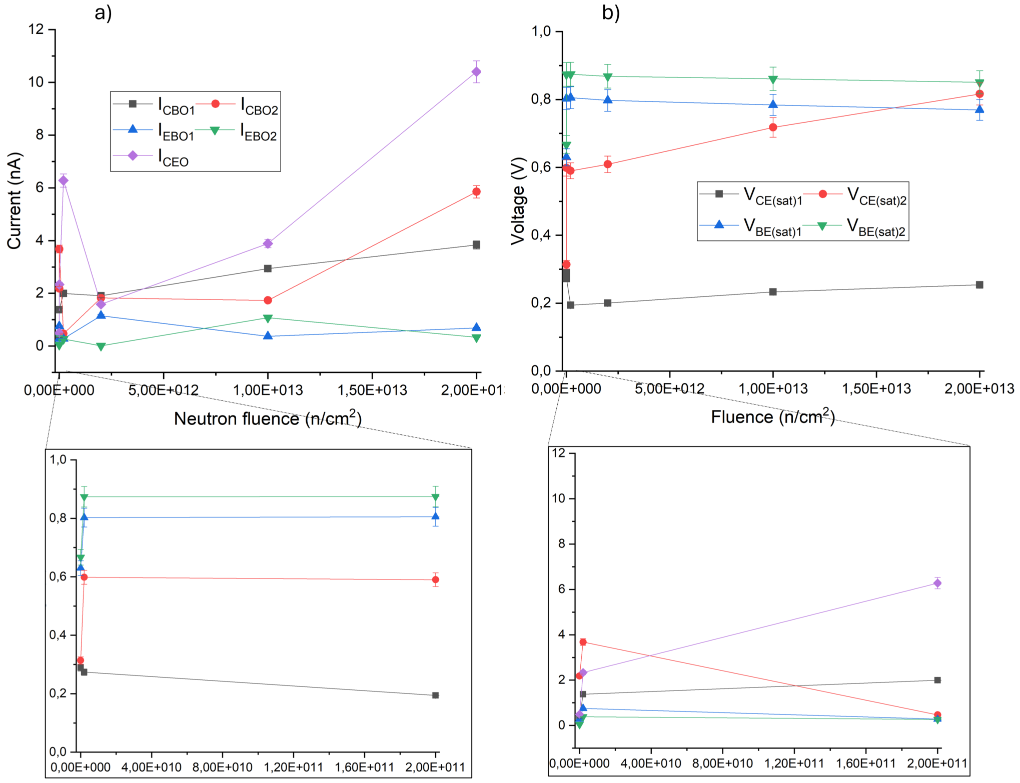

Figure 5.30. Trend of cutoff currents I_{CBO}, I_{EBO}, and I_{CEO} (a) and saturation voltages $V_{CE(sat)}$ and $V_{BE(sat)}$ (b) for PNP transistors as a function of neutron fluence. Insets show a zoom in the neutron fluence range 0 - $2 \cdot 10^{11}$ n/cm^2. Error bars (±4%) represent measurement uncertainties.

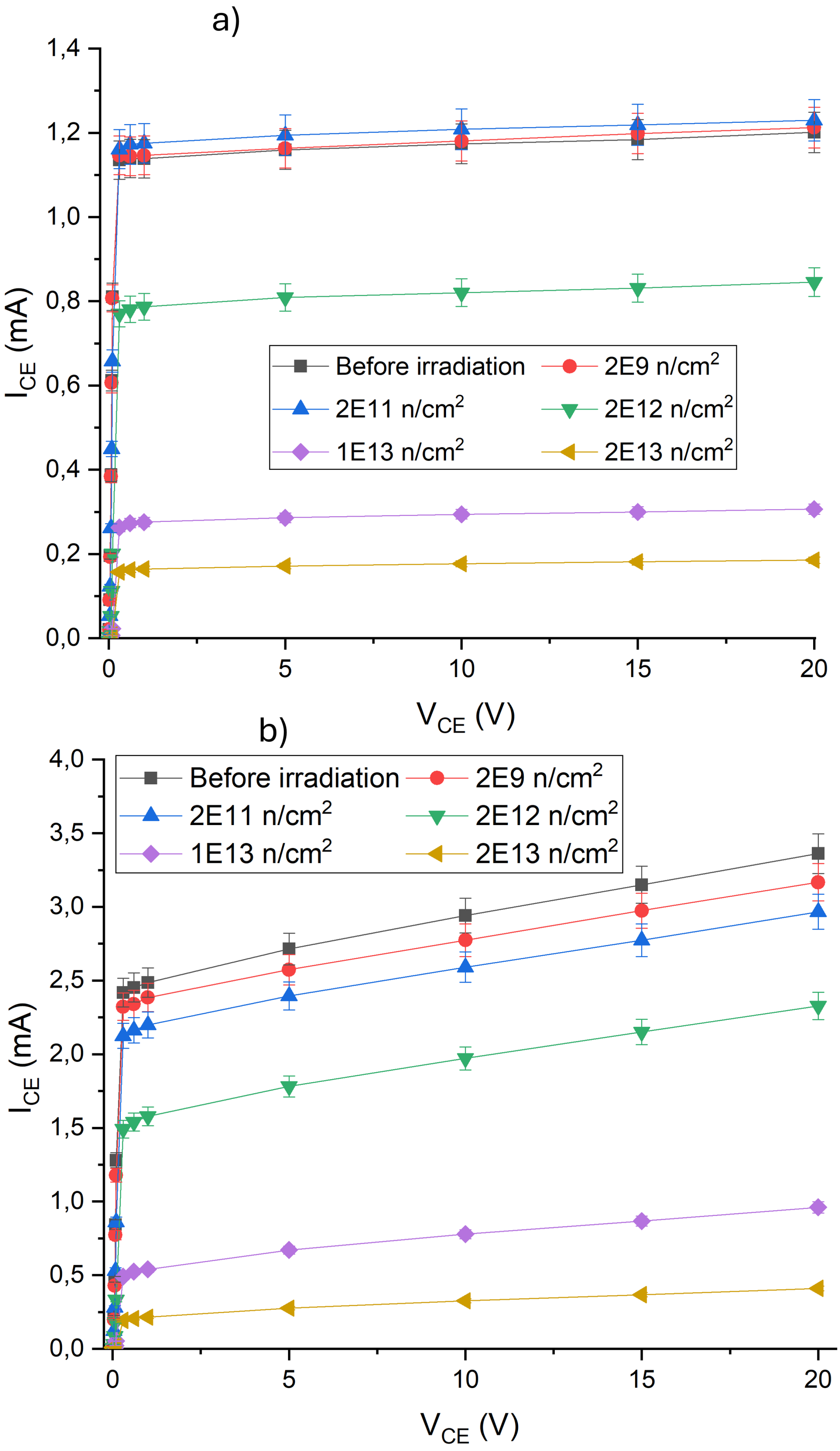

Figure 5.31. I_C-V_{CE} characteristic curves of NPN (a) and PNP (b) BJTs before and after irradiation at different neutron fluence levels. For PNP transistors, the absolute values of I_C and V_{CE} are shown.

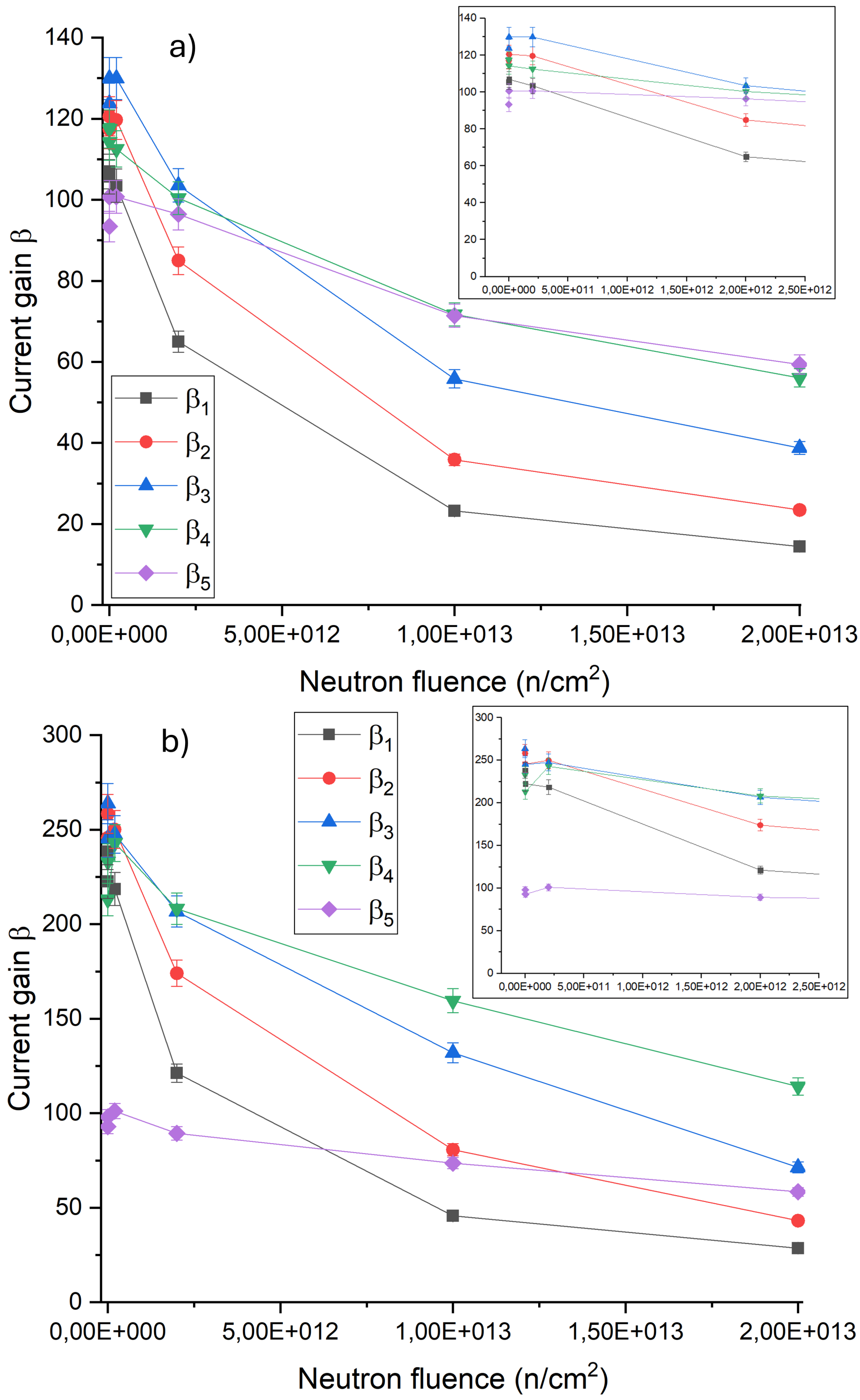

Figure 5.32. NPN (a) and PNP (b) current gains behavior as a function of the neutron fluence for $I_C = 0.1, 1, 10, 150, 500$ mA. Error: (±4%).

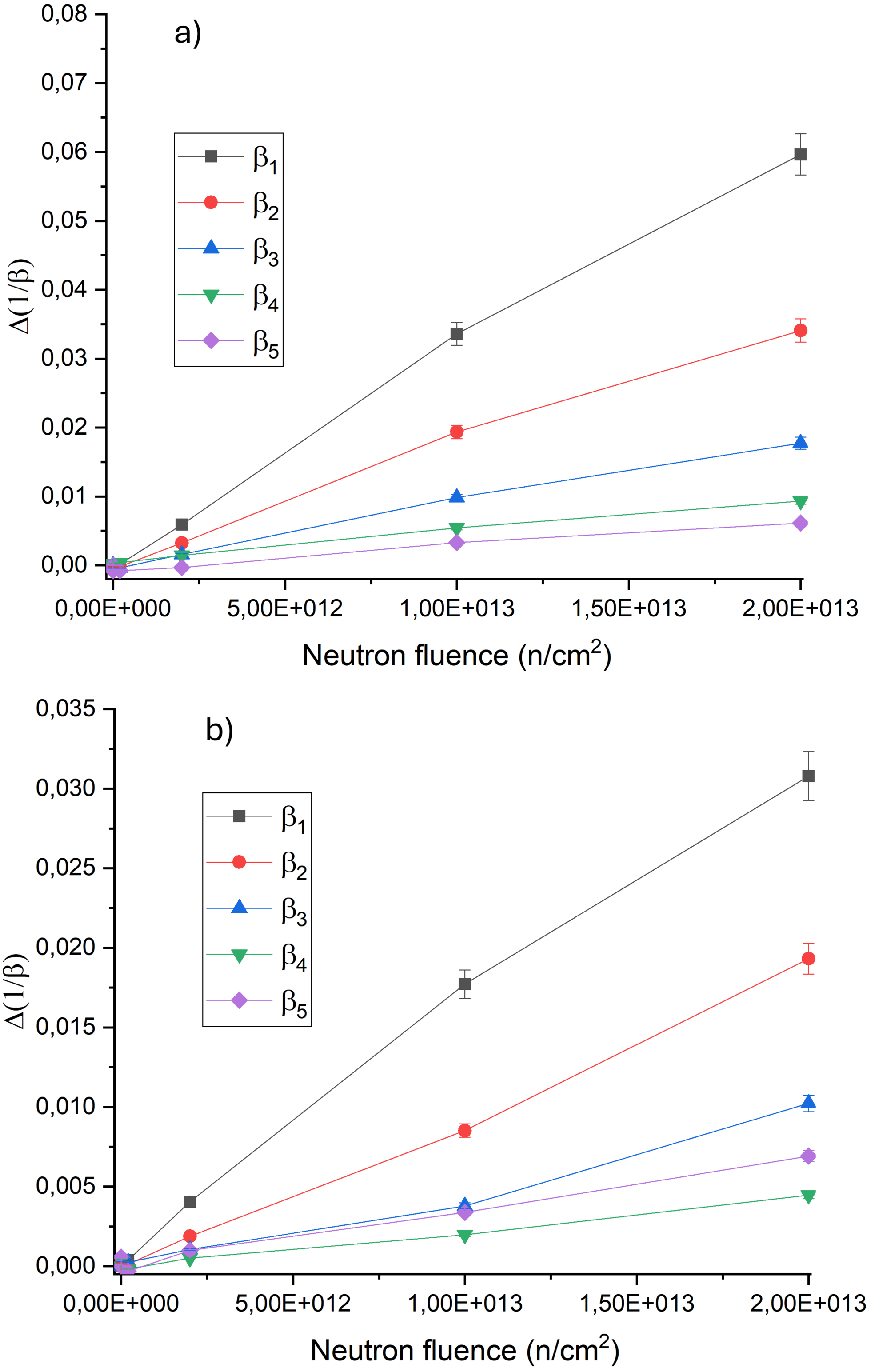

Figure 5.33. NPN (a) and PNP (b) $\Delta(1/\beta)$ behavior as a function of the neutron fluence for I_C = 0.1, 1, 10, 150, 500 mA. Error: (±5%).

ranges specified by the datasheet after reaching a neutron fluence of approximately 3.5-5 $\cdot$ 10^{12} n/cm^2, and β_3 and β_4 after reaching approximately 2 $\cdot$ 10^{12} n/cm^2. For PNP transistors, β_1, β_2, and β_3 were no longer within specifications after reaching neutron fluences of approximately 7 $\cdot$ 10^{12} n/cm^2, 8 $\cdot$ 10^{12} n/cm^2, and 1.6 $\cdot$ 10^{13} n/cm^2, respectively.

Looking at the reciprocal of current gain (Fig. 5.33), it is observed that for nearly all collector current conditions, the behavior of $\Delta(1/\beta)$ can be approximated by a linear relationship. Specifically, this applies to the data corresponding to neutron fluences of 2 $\cdot$ 10^{12} n/cm^2, 1 $\cdot$ 10^{13} n/cm^2, and 2 $\cdot$ 10^{13} n/cm^2. Since a linear relationship between $\Delta(1/\beta)$ and particle fluence is characteristic of bulk damage mechanisms, this suggests that within this range, bulk effects dominate over surface effects (ionization damage) [79, 77]. The fitted lines are shown in Figure 5.34. Given that the Messenger-Spratt equation is expressed as $\Delta(1/\beta) = \mathrm{K}_\beta\Phi$, where $\mathrm{K}_\beta = \frac{K}{\omega_T}$ (as per Equation 2.25), the slopes of the linear curves correspond to the values of K_β for each case. This finding aligns with previous literature [153], which indicates that the slope is influenced by the collector current I_c and the transistor type.

The irradiation tests were followed by the two above mentioned annealing steps. The samples did not recover after the annealing tests. This is likely due to the limitations of annealing in repairing bulk damage. Annealing effectively mitigates certain radiation-induced defects like point defects and dislocations in the crystal lattice. However, bulk damage, which includes more extensive and complex defects such as clusters of vacancies, interstitials, and other forms of lattice disorder, may not be effectively addressed by standard annealing processes. These extensive defects can create deep energy levels within the semiconductor bandgap, significantly altering the electrical properties of the material.

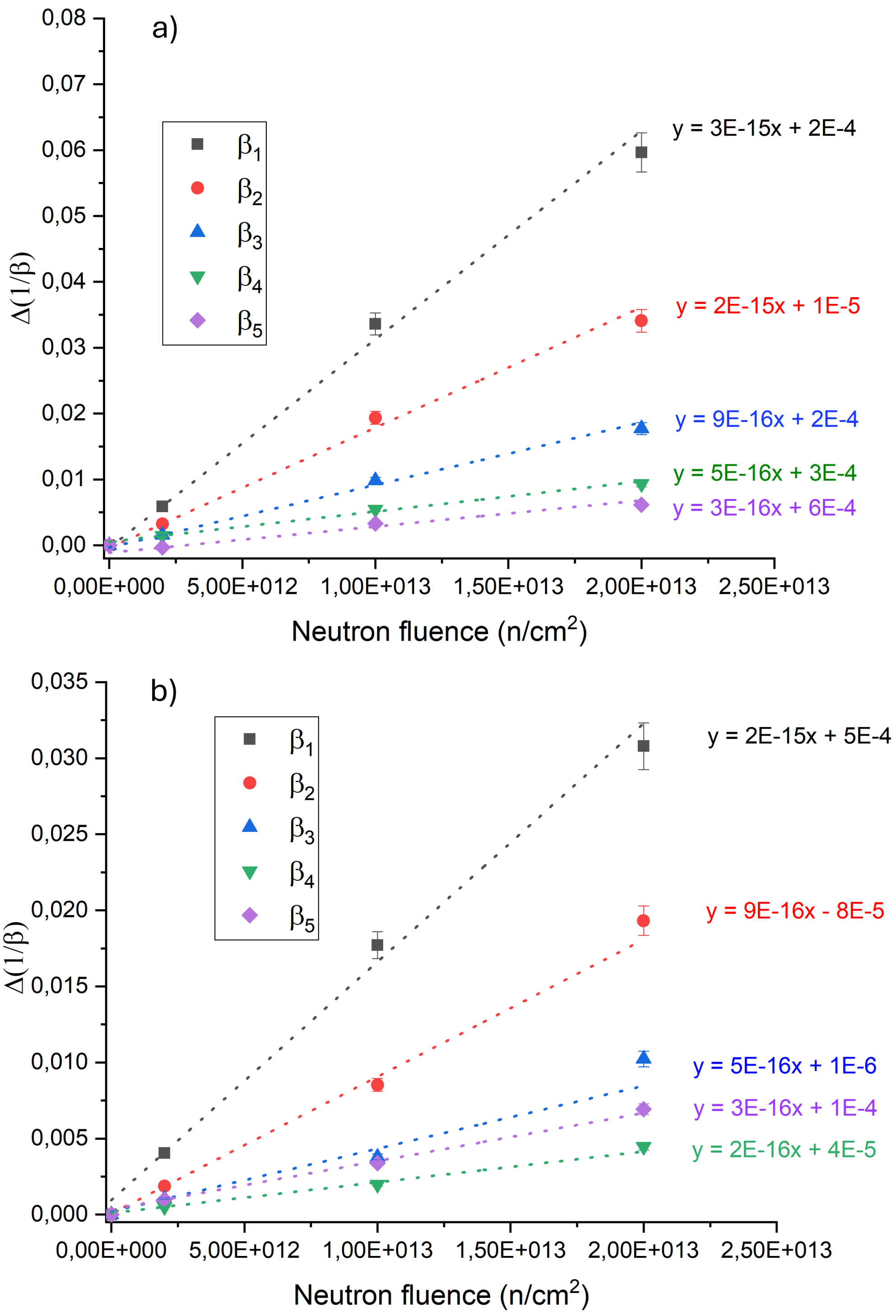

Figure 5.34. NPN (a) and PNP (b) $\Delta(1/\beta)$ behavior as a function of neutron fluence for I_C = 0.1, 1, 10, 150, 500 mA, along with corresponding linear trends.

5.3 Dose deposition study

The second part of this work focuses on investigating the relationship between dose deposition in the irradiation of electronic components using a classical radiation source (such as ^{60}Co photons, protons and neutrons from a conventional accelerator) and laser-accelerated protons, a novel radiation source [71, 154]. Since bulk and surface effects can be regarded as independent of each other [58], both the dose deposited by ionizing processes (TID) and non-ionizing processes (NIEL dose) were studied for all the stress test sources. Specifically, the sum of these two contributions gives the total deposited dose D^{total}, as follows:

$$D^{total} = D^{TID} + D^{NIEL} \tag{5.2}$$

where D^{TID} is the dose deposited by ionizing processes, while D^{NIEL} accounts for the dose released after non-ionizing processes.

The investigation of NIEL deposited dose is a crucial point since, unlike TID, which depends on radiation type and irradiation conditions, the dose deposited by NIEL processes allows for predicting the damage almost independently of the radiation type and energy. The variation of the reciprocal of current gain $\Delta(1/\beta)$, as explained in Section 2.2.4, is proportional to the concentration of Frenkel pairs according to Equation 2.26. Experimental results on bipolar junction transistors [77, 153, 155] proved the dependence of $\Delta(1/\beta)$ on the concentration of FP created in the silicon by displacement damage (i.e. by NIEL processes). For example, the relation between $\Delta(1/\beta)$ and the concentration of FP is shown in Figure 5.35 for a specific type of BJT [77].

This relation allows to predict the gain degradation. Moreover, if the value of $\Delta(1/\beta)$ at which the component operation is compromised is known (this can be determined from the definition of $\Delta(1/\beta)$ using the initial and minimum values of current gain as specified in the component datasheet), it is possible to assess the concentration of displacement damage (and hence the NIEL dose) that causes malfunction.

Finally, the dose values at which the BJTs functioning is compromised (according to the ranges allowed by the datasheet) were calculated and compared for all the employed radiation sources.

5.3.1 Gamma radiation deposited dose

Gamma radiation deposits energy in matter mainly through ionization processes since ^{60}Co photons (mean energy 1.25 MeV) cannot directly induce displacement damage. However, they can produce electrons that have sufficient energy to induce displacement damage, i.e., to deposit energy via NIEL processes.

The dosimetric systems used at the Calliope facility (detailed in Chapter 4) provide the value of the total deposited dose. The single contribution of the NIEL dose was obtained through calculations involving the spectrum of Compton electrons generated by the interaction of gamma radiation with the irradiated sample, as explained below.

To obtain the electron spectrum generated within the sample after exposure, a Monte

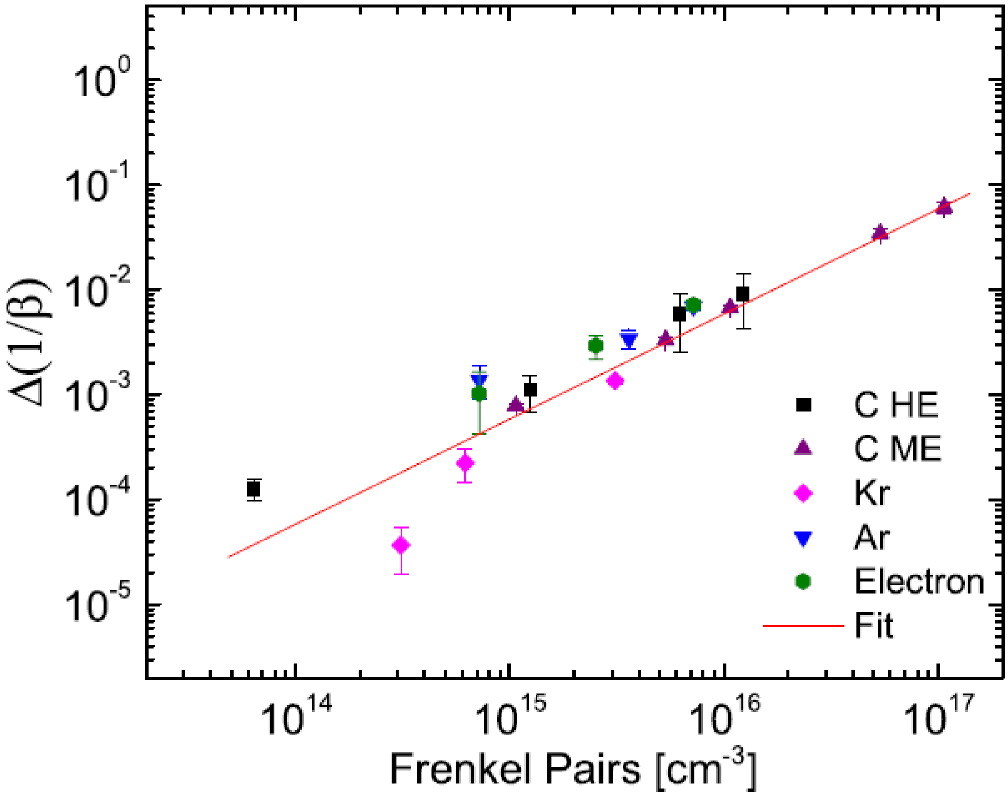

Figure 5.35. Linear dependence of $\Delta(1/\beta)$ on the concentration of FP for a specific NPN BJT at collector current $I_c = 1$ mA, after irradiation with ^{12}C- (C HE), ^{13}C- (C ME), Kr- and Ar-ions and high energy electrons [77].

Carlo N-Particle®(MCNP®) code was used. It is a Monte Carlo code based on a probabilistic approach that transports all types of particles. A model of the Calliope irradiation cell was constructed to simulate the dose rate and the energy spectrum of all particle types at various points within the irradiation cell.

Using the irradiation conditions of the device (its position inside the irradiation cell and its geometry), the electron spectrum generated within the sample active region was obtained. Specifically, gamma rays (primary radiation) and electrons (secondary particles) were transported using the MCNP®code [156] to evaluate their spectrum within the region of interest, i.e. corresponding to the required dose rate. The data were provided by Dr. Fabio Panza (ENEA Nuclear Department, Division of Plasma Studies and DTT, Frascati R. C.), MCNP®licensed.

The electron spectrum given by MCNP®, expressed as flux in units of electrons/cm^2/s, resulting from the interaction of gamma radiation with the silicon active region of the transistor in the position corresponding to a dose rate of 1 kGy/h (high dose rate test condition), is shown in Figure 5.36. The NIEL dose absorbed by the sample from electron irradiation was calculated using the online *Screened Relativistic Treatment for NIEL Dose Nuclear and Electronic Stopping Power Calculator*, available on the Italian Space Agency (ASI) website [157, 158]. This tool, which is part of ASIF space radiation environment research, computes the Screened Relativistic (SR) NIEL curve for particles interacting with materials. Detailed information on the calculation method can be found in [159]. The calculator requires inputs such as particle type, energy spectrum (in particles/MeV/cm^2) and the target material and gives a NIEL dose value (in Gy). By utilizing the NIEL function (Section 2.2.1) of the incident particle, it provides the corresponding NIEL dose. The graphs generated by the ASI calculator for the NIEL dose calculation due to electrons are shown in Figure 5.37. In this case, the electron spectrum per second of irradiation served as input to the

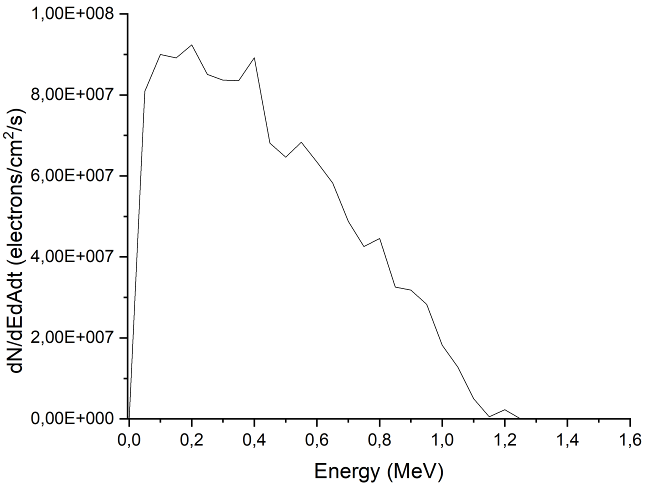

Figure 5.36. Electron spectrum (electrons/cm^2/s) generated by the interaction of gamma radiation with the transistor silicon active region for irradiation at 1 kGy/h (high dose rate test condition).

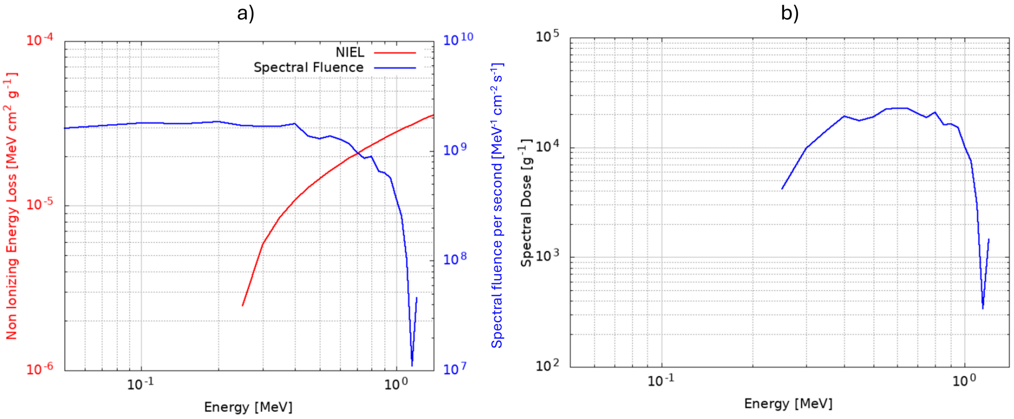

Figure 5.37. Electron spectral fluence per second (MeV^{-1} cm^{-2} s^{-1}) and electron NIEL function (a) and convolution (b).

ASI calculator to obtain a value in Gy/s (i.e. a NIEL dose rate).
The calculator utilized both the electron spectrum and the electron NIEL function (Fig. 5.37a) to perform a convolution (5.37b). The resulting spectrum from Figure 5.37b is integrated to provide NIEL values for each energy bin, along with their sum. In this case, a NIEL dose rate value was obtained. Multiplying the NIEL dose rate by the irradiation time yielded a NIEL dose value. Specifically, a NIEL dose rate of approximately $2.2 \cdot 10^{-6}$ Gy/s was obtained for the electron flux shown in Figure 5.36. Therefore, after one hour of irradiation, a NIEL dose $D^{NIEL} \simeq 8 \cdot 10^{-3}$ Gy is deposited. The corresponding total absorbed dose D^{total} is 1 kGy. Hence, the dose deposited by ionization processes is approximately five orders of magnitude higher than that deposited by NIEL processes, confirming that for gamma radiation, up to high levels of absorbed dose, the NIEL contribution to the total deposited dose is negligible.

5.3.2 Laser-driven protons deposited dose

To evaluate the dose deposition by laser-driven protons from a single laser shot, a Matlab®code was utilized. This code models energy deposition using data from *The Stopping and Range of Ions in Matter* (SRIM) [160]. SRIM is a collection of software packages that deal with the transport of ions in matter. Among its many applications, it provides the stopping power and the ranges of ions in matter.
The Matlab®code estimates the temperature increase due to proton heating and provides the absorbed dose value in a specified volume of the sample [161]. As outlined in [71], the heating contribution from electrons and heavy ions generated by the TNSA mechanism after laser plasma interaction is negligible compared to that produced by protons (<20% for electrons within the first 500 nm and negligible deeper in the sample; below 0.5% for heavy ions). Therefore, this study considers only the contribution of protons to dose deposition.
Assuming a uniform distribution of deposited energy in the target material, the dose D^{total} deposited by protons and the local temperature increase ΔT can be correlated.

The equation [161]:

$$\Delta T = \frac{dE}{dx}\frac{\phi}{\rho c_p} \tag{5.3}$$

where $\frac{dE}{dx}$ represents the particle stopping power, ϕ denotes the particle fluence, ρ is the material density and c_p is the specific heat capacity of the material, implies:

$$D^{total} = c_p \cdot \Delta T \tag{5.4}$$

This equation directly relates the dose D^{total} to the increase in temperature Δ T. The code takes as input the beam parameters (energy, number of protons and cone half-angle divergence θ), the distance between the proton source and the sample d, and the sample features (thickness z, area and material). The setup simulated in the Matlab code is depicted in Figure 5.38.

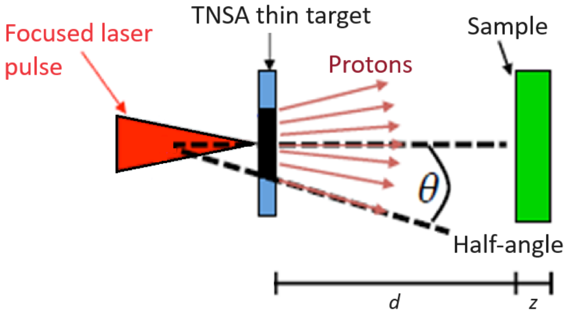

Figure 5.38. Geometry of the experimental setup inside the irradiation chamber simulated in the Matlab code. Adapted from [161].

To allow optimal evaluation of the deposited dose in the active region of the BJT, a decapped device was examined using a SEM available at INRS. Figure 5.39 shows a picture of the decapped BJT (Fig. 5.39a) and the BJT die (Fig. 5.39b) obtained with the SEM. Specifically, the SEM images were acquired using an accelerating voltage of 10 keV, a working distance of approximately 17.5 mm for both images, and a field of view of 4.18 mm for the picture in Figure 5.39, resulting in a magnification of 66x. For the image in Figure 5.39b, the field of view was 692 μm, resulting in a magnification of 400x. Afterward, the sample active region area (approximately 530 μm × 530 μm), thickness (approximately 200 μm) and material (silicon) were used in the Matlab®code to evaluate the dose deposited by protons. Regarding the proton spectrum, the one depicted in Figure 5.17 was used. Only the decreasing part of the Thomson spectrum was considered in the calculation because the rising part, does not represent a real signal but rather reflects the limitations of the Thomson method at low energies. Given these limitations, the spectrum was analyzed starting from approximately 0.7 MeV, where the data becomes more reliable and accurate. The Matlab®code provides a matrix dT corresponding to temperature increase as a function of the sample depth (dz) and radius (dr). The matrix obtained is presented in Figure 5.40. To examine the temperature increase within the active region of the sample, the region from 0-200 μm in depth and 0-265 μm in radial distance, which corresponds to the sample thickness z and radius R, should be considered. As illustrated in Figure 5.40, the energy deposition is primarily concentrated in the

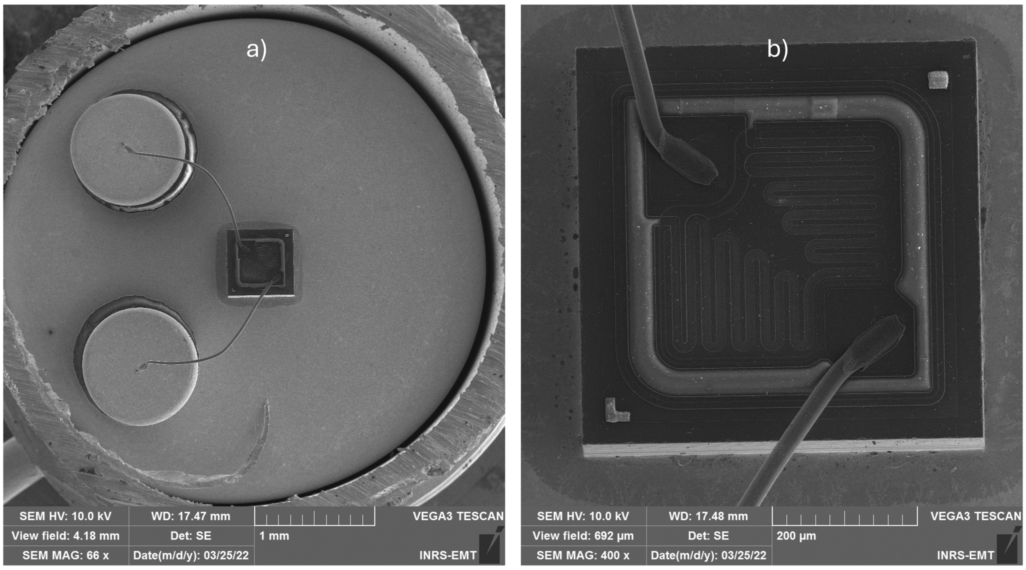

Figure 5.39. Picture of (a) decapped BJT (magnification 66x) and of (b) BJT die (magnification 400x).

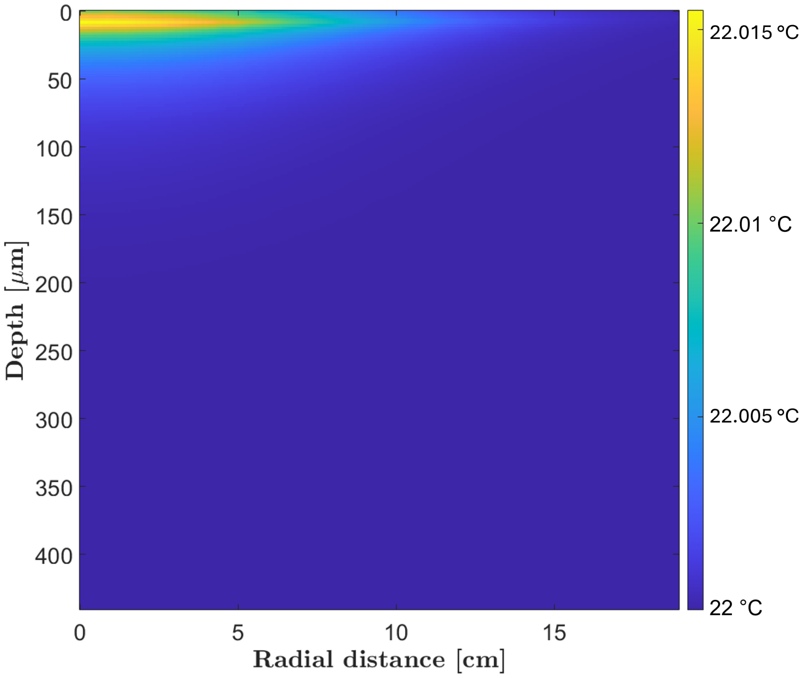

Figure 5.40. Temperature distribution inside the sample after laser-driven proton irradiation simulated with MATLAB®code [161]. The y-axis represents the sample depth and the x-axis represents its radius.

first 10-15 μm of the sample. Using this matrix of temperature increase values dT, dependent on the sample radius and thickness (dT(dr, dz)), the total absorbed dose due to protons was obtained according to the following formula:

$$\int_0^R dr 2\pi r \int_0^z dz dT(dr, dz) \frac{1}{V} c_p \tag{5.5}$$

where dr is the increment in the samples radius, dz is the increment in its thickness, c_p is its specific heat capacity and V is its volume, approximated as a cylinder. For each laser shot, a dose value $D_{shot}^{total} = 3.4$ Gy was obtained.

Regarding the dose deposited by NIEL processes after a single laser shot, it was obtained using the ASI calculator [162], as performed for electrons in the previous section. Specifically, the proton spectrum shown in Figure 5.17 was considered starting from 0.6 MeV. Since it is expressed in units of protons/MeV/sr and the ASI calculator requires a fluence in protons/MeV/cm^2, the solid angle corresponding to the sample was calculated, considering the sample radius and its distance from the TNSA target. The proton spectrum was then corrected by multiplying by the solid angle and similarly divided by the sample area (the sample cross-section was approximated as a circle).
The graphs generated by the ASI calculator for the NIEL dose calculation due to laser-driven protons are shown in Figure 5.41. For a single laser shot, the NIEL dose deposited in the sample is $D_{shot}^{NIEL} = 2.5 \cdot 10^{-3}$ Gy. Therefore, after a single laser shot, the dose deposited by ionization processes is approximately 3 orders of magnitude higher than that deposited by NIEL processes.

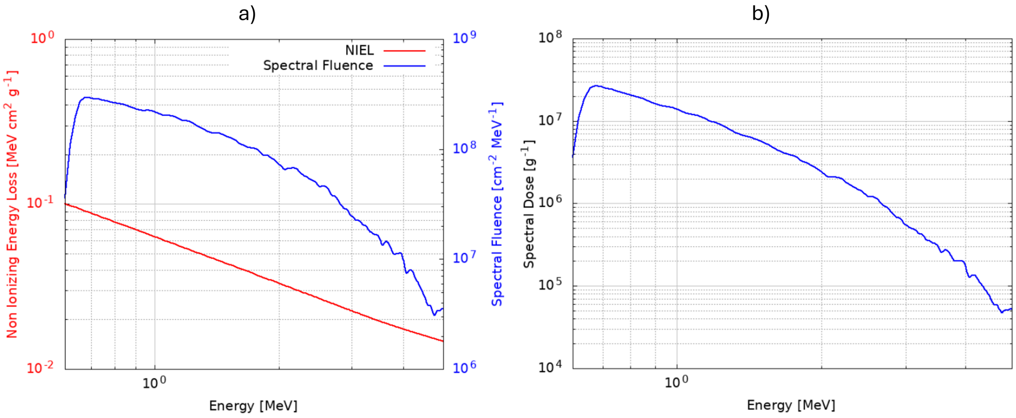

Figure 5.41. Laser-driven proton spectrum on the sample (protons/MeV/cm^2) and proton NIEL function (a) and convolution (b).

5.3.3 Conventional protons deposited dose

The 2.8 MeV protons used at the TOP-IMPLART facility are completely absorbed by the silicon depth of the transistor die. Therefore, the total deposited dose by a given fluence of 2.8 MeV protons was calculated according to the formula:

$$D^{total} = \frac{dE}{dx}|_{2.8MeV} \cdot \Phi_p \cdot 1.6 \cdot 10^{-10} \tag{5.6}$$

where $\frac{dE}{dx}|_{2.8MeV}$ is the stopping power of 2.8 MeV proton in silicon, Φ_p is the proton fluence and $1.6 \cdot 10^{-10}$ accounts for the conversion factor from MeV to Joule to obtain the dose value in Gray. For example, for the lowest used proton fluence ($\Phi_p = 3.38 \cdot 10^9$ p/cm^2), the total deposited dose in the sample is $D^{total} \simeq 48$ Gy.
The NIEL deposited dose was computed with the ASI calculator using the proton fluence, the proton energy and the sample material. For a proton fluence of 3.38 $\cdot\ 10^9$ p/cm^2, it is about $D^{NIEL} \simeq 1.33 \cdot 10^{-2}$ Gy. Hence, the dose deposited by ionization processes is approximately three orders of magnitude higher than that deposited by NIEL processes. This is consistent with the results obtained at the end of the laser-accelerated protons deposited dose section.

5.3.4 Neutrons deposited dose

The total dose deposited by 14 MeV neutrons was obtained by considering the quantity *Kinetic Energy Release in MAtter* (KERMA) K. It is defined as the mean sum of the initial kinetic energies dE_{tr} of all the charged particles released in a mass dm of a material by indirectly ionizing radiation incident on dm, divided by the sample mass [124]:

$$K = \frac{dE_{tr}}{dm}. \tag{5.7}$$

It is expressed in Gray and its value approaches that of the total absorbed dose under the conditions where charged-particle equilibrium exists, radiative losses are negligible, and the kinetic energy of uncharged particles greatly exceeds the binding energy of liberated charged particles [124]. The kerma per fluence is called *kerma coefficient* and is expressed as $k = \frac{K}{\Phi}$, in rad cm^2.
The kerma coefficient k for 14 MeV neutrons in silicon was obtained from the table reported in [163] and therefore, it was possible to obtain the K factors corresponding to different neutron fluences. For example, for a neutron fluence $\Phi_n = 2 \cdot 10^{12}$ n/cm^2 the kerma factor is $K \simeq 25$ Gy (i.e. $\mathrm{D}^{total} \simeq 25$ Gy).
The NIEL deposited dose was obtained with the ASI calculator, using the neutron fluence, neutron energy and sample material. For a neutron fluence of $2 \cdot 10^{12}$ n/cm^2, it is about $D^{NIEL} \simeq 1.2$ Gy. This means that for 14 MeV neutrons, the dose deposited by ionizing processes is one order of magnitude higher than that deposited by NIEL processes.

In summary, for the analyzed radiation sources, the energy deposited by ionization largely exceeds that deposited by displacement damage, except for neutrons.

5.4 Results comparison

This section aims to merge the results obtained in Section 5.2 and Section 5.3 to determine the dose values at which the current gains exit specification to compare different radiation sources.

The threshold levels at which the components functioning is compromised, are reported in Table 5.12 and Table 5.13 for NPN and PNP transistors, respectively, for all the analyzed collector current values. Specifically, the values of total absorbed dose for gamma radiation, the number of shots for laser-driven protons, and proton and neutron fluence for protons and neutrons from conventional accelerators, after which the gain values fall outside the ranges allowed by the datasheet, are presented. The symbol "/" in the tables indicates that the parameter of interest did not exit the allowed range up to the maximum analyzed deposited dose, number of shots or fluence. These thresholds are crucial for the reliability and longevity of electronic systems in radiation-intensive environments. Referring to Table 1.1 which summarizes radiation levels characterizing high-radiation environments, several observations can be made.

Table 5.12. Values of total absorbed dose, fluence and number of shots, for gamma radiation, conventional protons and neutrons and laser-driven protons, respectively, after which the gain values go out of specifications for NPN transistors.

	Gamma	**Conventional protons**	**Neutrons**	**Laser-driven protons**
β_1	8 kGy	$1.2 \cdot 10^{11}$ p/cm^2	$5.0 \cdot 10^{12}$ n/cm^2	4 shots ($\simeq 10^{11}$ p/cm^2)
β_2	7 kGy	$8.0 \cdot 10^{10}$ p/cm^2	$3.5 \cdot 10^{12}$ n/cm^2	3 shots ($\simeq 10^{11}$ p/cm^2)
β_3	3 kGy	$5.0 \cdot 10^{10}$ p/cm^2	$2.5 \cdot 10^{12}$ n/cm^2	2 shots ($\simeq 10^{10}$ p/cm^2)
β_4	600 Gy	$4.0 \cdot 10^{10}$ p/cm^2	$2.0 \cdot 10^{12}$ n/cm^2	2 shots ($\simeq 10^{10}$ p/cm^2)
β_5	100 kGy	$1.8 \cdot 10^{11}$ p/cm^2	/	/

Table 5.13. Values of total absorbed dose and fluence for gamma radiation, conventional protons and neutrons, respectively, after which the gain values go out of specifications for PNP transistors.

	Gamma	**Conventional protons**	**Neutrons**
β_1	15 kGy	$2.1 \cdot 10^{11}$ p/cm^2	$7.0 \cdot 10^{12}$ n/cm^2
β_2	20 kGy	$2.5 \cdot 10^{11}$ p/cm^2	$8.0 \cdot 10^{12}$ n/cm^2
β_3	35 kGy	/	$1.5 \cdot 10^{13}$ n/cm^2
β_4	20 kGy	/	/
β_5	70 kGy	/	/

To evaluate the radiation resistance properties of devices to total ionizing dose levels, the gamma radiation results from Table 5.12 and Table 5.13 are considered. At High Luminosity-LHC, TID levels of approximately 1 Gy/year are expected in the arcs. Over 10 years of HL-LHC operation, electronics in those positions must withstand approximately 10 Gy. The functionality of the irradiated components was not compromised after exposure to these TID radiation levels. Near the interaction point, TID levels of 10 kGy/year are expected, indicating that the analyzed COTS components are not suitable for application in those locations.

To evaluate radiation resistance concerning HL-LHC 1 MeV neutron equivalent fluence, the proton and neutron fluences from Table 5.12 and Table 5.13 were converted into 1 MeV neutron equivalent fluence using Equation 2.9 (described in Chapter 1):

$$\Phi_{1MeVn_{eq}} = k_{particle}\Phi_{particle} \tag{5.8}$$

Specifically, the hardness factor k$_{2.8MeVprotons}$ for 2.8 MeV protons (conventional protons used at TOP-IMPLART) is equal to [62]:

$$k_{2.8MeVprotons} = 11.73 \tag{5.9}$$

and the hardness factor k$_{14MeVneutrons}$ for 14 MeV neutrons (neutrons used at FNG) [62]:

$$k_{14MeVneutrons} = 1.8. \tag{5.10}$$

The resulting 1 MeV neutron equivalent fluence values corresponding to conventional proton ($\Phi^{conventionalprotons}_{1MeVn_{eq}}$) and neutron ($\Phi^{neutrons}_{1MeVn_{eq}}$) fluences after which transistor gain values exceed specifications for NPN and PNP transistors are presented in Table 5.14 and Table 5.15, respectively.

Table 5.14. Values of 1 MeV neutron equivalent fluence (in n$_{eq}$/cm^2) corresponding to conventional proton and neutron fluence from Table 5.12, respectively, after which gain values exit specifications for NPN transistors.

	$\boldsymbol{\Phi^{conventionalprotons}_{1MeVn_{eq}}}$	$\boldsymbol{\Phi^{neutrons}_{1MeVn_{eq}}}$
$\boldsymbol{\beta_1}$	$1.4 \cdot 10^{12}$ n$_{eq}$/cm^2	$9.0 \cdot 10^{12}$ n$_{eq}$/cm^2
$\boldsymbol{\beta_2}$	$9.3 \cdot 11^{11}$ n$_{eq}$/cm^2	$6.3 \cdot 10^{12}$ n$_{eq}$/cm^2
$\boldsymbol{\beta_3}$	$5.9 \cdot 10^{11}$ n$_{eq}$/cm^2	$4.5 \cdot 10^{12}$ n$_{eq}$/cm^2
$\boldsymbol{\beta_4}$	$4.7 \cdot 10^{11}$ n$_{eq}$/cm^2	$3.6 \cdot 10^{12}$ n$_{eq}$/cm^2
$\boldsymbol{\beta_5}$	$2.1 \cdot 10^{12}$ n$_{eq}$/cm^2	/

Table 5.15. Values of 1 MeV neutron equivalent fluence (in n$_{eq}$/cm^2) corresponding to conventional proton and neutron fluence from Table 5.13, respectively, after which gain values exit specifications for PNP transistors.

	$\boldsymbol{\Phi^{conventionalprotons}_{1MeVn_{eq}}}$	$\boldsymbol{\Phi^{neutrons}_{1MeVn_{eq}}}$
$\boldsymbol{\beta_1}$	$2.5 \cdot 10^{12}$ n$_{eq}$/cm^2	$1.3 \cdot 10^{13}$ n$_{eq}$/cm^2
$\boldsymbol{\beta_2}$	$2.9 \cdot 10^{12}$ n$_{eq}$/cm^2	$1.4 \cdot 10^{13}$ n$_{eq}$/cm^2
$\boldsymbol{\beta_3}$	/	$2.7 \cdot 10^{13}$ n$_{eq}$/cm^2
$\boldsymbol{\beta_4}$	/	/
$\boldsymbol{\beta_5}$	/	/

As described in Chapter 1, 1 MeV neutron equivalent fluence is used at LHC to quantify the amount of displacement damage induced in silicon. From Table 5.14 and Table 5.15, it is evident that transistor gain values were compromised after exposure to 1 MeV n_{eq} fluence of approximately 10^{12}-10^{13} n_{eq}/cm^2. Therefore, these components are suitable for use in LHC positions with low levels of 1 MeV n_{eq} fluence but not in the most critical areas concerning radiation levels.

As outlined in Chapter 1, in challenging interplanetary space missions such as JUICE, the expected TID value over the mission lifetime, primarily due to trapped electrons, is above 10 kGy for a typical aluminum shielding thickness of 1.5 mm [9]. Therefore, the analyzed COTS components are not suitable for these applications. However, they can be employed in low orbit missions aboard the ISS, where the expected TID dose is around 0.01-3 Gy/year, as specified in Chapter 1.

Within the DTT environment, electronics must withstand the expected absorbed dose levels in silicon as outlined in [25]. Specifically, for the building outside the DTT cryostat, absorbed doses ranging from 0.5 to 2.5 kGy were estimated. Therefore, considering the gamma total absorbed dose threshold levels reported in Table 5.12 and Table 5.13, the analyzed COTS BJTs appear to be suitable for application in the DTT radiation environment.

The methodology presented in Section 5.3 for evaluating the deposited dose from various radiation sources is crucial for assessing the dose delivery efficiency of novel sources, such as laser-accelerated protons, and for comparing the effects induced by different radiation sources used in this research on the investigated samples.

Firstly, all the values reported in Table 5.12 and Table 5.13 were transformed into a total absorbed dose value (D^{total}). The contributions D^{NIEL} to the total dose were then calculated, according to the methods described in Section 5.3 for the different radiation sources. Moreover, the dose deposited by ionizing processes was obtained by subtracting the NIEL dose from the total deposited dose.

The corresponding results are shown in Table 5.16 and Table 5.17 for NPN and PNP transistors, respectively. Specifically, as not all the gain values exit specifications up to the investigated irradiation conditions, β_1, β_2, β_3 and β_4 will be considered for NPN transistors and β_1 and β_2 for PNP transistors.

For NPN transistors, gamma radiation resulted in the highest required value of total absorbed dose (up to 8 kGy) to cause the gain value to exit technical datasheet specification, while laser-driven protons required significantly lower doses (up to 13.6 Gy) to achieve similar effects. Conventional protons and neutrons also showed considerable differences in their dose requirements, with neutrons depositing total absorbed dose values approximately two orders of magnitude lower than conventional protons for similar outcomes.

For PNP transistors, gamma radiation again showed high required total absorbed doses. Notably, conventional protons require a deposited dose two orders of magnitude higher than neutrons to cause the current gain values to go out of allowed ranges.

This effect is due to the different kinds of damage that ionizing and non-ionizing dose induce in the components. Although the NIEL dose values are much lower than the values of the dose deposited by ionization processes, the effect of the NIEL dose is not negligible. As expected from the literature [59, 57], the NIEL contribution

Table 5.16. Values of dose deposited (D^{total}, D^{TID}, and D^{NIEL}) after irradiation with gamma radiation, conventional protons and neutrons, and laser-driven protons, after which the gain values go out of specifications for NPN transistors. The values error is ± 5% and accounts for uncertainties in dose estimation and the extrapolation of dose values.

		Gamma	**Conventional protons**	**Neutrons**	**Laser-driven protons**
β_1	D^{total}	8 kGy	2.05 kGy	62.5 Gy	13.6 Gy
	D^{TID}	8 kGy	2.05 kGy	59.5 Gy	13.5 Gy
	D^{NIEL}	0.06 Gy	0.46 Gy	3.0 Gy	0.01 Gy
β_2	D^{total}	7 kGy	1.37 kGy	43.8 Gy	10.2 Gy
	D^{TID}	7 kGy	1.37 kGy	41.7 Gy	10.2 Gy
	D^{NIEL}	0.06 Gy	0.31 Gy	2.1 Gy	0.01 Gy
β_3	D^{total}	3 kGy	856 Gy	31.3 Gy	6.8 Gy
	D^{TID}	3 kGy	856 Gy	29.8 Gy	6.8 Gy
	D^{NIEL}	0.02 Gy	0.24 Gy	1.5 Gy	$5.0 \cdot 10^{-3}$ Gy
β_4	D^{total}	600 Gy	685 Gy	25 Gy	6.8 Gy
	D^{TID}	600 Gy	685 Gy	23.8 Gy	6.8 Gy
	D^{NIEL}	$5.0 \cdot 10^{-3}$ Gy	0.14 Gy	1.2 Gy	$5.0 \cdot 10^{-3}$ Gy

Table 5.17. Values of dose deposited (D^{total}, D^{TID}, and D^{NIEL}) after irradiation with gamma radiation, conventional protons and neutrons, after which the gain values go out of specifications for PNP transistors. The values error is ± 5% and accounts for uncertainties in dose estimation and the extrapolation of dose values.

		Gamma	**Conventional protons**	**Neutrons**
β_1	D^{total}	15 kGy	3.02 kGy	87.5 Gy
	D^{TID}	15 kGy	3.02 kGy	83.2 Gy
	D^{NIEL}	$1.2 \cdot 10^{-1}$ Gy	0.83 Gy	4.25 Gy
β_2	D^{total}	20 kGy	3.6 kGy	100 Gy
	D^{TID}	20 kGy	3.6 kGy	95.1 Gy
	D^{NIEL}	$1.6 \cdot 10^{-1}$ Gy	0.95 Gy	4.85 Gy

to the total absorbed dose due to neutron irradiation is the largest in percentage compared to the other employed radiation sources (one order of magnitude between NIEL and TID while four orders of magnitude occur for protons and six for gamma radiation). Consequently, lower total absorbed doses of neutrons are required to cause the same effects on the devices. Conversely, higher total absorbed dose values of gamma radiation are required since the NIEL dose contribution is approximately five orders of magnitude lower than the ionizing one, confirming that high gamma radiation levels are required to cause bulk damage [58].
Very interesting results were obtained. Experimental evidence suggests that laser-accelerated protons are suitable for stress testing [71], but more data are required to assess their suitability for electronics irradiation. Looking at the results obtained after irradiation of NPN bipolar transistors with laser-driven protons and protons from conventional accelerators, some considerations can be outlined. To obtain the same damage in terms of current gain degradation, a difference of two orders of magnitude in total absorbed dose is required. Laser-driven protons appear to be much more efficient regarding dose delivery. The proton sources used in the study shared similar energy ranges (approximately 0.7 MeV to 5 MeV for laser-driven protons and 2.8 MeV with a 0.2 MeV energy spread for TOP-IMPLART protons). Considering the threshold values for β_1, approximately 10^{11} protons were required to induce comparable damage in the BJT active region, with approximately $0.8 \cdot 10^{11}$ protons delivered over four laser shots using the ALLS proton spectrum. A significant distinction lies in the total irradiation time and pulse length between laser-driven and conventional proton bunches. As detailed in Chapter 3, the TOP-IMPLART proton beam has a pulse length of about 15 μs, delivering approximately 10^7 protons per pulse to the sample active region. Thus, it required approximately 10^4 pulses over 400 seconds (with a pulse repetition frequency of 25 Hz) to deliver 10^{11} protons from the TOP-IMPLART source. In contrast, the pulse length of the laser-driven protons, considering the samples were positioned at 23.5 cm from the TNSA target and that the protons velocity depends on their energy, ranging from approximately 0.7 MeV to 5 MeV in this case, was found to be approximately 13 ns. This means that approximately $0.2 \cdot 10^{11}$ protons are delivered within tens of nanoseconds during laser-driven proton irradiation. To perform four shots, given a repetition frequency of 0.6 Hz, approximately 6 seconds were required. Therefore, compared to conventional proton sources, laser-driven protons require two order of magnitude less time to deliver the same amount of protons. According to the literature [71], laser-driven protons can cause intense mechanical and thermal damage within a very short timeframe, preventing material recovery and potentially leading to device malfunction due to silicon degradation. The study did not consider the contribution of carbon ions accelerated during the TNSA mechanism, as explained in Section 5.3, as their effect on temperature increase was found to be negligible [71]. Future research should explore their contribution to confirm the higher dose delivery efficiency of laser-driven protons compared to conventional sources, attributed to the high induced stress in a short irradiation time.

The results emphasize laser-driven protons as effective and promising tools for electronics testing, although further research is needed to confirm their suitability compared to conventional sources. The efficiency of laser-driven protons in delivering damage, requiring significantly less time and inducing higher impact levels within nanoseconds, underscores their potential in advanced radiation testing protocols. This efficiency could revolutionize applications requiring precise and efficient dose delivery, positioning laser-driven protons as strong candidates for future electronic device testing and enhancement.

5.5 Optoisolators characterization

The optoisolator is composed of components that rely on carefully grown, well-defined microscopic structures with very low tolerance for slight changes in their characteristics. Such changes can significantly affect component parameters, depending on the type of incoming radiation and the location of energy deposition within the optocoupler. The functioning of the LED in the optoisolator is primarily affected by the DD dose, while TID and SEE are the most important effects for the photodetector and the coupling medium [55].

The radiation resistance properties of three OLS249 optoisolators from the same batch were investigated by testing many parameters before and after each irradiation and annealing step. Among these parameters, the trend of the collector-to-emitter saturation voltage $V_{CE(sat)}$ was specifically chosen to assess the radiation effects on this type of device. V_{CE} represents the collector-to-emitter voltage relative to a fixed output current I_C of the phototransistor when a forward current I_F flows through the LED (as described in Section 2.1.4). $V_{CE(sat)}$ specifically denotes the voltage drop across the transistor when it is fully saturated, meaning the collector current I_C reaches its maximum and is independent of the base current I_B. This parameter is crucial as it indicates the transistor effectiveness in saturation mode, essential for rapid switching between saturation and cutoff states in optoisolators. Any deviation in $V_{CE(sat)}$ can potentially affect the device switching speed and overall efficiency. An increased $V_{CE(sat)}$ often signifies degraded transistor performance, leading to slower response times or increased power dissipation within the circuit.

In this study, following the test conditions outlined in the OLS249 technical datasheet [144], $V_{CE(sat)}$ was evaluated under specific operating conditions: with a fixed forward current I_F of 2 mA and output current I_C also set at 2 mA. Under these conditions, the maximum allowable value for $V_{CE(sat)}$ is specified as 0.3 V.

Furthermore, the reverse current I_R was measured. This is defined as the current that flows when a reverse voltage V_R is applied to the LED side. It is a leakage current since there should not be any current passing through the LED when it is reverse biased. However, increasing the reverse voltage or, for example, rising ambient temperature can cause this current to increase, and values of $I_R < 100\ \mu$A are acceptable. For these tests, I_R was measured for $V_R = 2$ V.

The forward voltage V_F, defined as the voltage across the LED when a forward current I_F flows, was also measured for $I_F = 10$ mA. In this condition, V_F cannot exceed 1.8 V [144]. The product of this value and the forward current value expresses the internal loss of the light-emitting side [164].

Since optocouplers are renowned for their high reliability in isolation, the collector-to-emitter off-state leakage current I_{CEO} of the phototransistor collector, when no forward current flows through the LED (no light emission from the LED), is another

important parameter to be evaluated. After each irradiation step, it was evaluated for $V_{CE} = 20$ V and its maximum allowed value in this case is 100 nA.
The output current I_C, corresponding to the collector current of the phototransistor, was also evaluated for $V_{CE} = 5$ V and $I_F = 1$ mA.

The radiation tolerant optoisolators have been irradiated only with gamma radiation so far. Since they are more expensive than the analyzed COTS components, the plan is to irradiate them with other radiation sources, particularly with laser-driven protons, once the irradiation parameters are optimized. Due to time constraints, only the results obtained after gamma irradiation will be presented for this component. However, preliminary analyses for laser-driven proton irradiation have been performed on these samples. One optoisolator was decapped, and the silicon die was analyzed with a SEM (Figure 5.42). Afterwards, a simulation of the dose deposition from protons due to a single laser shot was performed using the previously described Matlab®code. The dose deposited in the phototransistor active region by laser-accelerated protons from a single shot is approximately 4.3 Gy.

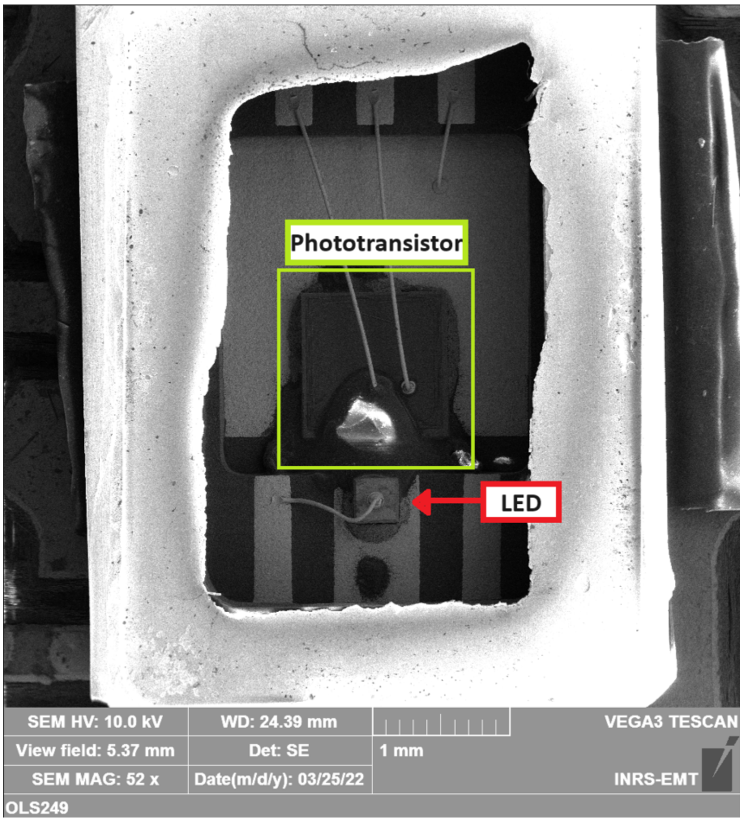

Figure 5.42. SEM picture of a decapped optocoupler (magnitude 52x). The phototransistor die and the LED are visible.

5.5.1 Gamma irradiation

Three OLS249 radiation tolerant optoisolators (Figure 5.2) from the same batch were irradiated with gamma radiation in different steps up to an absorbed dose of 300 Gy at a dose rate of 3.3 Gy/h. A summary of the absorbed dose after each step is reported in Table 5.18.

The irradiation tests were performed according to ESCC Basic Specification No. 22900 (Issue 5) [141]: the samples were irradiated at room temperature, and after each irradiation step, all the parameters described above were measured. After the final step of irradiation, the optoisolators were kept at room temperature for 24 hours, followed by another parametric test. Subsequently, they were placed in a furnace at 100°C for one week and characterized again. All the samples were biased during the irradiation and annealing tests, as shown in Figure 5.43. After irradiation,

Table 5.18. Steps of irradiation for the first set of samples irradiated with gamma radiation at a dose rate of 3.3 Gy/h.

Irradiation step	**Absorbed dose per step (Gy)**	**Total absorbed dose (Gy)**
1	56.7	56.7
2	74.3	131.0
3	19.1	150.1
4	68.6	218.7
5	74.6	293.3

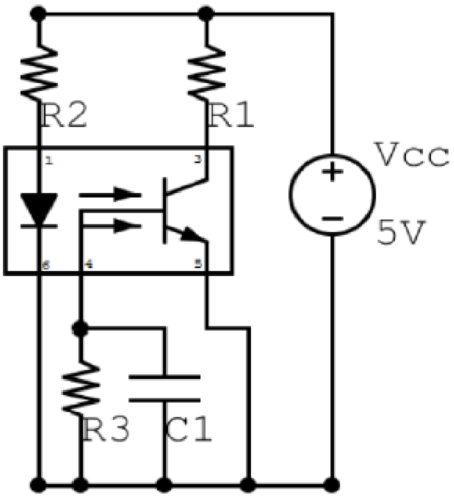

Figure 5.43. OLS249 bias condition during irradiation. R1 = 10 kΩ; R2 = 1.8 kΩ; R3 = 1 MΩ; C1 = 1 nF.

all the samples showed an increase in $V_{CE(sat)}$, indicating a degradation of this parameter, as reported in Figure 5.44. After each step of irradiation, the $V_{CE(sat)}$ value increases but it remains acceptable for all the irradiated samples ($V_{CE(sat)}$) < 0.3 V).

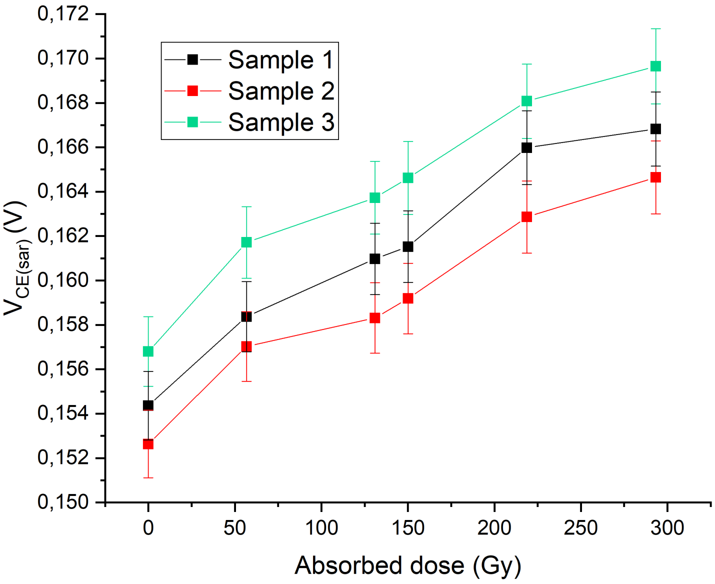

Figure 5.44. Trend of $V_{CE(sat)}$ as a function of the dose deposited by gamma radiation for all the irradiated samples. The error is due to the measurement uncertainty of $V_{CE(sat)}$ (±1%).

The trend of the other analyzed parameters after irradiation is shown in Figure 5.45 for each sample. A slight decrease in the output current I_C (Fig. 5.45d), and consequently in the CTR, is appreciable for each sample after irradiation. However, all the investigated parameters remained within the range allowed by the sample datasheet:

- $I_R < 100\ \mu A$
- $1.2\ V < V_F < 1.8\ V$
- $I_{CEO} < 100\ nA$
- $2\ mA < I_C < 12\ mA$

Generally, TID causes parametric degradation of optoisolator components due to charge trapping [55]. In the optical medium, ionizing radiation creates color centers (charge trapped by defects) that can degrade light transmission efficiency by absorbing signal photons. The efficiency of optical detectors can also be affected by semiconductor damage. The photodetector in an optoisolator detects photocurrent generated by photons with energy greater than the semiconductor bandgap, and any changes in semiconductor properties can degrade its performance. However, color centers can recover through annealing. Therefore, after irradiation, the samples were kept at room temperature for 24 hours and then in an oven at 100 °C for one

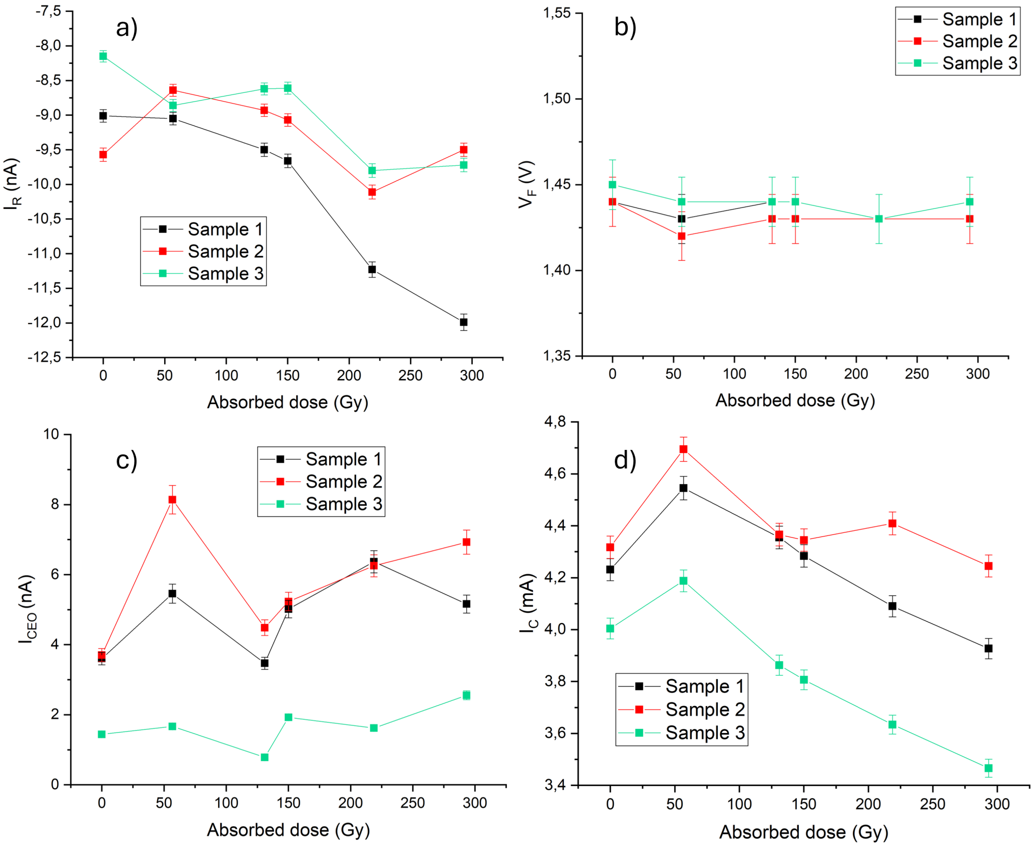

Figure 5.45. Trend of the reverse current I_R (a), forward voltage V_F (b), collector to emitter off-state leakage current I_{CEO} (c) and output current I_C (d) as a function of the absorbed dose.

week for annealing tests. As shown in Figure 5.46, all samples recovered their initial values of $V_{CE(sat)}$ and I_C after the second annealing treatment.

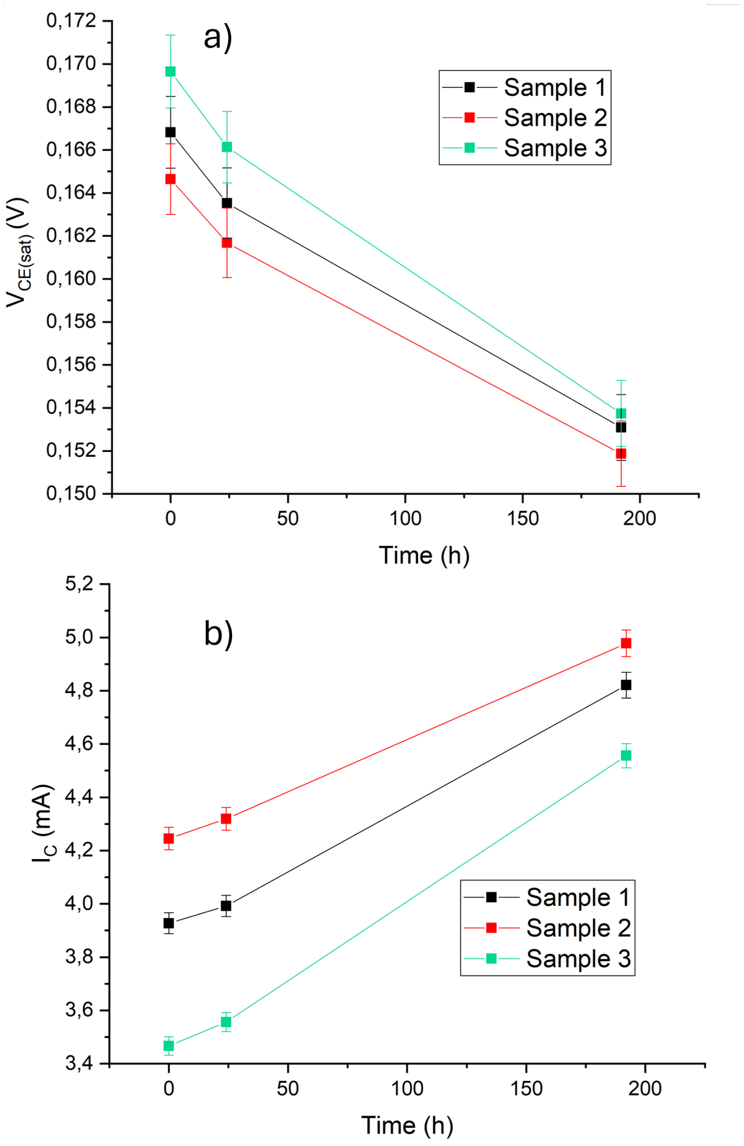

Figure 5.46. Behavior of $V_{CE(sat)}$ and I_C as a function of the annealing time. The samples were kept for 24 hours at room temperature and for 168 hours at 100 °C.

In summary, a degradation in $V_{CE(sat)}$ was observed for all the analyzed samples after each irradiation step; however, all values remained within acceptable limits. Other parameters, such as reverse current (I_R), forward voltage (V_F), and collector to emitter off-state leakage current (I_{CEO}), also showed changes but stayed within datasheet specifications. Post-annealing recovery was successful in restoring initial $V_{CE(sat)}$ values. This underscores the importance of annealing in reversing total ionizing dose radiation-induced damage in optoisolators, within the range of the analyzed absorbed dose.

Conclusion and perspectives

The main purpose of this thesis was to investigate the radiation resistance properties of two types of electronic components, with particular emphasis on evaluating the efficiency of dose delivery of an innovative stress-test source, specifically laser-driven protons, compared to more conventional radiation sources. Electronic devices play pivotal roles in numerous applications, but their operational reliability can be severely affected by the challenging radiation environments encountered in fields such as high-luminosity particle physics accelerators, space missions and fusion facilities. Understanding the effects of ionizing radiation is therefore essential to ensure the long-term functionality of these devices.

To achieve these goals, this study extensively explored various radiation sources impacting electronic devices, focusing on the interactions between incoming particles and the semiconductor materials of these devices, which lead to atomic displacements and energy losses through ionization processes. Specifically, this research aimed to clarify how defects induced by Total Ionizing Dose (TID) and Displacement Damage Dose (DDD) influence the electrical behavior of semiconductor devices through a series of post-irradiation investigations.

To simulate adverse radiation environments experienced during device operation, laboratory irradiation with various particle sources was conducted, investigating the effects of total ionizing dose and displacement damage after exposure. Recent advancements in laser-driven particle acceleration have opened new avenues for stress-testing materials and assessing device resilience, with laser-accelerated protons—generated by irradiating solid targets with ultra-intense ultra-short pulse lasers, providing a unique method for rapidly inducing damage and evaluating component durability.
This investigation specifically evaluated the radiation hardness of two types of electronic components: *Commercial Off-The-Shelf* (COTS) Bipolar Junction Transistors (BJTs), both NPN and PNP types, and *radiation tolerant* optoisolators. While radiation tolerant components are guaranteed by manufacturers for radiation performance and are relatively costly, COTS components are cost-effective and readily available, making them increasingly prevalent in space and high-energy physics environments, even if they require thorough testing before their employment.

The BJTs analyzed in this study were subjected to irradiation with gamma radiation at the Calliope facility, laser-driven protons at the ALLS facility, and protons and neutrons at the TOP-IMPLART and FNG facilities, respectively, while the optoisolators were exposed solely to gamma radiation. To further enrich this study and offer a comprehensive understanding of radiation damage induced by various sources, COTS BJTs will be irradiated with the REX 5 MeV electron beam under the irradiation conditions determined in Chapter 4, where the results obtained from the dosimetric intercalibration of the Calliope and REX facilities are presented. These results provided valuable insights into the radiation dose distribution within the REX irradiation chamber, which is crucial for optimizing the accuracy and consistency of radiation processing applications in electronics testing.

The second part of this study assessed the suitability of COTS components for use in various radiation environments. For instance, gamma radiation results were instrumental in assessing TID resistance within the HL-LHC environment. In positions where TID levels of approximately 1 Gy/year are expected in the arcs over 10 years of HL-LHC operation, the tested components demonstrated to be suitable. Conversely, near the interaction point where TID levels of 10 kGy/year are expected, the analyzed COTS components proved unsuitable. Similarly, interplanetary space missions such as JUICE, with expected TID values exceeding 10 kGy over mission lifetimes, also made the analyzed COTS components inadequate. However, they remain usable for low Earth orbit missions like those aboard the ISS, where expected doses range from 0.01 to 3 Gy/year. Within the Divertor Tokamak Test (DTT) facility, where electronics must withstand absorbed dose levels in silicon ranging from 0.5 to 2.5 kGy, the analyzed COTS BJTs proved again to be suitable.
Additionally, post-irradiation annealing tests were performed, to evaluate thermal recovery of the induced defects. These tests were found to be successful as regards recovery for BJTs irradiated at absorbed doses below approximately 2.3 kGy, whereas components heavily damaged by gamma radiation (above approximately 25 kGy), neutrons, and protons showed negligible recovery. This underscores that not all radiation-induced damages can be mitigated through annealing, particularly for high-dose scenarios.

Following this, the research aimed to investigate the dose delivery efficiency of novel sources, such as laser-accelerated protons. Consequently, the damage induced by different radiation sources was compared. Critical dose thresholds, at which the performance of NPN and PNP transistors deviated from specifications due to radiation exposure, were examined across all analyzed sources. For NPN transistors, gamma radiation required the highest total absorbed doses (up to 8 kGy) to induce gain deviations, while laser-driven protons achieved similar effects at significantly lower doses (up to approximately 14 Gy). Similarly, conventional protons and neutrons demonstrated notable differences in dose requirements, with neutrons requiring doses (up to approximately 62 Gy) approximately two orders of magnitude lower than conventional protons (up to approximately 2 kGy) for comparable outcomes. PNP transistors also showed high dose requirements with gamma radiation and varied efficiencies between conventional protons and neutrons, with conventional protons necessitating doses two orders of magnitude higher than neutrons to affect current gain values.
These variations arise from the distinct mechanisms of damage induced by ionizing and non-ionizing radiation doses. Although NIEL doses for neutrons are lower than

TID, they contribute the highest percentage of NIEL to the total absorbed dose compared to other radiation sources and cause significant damage. This indicates that even a relatively small amount of NIEL from neutrons can have a considerable impact. Notably, neutrons require a lower total dose to induce damage comparable to that caused by other radiation sources, underscoring their efficiency. This pronounced effect is likely due to the interaction of neutrons with matter. Neutrons, being heavy and uncharged, penetrate materials deeply with minimal deflection or scattering, leading to a higher probability of displacing atoms. They primarily cause damage through elastic scattering with atomic nuclei, transferring a significant portion of their kinetic energy to target nuclei in a single collision. This efficient energy transfer amplifies their damage potential, even though their NIEL values are lower. Conversely, gamma radiation necessitates higher total absorbed doses due to its lower NIEL contribution relative to ionizing doses, highlighting the need for elevated radiation levels to induce bulk damage.

Of particular interest were the outcomes following laser-driven proton irradiation, which suggested their potential for stress testing. Comparative analysis of NPN bipolar transistors irradiated with laser-driven protons versus conventional accelerator protons revealed a significant difference: laser-driven protons achieved equivalent damage to current gain degradation with doses two orders of magnitude lower. This efficiency can be attributed to their rapid delivery of protons within a short timeframe. Laser-driven protons, with energies ranging from approximately 0.7 MeV to 5 MeV and a pulse length of approximately 13 ns at a sample distance of 23.5 cm from the TNSA target, demonstrated an efficient dose delivery mechanism. Approximately $0.2 \cdot 10^{11}$ protons were delivered within tens of nanoseconds per irradiation, requiring only 6 seconds for four shots at a 0.6 Hz repetition rate. In contrast, conventional protons required significantly longer irradiation times due to their pulse length of about 15 μs and lower repetition frequencies, highlighting the efficiency gains of laser-driven proton irradiation. This efficiency advantage of laser-accelerated proton irradiation is likely due to the shorter irradiation times, which do not permit material recovery between exposures. Further studies are required to fully assess the potential of laser-driven protons, particularly to determine whether the damage scales linearly with dose compared to other sources—that is, whether comparable damage can consistently be achieved with doses that are orders of magnitude lower. Therefore, additional tests are needed to verify this method for stress testing and to explore its feasibility for use in qualification applications.

In conclusion, this comparative study emphasizes the potential of laser-driven protons as efficient radiation sources for applications requiring precise and effective dose delivery. The findings highlight the interplay between ionizing and non-ionizing processes in radiation damage mechanisms within transistors, offering valuable insights for future developments in radiation testing methodologies utilizing novel sources such as laser-accelerated protons.

At last, the results from the investigation of radiation tolerant optoisolators demonstrated that the parameters characterizing these devices remained well within the ranges specified by the samples technical datasheets after irradiation, confirming their radiation resistance up to the exploited dose range. The successful post-annealing recovery observed in optoisolators further highlights the potential of mitigation strategies in reversing radiation-induced degradation.

Future steps of this work involve irradiating other types of electronic components, including radiation tolerant optoisolators, with the aforementioned radiation sources to advance the investigation of radiation resistance properties of electronics and validate stress testing with innovative radiation sources.

Based on all these results, this research project significantly contributes to clarifying the role of ionizing radiation on materials used in applications ranging from electronics to space. Furthermore, the research aligns with the interests of several scientific areas, including materials science, physics, and engineering, and provides new insights into the topic of COTS components. Therefore, this study will not only benefit academics working across a wide range of interrelated disciplines but also be of great interest to specialists in the high-tech industry. Moreover, this thesis underscores the transformative potential of laser-driven proton sources in revolutionizing radiation testing, paving the way for more robust electronic components that can withstand the rigors of extreme environments, ensuring the reliability and longevity of future technological advancements in space, particle physics, and beyond.

Bibliography

[1] G. Lerner, R. Garcìa Alìa, and K. Bilko *et al.* Radiation level specifications for HL-LHC. *CERN-ACC-NOTE-2019-xxx*, 2019.

[2] R. Garcìa Alìa, M. Brugger, and F. Cerutti *et al.* LHC and HL-LHC: Present and future radiation environment in the high-luminosity collision points and RHA implications. *IEEE Transactions on Nuclear Science*, PP(99), 2017.

[3] A. Tsinganis and F. Cerutti. Impact of Collision Debris in the HL-LHC ATLAS and CMS Insertions. *Proceedings of IPAC2017 - TUPVA021*, 2017.

[4] Y. Aguiar, A. Apollonio, F. Cerutti, S. Danzeca, R. García Alía, G. Lerner, D. Prelipcean, and M. Sabaté-Gilarte. Radiation to electronics impact on CERN LHC operation: Run 2 overview and HL-LHC outlook. *12th International Particle Accelerator Conference*, pages 80–83, 2021.

[5] G. Apollinari, I. Béjar Alonso, O. Brüning, M. Lamont, and L. Rossi. *High-Luminosity Large Hadron Collider (HL-LHC): Preliminary Design Report.* CERN Yellow Reports: Monographs. CERN, Geneva, 2015.

[6] R. Baumann and K. Kruckmeyer. *Radiation Handbook for Electronics.* Texas Instruments, 2019.

[7] M. Imaizumi, Y. Okuno, T. Takamoto, S. Sato, and T. Ohshima. Displacement damage dose analysis of the output characteristics of $\mathrm{in}_{0.5}\mathrm{ga}_{0.5}\mathrm{p}$ and $\mathrm{cu(in,ga)(s,se)}_2$ solar cells irradiated with alpha ray simulated helium ions. *Japanese Journal of Applied Physics*, 61(4):044002, 2022.

[8] G. Ginet, D. Madden, and B.K. Dichter. Energetic proton maps for the south atlantic anomaly. *Proceedings of IEEE Radiation Effects Data Workshop*, pages 1 – 8, 2007.

[9] O. Gutiérrez, M. Prieto, A. Perales-Eceiza, A. Ravanbakhsh, M. Basile, and D. Guzmán. Toward the use of electronic commercial off-the-shelf devices in space: Assessment of the true radiation environment in Low Earth Orbit (LEO). *Electronics*, 12(19), 2023.

[10] ESA. *Juice factsheet.* `https://www.esa.int/Science_Exploration/Space_Science/Juice/Juice_factsheet`.

[11] ESA. *Solar Orbiter overview.* `https://www.esa.int/Science_Exploration/Space_Science/Solar_Orbiter_overview`.

[12] Energy Encyclopedia. *Nuclear fusion - Tokamaks - Main principles.* `https://www.energyencyclopedia.com/en/nuclear-fusion/tokamaks/main-principles`.

[13] Consorzi RFX. *La fisica del Tokamak – la centrale a fusione.* `https://www.igi.cnr.it/ricerca/magnetic-confinement-research-in-padova/la-fisica-del-tokamak-la-centrale-a-fusione/`.

[14] Fusion for Energy. *What is fusion.* `https://fusionforenergy.europa.eu/what-is-fusion/`.

[15] S. Atzeni and J. Meyer ter Vehn. *Physics of Inertial Fusion: Beam Plasma Interaction, Hydrodynamics, Hot Dense Matter.* Cambridge University Press, 2005.

[16] R. Betti and O. Hurricane. Inertial-confinement fusion with lasers. *Nature Physics*, 12:435–448, 2016.

[17] D. Batani. *Inertial Confinement Fusion: recent results and perspectives.* `https://static.sif.it/SIF/resources/public/files/energy2023/Batani.pdf`.

[18] W. Hogan, E. Moses, B. Warner, M. Sorem, and J. Soures. The National Ignition Facility. *IAEA-CSP-8/C*, 2001.

[19] Commissariat à l'Énergie Atomique et aux Énergies Alternatives. *Laser Mégajoule.* `https://www-lmj.cea.fr/`.

[20] M. Mitchell Waldrop. *Can the dream of fusion power be realized?* `https://www.canarymedia.com/articles/nuclear/can-the-dream-of-fusion-power-be-realized`.

[21] Lawrence Livermore National Laboratory. National ignition facility. *FY 2022 Annual Report*, 2022.

[22] Q. Li, L. Hu, H. Cao, J. Zhao, Z.M. Hu, K. Chen, J. Zhang, L. Niu, H. Yu, W. Chen, and Y. Zhang. Radiation-hard performance research of front-end electronics for fusion diagnostic by gamma irradiation experiment. *Fusion Engineering and Design*, 199:114160, 2024.

[23] ENEA. *DTT: Divertor Tokamak Test facility - Project Proposal.* ENEA, 2015.

[24] G. Mazzitelli, R. Albanese, F. Crisanti, P. Martin, A. Pizzuto, A.A. Tuccillo, R. Ambrosino, A. Appi, G. Di Gironimo, A. Di Zenobio, A. Frattolillo, G. Granucci, P. Innocente, A. Lampasi, R. Martone, G.M. Polli, G. Ramogida, P. Rossi, S. Sandri, M. Valisa, R. Villari, and V. Vitale. Role of italian DTT in the power exhaust implementation strategy. *Fusion Engineering and Design*, 146:932–936, 2019.

[25] R. Villari, M. Angelone, B. Caiffi, A. Colangeli, F. Crisanti, D. Flammini, N. Fonnesu, R. Luis, G. Mariano, D. Marocco, F. Moro, G.M. Polli, and

S. Sandri. Nuclear design of Divertor Tokamak Test (DTT) facility. *Fusion Engineering and Design*, 155:111551, 2020.

[26] ENEA. *DTT: Divertor Tokamak Test facility- Interim Design Report.* ENEA, 2019.

[27] G. Di Gironimo, D. Marzullo, R. Mozzillo, A. Tarallo, and F. Villone. The DTT device: First wall, vessel and cryostat structures. *Fusion Engineering and Design*, 122:333–340, 2017.

[28] S. Sandri, G.M. Contessa, M. D'arienzo, M. Guardati, M. Guarracino, C. Poggi, and R. Villari. A review of radioactive wastes production and potential environmental releases at experimental nuclear fusion facilities. *Environments*, 7:6, 2020.

[29] E.R. Benton and E.V. Benton. Space radiation dosimetry in low-earth orbit and beyond. *Nuclear Instruments and Methods in Physics Research Section B: Beam Interactions with Materials and Atoms*, 184(1):255–294, 2001.

[30] A. Colangeli, M. Angelone, D. Flammini, N. Fonnesu, L. Gabellieri, G. Mariano, F. Moro, F. Panza, M. Valisa, R. Villari, and P. Zito. Neutronic and shielding analyses for the DTT electronics. *IEEE Transactions on Plasma Science*, 50(11):4545–4550, 2022.

[31] W. Wu, H.J. Zhou, Q.H. Zhou, Z.G. Zhao, G.R. Li, and Q. Liu. Combined effects of total ionizing dose and electromagnetic pulse on a bipolar junction transistor. *Journal of Instrumentation*, 18:P04037, 2023.

[32] X. Xiaowen, C. Changchun, R. Xingrong, Y. Yang, Z. Bing, and H. Xiao. EMP injection damage effects of a bipolar transistor and its relationship between the injecting voltage and energy. *Journal of Semiconductors*, 31:044005, 2010.

[33] F.P. Chee, H. Amir, S. Salleh, and M. Azali. Effects of total ionizing dose on bipolar junction transistor. *American Journal of Applied Sciences*, 7, 2010.

[34] J. S. George. An overview of radiation effects in electronics. *Proceedings of AIP Conference 2160, 060002*, 2019.

[35] A. Ray. Radiation effects and hardening of electronic components and systems: an overview. *Indian Journal of Physics*, 97(10):3011–3031, 2023.

[36] P. Casolaro, L. Campajola, and F. Di Capua. The physics of radiochromic process: one calibration equation for all film types. *Journal of Instrumentation*, 14(08):P08006, 2019.

[37] F. Faccio. *Radiation effects in the electronics for CMS.* `http://cern.ch/lhcb-elec/papers/radiation_tutorial.pdf`.

[38] P. Matthews. *The Great Debate: Should COTS Components Be Used in Space?* `https://www.microwavejournal.com/articles/38974-the-great-debate-should-cots-components-be-used-in-space`.

[39] K. A. LaBel. Commercial Off The Shelf (COTS): Radiation Effects Considerations and Approaches. *Proceedings of NEPP Electronic Technology Workshop*, 2012.

[40] Vorago Technologies. *Guide to Rad-hard vs. Rad-tolerant.* `https://www.voragotech.com/blog/rad-hard-vs-radtolerant#:~:text=While$%$20radiation$%$2Dhardened$%$20parts$%$20are,fail$%$20during$%$20the$%$20planned$%$20mission`.

[41] F. Faccio. COTS for the LHC radiation environment: The rules of the game. *Proceedings of the 6th Workshop on Electronics for LHC Experiments*, pages 50–65, 2000.

[42] R. Ferraro, G. Foucard, A. Infantino, L. Dilillo, M. Brugger, A. Masi, R. García Alía, and S. Danzeca. COTS optocoupler radiation qualification process for LHC applications based on mixed-field irradiations. *IEEE Transactions on Nuclear Science*, 67(7):1395–1403, 2020.

[43] J. Budroweit and H. Patscheider. Risk assessment for the use of COTS devices in space systems under consideration of radiation effects. *MDPI*, 10(9):1008, 2021.

[44] NASA. Cots components in spacecraft systems: Understanding the risk. *The NESC 2014 Technical Update*, 2014.

[45] Turbosquid. *Silicio Crystal Lattice Modello 3D.* `https://www.turbosquid.com/it/3d-models/silicon-crystal-lattice-3d-model-1183566`.

[46] M. Guzzi. *Principi di fisica dei semiconduttori.* HOEPLI, 2008.

[47] Electronics Tutorials. *PN Junction Theory.* `https://www.electronics-tutorials.ws/diode/diode_2.html`.

[48] Hyper Physics. *P-N Energy Band.* `http://hyperphysics.phy-astr.gsu.edu/hbase/Solids/pnjun2.html#c1`.

[49] L. Xing-Ji, G. Hong-Bin, L. Mu-Jie, Y. De-Zhuang, H. Shi-Yu, and L. Chao-Ming. Degradation mechanisms of current gain in NPN transistors. *Chinese Physics B*, 19(6):066103, 2010.

[50] Z. You-Run, Z. Bo, L. Ze-Hong, L. Chang-Jin, and L. Zhao-Ji. Thermal analytic model of current gain for bipolar junction transistor-bipolar static induction transistor compound device. *Chinese Physics B*, 18(2):763, 2009.

[51] C. Claeys and E. Simoen. *Radiation Effects in Advanced Semiconductor Materials and Devices.* Springer, 2002.

[52] M. Oo *et al.* Neutron Radiation Effect On 2N2222 And NTE 123 NPN Silicon Bipolar Junction Transistors. *Proceedings of IOP Conference Series: Materials Science and Engineering*, 53, 2013.

[53] Electronics Tutorials. *NPN Transistor.* `https://www.electronics-tutorials.ws/transistor/tran_2.html`.

[54] Electronics Tutorials. *Transistor Tutorial Summary.* `https://www.electronics-tutorials.ws/transistor/tran_8.html`.

[55] R. Reed. *Guideline for Ground Radiation Testing and Using Optocouplers in the Space Radiation Environment.* NASA, 2002.

[56] A. Markus and K. Achim. Guidelines for reading an optocoupler datasheet. *Application Note 01 - Vishay Semiconductors*, 2015.

[57] C. Leroy and P.G. Rancoita. *Principles of Radiation Interaction in Matter and Detection.* World Scientific Publishing Co. Pte. Ltd., 2016.

[58] V.S. Vavilov and N.A. Ukhin. *Radiation effects in semiconductors and semiconductor apparatuses.* Consultants Bureau, New York, 1977.

[59] C. Leroy and P.G. Rancoita. Particle interaction and displacement damage in silicon devices operated in radiation environments. *Reports on Progress in Physics*, 70:493–625, 2007.

[60] D. Bechevet, M. Glaser, A. Houdayer, C. Lebel, C. Leroy, M. Moll, and P. Roy. Results of irradiation tests on standard planar silicon detectors with 7–10 MeV protons. *Nuclear Instruments and Methods in Physics Research Section A: Accelerators, Spectrometers, Detectors and Associated Equipment*, 479(2):487–497, 2002.

[61] J.R. Srour, C.J. Marshall, and P.W. Marshall. Review of displacement damage effects in silicon devices. *IEEE Transactions on Nuclear Science*, 50(3):653–670, 2003.

[62] G. Lindstroem and A. Vasilescu. *Displacement Damage in Silicon.* `https://rd50.web.cern.ch/NIEL/`.

[63] E. Lavrik. *Development of quality assurance procedures and methods for the CBM Silicon Tracking System.* PhD Thesis - U. Tubingen, 2017.

[64] M.J. Norgett, M.T. Robinson, and I.M. Torrens. A proposed method of calculating displacement dose rates. *Nuclear Engineering and Design*, 33(1):50–54, 1975.

[65] S. Chen and D. Bernard. On the calculation of atomic displacements using damage energy. *Results in Physics*, 16:102835, 2020.

[66] G. H. Kinchin and R. S. Pease. The displacement of atoms in solids by radiation. *Reports on Progress in Physics*, 18(1):1, 1955.

[67] A. R. Sattler. Ionization produced by energetic silicon atoms within a silicon lattice. *Physical Review*, 138:A1815–A1821, 1965.

[68] G.C. Messenger. A summary review of displacement damage from high energy radiation in silicon semiconductors and semiconductor devices. *IEEE Transactions on Nuclear Science*, 39(3):468–473, 1992.

[69] S. Baccaro and A. Cecilia. *Radiation effects on electronic components.* ENEA Technical Report RT/2002/25/FIS, 2002.

[70] R. Mo, P. Li, H. Lyu, B. Mei, Y. Sun, Q. Yu, S. Cao, Q. Wang, and H. Zhang. Study on annealing effect of bipolar transistors at different temperatures after total dose irradiation. *Microelectronics Reliability - Special issue of 34th European Symposium on Reliability of Electron Devices, Failure Physics and Analysis (ESREF2023)*, 150:115125, 2023.

[71] M. Barberio, M. Scisciò, S. Vallières, F. Cardelli, S. Chen, G. Famulari, T. Gangolf, G. Revet, A. Schiavi, M. Senzacqua, and P. Antici. Laser-accelerated particle beams for stress testing of materials. *Nature Communications*, 9, 2018.

[72] M. Guthoff, W. de Boer, and S. Müller. Simulation of beam induced lattice defects of diamond detectors using FLUKA. *Nuclear Instruments and Methods in Physics Research A*, 735, 2013.

[73] R. C. Alig and S. Bloom. Electron-hole-pair creation energies in semiconductors. *Physical Review Letters*, 35:1522–1525, 1975.

[74] G. C. Messenger and M. S. Ash. *The effects of radiation on electronic systems.* Springer, 1986.

[75] R. F. Laitano. *Fondamenti di dosimetria delle radiazioni ionizzanti.* ENEA, 2019.

[76] General Atomics. *TRIGA Nuclear Reactors.* `https://www.ga.com/triga/`.

[77] C. Consolandi, P. D'Angelo, G. Fallica, R. Mangoni, R. Modica, S. Pensotti, and Pier Giorgio Rancoita. Systematic investigation of monolithic bipolar transistors irradiated with neutrons, heavy ions and electrons for space applications. *Nuclear Instruments and Methods in Physics Research Section B-beam Interactions With Materials and Atoms*, 252:276–284, 2006.

[78] PV-Manifacturing. *Recombination processes.* `https://pv-manufacturing.org/metrology/recombination-processes/#:~:text=Recombination%20is%20classified%20as%20either,as%20trap%2Dassisted)%20recombination.`

[79] J. Assaf. Bulk and surface damages in complementary bipolar junction transistors produced by high dose irradiation. *Chinese Physics B*, 27(1):016103, 2018.

[80] G. C. Messenger and J. P. Spratt. The effects of neutron irradiation on germanium and silicon. *Proceedings of the IRE*, 46(6):1038–1044, 1958.

[81] ASIF. *Generalized Messenger-Spratt Equation for Gain Degradation of Bipolar Transistors.* `https://www.sr-niel.org/index.php/sr-niel-long-write-up/displacement-damage-and-gain-degradation-of-bjt`.

[82] L. Xing, L. Chao-Ming, and Y. Jianqun. Synergistic effect of ionization and displacement damage in NPN transistors caused by protons with various energies. *IEEE Transactions on Nuclear Science*, 62(3):1375–1382, 2015.

[83] Bhaskar Mukherjee and Stefan Simrock. *Application of low cost GaAs LED as neutron kerma dosimeter and fluence monitor at FLASH.* TESLA-FEL 2007-03, 2007.

[84] A. Cemmi. Optical characterization and irradiation tests at ENEA calliope lab. *17th B2GM ECL meeting*, 2014.

[85] *Advanced Laser Light Source (ALLS) Laboratory.* `https://inrs.ca/en/research/research-facilities/find-a-research-facility/advanced-laser-light-source-laboratory/`.

[86] D. Strickland and G. Mourou. Compression of amplified chirped optical pulses. *Optics Communications*, 55(6):447–449, 1985.

[87] *ALLS - Beamlines and endstations.* `https://alls.inrs.ca/en/beamlines-endstations`.

[88] S. Vallieres, M. Salvadori, P. Puyuelo-Valdes, S. Payeur, S. Fourmaux, and F. Consoli *et al.* Thomson parabola and time-of-flight detector cross-calibration methodology on the ALLS 100 TW laser-driven ion acceleration beamline. *Review of Scientific Instruments*, 91, 2020.

[89] M. Barberio and P. Antici. Laser-PIXE using laser-accelerated proton beams. *Scientific Reports*, 9:6855, 2019.

[90] A. Morabito, M. Scisciò, S. Veltri, M. Migliorati, and P. Antici. Design and optimization of a laser-PIXE beamline for material science applications. *Laser and Particle Beams*, 37:1–10, 2019.

[91] M. Roth and M. Schollmeier. Ion Acceleration - Target Normal Sheath Acceleration. *Proceedings of CAS CERN Accelerator School: Plasma Wake Acceleration*, pages 231–271, 2016.

[92] A. Maffini, F. Mirani, and M. Galbiati *et al.* Towards compact laser-driven accelerators: exploring the potential of advanced double-layer targets. *EPJ Techn Instrum*, 10, 2023.

[93] C. J. Joachain. High-intensity laser-atom interactions. *Europhysics Letters*, 108(4):44001, 2014.

[94] P. Gibbon. *Short Pulse Laser Interactions with Matter.* Imperial College Press, 2005.

[95] N. A. Krall. *Principles of Plasma Physics.* McGraw-Hill, 1973.

[96] W. L. Kruer. *The physics of laser plasma interactions.* CRC Press, 2003.

[97] P. Gibbon. Introduction to Plasma Physics. *CAS - CERN Accelerator School: Plasma Wake Acceleration*, pages 51–65, 2016.

[98] D. Giulietti and L. Gizzi. X-ray emission from laser-produced plasmas. *La Rivista del Nuovo Cimento*, 21, 1998.

[99] M. Salvadori. *Advanced time-of-flight diagnostics for real-time characterization of ions accelerated by high energy lasers.* PhD Thesis - Sapienza University of Rome - Institut National de la Recherche Scientifique (Québec), 2021.

[100] A. McIlvenny, H. Ahmed, C. Scullion, D. Doria, L. Romagnani, P. Martin, K. Naughton, A. Sgattoni, D. R. Symes, A. Macchi, P. McKenna, M. Zepf, S. Kar, and M. Borghesi. Characteristics of ion beams generated in the interaction of ultra-short laser pulses with ultra-thin foils. *Plasma Physics and Controlled Fusion*, 62(5):054001, 2020.

[101] H. Daido, M. Nishiuchi, and A. Pirozhkov. Review of laser-driven ion sources and their applications. *Reports on progress in physics. Physical Society (Great Britain)*, 75:056401, 2012.

[102] A. Macchi, M. Borghesi, and M. Passoni. Ion acceleration by superintense laser-plasma interaction. *Reviews of Modern Physics*, 85:751–793, 2013.

[103] J. Fuchs, P. Antici, E. D'Humières, E. Lefebvre, M. Borghesi, E. Brambrink, C. Cecchetti, M. Kaluza, V. Malka, M. Manclossi, S. Meyroneinc, P. Mora, J. Schreiber, T. Toncian, H. Pépin, and P. Audebert. Laser-driven proton scaling laws and new paths towards energy increase. *Nature Physics*, 2, 2006.

[104] A. Fukumi, M. Nishiuchi, H. Daido, Z. Li, A. Sagisaka, K. Ogura, S. Orimo, M. Kado, Y. Hayashi, M. Mori, S. V. Bulanov, T. Esirkepov, K. Nemoto, Y. Oishi, T. Nayuki, T. Fujii, A. Noda, and S. Nakamura. Laser polarization dependence of proton emission from a thin foil target irradiated by a 70fs, intense laser pulse. *Physics of Plasmas*, 12(10):100701, 2005.

[105] A. Măgureanu, L. Dincă, C. Jalbă, R. F. Andrei, I. Burducea, D. G. Ghiţă, V. Nastasa, M. Gugiu, T. Asavei, O. Budrigă, D. Ticoş, V. Crăciun, B. Diaconescu, and C. M. Ticoş. Target characteristics used in laser-plasma acceleration of protons based on the TNSA mechanism. *Frontiers in Physics*, 10, 2022.

[106] E. Catrix, F. Boivin, K. Langlois, and S. Vallieres *et al.* Stable high repetition-rate laser-driven proton beam production for multidisciplinary applications on the advanced laser light source ion beamline. *Review of Scientific Instruments*, 94, 2023.

[107] M. Afshari, J. Hornung, A. Kleinschmidt, P. Neumayer, D. Bertini, and V. Bagnoud. Proton acceleration via the TNSA mechanism using a smoothed laser focus. *AIP Advances*, 10(3):035023, 2020.

[108] G. Cantono, A. Permogorov, and J. Ferri *et al.* Laser-driven proton acceleration from ultrathin foils with nanoholes. *Scientific Reports*, 11, 2021.

[109] M. Borghesi. Laser-driven ion acceleration: State of the art and emerging mechanisms. *Nuclear Instruments and Methods in Physics Research Section A: Accelerators, Spectrometers, Detectors and Associated Equipment - Proceedings of the first European Advanced Accelerator Concepts Workshop*, 740:6–9, 2014.

[110] Y. Takagi, N. Iwata, E. d'Humieres, and Y. Sentoku. Multivariate scaling of maximum proton energy in intense laser driven ion acceleration. *Phys. Rev. Res.*, 3:043140, 2021.

[111] A. Higginson, R. Gray, M. King, R. Dance, S. Williamson, N. Butler, R. Wilson, R. Capdessus, C. Armstrong, J. Green, S. Hawkes, P. Martin, W. Wei, S. Mirfayzi, X. Yuan, S. Kar, M. Borghesi, R. Clarke, D. Neely, and P. McKenna. Near-100 MeV protons via a laser-driven transparency-enhanced hybrid acceleration scheme. *Nature Communications*, 9:724, 2018.

[112] S. Keppler, N. Elkina, G. Becker, J. Hein, M. Hornung, M. Mäusezahl, C. Rödel, I. Tamer, M. Zepf, and M. Kaluza. Intensity scaling limitations of laser-driven proton acceleration in the TNSA-regime. *Physical Review Research*, 4, 2022.

[113] E. L. Clark, K. Krushelnick, M. Zepf, F. N. Beg, M. Tatarakis, A. Machacek, M. I. K. Santala, I. Watts, P. A. Norreys, and A. E. Dangor. Energetic heavy-ion and proton generation from ultraintense laser-plasma interactions with solids. *Physical Review Letters*, 85:1654–1657, 2000.

[114] F. Nürnberg, M. Schollmeier, E. Brambrink, A. Blazevic, D. Carroll, K. Flippo, D. Gautier, M. Geissel, K. Michel, B. Hegelich, O. Lundh, K. Markey, P. McKenna, D. Neely, J. Schreiber, and M. Roth. Radiochromic film imaging spectroscopy of laser-accelerated proton beams. *The Review of scientific instruments*, 80:033301, 2009.

[115] A. Niroomand-Rad, C.R. Blackwell, B.M. Coursey, K.P. Gall, J.M. Galvin, W.L. McLaughlin, A.S. Meigooni, R. Nath, J.E. Rodgers, and C.G. Soares. Radiochromic film dosimetry: Recommendations of AAPM Radiation Therapy Committee Task Group 55. American Association of Physicists in Medicine. *Medical Physics*, 25(11):2093–2115, 1998.

[116] A. Mancic, J. Robiche, P. Antici, P. Audebert, C. Blancard, P. Combis, F. Dorchies, G. Faussurier, S. Fourmaux, M. Harmand, R. Kodama, L. Lancia, S. Mazevet, M. Nakatsutsumi, O. Peyrusse, V. Recoules, P. Renaudin, R. Shepherd, and J. Fuchs. Isochoric heating of solids by laser-accelerated protons: Experimental characterization and self-consistent hydrodynamic modeling. *High Energy Density Physics*, 6(1):21–28, 2010.

[117] D. C. Carroll, P. McKenna, O. Lundh, F. Lindau, C.-G. Wahlström, S. Bandyopadhyay, D. Pepler, D. Neely, S. Kar, P. T. Simpson, K. Markey, M. Zepf, C. Bellei, R. G. Evans, R. Redaelli, D. Batani, M. H. Xu, and Y. T. Li. Active manipulation of the spatial energy distribution of laser-accelerated proton beams. *Physical Review E*, 76:065401, 2007.

[118] S. Baccaro, A. Cemmi, I. Di Sarcina, and G. Ferrara. *Gamma Irradiation Calliope Facility at ENEA Casaccia Research Centre.* ENEA Technical Report RT/2019/4/ENEA, 2019.

[119] Jyoti Bashyal. *Beer-Lambert Law: Statement, Derivation, Applications, Limitations.* `https://scienceinfo.com/beer-lambert-law-statement/`.

[120] ASTM International. *ISO/ASTM 51607-13 - Standard practice for use of an alanine-EPR dosimetry system.* `https://www.astm.org/e1607-13.html`.

[121] Libre Texts Chemistry. *EPR - Theory.* `https://chem.libretexts.org/Bookshelves/Physical_and_Theoretical_Chemistry_Textbook_Maps/Supplemental_Modules_(Physical_and_Theoretical_Chemistry)/Spectroscopy/Magnetic_Resonance_Spectroscopies/Electron_Paramagnetic_Resonance/EPR_-_Theory`.

[122] Università Politecnica delle Marche. *La spettroscopia EPR.* `https://www.univpm.it/Entra/Engine/RAServeFile.php/f/P002330/allegati_ins/ChiII(0910)Dia04EPR.pdf`.

[123] The University of Texas at Austin. *What is EPR?* `https://sites.cns.utexas.edu/epr_facility/what-epr`.

[124] The International Commission on Radiation Units and measurements (ICRU). *Fundamental quantities and units for ionizing radiation (Report No. 85)*, volume 11. Oxford University Press, 2011.

[125] F. H. Attix, W C. Roesch, and E. Tochilin. *Radiation Dosimetry.* Academic Press, 1968.

[126] National Institute of Standars and Technology. *X-Ray Mass Attenuation Coefficients - Silicon.* `https://physics.nist.gov/PhysRefData/XrayMassCoef/ElemTab/z14.html`.

[127] C. Ronsivalle, M. Carpanese, C. Marino, G. Messina, L. Picardi, S. Sandri, E. Basile, B. Caccia, D. Castelluccio, E. Cisbani, S. Frullani, F. Ghio, V. Macellari, M. Benassi, M. D'Andrea, and L. Strigari. The TOP-IMPLART project. *The European Physical Journal Plus*, 126:1–15, 2011.

[128] C. Ronsivalle, A. Ampollini, M. D. Astorino, and G. Bazzano *et al.* L'impianto TOP-IMPLART. *Focus ENEA*, pages 67–69, 2023.

[129] L. Picardi, C. Ronsivalle, and A. Vignati. Measurements of cavities of the Side Coupled Drift Tube Linac (SCDTL). *CERN Acceleratore Conference*, 1996.

[130] M. Martone, M. Angelone, and M. Pillon. The 14 MeV Frascati Neutron Generator. *Journal of Nuclear Materials*, 212-215:1661–1664, 1994. Fusion Reactor Materials.

[131] A. Pietropaolo, F. Andreoli, M. Angelone, U. Besi Vetrella, S. Fiore, S. Loreti, G. Pagano, R. Pilotti, and M. Pillon. The Frascati Neutron Generator:

A multipurpose facility for physics and engineering. *Journal of Physics: Conference Series*, 1021:012004, 2018.

[132] G. Bazzano, A. Ampollini, M.D. Astorino, F. Fortini, P. Nenzi, L. Picardi, C. Ronsivalle, E. Trinca, V. Surrenti, M. Vadrucci, F. Borgognoni, and E. Nichelatti. Electron beam qualification at ENEA frascati particle accelerators laboratory. *Proceedings of the 14th International Particle Accelerator Conference (IPAC'23)*, 2023.

[133] M. Vadrucci, P. Ferrari, F. Borgognoni, and L. Campani. The REX irradiation facility and its applications. *Nuclear Instruments and Methods in Physics Research Section A: Accelerators, Spectrometers, Detectors and Associated Equipment*, 930:126–131, 2019.

[134] J.C. Hourdakis and R. Nowotny. *Diagnostic Radiology Physics: a handbook for teachers and students.* IAEA, 2014.

[135] ASI Supported Irradiation Facilities (ASIF). *ASIF: ASI, ENEA, INFN agreements.* `https://www.asif.asi.it/`.

[136] Aerial. *Aerial.* `https://aerial-crt.com/en/home/`.

[137] B. D'Orsi, R. Carcione, and I. Di Sarcina *et al.* *Optimization of paper characterization procedures for Cultural Heritage.* ENEA Technical Report RT/2024/2/ENEA, 2024.

[138] IBA. *PPC05 Plane Parallel Chamber.* `https://www.iba-dosimetry.com/product/ppc05-plane-parallel-chamber`.

[139] A. Al-Sayed, M. El Ghazaly, E. M. Hussein, N. A. Kelany, M. A. Ibrahim, M. H. Younes, M. Abdel-Mageed, and A. Mohamed. On the color channel's effect on the dose-response of gafchromic ebt2 and ebt3 radiochromic films to 6 mev electron beam. *Radiation Physics and Chemistry*, 218:111565, 2024.

[140] Ashland. *GAFCHROMIC HD-V2.* `http://www.gafchromic.com/gafchromic-film/radiotherapy-films/HD-V2/index.asp`.

[141] European Space Components Coordination. *Total dose steady-state irradiation test method - ESCC Basic Specification No. 22900 (Issue 5).* ESA, 2016. `https://www.esa.int/Enabling_Support/Space_Engineering_Technology/European_Space_Components_Coordination`.

[142] Microsemi. *TECHNICAL DATASHEET - NPN silicon switching transistor.* `https://www.microsemi.com/document-portal/doc_view/8898-lds-0060-datasheet`.

[143] Microsemi. *TECHNICAL DATASHEET - PNP small signal silicon transistor.* `https://datasheet.octopart.com/JANTX2N2907A-Microsemi-datasheet-8328644.pdf`.

[144] Skyworks. *TECHNICAL DATASHEET - OLS249: Radiation-Tolerant Phototransistor Hermetic Surface-Mount Optocoupler.* `https://www.skyworksinc.com/-/media/SkyWorks/Documents/Products/2601-2700/OLS249_202682E.pdf`.

[145] Ingegneria Marketing Tecnologia. *IMT srl.* `https://www.imtsrl.it/`.

[146] Keysight. *B2902A Precision Source/Measure Unit.* `https://www.keysight.com/us/en/product/B2902A/precision-source-measure-unit-2-ch-100fa-210v-3a-dc-10-5a-pulse.html`.

[147] Keysight. *E3649A 100W Dual-Output Power Supply.* `https://www.keysight.com/us/en/support/E3649A/100w-dual-output-power-supply-two-35v-1-4a-60v-0-8a.html`.

[148] FTDI Chip. *USB Hi-Speed FT232H Evaluation Module.* `https://ftdichip.com/products/um232h/`.

[149] L. Chao-Ming, X. Li, G. Hong-Bin, Y. De-Zhuang, and H. Shi-Yu. Effect of bias condition on heavy ion radiation in bipolar junction transistors. *Chinese Physics B*, 21, 2012.

[150] European Space Components Coordination. *Guidelines for displacement damage irradiation testing - ESCC Basic Specification No. 22500 (Issue 1).* ESA, 2019. `https://escies.org/download/specdraftapppub?id=3804`.

[151] National Institute of Standars and Technology. *X-Ray Mass Attenuation Coefficients - Nickel.* `https://physics.nist.gov/PhysRefData/XrayMassCoef/ElemTab/z28.html`.

[152] İ. Baylakoğlu, A. Fortier, S. Kyeong, R. Ambat, H. Conseil-Gudla, M. H. Azarian, and M. G. Pecht. The detrimental effects of water on electronic devices. *e-Prime - Advances in Electrical Engineering, Electronics and Energy*, 1:100016, 2021.

[153] D. Codegoni, A. Colder, N. Croitoru, P. D'Angelo, M. DeMarchi, G. Fallica, A. Favalli, S. Leonardi, M. Levalois, P. Marie, R. Modica, P.G. Rancoita, and A. Seidman. Investigation of irradiated monolithic transistors for space applications. *Nuclear Instruments and Methods in Physics Research Section B: Beam Interactions with Materials and Atoms*, 217(1):65–76, 2004.

[154] M. Scisciò, M. Barberio, C. Liberatore, S. Veltri, A. Laramée, L. Palumbo, F. Legaré, and P. Antici. Analysis of induced stress on materials exposed to laser-plasma radiation during high-intensity laser experiments. *Applied Surface Science*, 421:200–204, 2017.

[155] A. Colder, N. Croitoru, P. D'Angelo, M. De Marchi, G. Fallica, S. Leonardi, M. Levalois, S. Marcolongo, P. Marie, R. Modica, P.G. Rancoita, and A. Seidman. Study of radiation effects on bipolar transistors. *Nuclear Instruments and Methods in Physics Research Section B: Beam Interactions with Materials and Atoms*, 179(3):397–402, 2001.

[156] *Los Alamos National Laboratory.* The mcnp®code. `https://mcnp.lanl.gov/`.

[157] Italian Space Agency (ASI). *Screened Relativistic (SR) Treatment for NIEL Dose Nuclear and Electronic Stopping Power Calculator.* `https://www.sr-niel.org/index.php/sr-niel-web-calculators`.

[158] ASIF. *NIEL Dose Calculator for electrons spectral fluence.* `https://www.sr-niel.org/index.php/sr-niel-web-calculators/niel-dose-calculator-for-spectral-fluence-of-electrons-protons-and-ions/electrons-niel-dose-calculator`.

[159] ASIF. *Calculation of NIEL and Displacement Stopping Power for Elements and Compounds.* `https://www.sr-niel.org/index.php/sr-niel-long-write-up/niel-and-displacement-stopping-power`.

[160] J.F. Ziegler. *SRIM - The Stopping and Range of Ions in Matter.* `http://www.srim.org/`.

[161] S.C. Vallieres. *Towards reliable, intense and high repetition-rate laser-driven ion beamlines.* PhD thesis - Université de Bordeaux - Institut National de la Recherche Scientifique (Québec), 2020. `https://tel.archives-ouvertes.fr/tel-03149754`.

[162] ASIF. *NIEL Dose Calculator Protons & Ions spectral fluence.* `https://www.sr-niel.org/index.php/sr-niel-web-calculators/niel-dose-calculator-for-spectral-fluence-of-electrons-protons-and-ions/protons-ions-niel-dose-calculator`.

[163] R.S. Caswell, J.J. Coyne, and M.L. Randolph. Kerma factors of elements and compounds for neutron energies below 30 MeV. *The International Journal of Applied Radiation and Isotopes*, 33(11):1227–1262, 1982.

[164] Renesas. *Explanation of Photocoupler / Optocoupler Specifications.* `https://www.renesas.com/us/en/products/interface/optoelectronics/explanation-photocoupler-optocoupler-specifications`.